

# Multi-Species Atmospheric Continuous Measurements as a Tool to Study Changes in the Carbon Cycle

Elena A. Kozlova

A thesis presented to the  
School of Environmental Sciences  
University of East Anglia  
in candidature for the degree of  
Doctor of Philosophy

January 2010

© This copy of the thesis has been supplied on condition that anyone who consults it is understood to recognise that its copyright rests with the author and that no quotation from the thesis, nor any information derived therefrom, may be published without the author's prior written consent.



## ABSTRACT

Observations of atmospheric gas concentrations are very useful in the study of globally important ecosystems. Past observational efforts, however, have been focused on atmospheric measurements of ‘background air’, leaving the continental interiors under-represented. I present results from pilot, multi-species, atmospheric measurement campaigns in the Hainich Forest, Germany in 2005, and I describe the development, deployment, and results from high-precision continuous atmospheric measurements of CO<sub>2</sub>, O<sub>2</sub>, CH<sub>4</sub>, CO and N<sub>2</sub>O at the Zotino Tall Tower Observatory (ZOTTO) in the boreal forest of central Siberia from November 2005 to June 2007. Atmospheric variations were studied on seasonal, synoptic and diurnal time scales. Among the interesting features of the ZOTTO record are:

- 1) CO<sub>2</sub> and O<sub>2</sub> seasonal amplitudes of 26.6 ppm and 190 per meg (equivalent to 39.8 ppm in CO<sub>2</sub>);
- 2) a west-east gradient of -7 ppm of CO<sub>2</sub> (in July 2006) between Shetland Islands (Scotland) and ZOTTO that reflects summertime continental CO<sub>2</sub> uptake;
- 3) attenuation of the oceanic component of the O<sub>2</sub> seasonal amplitude (Atmospheric Potential Oxygen; APO) at ZOTTO resulting in an amplitude of 45 per meg compared to 56 per meg observed at Shetlands;
- 4) high fire emissions of CH<sub>4</sub> and CO in summertime with the minima of their monthly averages similar to seasonal cycles of these gases in the marine boundary layer;
- 5) large vertical gradients in CO<sub>2</sub>, CH<sub>4</sub> and CO during ‘cold events’ (air temperatures below -30°C), suggesting separated layers of air and local sources possibly combined with other effects;
- 6) lower CO/CO<sub>2</sub> ratios (1-4 ppb/ppm) from fossil fuel burning compared to those measured in Europe, with large CH<sub>4</sub> contributions;
- 7) diurnal vertical CO<sub>2</sub> gradients in spring 2007 giving estimates of night-time respiration fluxes of  $0.04 \pm 0.02 \text{ mol C m}^{-2} \text{ d}^{-1}$ .

A comparison with REgional MOdel (REMO) simulations showed discrepancies in daily averages of CO<sub>2</sub> attributed to errors in the model’s vertical mixing and prescribed terrestrial fluxes. Nevertheless, REMO exhibited good agreement in meteorological variables (compared to weather stations close to ZOTTO) and seasonal cycles of CO<sub>2</sub>, APO and CO. Studies of fire events showed high emission ratios of CO/CO<sub>2</sub> and CH<sub>4</sub>/CO<sub>2</sub>, comparable with those reported for similar ecosystems, and in relatively good agreement with the model estimates.



# TABLE OF CONTENTS

ABSTRACT .....	iii
TABLE OF CONTENTS .....	v
LIST OF FIGURES .....	ix
LIST OF TABLES .....	xiii
DEDICATION .....	xv
ACKNOWLEDGEMENTS .....	xvii
CHAPTER 1. Introduction.....	1
1.1 Introduction to Chapter .....	1
1.2 Global climate change and composition of the atmosphere: what is the greenhouse effect?.....	1
1.3 Why study climatic and atmospheric changes in Siberia?.....	5
1.4 Tall tower atmospheric measurements in central Siberia – an approach for studying long-term atmospheric changes in continental interiors.....	8
1.5 Gas species measured at ZOTTO: general overview and motivation for their continuous measurement.....	10
1.5.1 CO <sub>2</sub> .....	10
1.5.2 O <sub>2</sub> .....	12
1.5.3 CH <sub>4</sub> .....	15
1.5.4 CO .....	16
1.5.5 N <sub>2</sub> O.....	17
1.6 Thesis overview .....	19
CHAPTER 2. Variations of biogeochemical gases and isotopes in an unmanaged forest .....	21
2.1 Introduction to Chapter .....	21
2.2 Site description.....	22
2.3 Variations of CO <sub>2</sub> , O <sub>2</sub> and <sup>13</sup> C-CO <sub>2</sub> .....	25
2.4 Variations of CH <sub>4</sub> , CO and N <sub>2</sub> O .....	33
2.5 Synoptic variations of sulphur hexafluoride (SF <sub>6</sub> ).....	36
CHAPTER 3. Methodology for autonomous continuous measurements .....	41
3.1 Introduction to Chapter .....	41
3.2 The ZOTTO measurement system: description and operation .....	43
3.2.1 Air intake subsystem.....	43
3.2.2 Air drying subsystem .....	46
3.2.3 O <sub>2</sub> and CO <sub>2</sub> measurement subsystem.....	48
3.2.4 Gas chromatographic (GC) measurement subsystem .....	54

3.2.5 GC peripherals subsystem.....	60
3.2.5.1 Nitrogen generating and purifying component .....	60
3.2.5.2 Synthetic air generating and purifying component .....	61
3.2.5.3 Hydrogen generating and purifying component .....	62
3.2.5.4 Argon-methane component.....	62
3.2.6 Data acquisition procedures .....	63
CHAPTER 4. Calibration methodology and results .....	67
4.1 Introduction to Chapter .....	67
4.2 Calibration methodology and scales .....	67
4.2.1 Definition of the O <sub>2</sub> units .....	73
4.2.2 Propagation of the S1 scale .....	74
4.3 Stability of WT concentrations .....	75
4.4 ZOTTO calibration cylinders.....	79
4.4.1 CH <sub>4</sub> , CO <sub>2</sub> , N <sub>2</sub> O and CO concentrations .....	79
4.4.2 O <sub>2</sub> concentrations .....	81
4.5 Data evaluation results: repeatability and comparability .....	83
4.6 O <sub>2</sub> fractionation issues .....	88
CHAPTER 5. Seasonal, synoptic and diurnal scale variability of biogeochemical trace gases and O <sub>2</sub> in central Siberia.....	91
5.1 Introduction to Chapter .....	91
5.2 The ZOTTO site.....	92
5.3 Seasonal variations of CO <sub>2</sub> , O <sub>2</sub> and APO .....	93
5.3.1 Comparison with TM3 model simulations.....	98
5.4 ZOTTO O <sub>2</sub> calibration scale and seasonal cycle revisions .....	101
5.4.1 Ar/N <sub>2</sub> correction of O <sub>2</sub> data.....	101
5.4.2 Seasonal variations of CO <sub>2</sub> , O <sub>2</sub> and APO from the revised data records at SIS and ZOTTO.....	106
5.4.3 Comparison with TM3 model simulations.....	109
5.5 Seasonal variations of CH <sub>4</sub> and CO .....	109
5.6 Synoptic variations.....	114
5.6.1 ‘Cold events’ .....	114
5.6.2 Pollution events.....	122
5.7 Diurnal variations.....	128
CHAPTER 6. Regional model (REMO) simulations over Eurasia as compared to the ZOTTO measurements.....	131
6.1 Introduction to Chapter .....	131

6.2 Description of REMO inputs and outputs.....	132
6.3. Simulations of meteorological variables in REMO .....	136
6.3.1 Surface temperature .....	137
6.3.2 Wind speeds .....	140
6.3.3 Wind direction.....	140
6.3.4 Surface pressure .....	143
6.3.5 Vertical mixing .....	144
6.4 Atmospheric concentrations of CO <sub>2</sub> : model-observations comparison .....	153
6.5 Atmospheric concentrations of O <sub>2</sub> and APO: model-observations comparison	157
6.6 Atmospheric concentrations of CO <sub>2</sub> , CO, O <sub>2</sub> and CH <sub>4</sub> during fire events: model- observations comparison.....	162
CHAPTER 7. Summary and Outlook .....	173
APPENDIX 1. Derivation of equation describing O <sub>2</sub> /N <sub>2</sub> changes in ambient air .....	185
APPENDIX 2. The practical implementation for propagating calibration scales for long- term atmospheric measurements .....	189
APPENDIX 3. Zotino Tall Tower File Structure.....	193
APPENDIX 4. Protocols for automated data quality control at ZOTTO .....	199
APPENDIX 5. Electronics schematic for temperature control of Servomex O <sub>2</sub> analyser in Pink Box.....	207
BIBLIOGRAPHY .....	209



## LIST OF FIGURES

<b>Figure 1.1:</b> A simplified model of the ‘greenhouse effect’ .....	3
<b>Figure 1.2:</b> Spatial distribution of the summer surface warming.....	6
<b>Figure 1.3:</b> Latitude-time section of surface mean temperature anomalies .....	7
<b>Figure 1.4:</b> A typical afternoon vertical profile of CO <sub>2</sub> concentration in the surface layer, mixed layer and free troposphere.....	9
<b>Figure 1.5:</b> CO <sub>2</sub> concentrations as observed at Mauna Loa (Hawaii) and South Pole from 1958 to 2010.....	11
<b>Figure 1.6:</b> Globally averaged CH <sub>4</sub> concentrations and their growth rate from 1984 to 2007.....	15
<b>Figure 2.1:</b> CO <sub>2</sub> , O <sub>2</sub> and δ <sup>13</sup> C-CO <sub>2</sub> concentrations of air samples collected from 15 to 18 May 2005. ....	24
<b>Figure 2.2:</b> Meteorological variables from 15 to 18 May 2005. ....	25
<b>Figure 2.3:</b> CO <sub>2</sub> , O <sub>2</sub> and δ <sup>13</sup> C-CO <sub>2</sub> concentrations of air samples on 16 and 17 July 2005.....	26
<b>Figure 2.4:</b> Meteorological variables on 16-17 July 2005. ....	27
<b>Figure 2.5:</b> O <sub>2</sub> /CO <sub>2</sub> ratios at different sampling heights and times of day.....	29
<b>Figure 2.6:</b> Nighttime and daytime isotopic signatures of air samples collected in Hainich Forest in May and July 2005. ....	32
<b>Figure 2.7:</b> CH <sub>4</sub> , CO and N <sub>2</sub> O concentrations of air samples collected from 15 to 18 May 2005. ....	33
<b>Figure 2.8:</b> CH <sub>4</sub> , CO and N <sub>2</sub> O concentrations of air samples collected on 16 and 17 July 2005.....	34
<b>Figure 2.9:</b> Daily variations of SF <sub>6</sub> concentrations during two sampling campaign in 2005.....	35
<b>Figure 2.10:</b> 24-hour back trajectories of air masses arriving at the Hainich tower site on 17 July 2005. ....	37
<b>Figure 2.11:</b> 48-hour back trajectories for 16 and 17 July 2005 using the FNL meteorological dataset.....	39
<b>Figure 3.1:</b> Gas-handling schematic for atmospheric measurements of O <sub>2</sub> , CO <sub>2</sub> , CH <sub>4</sub> , CO and N <sub>2</sub> O. ....	42
<b>Figure 3.2:</b> Air intake subsystem. ....	44
<b>Figure 3.3:</b> Blockage of the tower air inlets at 300 m.....	45
<b>Figure 3.4:</b> Air drying subsystem.....	47
<b>Figure 3.5:</b> O <sub>2</sub> and CO <sub>2</sub> measurement subsystem .....	49
<b>Figure 3.6:</b> The interior of the custom-built Pink Box.....	50

<b>Figure 3.7:</b> Uncalibrated signals from O <sub>2</sub> and CO <sub>2</sub> analysers.....	51
<b>Figure 3.8:</b> The Pink Box's temperature for four randomly selected days in December 2005.....	52
<b>Figure 3.9:</b> GC measurement and peripherals subsystems.....	54
<b>Figure 3.10:</b> Typical chromatograms of CH <sub>4</sub> , CO and N <sub>2</sub> O. ....	57
<b>Figure 3.11:</b> The screen diagram displaying main parts of the measurement system....	64
<b>Figure 3.12:</b> The screen diagram showing the diagnostic data quality indicators. ....	65
<b>Figure 3.13:</b> Diagnostic parameters .....	66
<b>Figure 4.1:</b> Thermally insulated enclosure (Blue Box) with horizontally placed calibration cylinders.....	68
<b>Figure 4.2:</b> Examples of a WSS calibration cycle for O <sub>2</sub> and CO <sub>2</sub> .....	71
<b>Figure 4.3:</b> CH <sub>4</sub> and CO calibration coefficients from May 2006 to June 2007.....	72
<b>Figure 4.4:</b> WT concentrations for CO <sub>2</sub> and O <sub>2</sub> from January to June 2007. ....	77
<b>Figure 4.5:</b> GCWT concentrations for CH <sub>4</sub> from May 2006 to June 2007.....	78
<b>Figure 4.6:</b> Changes in O <sub>2</sub> concentrations for WSS and TT cylinders.....	83
<b>Figure 4.7:</b> Results from O <sub>2</sub> /N <sub>2</sub> fractionation tests.....	89
<b>Figure 5.1:</b> Seasonal cycles of CO <sub>2</sub> , O <sub>2</sub> and APO from 52 m height of the ZOTTO tower.....	94
<b>Figure 5.2:</b> CO <sub>2</sub> concentration interpolated differences between 52 and 300 m sampling lines.....	95
<b>Figure 5.3:</b> Seasonal cycles of CO <sub>2</sub> , O <sub>2</sub> and APO from model simulations at ZOTTO and SIS.....	99
<b>Figure 5.4:</b> Measured and corrected O <sub>2</sub> /N <sub>2</sub> ratios from flask samples collected at ZOTTO from October 2006 to May 2007. ....	103
<b>Figure 5.5:</b> Seasonal cycles of CO <sub>2</sub> , O <sub>2</sub> and APO from 52 m height of the ZOTTO tower based on the revised dataset.....	107
<b>Figure 5.6:</b> Seasonal cycles of CO <sub>2</sub> , O <sub>2</sub> and APO from model simulations at ZOTTO and SIS.....	108
<b>Figure 5.7:</b> Seasonal variations of CH <sub>4</sub> concentrations at ZOTTO.....	110
<b>Figure 5.8:</b> Seasonal variations of CO concentrations at ZOTTO.....	112
<b>Figure 5.9:</b> CO <sub>2</sub> and O <sub>2</sub> variations at five heights of the tower over a period of 'cold events' in November 2006.....	115
<b>Figure 5.10:</b> CO <sub>2</sub> , O <sub>2</sub> and temperature variations over a period of 'cold events' in February 2007.....	118
<b>Figure 5.11:</b> O <sub>2</sub> and CO <sub>2</sub> concentration correlations as observed from five levels of the ZOTTO tower. ....	119

<b>Figure 5.12:</b> CH <sub>4</sub> and CO concentrations over a period of 'cold events' in February 2007.....	120
<b>Figure 5.13:</b> CO <sub>2</sub> , O <sub>2</sub> and CO concentrations during a pollution event on 27 February 2007.....	121
<b>Figure 5.14:</b> CO <sub>2</sub> , O <sub>2</sub> , CH <sub>4</sub> and CO variations at five levels of ZOTTO tower and REMO CO <sub>2</sub> and CO simulations in December 2006.....	123
<b>Figure 5.15:</b> 72-hour back trajectories for the air masses arriving at ZOTTO over the period of the pollution event on 07 December 2007.....	125
<b>Figure 5.16:</b> Diurnal variations of CO <sub>2</sub> and O <sub>2</sub> concentrations in May 2007.....	127
<b>Figure 5.17:</b> Vertical concentration gradients of CO <sub>2</sub> and CH <sub>4</sub> up to 300 m on 7-8 May 2007.....	129
<b>Figure 6.1:</b> Surface temperature records at four localities around ZOTTO compared to REMO simulations.....	137
<b>Figure 6.2:</b> Surface temperature records at four localities around ZOTTO and REMO simulations in July and November 2006.....	138
<b>Figure 6.3:</b> Wind speeds at four localities around ZOTTO compared to REMO simulations in July and November 2006.....	139
<b>Figure 6.4:</b> Wind vector components at four localities around ZOTTO and REMO simulations in July 2006.....	141
<b>Figure 6.5:</b> Wind vector components at four localities around ZOTTO and REMO simulations in November 2006.....	142
<b>Figure 6.6:</b> Surface pressure at four localities around ZOTTO and REMO simulations in July and November 2006.....	143
<b>Figure 6.7:</b> Correlation between the radiosonde potential temperature and simulated potential temperature at six vertical layers of the REMO vertical domain.....	146
<b>Figure 6.8:</b> Vertical profiles of potential temperatures from radiosonde and REMO simulated potential temperatures during four evenings in summer 2006.....	147
<b>Figure 6.9:</b> Vertical profiles of potential temperatures from radiosonde and REMO simulated potential temperatures during four evenings in summer 2006.....	148
<b>Figure 6.10:</b> Observed and simulated ambient CO <sub>2</sub> concentrations at ZOTTO over the period of 'cold events' in November 2006.....	150
<b>Figure 6.11:</b> Vertical profiles of potential temperatures from radiosonde and REMO simulated potential temperatures in winter - early spring 2007.....	151
<b>Figure 6.12:</b> Vertical profiles of potential temperatures from radiosonde and REMO simulated potential temperatures during four afternoons in winter 2006-7.....	152
<b>Figure 6.13:</b> Observed and simulated seasonal cycles of CO <sub>2</sub> at ZOTTO.....	153

<b>Figure 6.14:</b> Observed and simulated seasonal cycles of CO <sub>2</sub> at ZOTTO in May - October 2006 and October 2006 – May 2007.....	155
<b>Figure 6.15:</b> CO <sub>2</sub> fluxes as observed at ZOTTO and simulated by the BIOME-BGC biosphere model in spring - summer 2004.....	156
<b>Figure 6.16:</b> Observed and simulated seasonal cycles of O <sub>2</sub> at ZOTTO from January 2005 to June 2007 at 52 and 300 m. ....	159
<b>Figure 6.17:</b> Observed and simulated seasonal cycles of APO at ZOTTO from January 2005 to June 2007 at 52 and 300 m. ....	160
<b>Figure 6.18:</b> Averages of weekly flask samples collected at Shetlands Islands (SIS) from 01 July 2004 to 01 January 2008 compared to weekly trimmed averages of REMO APO simulations. ....	162
<b>Figure 6.19:</b> CO measurements at ZOTTO compared to REMO simulations. ....	163
<b>Figure 6.20:</b> CO measurements at ZOTTO compared to REMO CO simulations during the fire event on 18-26 July 2006.....	164
<b>Figure 6.21:</b> CO measurements at ZOTTO compared to REMO CO simulations during the fire event on 12-18 July 2006.....	166
<b>Figure 6.22:</b> Average O <sub>2</sub> /CO <sub>2</sub> exchange ratios during the fire event on 18-26 July 2006 from ZOTTO measurements and REMO simulations. ....	168

## LIST OF TABLES

<b>Table 2.1:</b> O <sub>2</sub> /CO <sub>2</sub> ratios at different heights and time of day from flask air samples collected in May 2005.....	28
<b>Table 2.2:</b> O <sub>2</sub> /CO <sub>2</sub> ratios at different heights and time of day from flask air samples collected in July 2005.....	28
<b>Table 3.1:</b> Settings and specifications for CH <sub>4</sub> , CO and N <sub>2</sub> O measurements on the Agilent 6890A GC.....	55
<b>Table 3.2:</b> The GC method run table.....	60
<b>Table 3.3:</b> Parameters within ChemStation™ for optimal integration of CH <sub>4</sub> , CO and N <sub>2</sub> O peaks.....	61
<b>Table 4.1:</b> Initially assigned calibration cylinders concentrations used to define S1 scales for CH <sub>4</sub> , CO <sub>2</sub> , N <sub>2</sub> O and CO.....	80
<b>Table 4.2:</b> Calibration cylinders concentrations after re-analyses in December 2007 - February 2008.....	80
<b>Table 4.3:</b> Summary of O <sub>2</sub> cylinder (WSS and TT) concentrations.....	82
<b>Table 4.4:</b> Repeatability and comparability goals and achievements for all gas analysers at ZOTTO.....	84
<b>Table 5.1:</b> Emission ratios for a pollution event on 25-27 February 2007.....	122
<b>Table 5.2:</b> CO/CO <sub>2</sub> and CH <sub>4</sub> /CO <sub>2</sub> emission ratios from the bottom and top levels of the ZOTTO tower and modelled CO/CO <sub>2</sub> ratios from REMO simulations.....	126
<b>Table 6.1:</b> Summary of REMO characteristics.....	133
<b>Table 6.2:</b> Summary of all meteorological data.....	136
<b>Table 6.3:</b> Emission ratios (ER's) of gaseous species during the fire events in central Siberia in July 2006.....	168



*Посвящается моим родителям*

## Парус

*Белеет парус одинокой  
В тумане моря голубом....  
Что ищет он в стране далекой?  
Что кинул он в краю родном?..*

*Играют волны — ветер свищет,  
И мачта гнется и скрипит...  
Увы! он счастья не ищет,  
И не от счастья бежит!*

*Под ним струя светлей лазури,  
Над ним луч солнца золотой...  
А он, мятежный, просит бури,  
Как будто в бурях есть покой!*

М. Ю. Лермонтов



## ACKNOWLEDGEMENTS

To start with, I would like to sincerely thank my family and friends, both in Russia and abroad, whose continuous support and encouragement over the last several years have been a great help and incentive for my research.

I am very grateful to both of my scientific supervisors at UEA, Andrew Manning and Andy Watson, who have significantly helped me in many different ways throughout my studies. Apart from scientific supervision, I would also like thank Andrew for his great contribution to the technical set-up and development of the ZOTTO measurement system and for sharing his expertise with me, especially on the subject of the high-precision O<sub>2</sub> measurements.

I want to thank many of the staff of MPI-BGC, institution where I spent first two years of my Ph.D., for their continuous support and enthusiasm about the ZOTTO project despite its many challenges. I would like to personally thank Reimo Leppert, Thomas Seifert, Steffen Schmidt, Rene Schwalbe, Armin Jordan, Karl Kuebler, Michael Hielscher, Frank Voigt, Bernd Schlöffel and Martin Heimann for their various but all important and highly appreciated contributions to the project. I am very thankful for our fruitful scientific collaboration with another colleague from MPI-BGC, Ute Karstens, who provided me with the results of her model simulations, which have become an important part of my thesis study. I am obliged to Steffen Schmidt who prepared several schematics of the measurement system presented in Chapter 3. Many thanks to Reimo Leppert who put together the electronic schematics for our custom-built active temperature controlling unit for the O<sub>2</sub> analyser shown in Appendix 5.

Outside of Europe, I am indebted to Yegor Kisilyakhov (Sukachev Institute of Forest, Krasnoyarsk, Russia) for his enthusiastic support of this project both in Germany and at ZOTTO. His positive attitude to work and overcoming various difficulties (like climbing a 300-m tower at -30°C) have been inspirational to me and many others. I also want to thank Aleksey Panov (same institution), Volodya Kislitsin and Sascha Dolgushin for their help with equipment and logistics of the station. I would also like to mention and thank all workers from the Russian construction company ‘Stroitechinvest’.

I am very grateful to Doug Worthy (Environmental Canada) for his valuable and always prompt advice on the development of GC measurements, and to Ralph Keeling, Adam Cox and Bill Paplawsky (Scripps Institution of Oceanography) for a loan of the O<sub>2</sub> sensor, calibration cylinder preparations and discussions and advice on O<sub>2</sub> calibration scale. I am also thankful to Ronnie Robertson from Shetland Islands for the flask samples collection.

I would also like to thank Martin Manning (Victoria University, New Zealand) for sharing his expertise in mathematics by deriving the equation in Appendix 1. Many thanks go to Chris Rella (Picarro) whose volunteering to proof-reading and sharing his scientific ideas on my thesis were very helpful in the last months of my writing.

The ZOTTO project was funded by Max Plank Society through International Science and Technology Center (ISTC) partner project #2757p within the frame of the proposal “Observing and Understanding Biogeochemical Responses to Rapid Climate Changes in Eurasia”. My funding was provided by MPI-BGC internal studentship and later by a UEA Zuckerman Studentship.

# CHAPTER 1. Introduction

## 1.1 Introduction to Chapter

In this chapter I outline the general connections between global climate change and atmospheric composition (Section 1.2), explain the motivation for establishing an atmospheric monitoring station in central Siberia (1.3), and present the general philosophy of ‘tall tower’ measurements (1.4), followed by a description of the gas species I measured in Siberia (1.5). Section 1.6 provides an overview of the whole thesis, with outlines of the main subjects of discussions in each Chapter.

Although the largest part of this thesis is devoted to analyses of the measurements I collected from Siberia, I also present datasets from another location, namely an undisturbed old-aged beech forest in central Germany (Hainich National Park; Chapter 2). The data analysis based on the measurements collected at the Hainich Forest shows the benefits of multi-species measurements for studying processes in natural ecosystems, even for short, campaign-based studies. These data were obtained by collecting flask air samples during two intensive field campaigns in May and July 2005 and their subsequent analyses at Max Planck Institute for Biogeochemistry (MPI-BGC, Jena, Germany). These datasets also benefit from the complementary meteorological parameters from a 43-m-tall flux tower at the same location. The other chapters of this thesis are devoted to the development of an automated measurement system and analyses of multi-species continuous measurements in central Siberia. Since most of the data presented in this thesis were collected in Siberia this Introduction will be focused on the climate and biogeochemistry of relevance there.

## 1.2 Global climate change and composition of the atmosphere: what is the greenhouse effect?

The hypothesis of a potential link between changes in atmospheric composition and climate was first proposed by Joseph Fourier almost two centuries ago [*Fourier*, 1827]. It gradually evolved from simple observations of the sunlight reflection and absorption effects to more elaborate laboratory tests [*Weart*, 2003]. Several discoveries and formulations discussed below can be considered as milestones in the development of climate change research.

In 1859, John Tyndall discovered that, unlike the most abundant components of the atmosphere (nitrogen (N<sub>2</sub>) and oxygen (O<sub>2</sub>)), some other molecules, which comprise a much smaller percentage of the volume of the atmosphere, could absorb the infrared long-wave radiation emitted by the Earth’s surface [*Tyndall*, 1861]. As these molecules

represent a natural shield assisting in trapping radiation close to the land (or ocean) surface they contribute to the so-called ‘greenhouse effect’ which causes the warming of the atmosphere and the Earth’s surface. The term ‘greenhouse effect’ came from the analogy of its consequences, the warming of air, with the effect known and used for centuries for growing plants in greenhouses. In the latter case, however, the increase in air temperature is achieved through reducing airflow by growing plants in the glass surroundings, which allow the sunlight to come in, but traps the heat. In the case of the atmosphere, the gases capable of absorbing the heat reduce the infrared transparency of the atmosphere and trap the heat (which is then absorbed and re-emitted repeatedly, see Figure 1.1) close to the Earth’s surface. According to the findings of Tyndall the main gases responsible for this effect are water vapour (H<sub>2</sub>O) and carbon dioxide (CO<sub>2</sub>). It is important to note that this property of some of the atmospheric constituents to absorb infrared radiation is extremely important for maintaining comfortable living conditions on Earth. Without this process, Earth’s average surface temperature would be below 0°C [*Le Treut et al.*, 2007]. Thus the greenhouse effect can be considered as ‘dangerous’ only above some background concentration of the infrared-active gases, or so-called greenhouse gases (GHGs).

Several decades after Tyndall’s discovery, in 1896, Svante Arrhenius suggested that variations in atmospheric CO<sub>2</sub> concentration could be responsible for such dramatic climatic changes as glaciations [*Arrhenius*, 1896]. In the first half of the 20<sup>th</sup> century, an English engineer, G. S. Callendar, significantly advanced the understanding of the greenhouse effect by solving the mathematical equations relating climate change to the amount of CO<sub>2</sub> in the atmosphere and quantifying the potential increase in global temperature with the concurrent growth of CO<sub>2</sub> [*Callendar*, 1938].

The fact that the excess CO<sub>2</sub> accumulating in the atmosphere is absorbed by the oceans has been known since the times of Arrhenius who predicted the large potential of the oceans as a sink for CO<sub>2</sub> [*Arrhenius*, 1896]. However, as CO<sub>2</sub> continued to accumulate in the atmosphere it became clear that not all of it was absorbed by the oceans. The explanation for this phenomenon was offered by *Revelle and Suess* [1957]: although the oceans can easily absorb atmospheric CO<sub>2</sub> this process slows down dramatically as the surface waters get become saturated with CO<sub>2</sub>. The limiting factor in the oceanic CO<sub>2</sub> uptake is the rate of turnover of the deep waters, which was later estimated to be about 1000 years [*Broecker and Peng*, 1982]. This means that every particular water molecule in the ocean only ‘sees’ the surface and ‘gets a breath’ of atmospheric air on average once in a 1000 years. Nevertheless, despite this limitation, later findings showed that since the beginning of the industrial era the oceans have

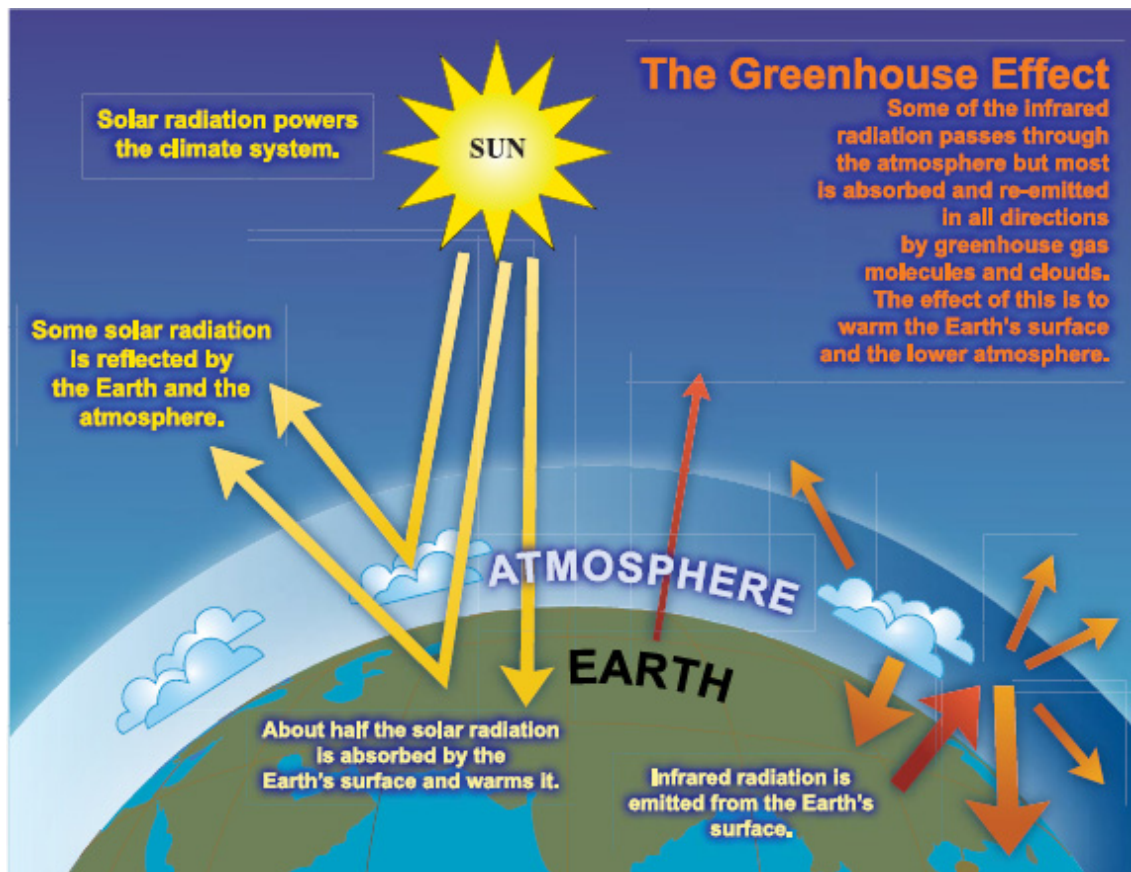


**Figure 1.1:** A simplified model of the ‘greenhouse effect’ (from [Le Treut *et al.*, 2007]). The Sun emits highly energetic short-wave radiation which is partly absorbed by the Earth’s surface leading to its warming, and partly reflected back to space. The Earth re-emits the absorbed sunlight as long-wave radiation within the infrared spectrum (as the Earth’s temperature is much colder than that of the Sun). Some constituents of the atmosphere such as gaseous H<sub>2</sub>O, CO<sub>2</sub>, CH<sub>4</sub>, N<sub>2</sub>O, CFCs and others can absorb this infrared radiation, thus not allowing them to escape and trapping the heat close to the Earth’s surface. This leads to an additional warming of both the atmosphere and the Earth’s surface. This phenomenon is called the ‘greenhouse effect’ while the group of gases capable of trapping infrared radiation are generally referred to as ‘greenhouse gases’.

absorbed almost 50% of all anthropogenic CO<sub>2</sub> added to the atmosphere from fossil fuel burning and cement manufacture [Sabine *et al.*, 2004].

As the early researchers of the greenhouse effect were focused on its two main contributors, H<sub>2</sub>O and CO<sub>2</sub>, it was not until the middle of the 20<sup>th</sup> century when the same ability to absorb the infrared radiation was shown for other atmospheric constituents such as methane (CH<sub>4</sub>), nitrous oxide (N<sub>2</sub>O) and synthetic chlorofluorocarbons (CFCs) [Forster *et al.*, 2007]. Despite the fact that these gases have much lower abundances in the atmosphere compared to that of water vapour or CO<sub>2</sub> (e.g., the average global CH<sub>4</sub> concentration is lower than that of CO<sub>2</sub> by more than two orders of magnitudes) they were soon recognised as even more powerful GHGs than CO<sub>2</sub> owing to their high ‘global warming potential’. The concept of ‘global warming potential’ or ‘GWP’ was introduced in an attempt to standardise and estimate the

potential global warming effect of different gas molecules over a chosen time period. With this concept, the GWP of a CO<sub>2</sub> molecule is accepted as a singular unit relative to which the potential of all other gases is estimated. For example, the GWP of a CH<sub>4</sub> molecule is ~25 (based on a 100-yr time horizon) [Forster *et al.*, 2007] compared to CO<sub>2</sub>. These GWP estimations also take into account the atmospheric lifetime of the given gas species. In addition, the estimates of GWP vary greatly depending on the chosen time horizon. The time horizons most widely used are 20, 100 and 500 years, mainly depending on the purpose of the exercise. For example, long-term projections of global warming and necessary changes to the energy production or related industries would require projections on longer time scales. In contrast, shorter time scales may provide a more realistic estimate of the warming potential over an ‘easily comprehensible’ period. Nowadays, the 100-yr time horizon is generally adopted for most purposes. To illustrate the importance of the chosen time horizon, the GWP estimate of CH<sub>4</sub> increases to 72 when a 20-yr time horizon is used for its calculations (compared to 25 based on a 100-yr horizon) [Forster *et al.*, 2007].

With the growth of scientific knowledge about the post-industrial greenhouse effect and its main drivers there came the understanding that it mainly represents a consequence of human-induced fossil fuel burning and land use changes. Although the role of humans in the changing climate was already suggested more than a century ago [e.g., Callendar, 1938; Arrhenius, 1896], public awareness of this constantly evolving process has remained very low until very recently. Even the scientific community itself was not uniform in defining the role of humans in the changing climate [e.g., Lindzen, 1997; Svensmark and Friis-Christensen, 1997]. Nevertheless, evidence of human-induced changes in the Earth’s climate system has been persistently increasing over the last decades [Denman *et al.*, 2007]. Public awareness and acceptance of these facts have been dramatically increasing as well. The next step after awareness and acceptance is to develop strategies to combat or at least mitigate the ongoing climatic changes. One of the most important questions for all of society is how to adapt with minimal losses and consequences, or in other words, how to make a relatively painless transition from a society almost wholly dependent on fossil fuels for their energy supply to a more or less self-sustainable one.

Owing to the complexity of the climate change problems and the necessity of urgent, large-scale measures to address them, the need for an integral international effort was evident by the end of the last century. As an example of such an effort, in 1988, the World Meteorological Organization (WMO) and the United Nations Environment Programme (UNEP) set up the Intergovernmental Panel on Climate Change (IPCC,

[www.ipcc.ch](http://www.ipcc.ch)). The goal of the IPCC has been to analyse and summarise all available scientific findings and evidence on global climate change, and most importantly, to provide the public and policy-makers with independent, exhaustively compiled scientific assessments. The role of the IPCC in communicating the underlying scientific research has been very significant. As recognition of its crucial contribution the Norwegian Nobel Committee awarded the Nobel Peace Prize to the IPCC in 2007, shared with Al Gore, former vice-President of the USA who now dedicates his time to promoting awareness, understanding and action on global climate change.

The other significant milestone in the perception of global climate change was the adoption of the Kyoto Protocol on 11 Dec 1997, under the auspices of the United Nations Framework Convention on Climate Change (UNFCCC), and, even more significantly, its subsequent ratification on 16 Feb 2005. This is the first-ever environmental legally binding international protocol that has set GHG emission reduction targets, in this case for 37 industrialised countries. The overall average emissions reduction that must be achieved over the first commitment period (2008-2012) is about 5% compared to 1990 emissions. Although the 5% reduction of the developed countries' emissions will obviously not solve the problems of climate change, it can still be considered as the first, and most importantly, legally binding, step towards international collaboration on this fundamentally global problem. Further implications and interpretations of the measures for emission reductions will be also discussed later in this thesis (Chapter 2).

### **1.3 Why study climatic and atmospheric changes in Siberia?**

In addition to already existing alterations in atmospheric composition, scenarios for the 21<sup>st</sup> century envisage even more rapid and abrupt changes [Denman *et al.*, 2007; Prentice *et al.*, 2001]. Recent scientific research has shown that the major driver of these changes is the increasing concentrations of infrared-active GHGs, although they have been rising at different rates and impacts on the environment (Section 1.5). Since the second half of the 20<sup>th</sup> century a large number of scientific studies have been dedicated to acquiring more knowledge about the accumulation rates of different GHGs in the atmosphere, and their interannual, seasonal and spatial patterns and variability, and to identify and quantify their anthropogenic and natural sources and sinks. Of particular concern is the possibility of changes in the magnitudes and/or nature of these sources and sinks induced by the changing climate [e.g., Pitter *et al.*, 2003; Sarmiento and Gruber, 2002].

Despite a large number of studies, there remain significant 'gaps' in our current

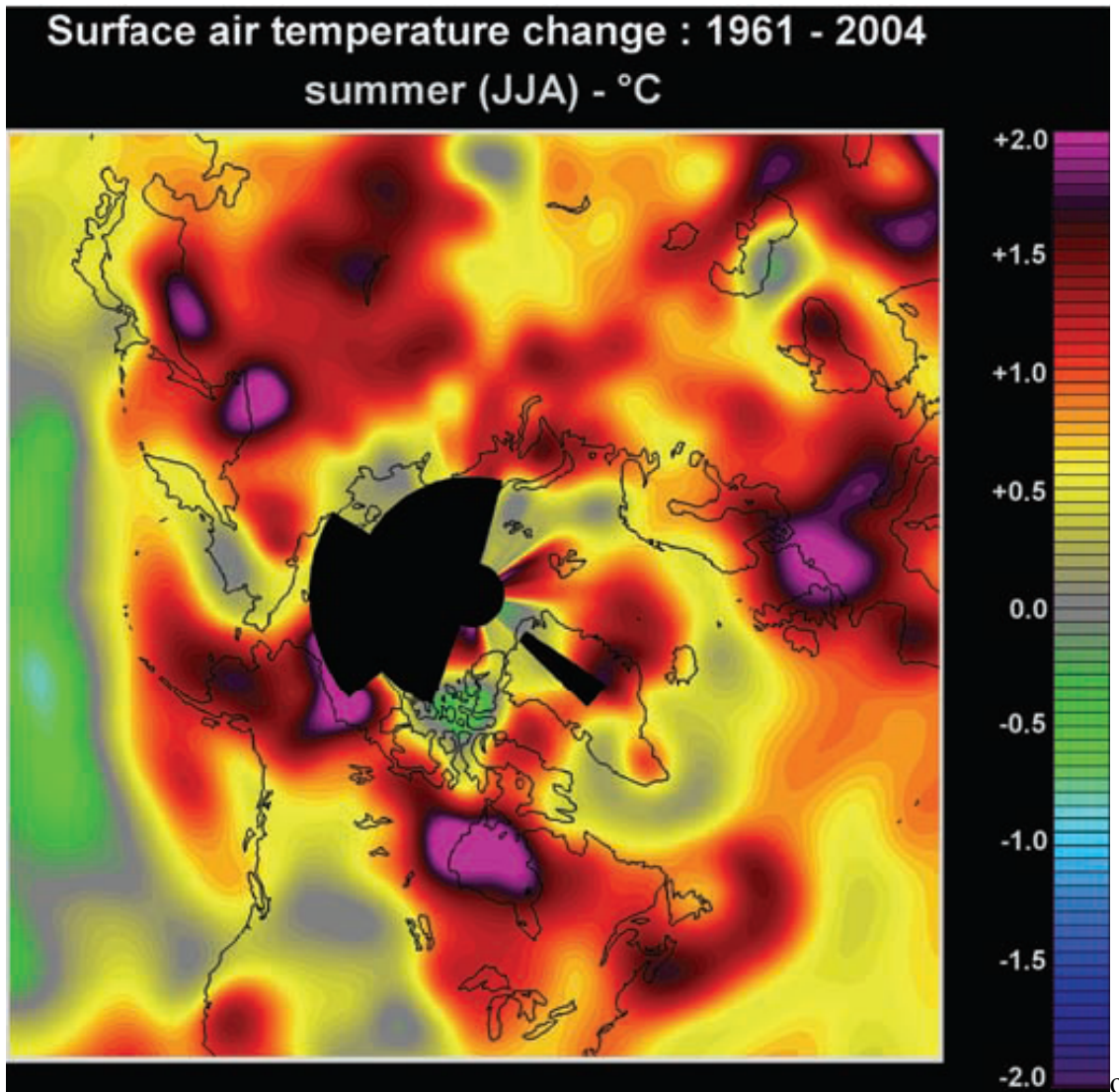


**Figure 1.2** (taken from [Chapin *et al.*, 2005]): Spatial distribution of the summer surface warming ( $^{\circ}\text{C}$ ) over 44 years (1961-2004) in the northern high-latitudes from monthly surface temperature anomalies (using data from stations in the NH). Black areas represent the periods for which no data were available.

bservational capacity, one of which is in the high latitudes of the Northern Hemisphere (NH), particularly Siberia. The continental boreal zone in Siberia represents one of the world's most vulnerable ecosystems. It contains large amounts of carbon stored in forests, wetlands and soils [McGuire *et al.*, 2009], with a sizeable fraction dominated by permafrost. The climate is characterised by an extreme seasonal temperature cycle (approximately  $70^{\circ}\text{C}$  amplitude) and large interannual variability. Chapin *et al.* [2005] demonstrated recently observed changes in the summer surface air temperature in the Arctic, Siberia, northern Canada and Scandinavia (Figure 1.2). The rate of the temperature increase in the Arctic and Siberia has increased from  $0.15\text{-}0.17^{\circ}\text{C}/\text{decade}^{-1}$  (1961-1990 [Chapman and Walsh, 1993] and 1966-1995 [Serreze *et al.*, 2000]) to  $0.3\text{-}0.4^{\circ}\text{C}/\text{decade}^{-1}$  (Figure 1.2). According to the results from several different experimental approaches such as studying changes in the structure of marine and lake

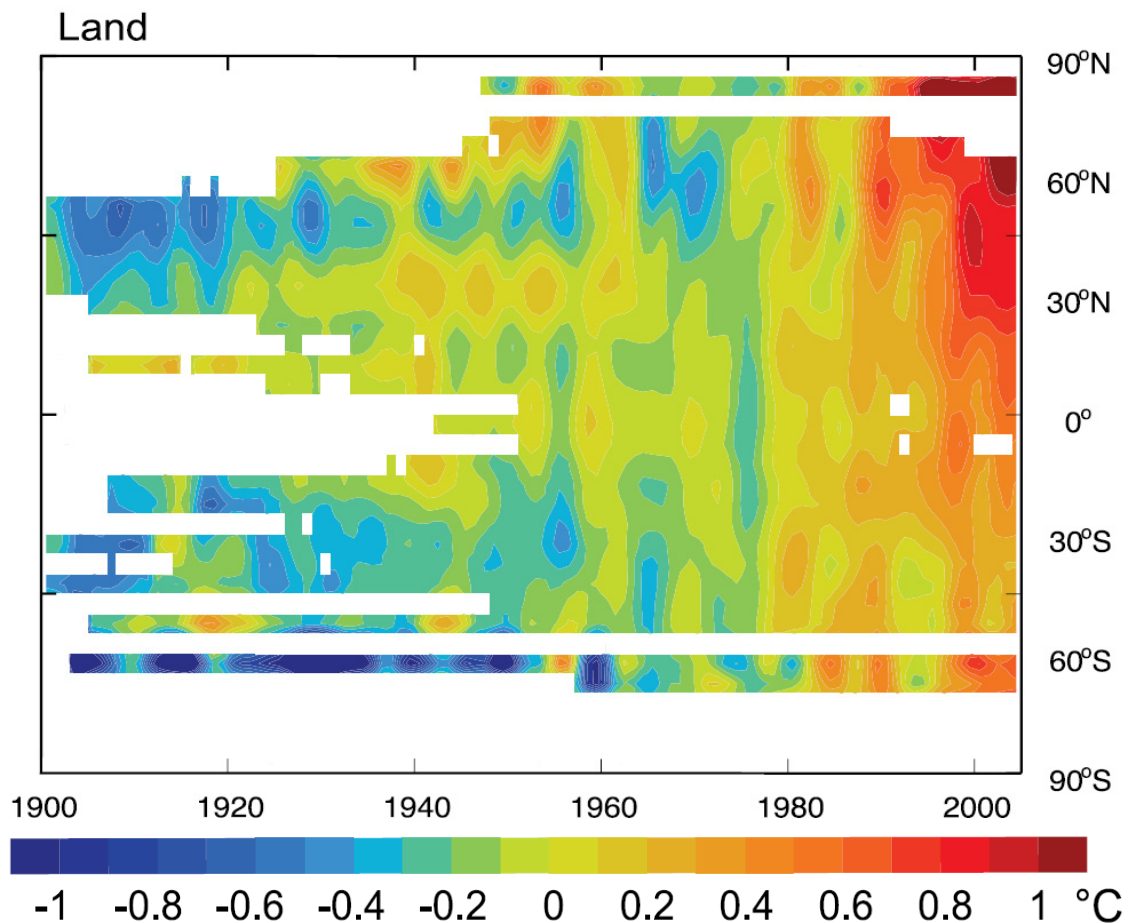


**Figure 1.3** (taken from [Fig. 3.5 *Trenberth et al.*, 2007]): Latitude-time section of surface mean temperature anomalies ( $^{\circ}\text{C}$ ) for land from 1900 to 2005, relative to the mean values from 1961 to 1990. White areas indicate missing data.

sediments, distribution of trees and extent of glaciers, the currently observed summer temperatures in the Arctic regions are the highest in the last 400 years [*Overpeck et al.*, 1997]. These higher temperatures in the northern regions have already caused permafrost melting in the Arctic and Siberia, retreat of glaciers and increased terrestrial precipitation since the beginning of the 20<sup>th</sup> century [*Overpeck et al.*, 1997]. Some evidence also exists that the northern tundra is gradually shifting towards being a source rather than a sink for  $\text{CO}_2$  [*Overpeck et al.*, 1997].

Figure 1.3 shows the distribution of mean temperature anomalies at different latitudes on land from 1900 to 2005, with the highest anomalies recorded between 60° and 90° N. Why are the temperature changes more pronounced in the northern regions in comparison to the rest of the planet? The reason is the complex set of positive feedbacks of global warming, which are particularly prominent in these regions. The main driver of the rapidly increasing temperatures here is the decrease in the surface albedo that occurs owing to the lengthening of the snow-free season and decrease in Arctic sea ice, and the northward advances of the shrubbery and tree line caused by the

warming and melting of permafrost soils [*Chapin et al.*, 2005]. The latter has the potential to become one of the most significant positive feedbacks of global warming.

Recent studies [e.g., *Schuur et al.*, 2008] indicate that accounting for carbon stored in permafrost soils could double the previously calculated carbon inventories for high-latitudes. Increased summer temperatures in regions with widespread melting of permafrost could potentially make a vast amount of carbon available for microbial decomposition. It is difficult to predict the overall potential effect on global climate caused by thawing permafrost owing to the complexity of the processes. For example, depending on the aerobic or anaerobic conditions (or their combination) during permafrost decomposition the carbon could be released in the form of CO<sub>2</sub> or CH<sub>4</sub>, which would lead to significantly different GWPs.

It is obvious that the environmental changes described above have the potential to accelerate, with strong and potentially irreversible impacts on local ecosystems. This is why it is particularly important to set up long-term monitoring of different ecosystem parameters and greenhouse gases to observe the future development of these changes in Siberia, which would help us to combat or at least mitigate their negative effects on these vulnerable ecosystems. The long-term character of monitoring is also particularly important owing to large natural interannual variations of the climate in this region that would make it impossible to draw robust conclusions and projections from only short-term observations or measurement campaigns.

#### **1.4 Tall tower atmospheric measurements in central Siberia – an approach for studying long-term atmospheric changes in continental interiors**

An important observational gap exists in monitoring continental ecosystems, which are under-represented in the current global observational networks [e.g., *Tans*, 1993]. On the one hand ‘background’ air concentration measurements (made at coastal and mountain sites) provide data on a hemispheric scale, which can be used in inverse models for inferring the large-scale distribution and variations of sources and sinks by means of the so-called ‘top-down’ approach [e.g., *Rödenbeck et al.*, 2003]. On the other hand, eddy covariance flux measurements provide ‘bottom-up’ information on local areas up to 1 km<sup>2</sup>. The large spatial scale gap between these two types of measurements can be partially filled with aircraft measurements, but they suffer from prohibitive costs and non-continuity. Thus ‘tall tower’ measurements, with footprints of up to 10<sup>6</sup> km<sup>2</sup> [*Gloor et al.*, 2001], have been identified as a means to fill this spatial scale gap, allowing us to examine ‘background’ behaviour of GHGs in continental interiors.

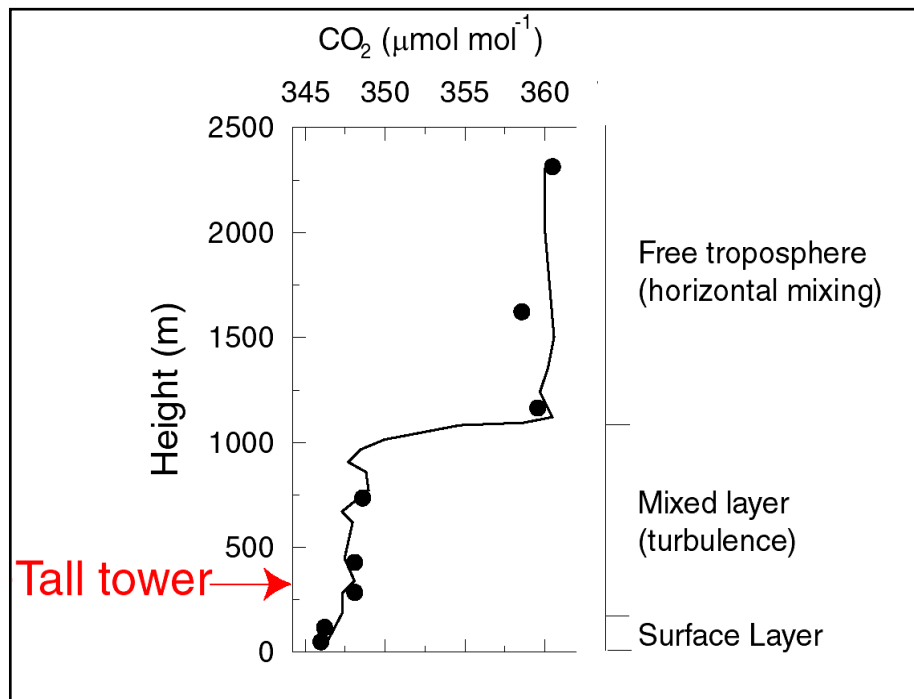


**Figure 1.4** (courtesy of J. Lloyd, University of Leeds, UK): A typical afternoon vertical profile of CO<sub>2</sub> concentration in the surface layer, mixed layer and free troposphere. Measurements from the top of a tall tower (~300 m) enable us to observe long-term ‘background’ changes in the atmospheric composition by probing the well-mixed layer of the atmosphere. The height of the mixed layer varies diurnally and seasonally (with maxima in the daytime and summertime), and additionally, depends on the latitude. The mixed layer is also much more pronounced over the continents, for example, in Siberia it extends from ~200 m up to 2000 m in summer [Styles *et al.*, 2002].

It is with the goal of beginning to address this gap, that we have established the 300-m Zotino Tall Tower Observatory (ZOTTO) in central Siberia (60.80°N, 89.35°E). The tower site is located in a relatively homogeneous, undisturbed continental boreal ecosystem, close to the southern border of discontinuous permafrost. The natural vegetation type is coniferous forest with significant areas of wetlands. The remoteness of the site leads to low anthropogenic influences, which, together with the homogeneity of the ecosystems and topography, allow for a large tower footprint area (see Chapter 5, Section 5.2 for more detailed site description).

In the U.S.A., the use of pre-existing tall towers has been made into an advanced measurement approach with towers in Wisconsin and North Carolina [Bakwin *et al.*, 1998; Bakwin *et al.*, 1997; Hurst *et al.*, 1997; Bakwin *et al.*, 1995]. The main advantage of tall tower measurements is the ability to probe a well-mixed part of the atmosphere (Figure 1.4), which, for example, in central Siberia extends from about 200 m up to 2000 m in summer [Styles *et al.*, 2002]. In the surface layer (from 0 to 200 m), air masses are significantly influenced by strong diurnal changes in the local ecosystems’ photosynthetic and respiration activities, as well as possible surface heterogeneity. Tall tower measurements, being somewhat removed from these relatively large source/sink

patterns at ground level, allow us to observe the gradual long-term changes in the background atmospheric composition as well as the vertical profiles of the measured species.

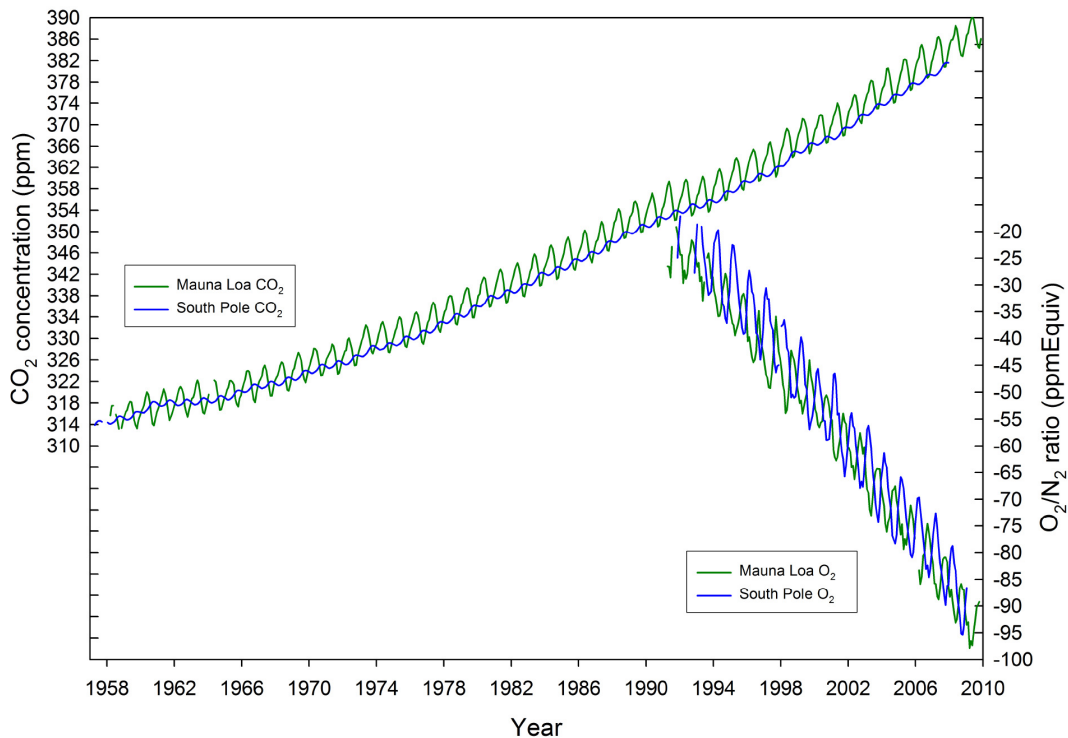
Outside of North America, GHG-related tall tower measurements have previously been made only in Hungary (CO<sub>2</sub>) [Haszpra *et al.*, 2001] and in The Netherlands [Vermeulen *et al.*, 2006] (CO<sub>2</sub> and CH<sub>4</sub>). In parallel to the ZOTTO project, the European Commission-funded *CHIOTTO (Continuous High precision Tall Tower Observations of greenhouse gases)* project [Vermeulen *et al.*, 2004] was launched in Europe, initiating air measurements from eight pre-existing tall towers in Europe. Contrasts with the ZOTTO tower site include the facts that there is almost no unmanaged primary forest remaining in central and western Europe (with the Hainich Forest (Chapter 2) being a rare exception), that almost the whole of Europe has been intensively used for agriculture and industry over the last few centuries, and that climatic variations are much less extreme than in central Siberia.

There are several key approaches to our tall tower methodology. First, our measurements are made on a semi-continuous basis (one data point every 12-16 min), allowing high frequency processes and events to be observed, and providing a dense dataset which facilitates more accurate results from long-term observations. The second approach is the multi-species nature of our measurements, including the major biogeochemical gases: carbon dioxide (CO<sub>2</sub>), oxygen (O<sub>2</sub>), methane (CH<sub>4</sub>), carbon monoxide (CO), and nitrous oxide (N<sub>2</sub>O). Third, and unique in continuous GHG observations, our analytical measurement system has been built as a single integrated cohesive unit, rather than a suite of independent analysers measuring different species. Finally, regular collection of air samples in glass flasks allows for isotopic composition analyses ( $\delta^{13}\text{C-CO}_2$  and  $\delta^{18}\text{O-CO}_2$ ). Taken together, these approaches provide us with an invaluable multi-functional strategy for observing large-scale regional biogeochemical processes and their response to climate change in Siberia.

## **1.5 Gas species measured at ZOTTO: general overview and motivation for their continuous measurement**

### **1.5.1 CO<sub>2</sub>**

According to data from the WMO-GAW global greenhouse gas network [WMO Greenhouse Gas Bulletin, 2008] the atmospheric burden of CO<sub>2</sub> has increased from 280 ppm in 1800 to 383.1 ppm in 2007 (~37% increase), mainly due to the combustion of fossil fuels and cement production, and to a lesser extent to land use changes. The



ab

**Figure 1.5:** CO<sub>2</sub> concentrations as observed at Mauna Loa (Hawaii) and South Pole from 1958 to 2010 shown on the left y-axis (website: <http://scrippsco2.ucsd.edu/>). O<sub>2</sub>/N<sub>2</sub> ratios (data courtesy of R. Keeling, Scripps Institution of Oceanography) shown for the same locations on the right y-scale. By plotting O<sub>2</sub>/N<sub>2</sub> in ppmEquiv units (see Chapter 4, Section 4.2.1), CO<sub>2</sub> and O<sub>2</sub>/N<sub>2</sub> are in visually comparable on a mole-to-mole basis.

solite growth rate of atmospheric CO<sub>2</sub>, however, has been variable over this period, with a maximum in the 10 years from 1995 to 2005 [Denman *et al.*, 2007].

The retrospective record of CO<sub>2</sub> concentrations in ice from the Law Dome (Antarctica) shows that there existed no analogy of such a rapid atmospheric CO<sub>2</sub> growth rate on a comparable time scale over the past 2000 years [Meure *et al.*, 2006].

Precise continuous measurements of atmospheric CO<sub>2</sub>, the most important anthropogenic GHG, were initiated over 50 years ago at the remote location of Mauna Loa (Hawaii) [Keeling, 1960], and are shown in Figure 1.5. During the next few decades, a global network of continuous CO<sub>2</sub> measurements was set up including several additional ‘background’ stations such as Baring Head, New Zealand (National Institute for Water and Atmospheric Research), Cape Grim, Tasmania (CSIRO Marine and Atmospheric Research) and the South Pole (Scripps Institution of Oceanography and NOAA Earth System Research Laboratory).

Enhanced CO<sub>2</sub> uptake by land biota and its dissolution in the oceans slows down the incremental increase of atmospheric CO<sub>2</sub> compared to the level predicted based on the amount of burned fossil fuels alone. Over the last 45 years only about 55%

of CO<sub>2</sub> emitted from fossil fuel burning and cement manufacture has remained in the atmosphere, representing the CO<sub>2</sub> ‘airborne fraction’ [Denman *et al.*, 2007]. Any changes in this fraction are crucial for the prediction of the future accumulation rates of CO<sub>2</sub> in the atmosphere, mainly via changes in the magnitudes and behaviour of the carbon sinks (ocean and land biosphere). Therefore, continuous observations of atmospheric CO<sub>2</sub> are essential for monitoring long-term changes and variability in the contemporary carbon cycle and its influence on global climate. In addition, in light of the ratified Kyoto Protocol and future international agreements, atmospheric CO<sub>2</sub> measurements along with regional source and sink estimates, will become crucial not only for the scientific community, but also for the general public and policy makers. The ZOTTO site is situated in the middle of the world’s largest continental boreal zone with considerable amounts of carbon stored in wood, soils and wetlands. Continuous measurements of atmospheric CO<sub>2</sub> and observations of its atmosphere/biosphere exchange are thus an essential part of any carbon cycle monitoring in this region.

### 1.5.2 O<sub>2</sub>

Data on the interannual and seasonal dynamics of CO<sub>2</sub> uptake by the land biota and oceans are key to a better understanding and mitigation of anthropogenic carbon emissions. This is where atmospheric O<sub>2</sub> measurements have become particularly valuable as a method to estimate the sources and sinks of CO<sub>2</sub> emitted to the atmosphere by humans, and their partitioning between the land biota and the oceans [e.g., Bender *et al.*, 1996; Keeling and Shertz, 1992]. Several approaches on the carbon sinks’ partitioning were developed over the last decades. One of the commonly used approaches relies on the differences in the uptake of the most abundant carbon isotopes (<sup>12</sup>C and <sup>13</sup>C) by the ocean and land biota. As the land biota prefers to assimilate the lighter (<sup>12</sup>C) atoms in the process of photosynthesis whilst ocean uptake has no preference, it is possible to separate the carbon fluxes using both atmospheric and oceanic CO<sub>2</sub> measurements [Ciais *et al.*, 1995]. Other approaches include the use of direct measurements of surface ocean pCO<sub>2</sub> [e.g., Takahashi *et al.*, 1999] and dissolved inorganic carbon [e.g., Sabine *et al.*, 2004], as well as inverse atmospheric transport modelling [e.g., Enting *et al.*, 1995] and ocean carbon models [e.g., Orr, 1997]. All of these approaches are based on direct measurements (or modelling) of various carbon compounds, and suffer from several constraints such as scarcity of data or large uncertainties due to complexity of the carbon cycle (for example, the disequilibrium effect in <sup>12</sup>C/<sup>13</sup>C land biotic exchanges).

In contrast, O<sub>2</sub> measurements provide a carbon-independent approach to the

partitioning of the global carbon sinks. The approach [Keeling *et al.*, 1993; Keeling, 1988b] makes use of the different behaviour of O<sub>2</sub> and CO<sub>2</sub>, otherwise coupled through photosynthesis, respiration and combustion, that occurs in seawater. First, the solubility of O<sub>2</sub> in seawater is much less than that of CO<sub>2</sub>, and second, when dissolved, O<sub>2</sub> is chemically inert, while CO<sub>2</sub>, in contrast, reacts with seawater forming a range of carbonic acid compounds, and thus allowing further dissolution of atmospheric CO<sub>2</sub>. It is these differences in the chemical and physical properties of O<sub>2</sub> and CO<sub>2</sub> that have made O<sub>2</sub> measurements a powerful tool in constraining various aspects of the global carbon cycle, including global carbon sink estimates of the land biota and oceans [Tohjima *et al.*, 2008; Manning and Keeling, 2006; Bender *et al.*, 2005].

As given in Manning and Keeling [2006], the simplified global budgets for CO<sub>2</sub> and O<sub>2</sub> can be represented by the following equations:

$$\Delta\text{CO}_2 = F - O - B, \text{ and} \tag{1.1}$$

$$\Delta\text{O}_2 = -\alpha_F F + \alpha_B B + Z, \tag{1.2}$$

where  $\Delta\text{CO}_2$  and  $\Delta\text{O}_2$  are the global atmospheric changes in CO<sub>2</sub> and O<sub>2</sub> concentration respectively; F is the anthropogenic carbon source (fossil fuel burning and cement production); O represents the net oceanic carbon sink; B is the net land biotic carbon sink (incorporates all land use change effects), and Z is the net effect from ocean warming of O<sub>2</sub> atmosphere-ocean exchanges (including changes in O<sub>2</sub> solubility, biological pump efficiency and oceanic circulation patterns). All quantities (apart from the coefficients  $\alpha_F$  and  $\alpha_B$  in the equation 1.2, explained below) are expressed in units of mole per annum.  $\alpha_F$  and  $\alpha_B$  represent the global average O<sub>2</sub>/CO<sub>2</sub> molar exchange ratios for fossil fuel combustion and land biota, respectively.

As follows from equation 1.2, the net land biotic carbon sink (B) can be quantified by using data on the global changes in atmospheric O<sub>2</sub> ( $\Delta\text{O}_2$ ) and amount of carbon released to the atmosphere as a result of fossil fuel burning (F). Then an estimate of the oceanic carbon sink (O) can be made by substituting the estimate of the net land biotic carbon sink (B) into equation 1.1, and using the observational data on the global changes in atmospheric CO<sub>2</sub> ( $\Delta\text{CO}_2$ ) and the amount of carbon released from the burned fossil fuels (F).

The two coefficients,  $\alpha_F$  and  $\alpha_B$ , however, introduce some uncertainties into this methodology. O<sub>2</sub>/CO<sub>2</sub> molar exchange ratios are defined throughout this dissertation as moles of O<sub>2</sub> produced per mole of CO<sub>2</sub> consumed (in any processes involving stoichiometric exchanges of O<sub>2</sub> and CO<sub>2</sub>). The O<sub>2</sub>/CO<sub>2</sub> exchange ratios for fossil fuel combustion ( $\alpha_F$ ) were examined in detail in Keeling [1988]. Their values are well defined for all major types of fossil fuels (1.17, 1.44 and 1.95 for coal, liquid fuels and

natural gas respectively [Keeling, 1988]), with an average global value in the 1990's of  $1.39 \pm 0.04$  [Manning and Keeling, 2006] (calculated with fossil fuel emissions data from Marland *et al.* [2002]). In contrast, the  $O_2/CO_2$  land biotic exchange ratios ( $\alpha_B$ ), defined as the stoichiometric coefficients of  $O_2$  and  $CO_2$  exchanges in the processes of photosynthesis and respiration, are poorly constrained. The average global value of  $1.1 \pm 0.05$ , which is widely used in the calculations of the land biotic carbon sink, was historically defined based on a very limited dataset from laboratory studies [Severinghaus, 1995]. Several recent studies [e.g., Ciais *et al.*, 2007; Randerson *et al.*, 2006] suggested that the average value of 1.1 is most likely overestimated. Any imbalances of the land biotic photosynthesis and respiration (for example, accelerated decomposition of soil carbon as a result of global temperature increase and/or land use changes) will be reflected in  $\alpha_B$ , and consequently, in the magnitude of the net land biotic carbon sink (B). Stephens *et al.* [2007] showed that  $\alpha_B$  also varies on temporal and spatial scales. Therefore, further studies of  $O_2/CO_2$  exchange ratios are required to obtain a more accurate and a better-constrained average global ratio.

Routine atmospheric  $O_2$  measurements were only started in the early 1990s and presently there exists a network of about ten remote locations collecting atmospheric  $O_2$  samples established and maintained by the Scripps Institution of Oceanography (SIO) (see e.g. Fig. 1.5). Until recently, another observational network of  $O_2$  measurements was operated by the Princeton University [e.g., Bender *et al.*, 1996], but this was shut down at the end of 2009. In addition to these two main contributors to the long-term data series of  $O_2$ , several other institutes in Europe (MPI-BGC (Germany), University of Bern (Switzerland), University of Groningen (The Netherlands), Laboratoire des Sciences du Climat et de l'Environnement (LSCE, France), University of East Anglia (United Kingdom)), National Institute for Environmental Studies (NIES, Japan), Tohoku University (Japan), National Center for Atmospheric Research (NCAR, USA) and National Institute of Water and Atmospheric Research (NIWA, New Zealand) have the facilities to make  $O_2$  measurements in their laboratories, with some of them running small flask sampling programs and continuous  $O_2$  measurements at remote locations.

Another tracer introduced to distinguish between the land biotic and oceanic carbon signals is Atmospheric Potential Oxygen ( $APO = O_2 + \alpha_B CO_2$ ), which reflects the weighted sum of  $O_2$  and  $CO_2$  concentrations, where the weighting is adjusted so that APO is essentially invariant with respect to  $O_2$  and  $CO_2$  exchanges with land biota [Manning and Keeling, 2006; Stephens *et al.*, 1998]. The seasonal cycle of APO, therefore, is primarily driven by seasonal air-sea fluxes of  $O_2$  (plus a small component from air-sea fluxes of  $N_2$ ). The dilution of the APO seasonal amplitude over the

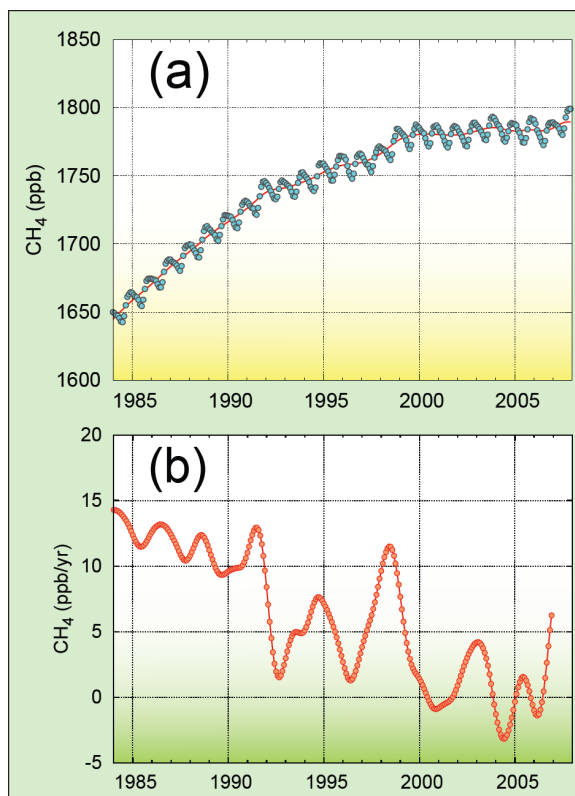


**Figure 1.6:** Globally averaged CH<sub>4</sub> concentrations (a) and its growth rate (b) from 1984 to 2007 (taken from [WMO Greenhouse Gas Bulletin, 2008]).

continents by atmospheric mixing provides a convenient way to evaluate models of atmospheric transport [e.g., *Blaine, 2005*]. The mid-continental location of the ZOTTO station provides an opportunity to study the dilution of the APO seasonal signal over the large continental area of Eurasia and evaluate the magnitude of the oceanic component in the atmospheric variations of O<sub>2</sub> observed at ZOTTO (see Chapter 5).

### 1.5.3 CH<sub>4</sub>

Since pre-industrial times the atmospheric burden of CH<sub>4</sub> has increased from ~715 to 1789 ppb in 2007 (a 150% increase) [WMO Greenhouse Gas Bulletin, 2008] caused by changes in both natural (e.g. wetlands) and

anthropogenic (e.g. energy production, biomass burning, rice agriculture, ruminant animals, and landfills) sources. The growth rate of CH<sub>4</sub> has been variable over the last few decades (Figure 1.6b), with periods of relatively rapid rise in the late 1980s, and periods of stabilisation and even decline in the 1990s and early 2000s which are not well understood [*Dlugokencky et al., 2003; Dlugokencky et al., 2001; Dlugokencky et al., 1994*]. The anomalous drop in the CH<sub>4</sub> growth rate in 1992, preceded by a maxima in 1991, could have been a consequence of the Mt. Pinatubo volcanic eruption (June 1991) [*Dlugokencky et al., 1996*] owing to changes in the atmospheric photochemistry caused by large amounts of ash and SO<sub>2</sub> emitted to the atmosphere, and lower temperatures and precipitation observed after this event globally [*Lelieveld et al., 1998*]. But the drop in growth rate since about 2000 is not well understood.

The global sources of CH<sub>4</sub> are relatively well known, however, the contribution of each individual source and the future trends in their behaviour and magnitude, particularly, in light of global warming, remain unclear. *Keppler et al.* [2006] suggested a new theory for a significant (up to 30% of the global source) ‘missing’ CH<sub>4</sub> source from living vegetation (under prevalence of aerobic conditions). The underlying mechanism that could potentially lead to formation of a highly reduced compound such

as CH<sub>4</sub> in living plant tissue, however, was unexplained by the authors [Keppler *et al.*, 2006]. Nisbet *et al.* [2009] have shown that it is very unlikely that living plant tissues can produce CH<sub>4</sub>. Nevertheless, they can transpire CH<sub>4</sub> dissolved in water and absorbed by roots. In addition, CH<sub>4</sub> emissions are observed when leaves or other living plant tissues are subjected to ultraviolet radiation [Nisbet *et al.*, 2009].

Photochemical reactions with hydroxyl radical (OH) are the largest sink of atmospheric CH<sub>4</sub>, with several minor sinks attributed to destruction in the stratosphere and soils [Denman *et al.*, 2007]. Thus, the atmospheric burden of CH<sub>4</sub> is highly dependent on the oxidative state of the atmosphere, specifically on the abundance of OH radical and its interannual and seasonal variability.

The most extensive CH<sub>4</sub> measurement network of about 50 flask sampling sites is run by the Global Monitoring Division of the National Oceanic and Atmospheric Administration (NOAA/GMD). The Advanced Global Atmospheric Gases Experiment (AGAGE) maintains the second largest network that delivers continuous CH<sub>4</sub> measurements from five sites in both hemispheres. Continuous measurements of atmospheric CH<sub>4</sub> have become an important part of most of the tall tower measurement programmes, which were first introduced at the tall tower sites in Wisconsin and North Carolina [e.g., Bakwin *et al.*, 1998; Hurst *et al.*, 1997]. Presently, continuous measurements of CH<sub>4</sub> are carried out at several tall tower sites in Europe (in the framework of the former CHIOTTO project) [Vermeulen *et al.*, 2004].

Despite the slowdown of the growth rate observed over the last decade, CH<sub>4</sub> has remained the second most important anthropogenic GHG, contributing up to 20% of the global mean direct radiative forcing of the atmosphere [Ramaswamy *et al.*, 2001]. In 2008 the growth rate of CH<sub>4</sub> began increasing again, as also shown in Figure 1.5 [Rigby *et al.*, 2008]. Apart from the persistent anthropogenic emissions, the potential increase of natural CH<sub>4</sub> emissions from wetlands that may be induced by regional increases in temperature or precipitation, make CH<sub>4</sub> measurements particularly pertinent in Siberia, which has the world's largest area of wetlands (~131 million ha [Sohnngen *et al.*, 2005]). In addition, Siberia's wetland area is most prone to increase under a changing climate owing to melting of permafrost regions.

#### 1.5.4 CO

The CO molecule does not absorb infrared radiation and therefore is not a direct GHG. Nevertheless, changes in its concentration have an impact on the oxidative capacity of the atmosphere and thus on the lifetimes of other GHGs, notably CH<sub>4</sub> and tropospheric ozone (O<sub>3</sub>), since reactions with OH radical are the largest sink of the

atmospheric CO. A certain amount of CO is also metabolised in the surface layers of soils by aerobic CO-oxidising bacteria - a wide group of bacteria including pathogens, plant symbions and many soil species [King and Weber, 2007]. The main sources of increasing CO emissions are anthropogenic, and most commonly attributed to biomass burning, fossil fuel combustion (e.g., traffic exhausts) and partial oxidation of CH<sub>4</sub> and non-methane hydrocarbons. High atmospheric CO concentrations can usually be easily traced back to local anthropogenic sources owing to the relatively short lifetime of the CO molecule in the atmosphere (from 20 to 50 days) [Warneck, 1988], which makes it a good tracer for polluted air masses, especially on local and regional scales.

Thus, simultaneous measurements of CO<sub>2</sub>, CO and CH<sub>4</sub> can enrich our knowledge about their local sources and sinks, and help to distinguish between natural and anthropogenic sources of CO<sub>2</sub> and CH<sub>4</sub>. Atmospheric CO concentrations vary significantly both temporally and spatially [e.g., Novelli *et al.*, 1992; Khalil and Rasmussen, 1988]. The highest CO concentrations are usually observed in the mid and high latitudes of the NH, where anthropogenic emissions are greatest. As the abundance of OH radical varies seasonally (with the minimum in winter), CO concentrations are higher in winter [e.g., Novelli *et al.*, 1992].

In boreal regions of the NH including Siberia, an increasing frequency in natural and human-induced fires have become one of the major sources of CO in summer [Kasischke *et al.*, 2005]. The global trend in CO concentration has been inconsistent and has experienced both increases and decreases during the last few decades [Novelli *et al.*, 2003; Novelli *et al.*, 1998; Khalil and Rasmussen, 1994], which are only partially understood. It is clear, however, that continuous measurements of CO would considerably assist our interpretation and future prediction of its atmospheric burden over the mid and high latitude areas of the NH which experience the highest annual and seasonal variability.

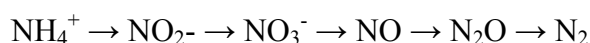
The regular (weekly) collection of flasks for evaluation of long-term trends in the global CO concentration has been carried out within the NOAA flask sampling network, initially developed for monitoring CO<sub>2</sub> and CH<sub>4</sub> background concentrations. Hurst *et al.* [1997] presented the results of continuous CO measurements from the tall tower in North Carolina. In addition, continuous monitoring of CO concentrations was introduced as a part of the multi-species measurement programmes at some tall tower sites in Europe [Vermeulen *et al.*, 2004].

### **1.5.5 N<sub>2</sub>O**

Finally, N<sub>2</sub>O is a long-lived GHG whose atmospheric concentration has increased

from 260 ppb in pre-industrial times (before 1750) to 320.9 ppb in 2007 [WMO Greenhouse Gas Bulletin, 2008]. According to analyses of air bubbles trapped in South Pole firn air [Battle *et al.*, 1996] and the ‘H15’ ice core [Machida *et al.*, 1995], the atmospheric concentration of N<sub>2</sub>O was growing much more rapidly during the second half of the last century compared to the first half. MacFarling Meure *et al.* [2006] have recently extended the retrospective record of pre-industrial N<sub>2</sub>O measurements by 2,000 years showing no considerable variations in natural N<sub>2</sub>O concentration in the first 1,800 years and its continuing rise starting from the year 1850. Land use changes and associated alterations in microbial production of N<sub>2</sub>O, greatly enhanced by intensive use of fertilizers, have been recognised as the main drivers of the increased levels of atmospheric N<sub>2</sub>O [Denman *et al.*, 2007]. Along with rivers, estuaries and coastal upwelling areas, soils remain one of the largest individual sources of N<sub>2</sub>O. Processes of microbial transformation of various organic and inorganic compounds in soils influence the atmospheric budgets of many trace gases [Conrad, 1996].

The transformation of nitrogen compounds in soils are performed by many different groups of bacteria and can be represented as follows:



Different groups of bacteria are involved in each stage of nitrogen transformation driven by specific ferments. Some bacteria are able to perform several transformations of this ‘food chain’ while others (e.g., nitrifying bacteria) are very substrate-specific, that is, they can only use one form of nitrogen for their growth and metabolism. N<sub>2</sub>O is released to the atmosphere as an intermediate compound during the process of denitrification (reduction of oxidised nitrogen compounds to gaseous N<sub>2</sub>). N<sub>2</sub>O released from water reservoirs and coastal areas is also produced in the processes of bacterial transformation of organic nitrogen. Denitrification is crucial to the nitrogen cycle as it allows all oxidised nitrogen compounds to return to the atmospheric pool of inert N<sub>2</sub>, which can then be utilised in the processes of microbial N<sub>2</sub>-fixation. The production of N<sub>2</sub>O instead of gaseous N<sub>2</sub> usually occurs when environmental conditions such as moisture content, O<sub>2</sub> availability and soil pH are not optimal for the production of the end product of denitrification (N<sub>2</sub>). Under the predominance of anaerobic conditions and availability of organic matter, the process of heterotrophic denitrification can also become a prevailing source of N<sub>2</sub>O emissions to the atmosphere [Conrad, 1996]. This process might become particularly important for high latitude continental regions like Siberia, which have extensive areas of wetlands and permafrost soils with large amount of organic matter. Increases in temperature and precipitation in this region could potentially lead to faster microbial decomposition of organic matter resulting in higher

emissions of CO<sub>2</sub>, CH<sub>4</sub> and N<sub>2</sub>O.

The seasonal cycle of N<sub>2</sub>O is better defined in the southern hemisphere, probably because of the dominance of N<sub>2</sub>O emissions that are microbially produced in the ocean, and without the confusing influences of anthropogenic emissions and microbial activity in soils [Nevison *et al.*, 2005].

Measurements of atmospheric N<sub>2</sub>O concentrations (in both hemispheres) have been carried out since the mid-1990s by the NOAA and AGAGE networks [e.g., Jiang *et al.*, 2007]. The analytical challenge of detecting changes in atmospheric N<sub>2</sub>O on the sub-ppb levels has restricted the number of sites and laboratories making continuous N<sub>2</sub>O measurements. For the same reasons, the uncertainties of global N<sub>2</sub>O sources and sinks are still relatively large and additional research and observations are required to reduce them.

## 1.6 Thesis overview

This chapter (Chapter 1) provided an overview of the concept of the greenhouse effect and its scientific development over the last several centuries. It also introduced tall tower measurements and their advantages over other methods of atmospheric sampling and data collection, with particular relevance to studying climatic changes in central Siberia and the importance of this region from the perspective of the global carbon cycle and climate change. Finally, I discussed the multi-species approach to continuous measurements and the role of each gas species measured, in general, and specific to this remote location.

Chapter 2 presents data collected during two flask sampling campaigns in an unmanaged old-aged forest ecosystem in central Germany (Hainich Forest). It is one of the very few remaining unmanaged forests in central Europe, which provides a unique opportunity to study processes of assimilation and respiration in a natural ecosystem. Data analyses and relevant discussions presented in this chapter aim to demonstrate the unique advantages of a multi-species measurement approach to interpret observations on diurnal and synoptic scales, thus laying a foundation for the multi-species approach used in all subsequent chapters.

Chapter 3 presents the methodology and development of a cohesive semi-continuous measurement system for measurements of CO<sub>2</sub>, O<sub>2</sub>, CH<sub>4</sub>, CO and N<sub>2</sub>O in central Siberia. Owing to the remoteness of the location and substantial delays in data availability, the system had to incorporate a lot of safety and reliability features to ensure high-precision measurements of all gas species. The largest emphasis is made on the development of the high-precision O<sub>2</sub> analyser as the O<sub>2</sub> measurements are the most

challenging of all species measured at ZOTTO.

Chapter 4 continues the technical presentation started in Chapter 3 but from the perspective of establishing and maintaining both short and long-term calibration scales for all measured species. The philosophy of internally consistent calibration scales and the challenge of their practical implementation is one of the biggest discussion subjects of this chapter. I also report results on the stability of measured species in aluminium cylinders (used to provide the system with reference and calibration gases) and changes that occurred in ZOTTO calibration cylinders and measurement scales for all gas species over the period of my measurements. I present a discussion on the required and obtained measurement precisions and accuracies for all gas species. Finally, results on  $O_2/N_2$  fractionation tests are also briefly reported in this chapter.

Chapter 5 presents atmospheric semi-continuous measurements obtained with the system described in Chapters 3 and 4 which was operational at ZOTTO from November 2005 to June 2007. Discussions and data analyses presented here take full advantage of the multi-species measurement approach that was also used to examine the Hainich Forest data in Chapter 2. Atmospheric variations are studied and discussed on seasonal, synoptic and diurnal scales, with special attention given to synoptic peculiarities of the ZOTTO site. Seasonal variations of  $CO_2$ ,  $O_2$  and APO at ZOTTO and Shetland Islands (Scotland), located at similar latitude, are compared with those simulated by a global transport model (TM3).

Chapter 6 continues with analyses of ZOTTO data, specifically discussing comparisons of atmospheric observations of  $CO_2$ , APO and CO with results of 'Regional MOdel' (REMO) simulations. The atmosphere's vertical structure as represented in the model is studied with the help of routine radiosonde measurements in the vicinity of the ZOTTO site. Discrepancies in the vertical mixing and terrestrial fluxes are then translated into those for the observed and modelled atmospheric  $CO_2$  concentrations. The chapter also presents the comparison of APO concentration records at ZOTTO and Shetlands with high-resolution modelled concentrations of APO. Model-observations comparison of CO data incorporate a detailed discussion on fire events (which were abundant at ZOTTO in summer 2006), and a study on gas emission ratios, including both observed and modelled estimates.

Chapter 7 summarises the results and conclusions discussed in the previous chapters. It also provides an outlook for future carbon cycle research that could follow and extend the work presented in this thesis.

## CHAPTER 2. Variations of biogeochemical gases and isotopes in an unmanaged forest

### 2.1 Introduction to Chapter

This chapter gives an overview of a local scale multi-species study on variations of trace gases, O<sub>2</sub> and isotopic composition of CO<sub>2</sub> in a relatively undisturbed, mid-latitude, deciduous forest ecosystem in central Germany. The study provides an example of how the multi-species measurement approach (introduced in Chapter 1) can be implemented (and benefited from) to study process changes in natural ecosystems - a subject that will be investigated in more detail in the following chapters of this thesis. The results presented here are based on flask sample analyses from two field campaigns (May and July 2005) in the 250-year-old unmanaged beech forest in the Hainich National Park. The flasks were analysed at MPI-BGC for a suite of trace gases (CO<sub>2</sub>, CH<sub>4</sub>, CO, N<sub>2</sub>O and SF<sub>6</sub>), isotopic composition of CO<sub>2</sub> ( $\delta^{13}\text{C-CO}_2$ ) and O<sub>2</sub>/N<sub>2</sub> ratios. In addition to flask data a suite of local meteorological variables was used to facilitate the interpretation of the observed atmospheric variations.

In light of the ratified Kyoto Protocol, it has become particularly important to obtain accurate estimates of regional carbon stocks and their changes. One effort that the Protocol emphasised was offsetting carbon emissions from fossil fuel burning by investing in forest plantations that would effectively sequester CO<sub>2</sub> owing to typically high growth rates of 'young' forests. The existing 'old' forests have thus become unaccountable owing to the believed slow or non-existent rate of net carbon sequestration, which would make them less 'valuable' investments in market-orientated schemes aiming to mitigate climate change. Scientific research on assimilation and respiration rates, however, has been mostly limited to relatively young, managed stands. One reason for this might be their better accessibility but another reason is that there are practically no 'old' unmanaged forests left in central Europe. Some studies, however, [e.g., *Luysaert et al.*, 2008; *Law et al.*, 2001; *Hollinger et al.*, 1994] reported high carbon assimilation rates from old forests, suggesting that further research is needed to assess the carbon balance of such ecosystems.

Under changing climate the sensitivity of respiration and assimilation of 'old' and 'young' forests might respond differently. As stated in *Valentini et al.* [2000], the overall carbon balance of a typical European forest is mainly determined by the rate of its respiration, which was shown to vary greatly with temperature [e.g., *Knohl et al.*, 2003]. A natural unmanaged forest represents a much more complex ecosystem, each part of which is closely linked and depends greatly on environmental factors. Such a complex multi-component ecosystem might also remain more 'robust' in a changing

environment as compared to artificial plantations of single-species stands. Thus, stability and robustness of different types of terrestrial carbon reservoirs might be as important as their ‘immediate’ or short-term capacity and ability to sequester carbon from the atmosphere.

It is also important to note that the ‘value’ of a given ecosystem should not be solely limited to its capacity to sequester CO<sub>2</sub>. Production (and consumption) of other greenhouse gases like CH<sub>4</sub>, N<sub>2</sub>O and partially CO, should also be evaluated and taken into consideration when estimating the total budget of a forest or an agricultural plantation. So far, climate induced sensitivity of processes controlling emissions of these gases to the atmosphere have not been well established. More research is needed to provide a fuller view of forests’ contributions to the budgets of the major GHGs. Results presented in this chapter certainly cannot provide an answer to this overarching goal; however, they show the advantage of multi-species measurements to interpret the observed atmospheric concentration changes of the major GHGs and O<sub>2</sub> that occur as a result of various processes in a forest ecosystem.

The Hainich Forest is one of very few remaining natural unmanaged forests in Europe with naturally varying tree ages from young re-growth to 250-year-olds. In addition, it has been an active area of scientific research since 1997 when a 43-m-tall tower was erected to provide a base for eddy-covariance flux measurements of CO<sub>2</sub>. An overview of the site and scientific studies conducted in its area is given in Section 2.2. Diurnal variations of CO<sub>2</sub>, O<sub>2</sub> and <sup>13</sup>C-CO<sub>2</sub> concentrations, including the vertical and temporal gradients of O<sub>2</sub>/CO<sub>2</sub> ratios, are discussed in Section 2.3. Section 2.4 summarises my observations on atmospheric concentrations of CH<sub>4</sub>, CO and N<sub>2</sub>O. The subjects of discussion in Section 2.5 are the atmospheric concentrations of SF<sub>6</sub> and back trajectory analysis of the polluted air masses which provide an example on how the atmospheric SF<sub>6</sub> measurements can be used to identify local emission of this anthropogenic trace gas.

## **2.2 Site description**

The measurement site (51.08° N, 10.45° E, 440 m a.s.l.) is situated within the Hainich National Park (~7600 ha) in central Germany. The forest received the status of a national park in 1997 in an effort to protect one of the few remaining natural forests in central Europe. Prior to 1997, the area was used as a base for military training, which consequently helped to minimise logging and deforestation of the area. Tree type is dominated by beech, ash and maple, with a small percentage of other deciduous and coniferous European species. The ‘unmanaged’ character of the forest is the reason for a

highly differentiated tree age structure: trees as old as ~250 years naturally occur together with very young growth. Preservation of the forest also resulted in large amounts of dead organic debris (leaves and dead wood). The soil type is cambisols (50-60 cm depth) on a limestone bedrock with high clay content (40%) and a thin layer of litter owing to its fast turnover. The climate is subcontinental, with annual averages of 750-800 mm, 7.5-8.0°C and 200-240° (Southwest) for precipitation, air temperatures and prevailing wind directions respectively. A more detailed description of the site and its micrometeorological characteristics is given in Knohl *et al.* [2003].

The flux tower site was established in 1997 as a part of the European flux network in the framework of the EU-project CARBOEUROFLUX. Within the network, the Hainich Forest is the oldest and the least influenced by management. The establishment of a measurement site in this relatively undisturbed area has provided a unique opportunity to study processes of carbon exchange in a very old and natural (even though not 'pristine') forest and has been a valuable addition to the European flux network. Results of the research carried out in the Hainich Forest have been discussed in many scientific publications [e.g., *Anthoni et al.*, 2004; *Knohl et al.*, 2003]. Recently, *Kutsch et al.* [2008], however, pointed out some potential systematic uncertainties in the estimates of carbon ecosystem exchanges from the flux tower, owing to the location of the site on a gentle but nevertheless significant slope of 2-3°.

Discussions presented in the following sections are based on analyses of flask samples collected during two intensive field campaigns (15-18 May and 16-17 July) in 2005. One-litre glass flasks (in triplicates) were filled (during 15-20 min) with air collected from three heights below the canopy (1, 4 and 12 m) every ~3-4 hours (canopy height is about 33 m). In addition, two-litre glass flasks for analysis of the radioactive isotope of carbon (<sup>14</sup>C) in CO<sub>2</sub> were collected in parallel but unfortunately the amount of carbon in those samples turned out to be insufficient for reliable analyses. The sampling lines (Synflex 1300 tubing, ¼" OD) were installed at the three heights specified above; additional tubing at ~5 cm above the ground was installed prior to the July campaign for better detection of the soil respiration signature. Stainless steel traps filled with magnesium perchlorate (Mg(ClO<sub>4</sub>)<sub>2</sub>) were used to dry the sample airstream prior to filling the flasks. The latter were filled with air up to ~1.6-1.8 bar a using a diaphragm compressor pump (KNF Neuberger, model N05-ATI). Prior to sample collection the flasks were flushed with air at the same pressure at which the sample were collected (to minimise the influence of pressure disturbances on O<sub>2</sub> concentrations) through a back pressure regulator (Fisher Controls, model 289A).

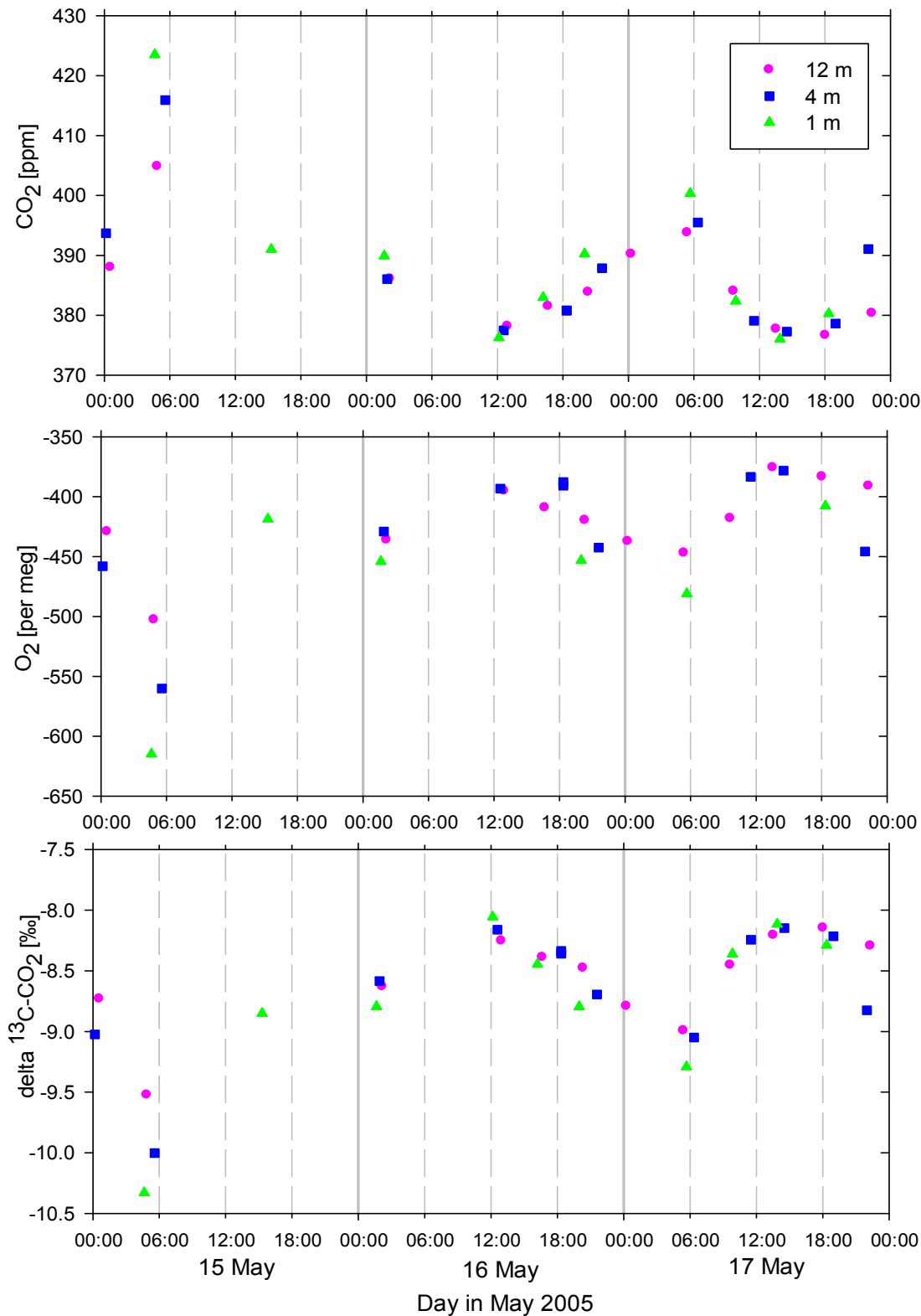


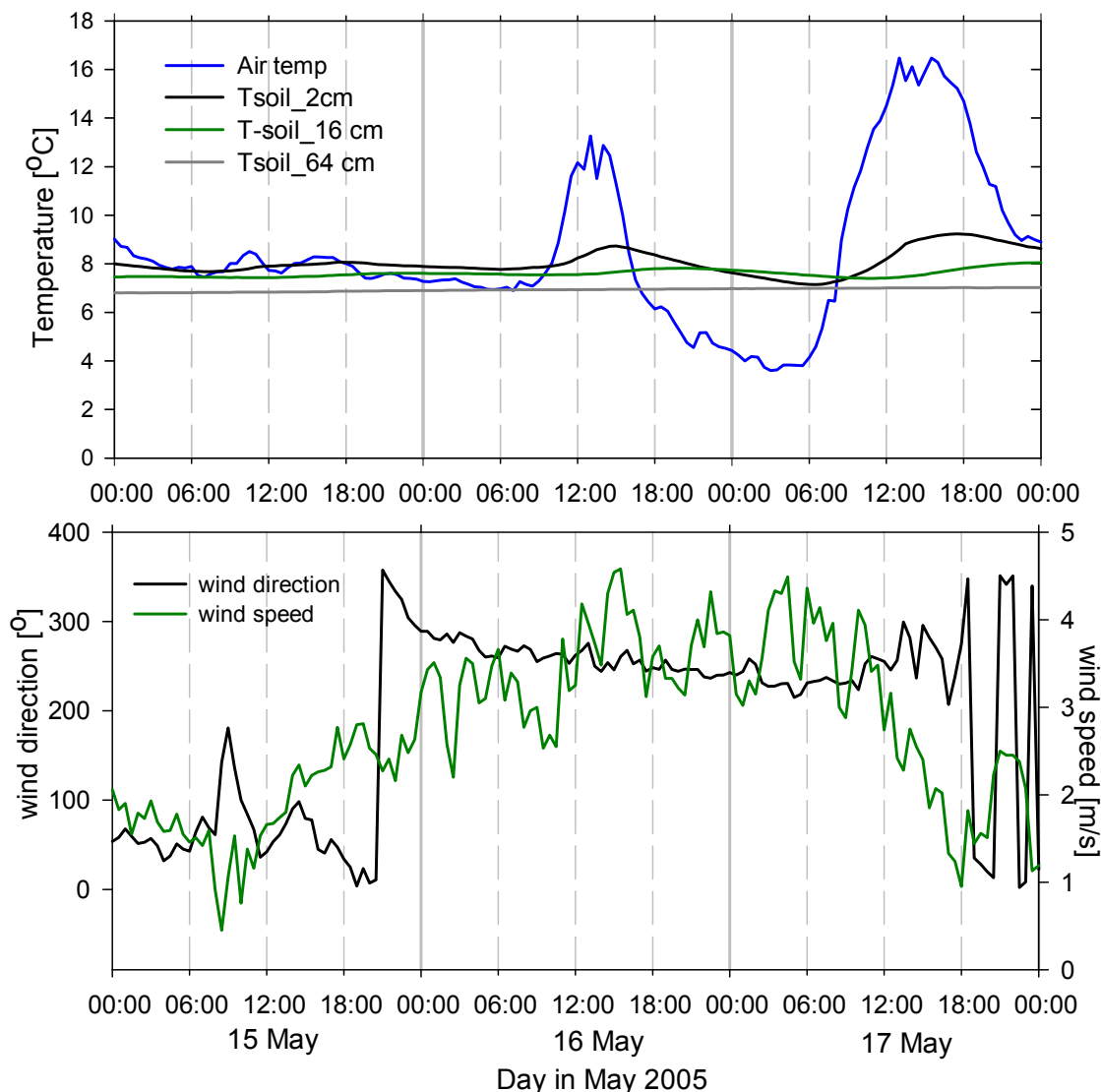
**Figure 2.1:** CO<sub>2</sub> (top panel), O<sub>2</sub> (middle panel) and  $\delta^{13}\text{C-CO}_2$  (bottom panel) concentrations of air samples collected from 15 to 18 May 2005. Changes in CO<sub>2</sub> and O<sub>2</sub> can be visually compared on a mole per mole basis. Each data point is an average of three flask measurements. The solid vertical lines correspond to midnight (local time: UTC+2 hrs).

The samples were then analysed at MPI-BGC laboratories for CO<sub>2</sub>, CH<sub>4</sub>, CO, N<sub>2</sub>O and SF<sub>6</sub> concentrations (with a gas chromatograph equipped with a Flame Ionization Detector (FID) and an Electron Capture Detector (ECD), Agilent Technologies, model

6890), O<sub>2</sub>/N<sub>2</sub> ratios (mass spectrometer Finnigan Mat, model Delta Plus XL) and isotopic composition of CO<sub>2</sub> ( $\delta^{13}\text{C}$  and  $\delta^{18}\text{O}$ ) (Finnigan Mat, model 252 IRMS).

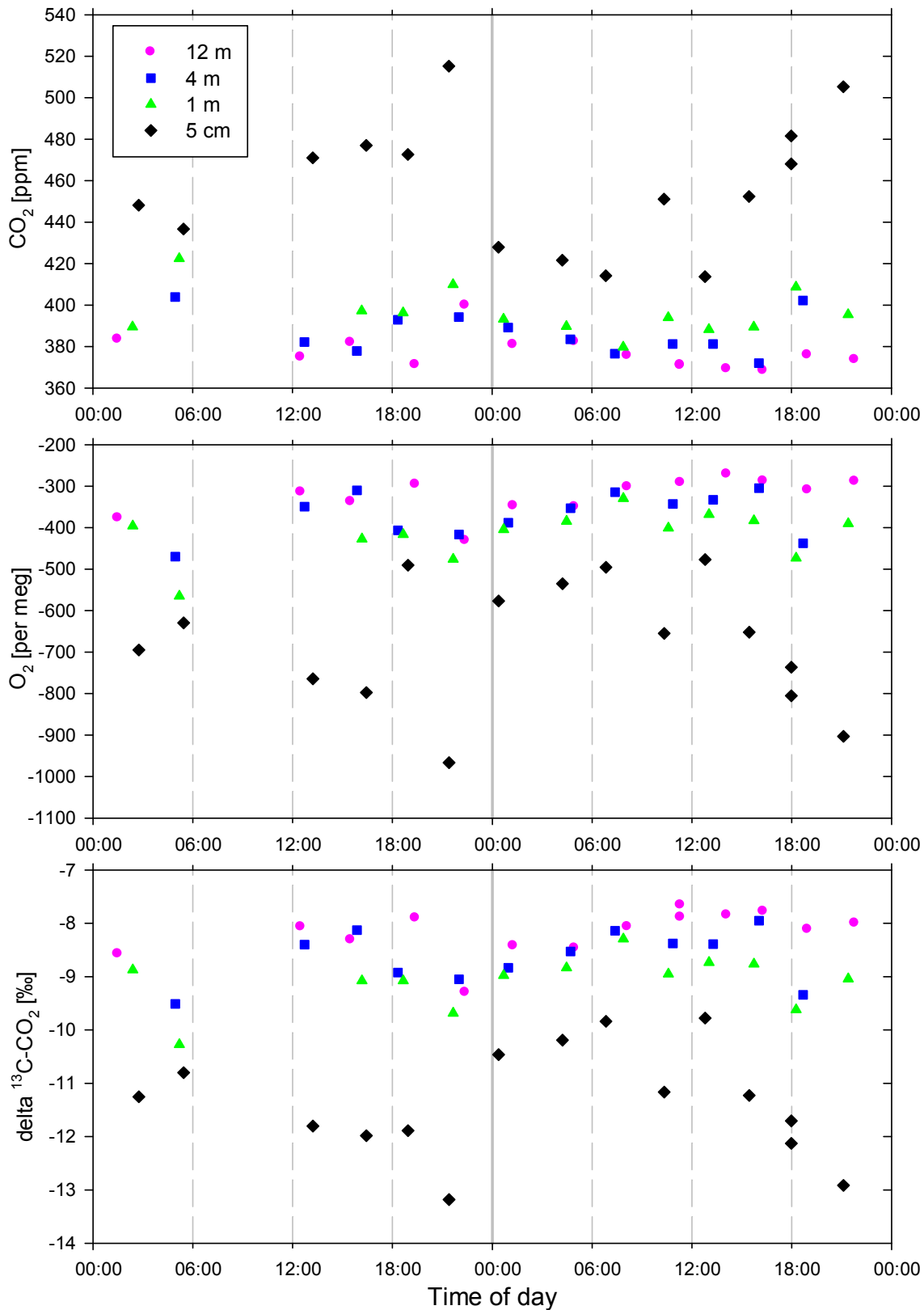
### 2.3 Variations of CO<sub>2</sub>, O<sub>2</sub> and <sup>13</sup>C-CO<sub>2</sub>

Figure 2.1 shows CO<sub>2</sub>, O<sub>2</sub> and <sup>13</sup>C-CO<sub>2</sub> concentrations of air samples collected from 15 to 18 May 2005. No vertical gradients can be seen in the concentrations of any species between 12 and 4 m heights, with slightly higher CO<sub>2</sub> and consequently



**Figure 2.2:** Top panel: Air (blue line) and soil temperature at 2, 16 and 64 cm depth (black, green and grey lines respectively) from 15 to 18 May 2005. Bottom panel: wind direction (black line) and wind speed (green line) from 15 to 18 May 2005. The solid vertical line corresponds to midnight (local time: UTC+2 hrs). Data are courtesy of O. Kolle (MPI-BGC).

lower O<sub>2</sub> and <sup>13</sup>C-CO<sub>2</sub> concentrations at 1 m above ground, which probably reflect their respiration signatures. The maximum nighttime CO<sub>2</sub> build-up is about 23 ppm (15-16 May), which is probably owing to the relatively low air temperatures (see Fig. 2.2 top panel).



**Figure 2.3:** CO<sub>2</sub> (top panel), O<sub>2</sub> (middle panel) and  $\delta^{13}\text{C-CO}_2$  (bottom panel) concentrations of air samples collected on 16 and 17 July 2005. Changes in CO<sub>2</sub> and O<sub>2</sub> can be compared visually on a mole per mole basis. Each data point is an average of three flask measurements. The solid vertical lines correspond to midnight (local time: UTC+2 hrs).

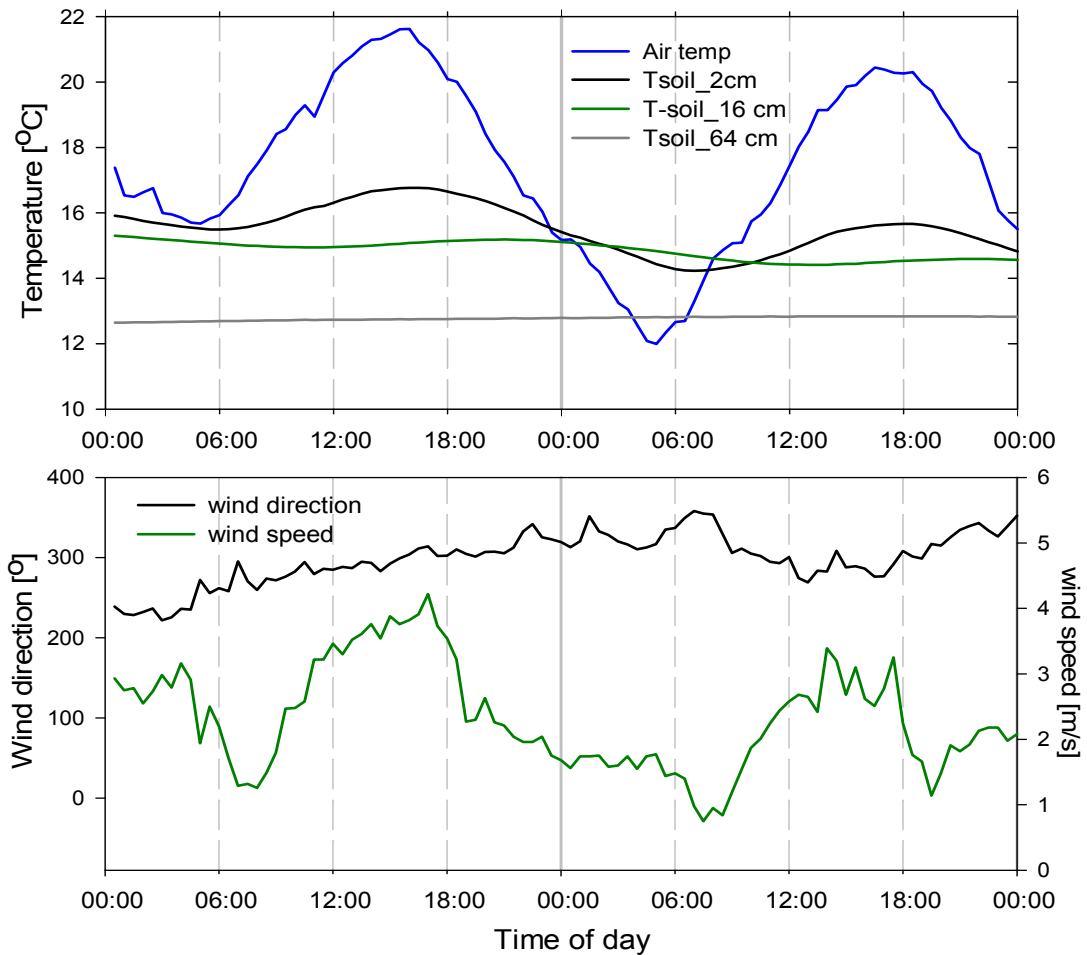


**Figure 2.4:** Top panel: Air (blue line) and soil temperature at 2, 16 and 64 cm depth (black, green and grey lines respectively) on 16-17 July 2005. Bottom panel: wind direction (black line) and wind speed (green line) on 16-17 July 2005. The solid vertical line corresponds to midnight (local time: UTC+2 hrs). Data are courtesy of O. Kolle (MPI-BGC).

Maximum  $\text{CO}_2$  concentrations were observed around 6 am as a result of the combination of nighttime respiration and relatively low wind speeds (Fig. 2.2 bottom panel). In contrast, minimum  $\text{CO}_2$  concentrations were recorded around midday as expected both from high  $\text{CO}_2$  uptake by plants and vigorous vertical mixing.

Figure 2.3 shows concentration variations of the same gas species but during the summer campaign on 16-17 July 2005. Figure 2.4 displays air and soil temperature (top panel) and wind speed and direction (bottom panel) for the same period. In addition to the sampling heights used during the May campaign, I also collected air samples very close to the ground ( $\sim 5$  cm, black line in Fig. 2.3). Concentrations of all gas species measured at this level show significant offsets from all the others. In addition, the 5 cm measurements are characterised by different temporal patterns of  $\text{CO}_2$  accumulation, with maximum  $\text{CO}_2$  concentration around 9 pm and minimum at about 6 am. The following day  $\text{CO}_2$  build-up starts in the late afternoon. Such differences from the more classical pattern of diurnal cycles of  $\text{CO}_2$  (observed in the May profiles) might be

attributed to the fact that CO<sub>2</sub> measured so close to the ground largely originates from soil respiration, which has different dynamics and temperature responses. A closer look at soil temperature measured at 2 cm depth (Fig. 2.4) where most soil respiration occurs shows that its diurnal cycle exhibits similar temporal patterns as those observed for CO<sub>2</sub>.

Sampling height or time of day	O <sub>2</sub> /CO <sub>2</sub> ratios	Number of measurements	Least squares fit (R <sup>2</sup> )
All measurements	0.98±0.08	30	0.97
12 m	0.94±0.12	12	0.96
4 m	1.06±0.14	10	0.98
1 m	0.88±0.20	8	0.95
nighttime	0.91±0.09	16	0.98
daytime	0.97±0.18	14	0.90

**Table 2.1:** O<sub>2</sub>/CO<sub>2</sub> ratios at different heights and time of day from flask air samples collected on 14-17 May 2005. ‘Nighttime’ data are defined as those collected from 21:00 to 5:30. The rest of the data is defined as ‘daytime’.

O<sub>2</sub> concentrations mirror CO<sub>2</sub> concentrations as expected from the tight correlation of these two gases in the processes of photosynthesis and respiration. To investigate the oxidative ratios of these processes I estimated O<sub>2</sub>/CO<sub>2</sub> exchange ratios for all air samples collected during the spring and summer campaigns. The significance of the oxidative ratios of photosynthesis and respiration ( $\alpha_B$  in equation 1.2) for estimates of global and regional carbon sinks was discussed in Chapter 1, Section 1.5.2. All information on the ratios (with uncertainty estimates) is summarised in Tables 2.1 (May data) and 2.2 (July data).

Sampling height or time of day	O <sub>2</sub> /CO <sub>2</sub> ratios	Number of measurements	Least squares fit (R <sup>2</sup> )
All measurements	1.03±0.03	49	0.99
12 m	1.38±0.31	13	0.94
4 m	1.22±0.04	9	1.00
1 m	1.08±0.11	13	0.97
5 cm	0.90±0.15	14	0.99
nighttime	1.04±0.04	19	0.99
daytime	1.02±0.03	30	0.99

**Table 2.2:** O<sub>2</sub>/CO<sub>2</sub> ratios at different heights and time of day from flask samples collected on 16-17 July 2005. ‘Nighttime’ data are defined as those collected from 21:30 to 5:20. The rest of the data is defined as ‘daytime’.

Figure 2.5 illustrates the observed variations in O<sub>2</sub>/CO<sub>2</sub> exchange ratios separately for each height (a) and time of day (b). The ratios observed at 5 cm above the ground cover a large range of values. As discussed above, samples taken at this height most likely reflect the signature of soil respiration. Depending on the type of respired

organic matter the oxidative ratios of this process might vary (based on how complex the oxidised molecules are), thus leading to variable ratios. The  $O_2/CO_2$  ratios at 1 and 4 m heights are not significantly different from each other, however, one sees an overall increasing trend from May to July. The error bars for May and July ratios at 12 m height do not overlap, which means that the ratios are significantly different from each other, with very large scatter observed in the July estimates. There is also tentative evidence to suggest increasing  $O_2/CO_2$  ratios with increasing height, with the May 12 m average the only point not fitting this pattern. The  $O_2/CO_2$  ratios shown in Figure 2.5a include both daytime and nighttime values, which should be considered when interpreting the results as the former tend to be more scattered owing to combination of both photosynthetic and respiratory processes contributing to the ratios. The high average ratio at 12 m height (1.38) in July may be considered to be influenced by fossil fuel burning, which could have happened both locally or brought from distance, however, the large uncertainty prohibits from making any robust conclusions.

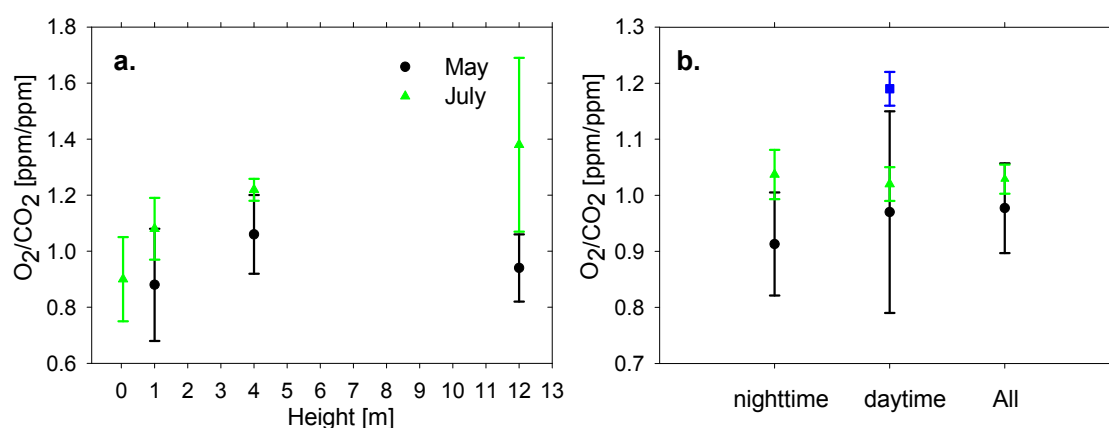


**Figure 2.5:** **a.**  $O_2/CO_2$  ratios (with error bars) at different sampling heights (0.05, 1, 4 and 12 m) for May (black circles) and July (green triangles) 2005. **b.**  $O_2/CO_2$  ratios (with error bars) for May (black circles) and July (green triangles) at nighttime, daytime and both. The mean  $O_2/CO_2$  ratio shown with the blue square was estimated from 13 measurements of canopy air during daytime in the Hainich Forest on 11 Aug 2002 [Seibt *et al.*, 2004].

Figure 2.5b. shows  $O_2/CO_2$  ratios from the same air samples when calculated separately for nighttime and daytime. Data were considered ‘nighttime’ if they were collected after (or around) sunset and before (or around) sunrise, which occurred at ~9 pm and 9:30 pm (sunset) and ~5:30 am and ~5:20 am (sunrise) in May and July respectively. Conversely, data were considered ‘daytime’ if they were collected between sunrise and sunset. The July nighttime ratio in Fig. 2.5b shows much smaller uncertainty than that for May and has a higher mean value. Although, error bars of these two estimates slightly overlap, both the mean and the error bars of the July ratio are

orientated towards the very end of the error estimate of the May nighttime ratio. The observed discrepancy might also be explained by differences in the type of the respired organic matter at different times of year. For example, in the beginning of the vegetative season (May) the ecosystem's respiration might be limited to respiring simple sugars (recently synthesised by rapidly growing leaves) by plants. In addition, soil (upper layer) temperature is still not very high (see Fig. 2.2) and is variable thus prohibiting decomposition of more complex molecules in the soil. In July, the respired organic matter might be different, with a combination of easily decomposed sugars and more complex molecules, in both plants and soil. Soil temperatures are also higher and more stable (see Fig. 2.4) compared to May leading to more favourable conditions for decomposition of various types of organic matter (the rate of which is directly proportional to temperature for most microbes).

Daytime  $O_2/CO_2$  ratios are very variable in May but much better defined in July, with overlapping error bars. As mentioned earlier, as daytime ratios of these gases represent several processes they are much more difficult to define. Finally, I plotted the ratios based on all data for May and July (Fig 2.5b), which demonstrates the similar tendency as already described above. The July values are better defined (with smaller uncertainties) and slightly (but not significantly) higher than those observed in May. The smaller uncertainties can also be partially attributed to differences in the number of measurements used for those calculations (see Tables 2.1 and 2.2), with many more in the July dataset. An earlier study on  $O_2/CO_2$  ratios of canopy air during daytime in the Hainich Forest [Seibt *et al.*, 2004] resulted in estimates of  $1.12 \pm 0.08$ ,  $1.14 \pm 0.04$  and  $1.19 \pm 0.03$  on 06, 07 and 11 August 2002, respectively (based on 7, 6 and 13 measurements respectively). I included the ratio observed on 11 August 2002 (as it was based on a larger dataset) in Fig. 2.5b (blue square) together with the daytime estimates obtained from my campaigns in May and July. The August  $O_2/CO_2$  ratio, although it was obtained 3 years before my measurements, is well-defined and is clearly higher than the May and July estimates. This gives me additional confidence in the observed (although small) increasing trend of  $O_2/CO_2$  ratios over the vegetative season. Unfortunately, no measurements from late August or September are available to investigate whether this tendency remained intact or changed at the end of summer – beginning of autumn. To estimate and quantify seasonal cycles of  $O_2/CO_2$  ratios more measurements are needed over the course of the year, especially in summer. Stephens [2001] has made such an analysis in above-canopy (30 m) air at the Wisconsin tall tower site, finding a seasonal cycle with higher ratios in winter. This seasonal cycle,

however, was predominantly caused by the influence of fossil fuel emissions in winter, and did not shed light on possible variability in these ratios caused by forest ecosystems.

Variations in  $\delta^{13}\text{C-CO}_2$  (bottom panels of Fig. 2.1 and 2.3) mirror concurrent  $\text{CO}_2$  concentrations and exhibit the same diurnal pattern as seen in  $\text{O}_2$  concentrations. Variations of  $\delta^{13}\text{C-CO}_2$  can be directly linked to  $\text{CO}_2$  concentrations using the so-called 'Keeling plots' [Ehleringer *et al.*, 2002; Keeling, 1958], which allow the determination of isotopic signatures of sources or sinks of  $\text{CO}_2$ . The approach assumes a well-mixed 'box' of air, where the  $\text{CO}_2$  entering (in the case of a source) or leaving (in the case of a sink) the box has a particular isotopic signature. When plotting variations in the isotopic composition of air ( $\delta^{13}\text{C-CO}_2$ ) against the inverse  $\text{CO}_2$  concentrations ( $1/\text{CO}_2$ ), the y-intercept of the resulting slope corresponds to the isotopic compositions of the respiration source ( $\delta^{13}\text{C}_R$ ) or assimilation sink ( $\delta^{13}\text{C}_a$ ). Thus, if such an analysis is made using daytime values for both species, then the obtained intercept will represent the isotopic signature of the combined effects of both respiration and assimilation. When the same procedure is performed with nighttime values only the result can be attributed to the isotopic signature of respiration.

Variations in Keeling plot intercepts on diurnal, weekly and seasonal scales based on measurements made in the Hainich Forest are described in more detail in Knohl [2004]. He found large day to day (2.65‰) and month to month (3.08‰) variations in the isotopic signature of the ecosystem's respiration ( $\delta^{13}\text{C}_R$ ), which were attributed to changes in various environmental factors (lagged by several days). Knohl [2004] also reported the robustness of Keeling plot calculations when comparing intercepts and slopes calculated for upper, lower and entire canopy air in the Hainich Forest. Processes of carbon assimilation and respiration influence the isotopic composition of canopy air in opposite ways: assimilation of  $\text{CO}_2$  leads to higher values of  $\delta^{13}\text{C-CO}_2$  in the atmosphere, whilst respiration leads to lower values. Thus, large vertical gradients might be observed especially under very calm wind conditions. The latter can be illustrated by the  $\delta^{13}\text{C-CO}_2$  variations at 5 cm above ground in Fig. 2.3 (bottom panel), which are on average 4‰ lower than those at 12 m. The fact that similar intercepts were obtained for both upper and lower heights of the canopy [Knohl, 2004] could be indicate either similar isotopic signatures of  $\delta^{13}\text{C}_R$  and  $\delta^{13}\text{C}_a$  or strong vertical mixing that mitigated their differences.

Figure 2.6 shows the Keeling Plot intercept isotopic signatures of the  $\text{CO}_2$  source/sink processes at the Hainich site. Daytime and nighttime values show significant differences between May and July data, with the July values being higher. A similar tendency, that is higher isotopic composition of  $\delta^{13}\text{C}_R$  later in the vegetative

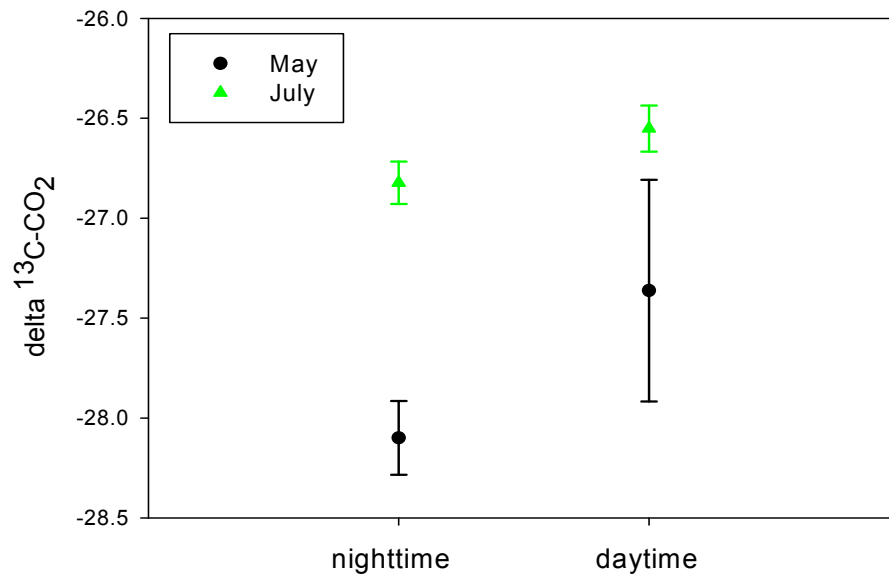


**Figure 2.6:** Nighttime ( $\delta^{13}\text{C}_R$ ) and daytime ( $\delta^{13}\text{C}_a + \delta^{13}\text{C}_R$ ) isotopic signatures of air samples collected in Hainich Forest in May (black circles) and July (green triangles).

season, was also observed by Knohl [2004] in 2001. The difference between intercepts calculated with nighttime and daytime values in May is about 0.7‰. The July nighttime and daytime intercepts are much better defined, with smaller uncertainties, and show better agreement (within 0.2‰). The latter can be probably explained by a larger number of samples used for the calculations and also higher  $\text{CO}_2$  concentration variations in July, which makes it easier to define the regression slope in Keeling plots. It is interesting to note that the observed results follow the same tendency as that observed for the  $\text{O}_2/\text{CO}_2$  ratios in Fig. 2.5b, with higher ratios in July compared to May. In addition, I calculated the isotopic signature of air samples collected at 5 cm above the ground using only nighttime values (in July) but it was only slightly different from the total July nighttime estimate shown in Fig. 2.6.

This study has demonstrated the potential of using combined measurements of  $\text{CO}_2$ ,  $\text{O}_2$  and  $\delta^{13}\text{C-CO}_2$  to study changes occurring in a natural ecosystem. Tight relationships between the three species allow for detailed analyses of obtained data, and demonstrate clear correlations in their temporal changes, possibly as a result of complex changes in respiration (rates or types of organic matter respired) occurring within the ecosystem over the vegetative season. Further research would require more frequent sampling, especially in summer and at the breaks of seasons. Another aspect of such a study could possibly incorporate making similar measurements in other natural ecosystems which could reveal not only temporal but also ecosystem-level differences and peculiarities of respiration and assimilation of organic matter.

## 2.4 Variations of CH<sub>4</sub>, CO and N<sub>2</sub>O

Figure 2.7 shows variations of CH<sub>4</sub>, CO and N<sub>2</sub>O concentrations from 15 to 18 May 2005. The last day was characterised by low wind speeds (Fig. 2.2) which resulted in some stratification of the air column with maximum concentrations in all species around 6 am. As small build-ups in nighttime concentrations are seen in all species they probably can be attributed to changes in vertical mixing of the air column rather than local sources. As CO does not have significant diurnal biogenic cycles, its vertical distribution can be partially used as an indication of the strength of vertical mixing for species with more complicated source/sink relationships, namely CH<sub>4</sub> and N<sub>2</sub>O.

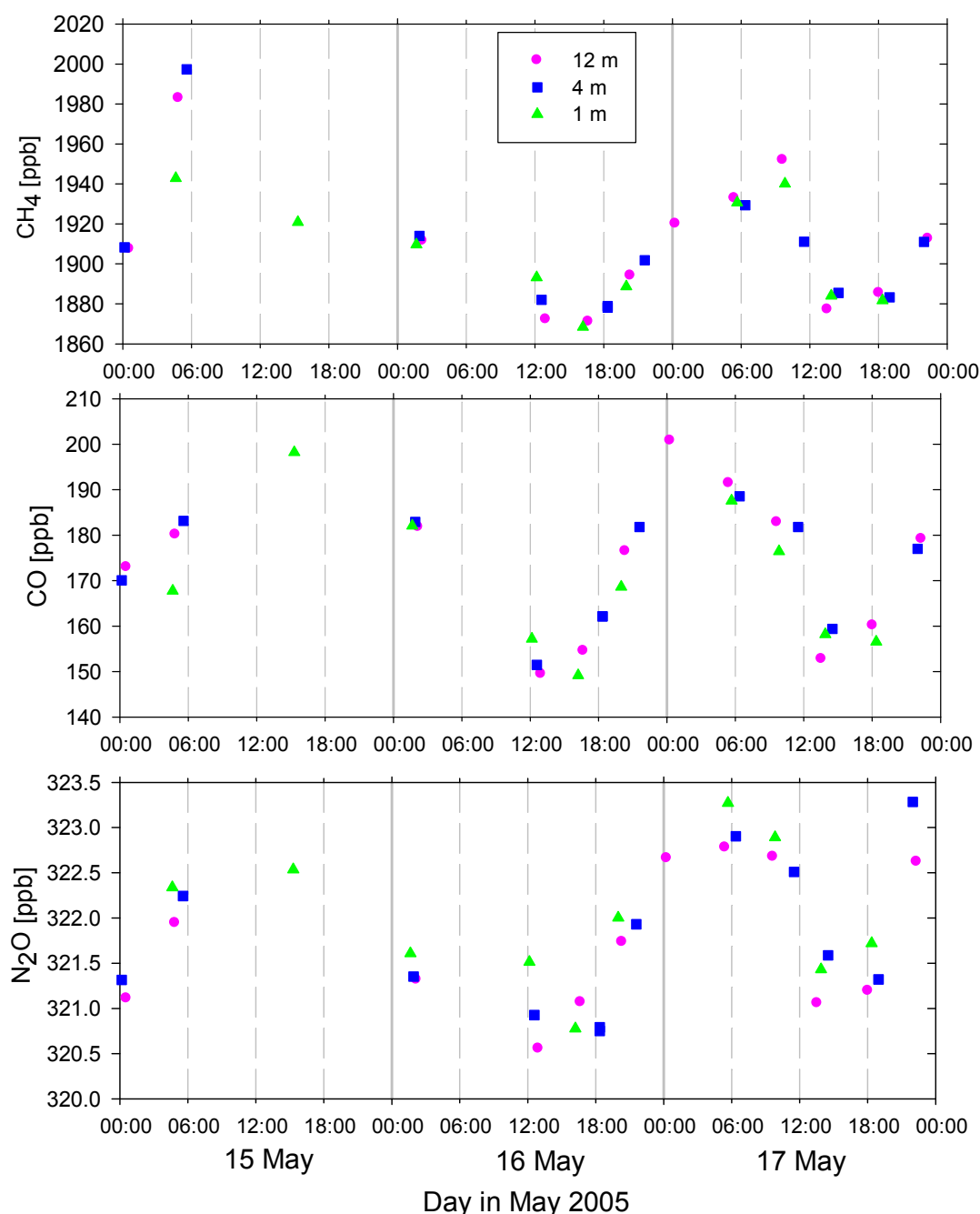


**Figure 2.7:** CH<sub>4</sub> (top panel), CO (middle panel) and N<sub>2</sub>O (bottom panel) concentrations of air samples collected from 15 to 18 May 2005. Each data point is an average of three flask measurements. The solid vertical lines correspond to midnight (local time: UTC+2 hrs).

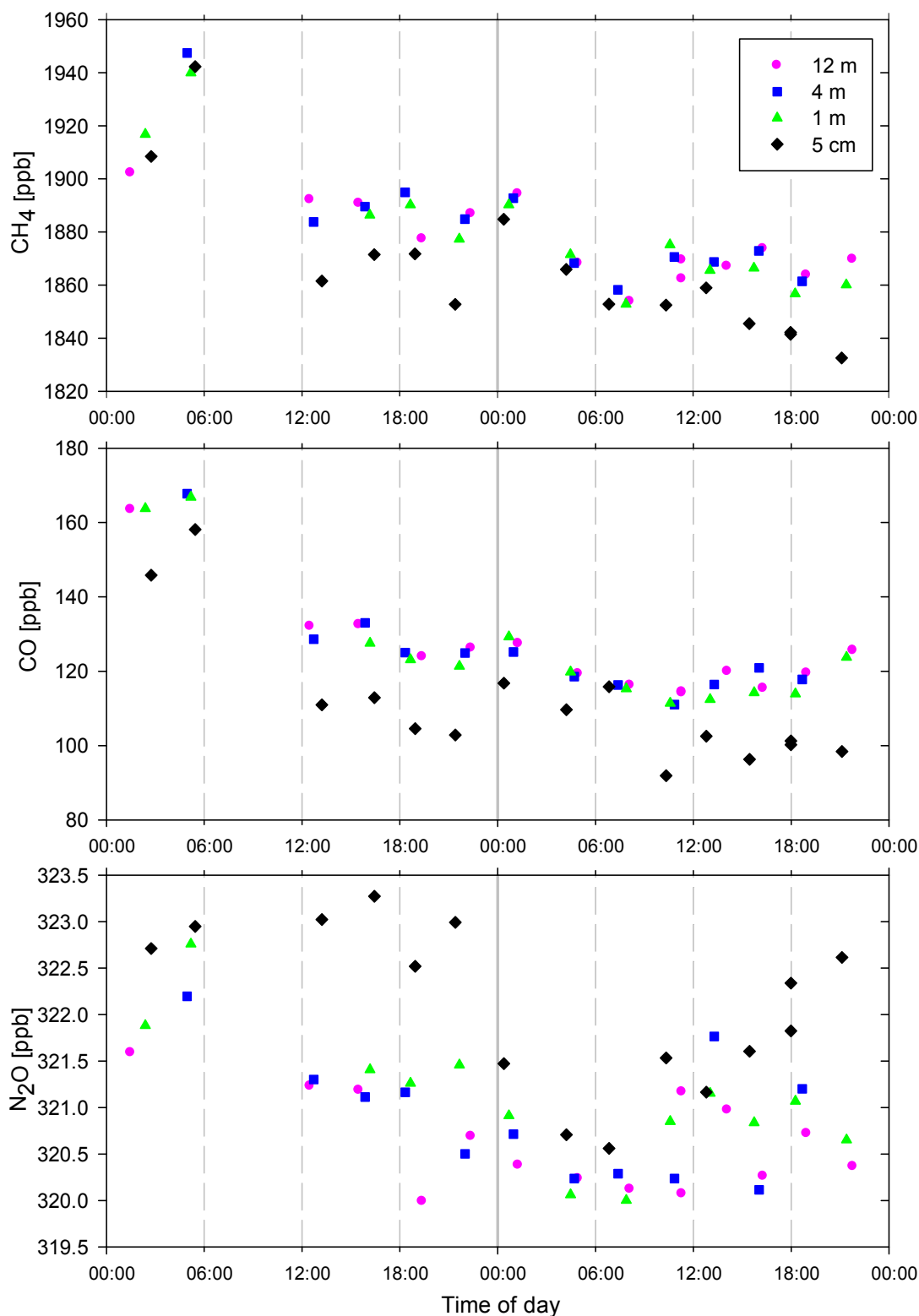


**Figure 2.8:** CH<sub>4</sub> (top panel), CO (middle panel) and N<sub>2</sub>O (bottom panel) concentrations of air samples collected on 16 and 17 July 2005. Each data point is an average of three flask measurements. Solid vertical lines correspond to midnight (local time: UTC+2 hrs)

Keppler *et al.* [2006] stated that plants emit much more CH<sub>4</sub> during daytime when exposed to light. Absence of clear diurnal cycles of CH<sub>4</sub> contradicts this hypothesis of significant emissions from plants, especially from forest ecosystems.

Figure 2.8 shows variations in concentrations of the same gas species but for July 2005. Similar to May data, concentrations of CH<sub>4</sub>, CO and N<sub>2</sub>O were practically

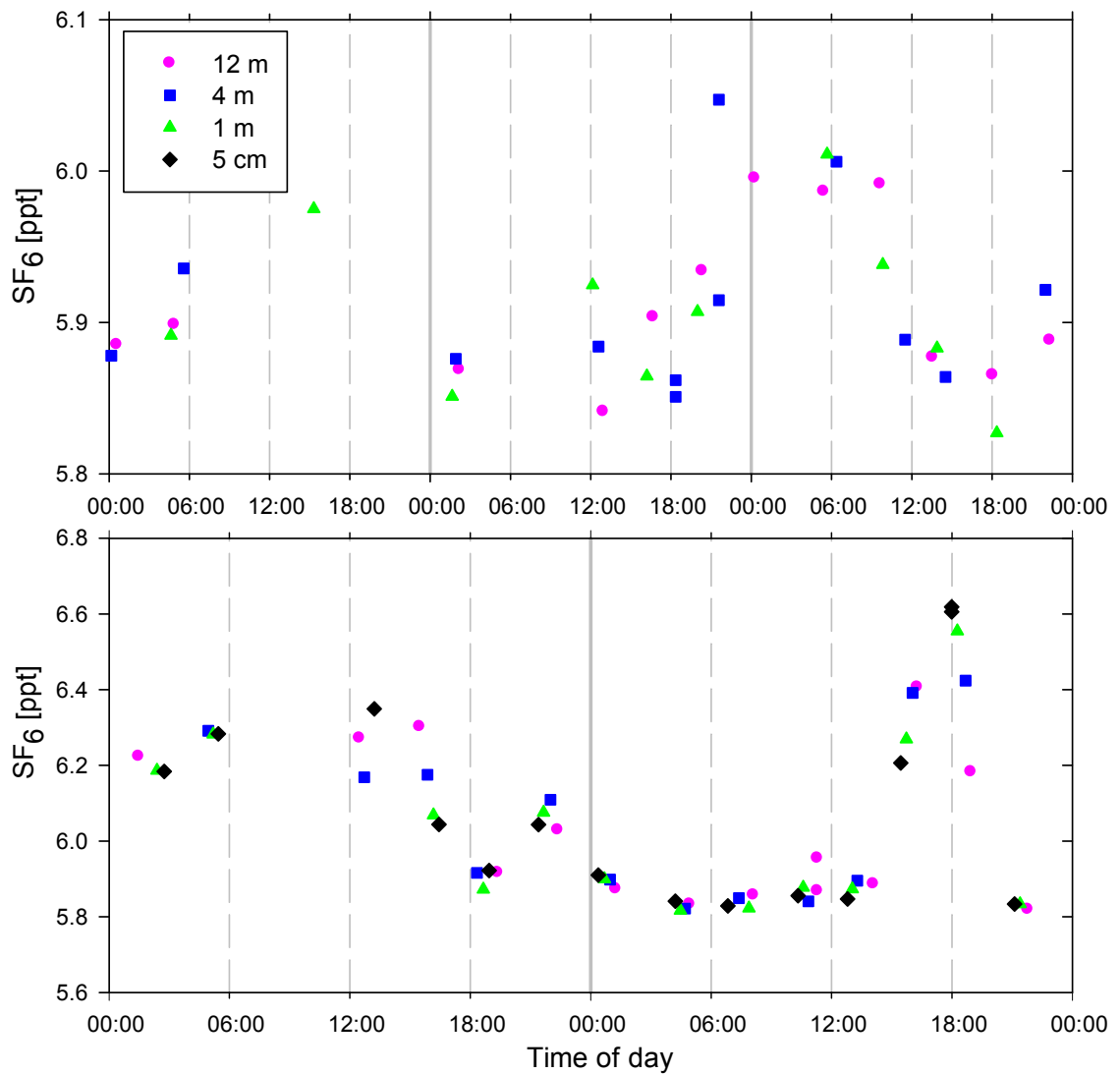


**Figure 2.9:** Daily variations of SF<sub>6</sub> concentrations during two sampling campaigns in 2005. The top panel displays SF<sub>6</sub> concentrations from 15 to 18 May whilst the bottom panel covers the sampling period on 16 and 17 July. All data are shown in local time (UTC+2 hours). The solid vertical lines represent midnight of each day shown. The SF<sub>6</sub> concentration units are ‘part per trillion’ (ppt).

indistinguishable at 1, 4 and 12 m heights. The only exception is with N<sub>2</sub>O concentrations at 5 cm above the ground (black diamonds and line in bottom panel of Fig. 2.8). N<sub>2</sub>O data collected at this level show a clear nighttime decline, starting at about 9 pm on 16 July and reaching their minimum around 6 am of the following day. The same tendency was also observed in O<sub>2</sub> concentrations and CO<sub>2</sub> but with the opposite sign) in Fig. 2.3 and was discussed in Section 2.5. The decline in N<sub>2</sub>O concentrations indicates a soil sink in the processes of nitrogen transformation, such as denitrification (See Chapter 1, Section 1.5.5). With larger datasets, including measurements made over different seasons and environmental conditions (e.g. soil moisture and temperature) it might be possible to determine a correlation between CO<sub>2</sub>

and N<sub>2</sub>O soil emissions in an undisturbed forest ecosystem, which would then be able to characterise different processes of organic matter decomposition.

## 2.5 Synoptic variations of sulphur hexafluoride (SF<sub>6</sub>)

SF<sub>6</sub> represents one of the fluorinated gases (together with hydrofluorocarbons (HFCs) and perfluorocarbons (PFCs)) whose concentration regulations are covered by the Kyoto Protocol. The global atmospheric concentration of SF<sub>6</sub> is relatively low (~6 ppt at present) but has been linearly increasing over the last decades (an increase of ~30% has been observed since 1998) implying that annual emissions have remained relatively constant [Forster *et al.*, 2007]. In addition, a very long lifetime (~3200 years) insures that all emissions stay intact and accumulate in the atmosphere. Natural emissions of SF<sub>6</sub> (from out-gassing of fluorite rocks) are negligible (they account for ~0.01 ppt of the global atmospheric concentration). Thus, all SF<sub>6</sub> emissions to the atmosphere can be considered purely anthropogenic (or industrial) and thus can be used as indicators for polluted air masses. SF<sub>6</sub> gas is widely used in the electric power industry as a dielectric medium for high-voltage circuit breakers, switchgear, etc, as it is much more effective than using oil, dry air or nitrogen gas. Owing to its purely anthropogenic origin and very low solubility in seawater, SF<sub>6</sub> has been also used as a tracer in numerous studies of ocean mixing [e.g., Watson and Ledwell, 2000].

The top panel of Figure 2.9 shows that SF<sub>6</sub> concentrations observed at Hainich Forest from 15 to 18 May 2005 did not vary by more than 0.2 ppt over the whole period of observation and were uniform at all sampling heights. This is as expected because SF<sub>6</sub> is inert with respect to the terrestrial biosphere. A small increase by about 0.2 ppt (above the background value) can be seen during the night and early morning on 15-16 May, subsequently decreasing around 10:00 local time (16 May). The observed nighttime accumulation is a result of changes in the vertical mixing, with more air column stratification during the night. This conclusion is further supported by meteorological data (Fig. 2.2) which shows very low wind speeds during that night. From this perspective, in the presence of a relatively local source of SF<sub>6</sub>, measurements of this anthropogenic gas could help the interpretation and analysis of concentration data of natural greenhouse gases (e.g., CO<sub>2</sub>, CH<sub>4</sub>, and N<sub>2</sub>O) whose daily and synoptic variations are more complex owing to the combination of transported and locally produced emissions, particularly in the absence of meteorological data. Thus periods with well-defined vertical gradients in nighttime SF<sub>6</sub> concentrations would be more suitable for studies on local emissions of the biogeochemical gases as the influences of horizontal and vertical mixing were minimised.

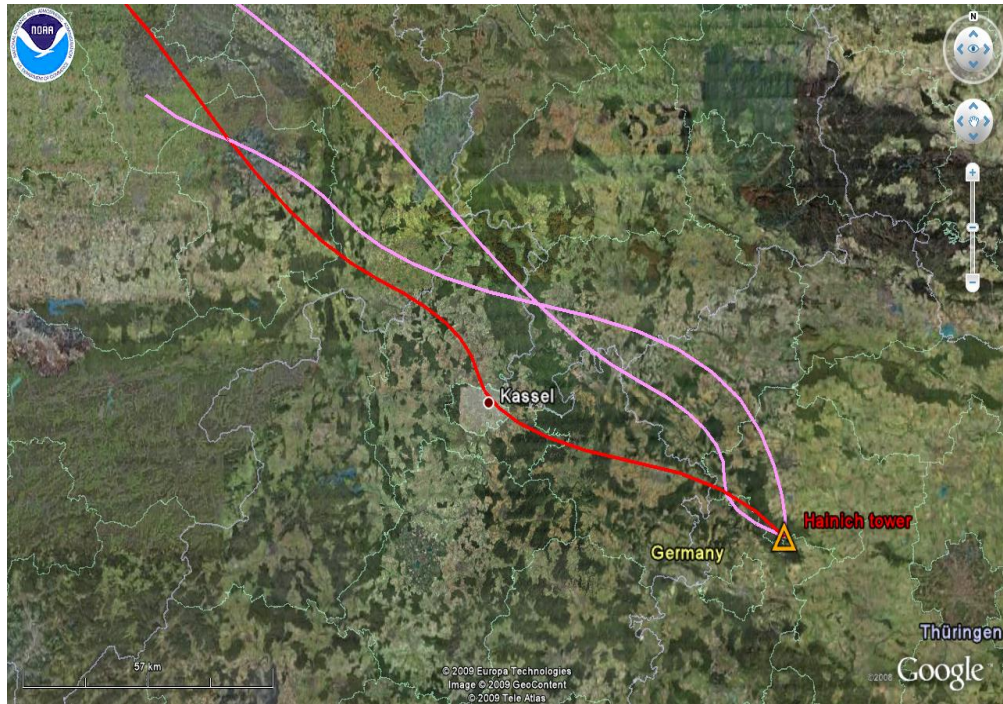


**Figure 2.10:** 24-hour back trajectories of air masses arriving at the Hainich tower site on 17 July 2005. The trajectory of air that transports elevated SF<sub>6</sub> concentrations (see also Fig. 6.9) around 18:00 (local time) is shown in red. The other two trajectories (both in pink) show the origin of air masses that arrived to the site 6 hours before (12:00) and after (00:00) the pollution event.

In contrast to the May data, SF<sub>6</sub> concentrations observed on 16-17 July were more variable, with a well-defined peak observed at all sampling heights during the day and early evening on 17 July. The SF<sub>6</sub> peak looks like a result of synoptic variations in the transport of air masses, even more likely because of relatively low SF<sub>6</sub> concentrations over a 12-hour period prior to the discussed event. Meteorological data show that the dominant wind direction during that day was from the northwest (Fig. 2.4 bottom panel). I attempted to identify the origin of elevated SF<sub>6</sub> concentrations at the Hainich Forest by computing back trajectories [Draxler and Hess, 1998] of air mass movements before, during and after the event. Figure 2.10 shows three 24-hour back trajectories of air masses arriving at the Hainich tower site at the time of the observed SF<sub>6</sub> peak (~18:00), and 6 hours before (12:00) and after (00:00). The back trajectory of air that appears to be responsible for the SF<sub>6</sub> pollution peak (shown in red) is slightly different from the other two (both shown in pink). Air masses that arrived at the site around 18:00 might have brought some pollution as they appear to have passed over Kassel, a small city in central Germany (population ~200,000 people), whilst air masses represented by the other two trajectories bypassed this city.

All trajectories were obtained with the FNL dataset for the NH (resolution of 191 km) and obviously cannot be considered very accurate owing to a relatively coarse resolution of the meteorological dataset. I tried to estimate the robustness of the

observed differences between the trajectories by using a different meteorological dataset. For the second set of back trajectories (not shown) I used the Global Data Assimilation System (GDAS) with slightly better but comparable resolution of  $\sim 1^\circ$  ( $\sim 100$  km at this latitude). As expected, trajectories obtained with the two different datasets were not exactly the same, however, they showed the same pattern. The 18:00 trajectory appears to be different from the other two based on analysis of both meteorological datasets. All trajectories were run with an input height of 43 m, which is the height of the Hainich tower. To test the influence of height on the trajectory analysis results I changed the input height twice (to 300 and 500 m) for the 18:00 trajectory on 17 July but no significant differences were observed.

Extended 48-hour trajectories showed that all air masses that arrived at the Hainich tower site on 17 July 2005 came from the North Sea. Similar results from both datasets provide me with more confidence to presume that there was an SF<sub>6</sub> source in the area around Kassel. Figure 2.8 shows that there were no associated elevated concentrations in CO<sub>2</sub>, CH<sub>4</sub> or CO, which one might have expected. I did not find any facts that would confirm that there are any industrial plants near Kassel where SF<sub>6</sub> gas is routinely used. However, since SF<sub>6</sub> is often used as an insulator for high-voltage gear, a leak (or malfunction) even at a small voltage transformation station could have accounted for the observed elevated concentration of SF<sub>6</sub>. These results indicate that caution must be taken in interpreting SF<sub>6</sub> data, since it appears that it is possible that SF<sub>6</sub> ‘spikes’ may not always suggest an anthropogenic influence on other trace gas species.

Another question is whether this short period of high SF<sub>6</sub> concentrations was a result of a single and random event or rather a continuous (or sporadic) leak from presumably high-voltage power lines. I performed another set of model runs to establish the origin of air during the other periods for which SF<sub>6</sub> data were available. Back trajectories of air masses arriving to the site on 15-16 May (not shown) did not pass over Kassel and originated either from the northwest or north, bypassing any large cities on their way to the Hainich Forest which explains the relatively low SF<sub>6</sub> concentrations observed. Figure 2.11 shows another set of back trajectories for 16 and 17 July 2005. The time when those trajectories arrive to the Hainich Forest coincides with SF<sub>6</sub> concentrations shown in Figure 2.9. Trajectories shown in pink, yellow and dark blue represent air masses arriving to the Hainich tower at 12:00, 18:00 and 00:00 on 16 July 2005 (all times are local). The light blue, red and brown trajectories represent air masses arriving to the site at 12:00, 18:00 and 00:00 on 17 July 2005. The Figure shows that all trajectories except the one at 18:00 on 17 July bypassed Kassel, with the closest one (shown in yellow) arriving at the Hainich Forest at 18:00 on 16 July, however, SF<sub>6</sub>

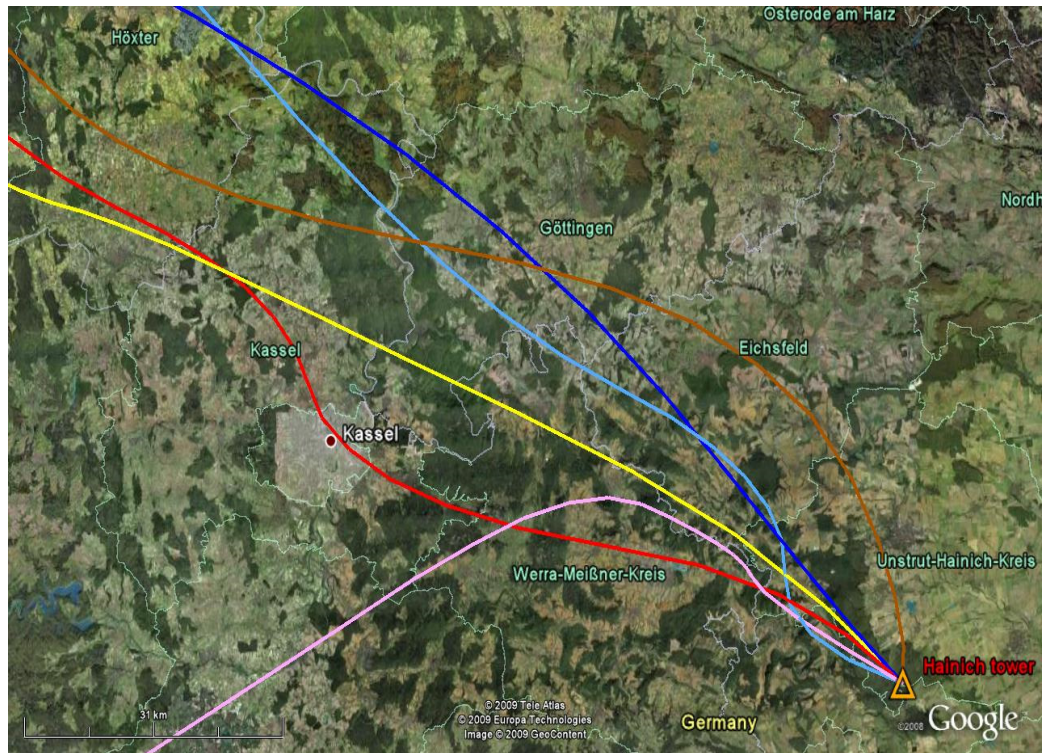


**Figure 2.11:** 48-hour back trajectories for 16 and 17 July 2005 using the FNL meteorological dataset. Trajectories shown in pink, yellow and dark blue correspond to the air masses arriving to the Hainich tower at 12:00, 18:00 and 00:00 on 16 July 2005 (all times are local). The light blue, red and brown trajectories represent air masses arriving to the site at 12:00, 18:00 and 00:00 on 17 July 2005 respectively (the red trajectory is for the same time as the red trajectory in Figure 2.10).

concentrations for this time period (see Fig. 2.9) were low. Thus, results of the last exercise show that air masses arriving to the site on the other days for which atmospheric SF<sub>6</sub> concentrations were measured at the Hainich Forest did not follow the same pathway as those that appear to be responsible for the elevated SF<sub>6</sub> concentrations at 18:00 on 17 July. So it seems that I do not have enough measurements to make a reliable conclusion on whether the observed SF<sub>6</sub> emission that most likely occurred in the area around city Kassel was sporadic or regular.

With requirements for cutting GHG emissions under the Kyoto Protocol it becomes even more important to be able to reliably identify and control those emissions, particularly in areas downwind of large industrial centres. Regular (or at least on a campaign basis) measurements of SF<sub>6</sub> or other anthropogenically produced gases downwind of densely populated areas could help to quantify and ultimately, to mitigate, such emissions. More accurate assessments of air trajectories can be achieved with regional back trajectory analyses (e.g., STILT (Stochastic Time Inverted Lagrangian Transport) model analysis) which have the potential to both track and quantify (via ‘inverse’ atmospheric modelling) anthropogenic emissions.

Unfortunately, the sampling campaigns described above were relatively short and it would be beneficial to extend such measurements to longer periods and other

months of the year. Results presented here, however, have demonstrated the potential of such measurements. In addition, these results lay a foundation for multi-species measurements that will be explored with a much richer dataset from the continuous atmospheric measurements in central Siberia (Chapters 5 and 6).

## CHAPTER 3. Methodology for autonomous continuous measurements

### 3.1 Introduction to Chapter

In this chapter, I present the methodology and operating principles for an integrated system for making measurements of CO<sub>2</sub>, O<sub>2</sub>, CH<sub>4</sub>, CO, and N<sub>2</sub>O in central Siberia. The system was initially designed by Dr. Andrew Manning in 2001, at the time the leader of the Tall Tower Group at Max Planck Institute for Biogeochemistry (MPI-BGC, Germany). Two prototypes of the system were previously installed and operated by Dr. Manning's group at two tall tower sites in Europe, Ochsenkopf (Germany) and Białystok (Poland). The system presented below, however, represents the most advanced set-up owing to numerous modifications, improvements, additional safety features and advanced programming (in comparison to the prototypes), which were crucial for its operation at such a remote site as central Siberia. The analytical measurement system was built as an integrated cohesive unit, rather than a suite of independent analysers measuring different species, and collects and processes the 'final' concentrations of the gas species in real-time, minimising the need for data post-processing.

Air was sampled from five heights on a custom-built 300-m tower and drawn into a measurement laboratory, where temperatures were necessarily controlled to at least  $\pm 2^\circ\text{C}$ , despite an ambient seasonal cycle of approximately  $70^\circ\text{C}$ . Common features to all species' measurements include air intakes, an air-drying system, sample flushing procedures, and data processing methods. Calibration standards are shared between all five measured species, extending a proven methodology for long-term O<sub>2</sub> calibration [Keeling *et al.*, 2007; Keeling *et al.*, 1998]. These approaches have resulted in reliable, autonomous measurements, while still achieving the exacting precision and accuracy requirements specified by the European Union's 'CarboEurope' and 'Integrated Carbon Observing System (ICOS)' programmes, in the case of CO<sub>2</sub>, O<sub>2</sub>, and CH<sub>4</sub>. CO and N<sub>2</sub>O, however, still require some further improvements as discussed below. A large fraction of material presented here was published in *Kozlova and Manning* [2009].

The remainder of this chapter describes the development and operating principles of the ZOTTO measurement system, which is for simplicity presented as the sum of the following subsystems: air intake (Section 3.2.1), air drying (Section 3.2.2), O<sub>2</sub> and CO<sub>2</sub> measurement (Section 3.2.3), gas chromatographic (GC) measurement (Section 3.2.4) and GC peripherals (Section 3.2.5). The data acquisition procedures are discussed in Section 3.2.6.



## 3.2 The ZOTTO measurement system: description and operation

The ZOTTO tall tower measurement system consists of 6 subsystems: an air intake, air drying, O<sub>2</sub> and CO<sub>2</sub> measurement, gas chromatographic (GC) measurement, GC peripherals, and calibration standards (the latter discussed in Chapter 4) (all shown in Figure 3.1).

The tower itself was constructed in Siberia in several stages. By the autumn of 2005 it had been built up to 55 m height, which allowed me to start testing the measurement system using temporarily installed sampling lines. In September 2006, the tower construction (up to 300 m) was completed, and the full tower measurement system became operational from the end of Oct 2006. The description of the air intakes and sampling lines below refer to the final sampling set-up, that is, when the tower was fully constructed.

### 3.2.1 Air intake subsystem

Air was sampled from five heights on the tower: 300, 227, 92, 52 and 4 m. At the 300 m platform there are three air intakes using 12 mm outside diameter (OD) sampling lines (Saint-Gobain Performance Plastics Corp., Synflex 1300 tubing) for O<sub>2</sub> and CO<sub>2</sub> measurements, GC species (CH<sub>4</sub>, CO and N<sub>2</sub>O) measurements, and flask sampling (not shown in Figure 3.1). Additionally, there is a ¼" OD Synflex line for O<sub>2</sub> and CO<sub>2</sub> measurements. This line is used to check for possible O<sub>2</sub> fractionation effects which can occur at the 'tee' junction in the 12 mm lines, as first observed and described by Manning [2001]. At 227, 92, and 52 m, there are two 12 mm sampling lines (for O<sub>2</sub> and CO<sub>2</sub>, and GC species), and at 52 m there is a supplementary ¼" line for O<sub>2</sub> fractionation tests (discussed in Chapter 4, Section 4.6). At 4 m, there are two ¼" lines, one each for O<sub>2</sub> and CO<sub>2</sub>, and GC species.

Air was pulled into each 12 mm line by a dedicated pump (Thomas Industries, model 607CD32) at a flowrate of 5 L/min (for example, pumps OXC7 and GCC5 in Figure 3.2). Since the analytical system is designed for a flowrate of 150 mL/min, a tee-junction (kept at constant temperature inside the laboratory, thus reducing the potential for fractionation) allows the excess air (4.85 L/min) to be purged. For the 12 mm O<sub>2</sub> and CO<sub>2</sub> lines cylindrical buffer volumes (3.1 L) were installed between the tees and the purge pumps to minimise pressure pulsations from the pump at the tee, which have been shown to cause O<sub>2</sub> fractionation [Manning, 2001]. The ¼" OD sampling lines were not equipped with purge pumps or tees and had flowrates of 150 mL/min directly from the tower inlets.

I experienced frequent problems with our air inlets, mainly due to ice blockages

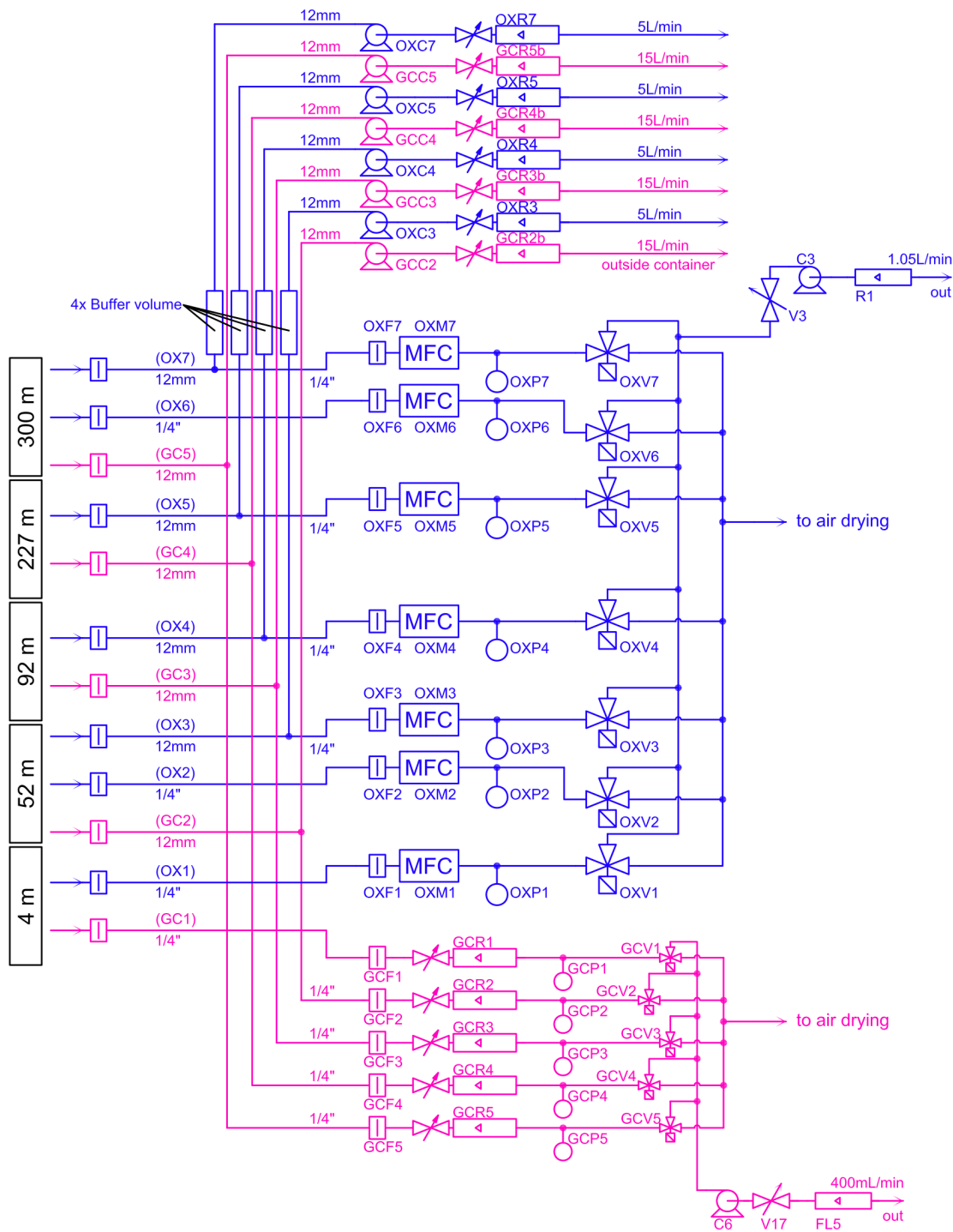


**Figure 3.2:** Air intake subsystem. Note that as schematically represented in the Figure, there appears to be dead volume downstream of the 3-way valves (OXV1-7 and GCV1-5); however in actuality they are mounted in a manifold arrangement with zero dead volume.

occurring most often during autumn and spring, when weather patterns change abruptly. This led to the unfortunate necessity of climbing the tower in very cold weather (see Acknowledgements). For the higher flowrate 12 mm lines inlets were designed as simple, inverted metal shielding for protection from snow/rainfall (coffee cups) (Figure 3.3). I had tested several different types of the air inlets, namely small metal coffee



**Figure 3.3:** Blockage of the tower air inlets at 300 m due to extensive snowfall. Left: GC air inlet (an inverted coffee cup); Right: aspirated air inlet for O<sub>2</sub> and CO<sub>2</sub> measurements.

cups, plastic funnels and different sizes of PVC tubes (2" and 4"-diameter and ~70 cm long) during the testing stage (Nov 2005 – Oct 2006). After the first winter, the metal cups were replaced by similar but larger ones (1.5 L volume) as I thought it might reduce the possibility of them being blocked by snow. I dismissed the 4"-diameter PVC tube as a GC air inlet as it adversely affected the measurements, particularly N<sub>2</sub>O, for unknown reasons. As a result of my tests, I decided on using large metal cups on the lower levels of the tower, 2"-diameter PVC tube (that proved to be the most resistant to snow blockages) at 227 m and a large metal shielding at 300 m (accommodating the sampling lines for GC, 12 mm line for O<sub>2</sub> and CO<sub>2</sub> measurements, and the 12 mm line for flask collection).

Comparisons of O<sub>2</sub> concentration data from both 'fast' and 'slow' flowrate lines are helpful in evaluating the tee junction fractionation contribution in continuous O<sub>2</sub> measurements (see Chapter 4, Section 4.6). O<sub>2</sub> fractionation has also been observed at air inlets under relatively slow flowrates [Manning, 2001], caused by ambient temperature variations and, especially, under the influence of direct sunlight [Blaine *et al.*, 2006]. To minimise these effects, we installed aspirated radiation shields (R. M. Young, model 43408) at the inlets on all slow flowrate (1/4" OD) O<sub>2</sub> and CO<sub>2</sub> sampling lines (at 4, 52 and 300 m), following Blaine *et al.* [2006]. All sampling lines are protected from dirt and particulate matter with replaceable 40 µ filters installed immediately after the inlets on the tower (shown unlabelled in Figure 3.2, Swagelok, TF series). During the testing phase, I used much finer Swagelok filters (2 µ) whose filter elements could not be replaced (FW series), which proved to be impractical due to more frequent filter blockages.

At the base of the tower, all sampling lines incorporate a nylon Swagelok union, to protect all analytical equipment from possible lightning strikes on the tower. For O<sub>2</sub> and CO<sub>2</sub> measurements the desired flowrate (150 mL/min) is achieved by mass flow

controllers (MFC, OXM1-7 in Figure 3.2, MKS Instruments Inc., model 1179B). Additional 2  $\mu$  filters (OXF1-7) protect the MFCs from possible particulate matter. Three-way manifold-mounted solenoid valves (OXV1-7 and GCV1-5 in Figure 3.2, Numatics Inc., S-series) allow selection of sampling lines for analysis; air from the selected lines travels to the analysers while air from all non-selected lines is constantly purged by pumps C3 and C6 (Thomas Industries, 107CCD18) to minimise the effects of pressure distortions and flushing times upon switching the selected airstream from one line to another. The GC inlet sampling lines are of similar design as those for O<sub>2</sub> and CO<sub>2</sub> with the only difference being that the required flowrate of 100 mL/min is set manually by rotameters with integrated needle valves (GCR1-5, Cole Parmer). This design is more economical than using MFCs while still functional since the GC measurements are not as sensitive to flowrate variations as O<sub>2</sub> measurements. However, owing to drift in the needle valves' settings it is sometimes necessary to adjust the flowrates for the GC lines, which is not very practical at such a very remote site, therefore, a design incorporating MFCs would be more practical (but more expensive).

For each airstream selected for analysis, a diaphragm compressor pump (C1 and C4 (for the O<sub>2</sub> and CO<sub>2</sub>, and GC systems respectively), KNF Neuberger, model N05-ATI) draws the air into the system. This pump (now an obsolete model) was previously thoroughly tested for possible influences on O<sub>2</sub> and CO<sub>2</sub> concentrations in an airstream (A. C. Manning, UEA, pers. comm., 2004). So far, no other pump model has been similarly tested. These pumps were internally modified by our workshop by machining O-rings grooves and adding O-rings to increase the integrity of the pump heads to avoid leakage. Any leakage occurring at the below-ambient pressure side of the pump would directly lead to a significant contamination of the sample with room air; this is why the initial integrity and regular maintenance of the pumps are particularly important. I found that regular (2 times per year) changes of the diaphragms and valve plates are required to eliminate the possibility of leaks and ensure best pump performance.

### **3.2.2 Air drying subsystem**

Sample air is pre-dried by passing through two glass traps in the O<sub>2</sub> and CO<sub>2</sub> (FT1 and FT2), and GC (FT3 and FT4) measurement subsystems (Figure 3.4). These traps are installed in a commercial refrigerator maintained at about +1-2°C to remove the bulk water content from the air. The traps are filled with borosilicate glass beads (Sigma Aldrich, 4 mm diameter) both to reduce the internal volume of each trap (from 61 to 36 mL), as well as to provide additional surface area for water vapour to condense. The condensed water is removed at a flowrate of 0.21 mL/min by a peristaltic pump

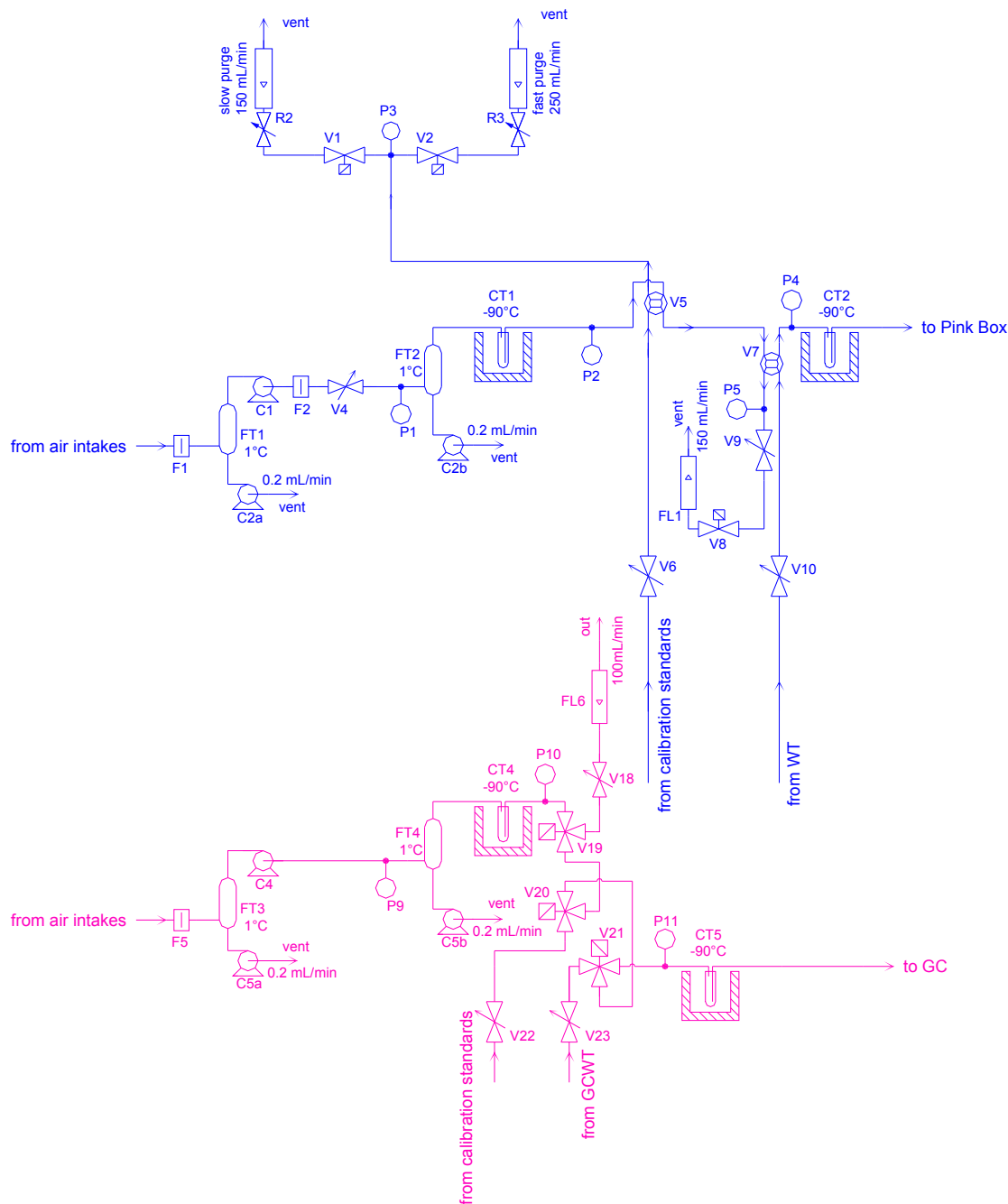


**Figure 3.4:** Air drying subsystem.

(C2a,b and C5a,b, for O<sub>2</sub> and CO<sub>2</sub>, and GC systems respectively) where ‘a’ and ‘b’ indicate two pump heads attached to the same pump motor (Cole Parmer, L/S<sup>®</sup> Fixed-Speed Economy Drive). The refrigerator traps upstream of pumps C1 and C4 prevent water vapour from condensing inside the pump, whereas the refrigerator traps downstream of the pumps are more efficient in water removal because of the pump overpressure (about 1600 mbar absolute). Further drying occurs by passing the air through cryogenic, electro-polished stainless steel traps (CT1 and CT4) immersed in an ethanol bath at -90°C (FTS Systems Inc., 8-litre Vapor Trap). On the assumption that the sample air has sufficient time to equilibrate with the cryogenic trap temperature the water content of the air would then be about 0.06 ppm. Direct dewpoint measurements

with an identical cryogenic setup in the laboratory gave a water content of less than 0.4 ppm (the lower limit of the dewpoint meter used; M. Patecki, UEA, pers. comm.). The refrigerator traps help to prolong the lifetime of these cryogenic traps but they still require replacement approximately every 2 weeks. To mitigate the analysers' 'sweep out' time (because of the large trap volume) we filled these traps with 4 mm diameter borosilicate glass beads, which reduced their total volume by a factor of two (from 105 to 45 mL). Three additional cryogenic traps (CT2, CT3 and CT5) of a smaller volume are used to dry cylinder air (pre-dried) to the same dewpoint as sample air, which improves the reproducibility of the measurements. The 'small' traps are also filled with borosilicate glass beads (3 mm diameter) and have a total volume of 7.6 mL (with beads). To eliminate the need to open and close the cryogenic traps manually when removing the built up ice (which significantly increases the potential to introduce leaks), we make use of the excess unused air from the GC purge pumps to dry the traps. All traps are equipped with quick connectors (Swagelok, QC series) which make the procedure of changing them fast and simple.

### 3.2.3 O<sub>2</sub> and CO<sub>2</sub> measurement subsystem

The 'Paramagnetic Oxygen Sensor, Paramax 101' from Columbus Instruments International Corp. was improved by adding high precision temperature and pressure control systems, and making fine-tuning adjustments very similar to those described in Manning *et al.* [1999], and Manning [2001]. The O<sub>2</sub> sensor inside the analyser (see Figures 3.5 and 3.6) is a 'PM1155' (Servomex Company Inc.) which exploits the paramagnetic properties of O<sub>2</sub> [Kocache, 1986]. Initially we received an analyser with an 'upgraded' PM1158 sensor, but this gave very poor performance. A second PM1158 gave similar poor performance; so finally, in Oct 2006 we installed a now obsolete PM1155 model, loaned to us by Prof. Ralph Keeling (Scripps Institution of Oceanography (SIO), USA). Our CO<sub>2</sub> measurements are made with a commercially available NDIR CO<sub>2</sub> analyser (Siemens AG, Ultramat 6F).

To improve the analysers' precision by minimising the influence of baseline drift (primarily induced by temperature), measurements of a reference standard with known O<sub>2</sub> and CO<sub>2</sub> concentrations (referred to as 'Working Tank' (WT)) always bracket each sample air measurement. A four-way valve (V7 in Figure 3.4, Swagelok, 40 Series ball valve) with a pneumatic actuator is programmed to alternately switch every 8 min between sample air or WT air being sent to the analysers. We analyse air from a given height on the tower for 8 minutes, referred to as an 'air jog', and bracket it with 8-minute 'WT jogs'. In both cases, we discard the first 4 minutes of data, and average the

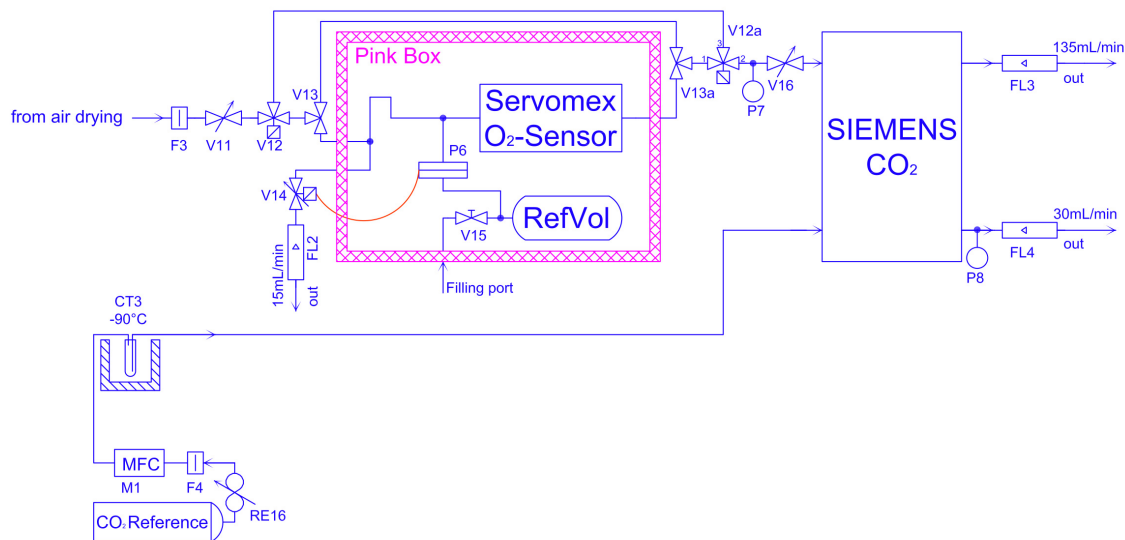


**Figure 3.5:** O<sub>2</sub> and CO<sub>2</sub> measurement subsystem.

last 4 minutes. The first 4 minutes must be discarded owing to a long sweep-out time resulting from the large cell volume of the Siemens CO<sub>2</sub> analyser (88 mL). A linear interpolation of the two WT jog averages is then subtracted from the 4 min jog average of air data. This procedure results in one tower air measurement (differenced from the WT) every 16 minutes. The Swagelok 40 Series valves are only rated for ~40000 switches, in other words a lifetime of about 7.5 months at the switching frequency of once every 8 min. After this, the valve is likely to develop cross-port leakage owing to extrusion of the packing material, a subtle problem that can easily go undetected. I found evidence of such cross-port leakage on more than one occasion, and so I implemented a policy of replacing these valves every 6 months. I also sent two of the ‘problematic’ valves back to the Swagelok manufacturer in the USA, and they confirmed that my valves had operated according to their specifications.

Figure 3.7 (top panel) shows an example of the O<sub>2</sub> paramagnetic sensor raw data output in the units of ppm (uncalibrated) over a 4 hour period on 15 Mar 2007. The data are shown both in real-time at the computer display in graphical format and recorded in data output files (see Appendix 3) once every second. For further calculations, only 30-sec averaged data are used. As shown in Figure 3.7, the Servomex baseline drifts significantly, clearly demonstrating the necessity of the switching between WT and sample air. The data influenced by spikes (seen as outliers in Fig. 3.7), resulting from the valve switching, are removed during the data filtering procedures (discarding of the first 4-min of any measurement). To maintain pressure and flow equilibrium in all tubing and equipment, air from the line which is not being analysed is flushed through a solenoid valve V8 (Numatics, S-series) and a flowmeter FL1 (McMillan, model S-113) at the same flowrate of 150 mL/min. This procedure is particularly important to achieve



**Figure 3.6:** The interior of the custom-built Pink Box (described in text) encloses the Servomex O<sub>2</sub> sensor, a differential pressure gauge and a pressure reference volume. The very high temperature stability ( $\pm 0.006^{\circ}\text{C}$ ) is achieved by six surface-mount heating elements (covering all interior walls, bottom and lid of the box), two fans, an active temperature controller and a custom-built electronic circuitry. As no moving parts were incorporated in the design of the Pink Box, it requires no regular maintenance – a highly desirable feature for operation at a remote location.

good O<sub>2</sub> concentration results. In the case of the WT, in order to save air, we only start flushing through V8 4 min before its next measurement (in other words, V8 is off for 4 min, saving 600 mL of air in each 16 min cycle). Another identical four-way valve, V5, selects between either calibration standard or sample air lines, and is employed whenever calibration standards are to be analysed (see Chapter 4 for details on calibration procedures).

The Servomex O<sub>2</sub> sensor is known to be extremely sensitive to flow, pressure and temperature variations [Manning, 2001]. To ensure a very stable temperature environment we built a well-insulated box ('Pink Box' in Figures 3.5 and 3.6) enclosing the Servomex O<sub>2</sub> sensor, a differential pressure gauge (P6, MKS Instruments Inc., Baratron 223B) and a pressure reference volume. Six surface-mount heating elements (Omega Engineering Inc., Kapton Flexible Heaters), thoroughly cover all interior walls, bottom, and lid of the box. Together with two fans (RS Components Ltd., Micronel Fan), an active temperature controller (Omega Engineering Inc., CN4800 Series Logic controller), and custom-built electronic circuitry, we are able to keep the inside

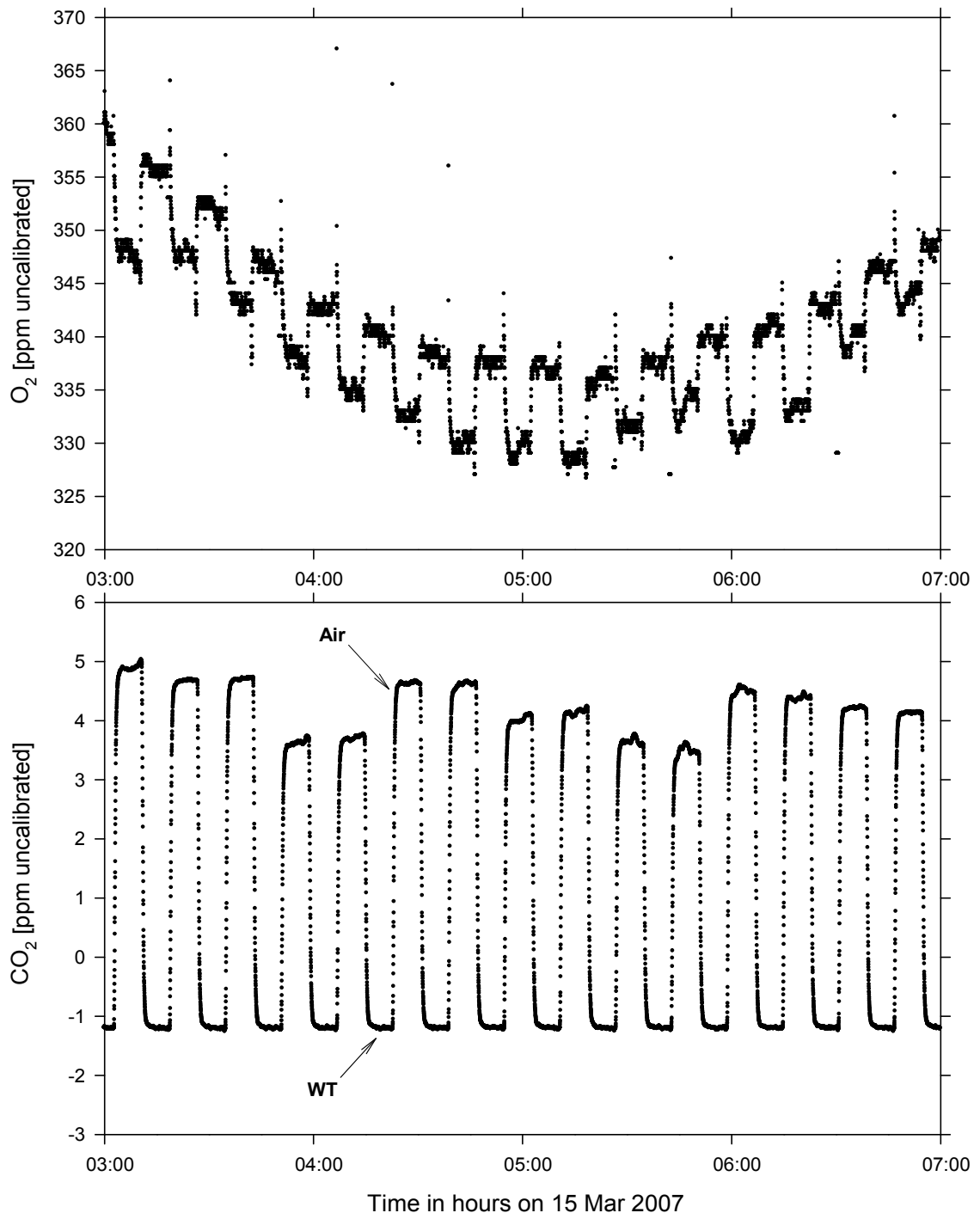


**Figure 3.7:** Uncalibrated signals from the O<sub>2</sub> (top panel) and CO<sub>2</sub> (bottom panel) analysers shown for a randomly selected period of 4 hours on 15 Mar 2007. In the O<sub>2</sub> panel the upper jogs are the 8-min WT measurements and the lower jogs are the 8-min tower measurements (reversed for CO<sub>2</sub>). Both O<sub>2</sub> and CO<sub>2</sub> are shown in uncalibrated units as given by the analysers, which to a very rough approximation are ppm. The data points are collected and recorded in the output files at a frequency of 1 Hz. The outliers in the top panel correspond to pressure pulsations caused by the switching of the four-way valve (V7) between WT and air. The ‘zero’ of the y-scale in the O<sub>2</sub> panel is entirely arbitrary; the concentration range is set manually and does not correspond to the real ambient O<sub>2</sub> content. The y-scale in the CO<sub>2</sub> plot shows the difference between the CO<sub>2</sub> concentrations of an air sample or WT air relative to the ‘CO<sub>2</sub> reference’ cylinder concentration in the analyser’s (uncalibrated) ppm units.

temperature both homogeneous and stable to  $\pm 0.006^{\circ}\text{C}$  (typical  $1\sigma$  standard deviation of an hourly average) with an absolute value of  $\sim 34\text{-}36^{\circ}\text{C}$  (Figure 3.8). This very high

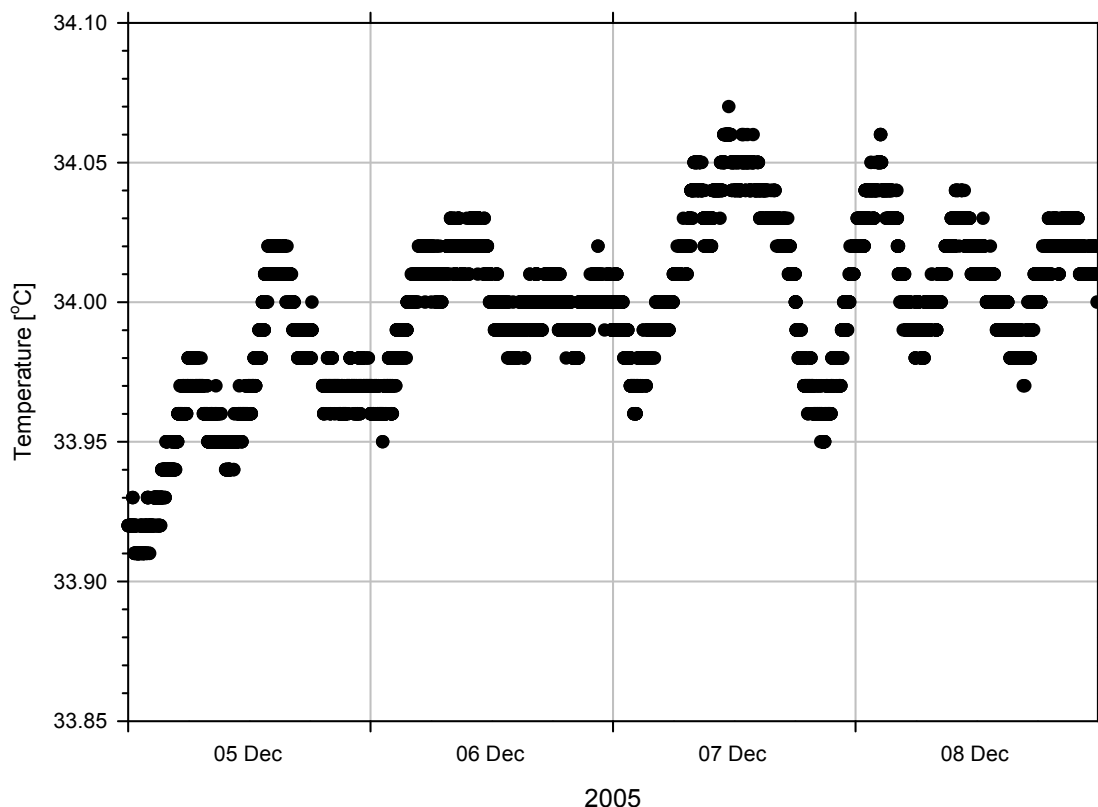


**Figure 3.8:** The ‘Pink Box’s’ temperature is shown for four randomly selected days in December 2005. The average temperature over the entire period was  $33.997\pm 0.030^{\circ}\text{C}$ . It is, however, more important to be able to keep the temperature constant over short-term periods since our frequent WT switching will cancel out any temperature-induced drift over longer time periods. Thus, for example, the average hourly temperature (calculated over the whole 4-day period) is  $33.996\pm 0.006^{\circ}\text{C}$ .

temperature stability was found to be necessary to achieve the acquired  $\text{O}_2$  precision (see Chapter 4, section 4.5). Another important advantage of the Pink Box is that unlike many other thermally controlled enclosures it has no moving parts (except fans) and therefore does not need any regular maintenance, a very desirable feature for operation at a remote location. To protect the  $\text{O}_2$  analyser against accidental high flowrate (flowrates above only 200 mL/min can cause irreversible damage to the sensor), an electronic switch is programmed to cut off the flow by closing two 3-way solenoid valves (V12 and V12a in Figure 3.5), forcing the air to bypass the Servomex sensor. This switch operates independently from any computer. Valves V13 and V13a are manual 3-way valves used to isolate the Servomex sensor during testing and start-up procedures. Precise pressure-compensating needle valves (Brooks Instrument, model 8504) were installed upstream (V11) and downstream (V16) of the  $\text{O}_2$  analyser to fine-tune the pressure in the sample line. Pressure control in the  $\text{O}_2$  sensor is achieved with

the differential pressure gauge P6 ( $\pm 1$  mbar full scale), a controlling solenoid valve (V14, MKS Instruments Inc, 248A) and an electronic controller (MKS Instruments Inc., 250E). By adjusting the solenoid, the controller maintains zero differential pressure (with  $\pm 0.0005$  mbar short-term precision) between the sensor and the reference volume (filled to 1270 mbar). To avoid a possibility of even a small leak, which would result in baseline drift, the reference volume was soldered to the differential pressure gauge (P6). Adjustable bypass flow through the control valve, V14 in Figure 3.5, allows both pressure and flowrate to be kept highly constant through the sensor [Manning *et al.*, 1999]. Because of this bypass arrangement, any variations in flowrate or pressure upstream of the O<sub>2</sub> analyser will affect solely the bypass flowrate (about 15 mL/min), maintaining constant flow through the analyser (135 mL/min).

After the airstream has been analysed for O<sub>2</sub> mole fraction (see Chapter 4, Section 4.2.1 for O<sub>2</sub> calculations), it enters the sample cell of the Siemens CO<sub>2</sub> analyser. Unlike the O<sub>2</sub> analyser which is a so-called ‘absolute’ analyser, the CO<sub>2</sub> analyser operates in a ‘differential’ mode, measuring the difference in CO<sub>2</sub> mole fraction between a sample and a reference cell, and therefore requires a constant reference cell air flow, provided by a dedicated cylinder (‘CO<sub>2</sub> Reference’ in Figure 3.5). The CO<sub>2</sub> reference air flowrate is set to 30 mL/min by a mass flow controller (M1, MKS Instruments Inc., 1179B). This reference air also passes through a ‘small’ cryogenic trap (CT3) before entering the CO<sub>2</sub> analyser. The outlets of both sample and reference cells are vented to the atmosphere. Figure 3.7 (bottom panel) shows an example of uncalibrated data from the CO<sub>2</sub> analyser over a 4-hour randomly selected period in March 2007. The CO<sub>2</sub> baseline (shown at approximately -1 ppm in Figure 3.7), which corresponds to WT measurements (differenced from CO<sub>2</sub> Reference), is very stable in contrast to the O<sub>2</sub> baseline. Nevertheless, I have found that switching between WT and sample (crucial for O<sub>2</sub> measurements) additionally improves the reproducibility of the CO<sub>2</sub> measurements (see Chapter 4, Section 4.5). Unlike the O<sub>2</sub> analyser, the Siemens CO<sub>2</sub> analyser has proved to be extremely robust (particularly important under the conditions of our field site) and not very sensitive to flowrate and pressure fluctuations. It does show some sensitivity to vibration or mechanical shock which thus should be avoided. The analyser has a significant sensitivity to temperature, which was somewhat mitigated with passive insulation, but which has no influence on the measurements’ reproducibility because of the very frequent WT analyses. Although significant, this temperature sensitivity is much less than that observed for Licor CO<sub>2</sub> analysers, previously installed at other tall tower sites, which require an active temperature controller and special arrangements to avoid baseline drifts due to ambient temperature

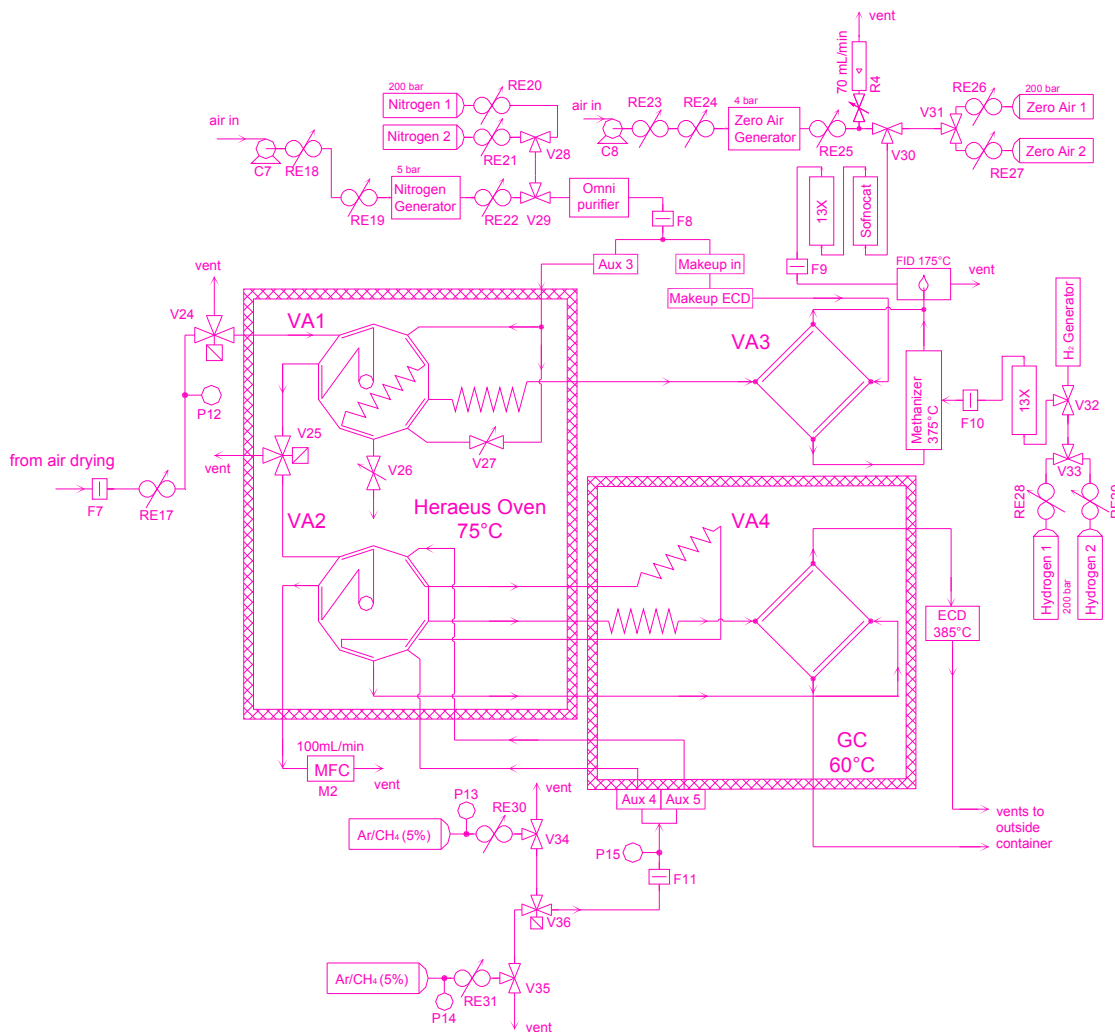


**Figure 3.9:** GC measurement and peripherals subsystems.

changes (A. C. Manning, UEA, pers. comm.). The reproducibility and repeatability of the measurements obtained from both O<sub>2</sub> and CO<sub>2</sub> analysers are discussed in detail in Chapter 4, Section 4.5.

### 3.2.4 Gas chromatographic (GC) measurement subsystem

The GC measurement subsystem (Figure 3.9) consists of a GC (Agilent Technologies, 6890A) equipped with a Flame Ionization Detector (FID) and a methaniser, used for CH<sub>4</sub> and CO measurements, and an Electron Capture Detector (ECD) for N<sub>2</sub>O measurements. An isothermal ( $\pm 0.1^\circ\text{C}$ ) oven (Heraeus Holding GmbH, model T6), sample loops, and packed columns are integrated with both detectors (specifications given in Table 3.1). Although, the GC itself is commercially available, our application, which is to achieve very accurate (and precise) long-term atmospheric measurements at a remote location, requires many additional modifications. The initial GC development was done based on the experience which already existed in the ‘GASLAB’ (MPI-BGC) run by Dr. Armin Jordan. The GC set-up at the prototype tall tower station at Ochsenkopf, Germany, was used as a starting point for the ZOTTO GC

development.

The ZOTTO GC measurement system is similar to that described in Worthy *et al.* [2003] and Jordan *et al.* [2005]. The ‘run table’ for all events and parameters (set within the ChemStation™ software (version B.01.03, Agilent Technologies)) is summarised in Table 3.2.

Setting or specification	FID (CH <sub>4</sub> and CO)	ECD (N <sub>2</sub> O)
Sample loop volume	15 mL	25 mL
Pre-column	SS 1/8" OD, 4 ft long, Molsieve 5A, Mesh 80-100	SS 3/16" OD, 6 ft long, Haysep-Q, 80-100 Mesh
Analytical column	SS 1/8" OD, 4ft long, Unibeads 1S, Mesh 60-80	SS 3/16" OD, 6 ft long, Haysep-Q, 80-100 Mesh
Carrier gas flow rate	N <sub>2</sub> at 100 mL/min	Ar-CH <sub>4</sub> (5%) at 190 mL/min
Back-flush flowrate	N <sub>2</sub> at 100 mL/min	Ar-CH <sub>4</sub> (5%) at 360 mL/min
Oven temperature	75°C	60°C
Detector and catalyst temperature and fuel gas flowrates	175°C NiO Catalyst: 375°C H <sub>2</sub> : 70 mL/min Zero Air: 300 mL/min	385°C
Run time	6.0 min	6.0 min

**Table 3.1:** Settings and specifications for CH<sub>4</sub>, CO and N<sub>2</sub>O measurements on the Agilent 6890A GC.

To ensure that air enters the sample loops at constant pressure we use a forward pressure regulator (RE17 in Figure 3.9, Porter Instrument Company Inc., model 8286) set to approximately 1280 mbar. Two 3-way solenoid valves (V24 and V25) downstream of RE17 simultaneously switch to their ‘on’ positions to allow air to flush through the sample loops. A constant flowrate of 100 mL/min through the sample loops is ensured with an MFC (M2) downstream. The loops are flushed for 1 minute at the beginning and at the end of each analysis (with the subsequent sample), resulting in a total flushing time of 2 min for each sample. After flushing, V24 and V25 switch to their ‘off’ positions (vented to the room) and the system pauses for 30 sec, allowing the air in the sample loops to equilibrate with oven temperature and atmospheric pressure [Worthy *et al.*, 2003]. V25 also serves the role of preventing possible CH<sub>4</sub> (which comprises 5% of the ECD carrier gas) contamination of the FID sample loop, where CH<sub>4</sub> is being measured at the ppb level.

Two 10-port, 2-position injection valves (VA1 and VA2, VICI Valco Instruments Co. Inc., UW Type with electric actuators) switch simultaneously to pass the air sample in the sample loops onto the respective pre-columns and analytical columns (see Table 3.1 for specifications). Both injection valves (VA1 and VA2) switch

again (at different times) to the pre-column back-flush position as soon as the gas species of interest have passed onto the analytical columns, in order to reduce the measurement time as well as to avoid contaminants entering the analytical columns. Since passing O<sub>2</sub> through an ECD is known to cause baseline drift and deterioration in the detector [Jordan *et al.*, 2005], the O<sub>2</sub> in the sample air is vented outside, bypassing the ECD. This was made possible by incorporating a 4-port, 2-position valve (VA4, Valco Instruments Co. Inc., W Type with micro-electric actuator). Similarly, another valve of the same configuration (VA3) is used to bypass O<sub>2</sub> away from the methaniser (nickel oxide catalyst) to avoid the degrading influence of O<sub>2</sub> on its efficiency. VA3 switches back to the methaniser pathway as soon as CH<sub>4</sub> elutes from the analytical column, so that CO can be reduced to CH<sub>4</sub> and then detected by the FID.

The Valco valves with the micro-electric actuators (VA3 and VA4), which were previously also used as injection valves (VA1 and VA2), turned out to be one of the main problematic issues in the GC system's continuous operation at ZOTTO. Repeated failures of these valves are responsible for most 'gaps' in our GC species data records, particularly for N<sub>2</sub>O. The remoteness of the site did not allow me to replace the broken pieces of the valves immediately after each failure, leading to long periods with no data being collected from one or even both detectors. The solution was finally found when an older version of the same valves (with electric actuators) was installed, which proved to be much more robust in long-term continuous operations at other remote locations (D. Worthy, Environment Canada, pers. comm.). I continued, however, to use a valve with a micro-electric actuator in the VA3 position, because of the faster switching required when an air sample is sent to the FID via the methaniser. Initially, all valves (except VA3) were installed inside the ovens (with the actuators being outside) to keep all tubing at the analysis temperature, however, it proved to be not necessary since the 1/16" tubing used in the GC set-up has a very fast temperature equilibration time. The replacement of the micro-electric actuated valves with the electric actuated valves, as well as installing them outside of the heating zones, made the GC measurements much more "continuous" and facilitated valve maintenance. The values of all physical parameters (pressures, flowrates and temperatures) shown in Tables 3.1 and 3.2 were carefully tuned to produce the most reproducible chromatograms. Since air was sampled from five heights one after the other, having as short a duration as possible for each air analysis was important to provide the best data coverage from each height. After running many tests, I was able to reduce the analysis time to 6.0 min, however, this required higher flowrates of the carrier gases, which was particularly notable for Ar-CH<sub>4</sub> because all other gases were supplied by gas generators (see details below).

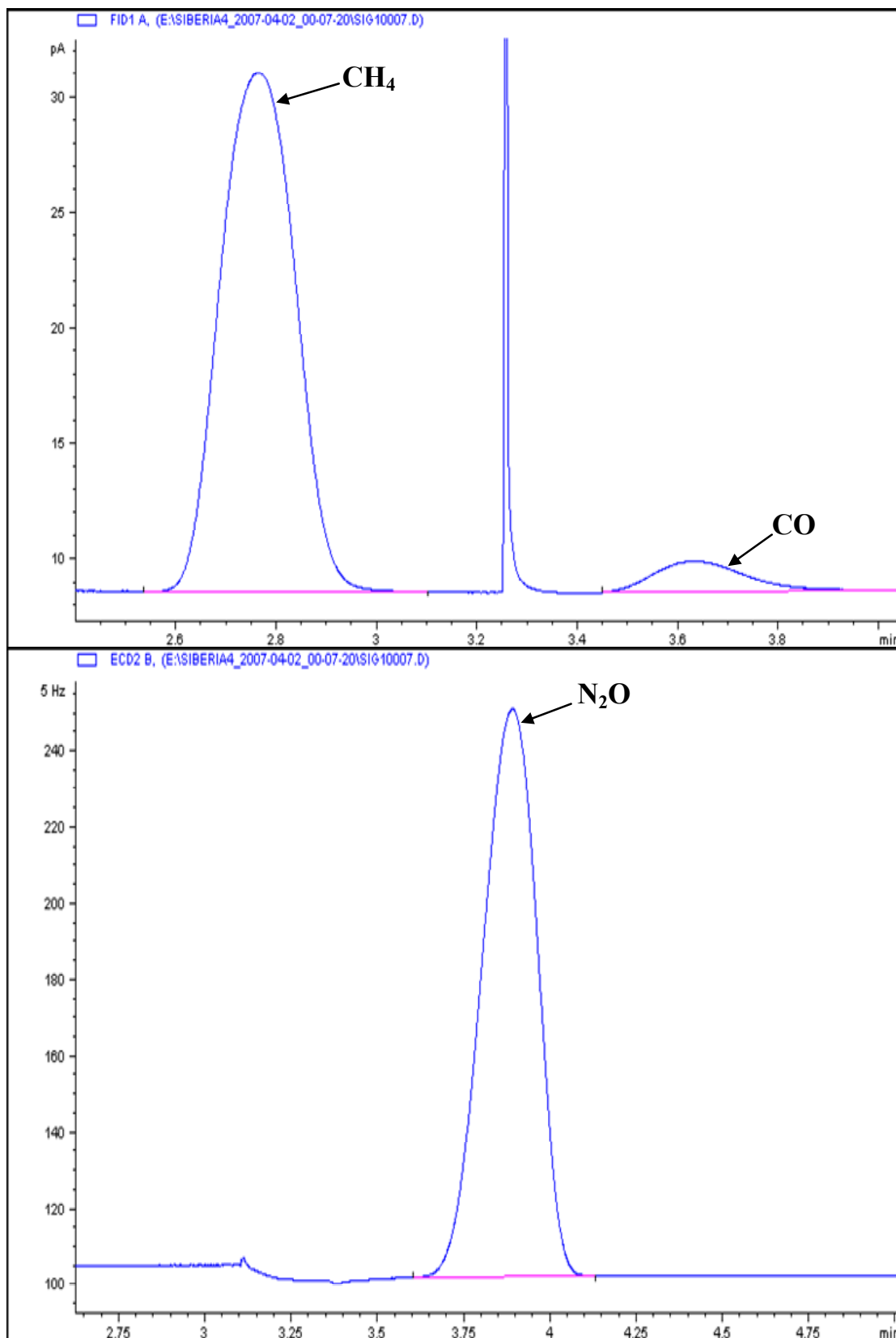


**Figure 3.10:** Typical chromatograms of CH<sub>4</sub>, CO and N<sub>2</sub>O. Pink lines on both panels show extrapolation of the baselines used for calculating the integrated areas and heights (based on the integration parameters in Table 3.3). The x-scales show the time (in min) of a method run (6 min total). The output signals are plotted on the y-scales in pA for the FID and Hz for the ECD. Large disturbances in both chromatograms (at 3.25 min for FID and 3.10 min for ECD) are caused by valves switching (see Table 3.2).

The 'raw' data (generated and recorded after each run by the ChemStation™

software) are represented by the height and area of a sample calculated based on the customised integration parameters (Table 3.3). The latter are set and manually adjusted within the ChemStation™ software to obtain the most reproducible chromatogram results. Typical chromatograms of CH<sub>4</sub>, CO and N<sub>2</sub>O are shown in Figure 3.10. The integration parameters require periodical adjustments as slight changes in the chromatograms may occur over time (for example, due to the columns' degradation, particularly in the case of the molecular sieve column). Unfortunately, I was unable to perform these regular checks and adjustments since on-line access to the measurement system was not permitted, and I only visited the site twice per year. Therefore, the integration parameters were set only during my trips to ZOTTO, and could not be re-adjusted until the next visit to the site, which did have an influence on the GC data reproducibility results.

Because of the relatively fast degradation of the molecular sieve column leading to fluctuations in the CO retention time, and therefore somewhat worse reproducibility, I did regular maintenance on this column by disconnecting it from the FID and 'baking' it at about 250°C at the analysis flowrate for ~24 hours. However, since this procedure changes the efficiency of the column, the CO peak usually then elutes much later after baking (sometimes it appears to be even 'missing' because of the analysis time being too short for CO to elute), which requires some further adjustments of the run table and, finally, the integration parameters.

Analyses of CH<sub>4</sub>, CO, and N<sub>2</sub>O on the GC follow a similar philosophy as that for O<sub>2</sub> and CO<sub>2</sub>, in that every tower air jog is bracketed by WT jogs (GCWT). GCWT is a dedicated cylinder, which is analysed on the GC every 6 min to avoid the influence of baseline drifts of the FID and, particularly, the ECD (which exhibits temperature correlated diurnal cycles). I divide the tower air peak measurement by the average of the two bracketing GCWT peak measurements. As with the O<sub>2</sub> and CO<sub>2</sub> system, when GCWT is being analysed, I continue to flush air from the selected tower air line through V18 and V19 (Figure 3.4). In contrast to the O<sub>2</sub> and CO<sub>2</sub> system, however, when tower air is being analysed, I do not flush GCWT gas. This was found not to be necessary because the relative precisions required for the GC species are much less than that for O<sub>2</sub> (approximately 65 times lower relative precision for the most sensitive GC species, N<sub>2</sub>O). since the total run-time for a single GC analysis is 6 minutes (Table 3.2), I achieve one tower air measurement every 12 minutes for CH<sub>4</sub>, CO, and N<sub>2</sub>O.

Time (min)	Specifier	Parameter and Setpoint
0.00	Aux 3 <sup>a)</sup> pressure	0.00 <sup>a)</sup> bar
0.01	Aux 4 <sup>b)</sup> pressure	3.00 bar
0.01	Aux 5 <sup>c)</sup> pressure	3.00 bar
0.01	Valves V24+V25 <sup>d)</sup>	On <sup>d)</sup>
0.02	M2 <sup>e)</sup>	Off <sup>e)</sup>
0.65	Valve VA3 <sup>f)</sup>	Off <sup>f)</sup>
0.75	Aux 3 pressure	4.00 bar <sup>a)</sup>
1.00	Valve V24+V25	Off <sup>d)</sup>
1.01	M2	On
1.50	Aux 4 pressure	0.3 bar
1.50	Aux 5 pressure	3.80 bar
1.50	Valve VA1 <sup>g)</sup>	On <sup>g)</sup>
1.50	Valve VA2 <sup>h)</sup>	On <sup>h)</sup>
1.50	Valve VA4 <sup>i)</sup>	On <sup>i)</sup>
3.10	Aux 4 pressure	2.80 bar
3.10	Aux 5 pressure	4.5 bar
3.10	Valve VA2	Off <sup>h)</sup>
3.10	Valve VA4	Off <sup>i)</sup>
3.25	Valve VA3	On <sup>f)</sup>
4.40	Valve VA1	Off <sup>g)</sup>
4.69	Valve V24+V25	On
4.70	M2	Off
5.68	Valve V24+V25	Off
5.69	Valve VA4	On
5.69	M2	On <sup>e)</sup>

<sup>a)</sup> FID carrier gas (N<sub>2</sub>) enters the GC from Aux 3 inlet (Fig. 3.9). By dividing the N<sub>2</sub> flow with a tee (see Fig. 3.9), it is possible to start the FID column's back-flush at any time of a method run (in this method at 4.40 min). Aux 3 pressure is brought back to 0.00 bar (relative to ambient pressure) at the beginning of each run because of the pressure pulsations occurring during the Valve VA3 (see below) switch which can lead to blowing the FID flame out. The operational pressure (4.00 bar) is restored after the Valve VA3 switches to the 'Off' position (at 0.75 min);

<sup>b)</sup> Aux 4 is one of the ECD carrier gas (Ar-CH<sub>4</sub>) inlets to the GC (Fig. 3.9). By having two independent Ar-CH<sub>4</sub> inlets (Aux 4 and 5) we provide an uninterrupted gas flow through the ECD while O<sub>2</sub> is vented to the atmosphere (see text), and have a freedom of starting the column's back-flush at any time of a method run;

<sup>c)</sup> Aux 5 is one of the ECD carrier gas (Ar-CH<sub>4</sub>) inlets to the GC;

<sup>d)</sup> When these valves are in the 'On' position, the sample is being flushed through the sample loops; when it switches to the 'Off' position, the remaining pressure in the sample loops is vented to the room;

<sup>e)</sup> The MFC (M2) has a fixed setpoint of 100 mL/min, but also can be switched on or off. When switched off, the internal solenoid valve is closed, making a leak-tight seal. It is connected with reverse polarity (the 'Off' position corresponds to the solenoid being opened, and the 'On' position to being closed). The reason for closing the solenoid at the end of each run (at 5.69 min) is to avoid its overheating and consequent damage, should our software fail or crash;

<sup>f)</sup> At the beginning of each run Valve VA3 is in the 'ON' position (set towards the end of the previous run), which indicates that the sample is sent to the FID via the methaniser. To avoid O<sub>2</sub> (which elutes first) influence on the methaniser (see text), Valve VA3 switches to the 'Off' position (bypassing the

methaniser) at time 0.65 min;

<sup>e)</sup> Valve VA1 is the FID injection valve. The (initial) 'Off' position corresponds to the sample loops being flushed with the sample; the 'On' position corresponds to its injection onto the columns;

<sup>h)</sup> Valve VA2 is the ECD injection valve. The 'Off' position (initial) corresponds to the sample loops being flushed with the sample; the 'On' position corresponds to its injection onto the columns;

<sup>i)</sup> The (initial) 'Off' position of VA4 corresponds to the sample being sent directly to the ECD; the 'On' position corresponds to the sample bypassing the ECD (see text).

**Table 3.2:** The GC method run table.

### 3.2.5 GC peripherals subsystem

The GC peripherals consist of gas generators to supply the carrier and fuel gases, combined with high-pressure gas cylinders should any problems with the generators occur. Due to the very remote and difficult to access nature of the site, the use of gas generators is particularly preferable. In addition, use of the generators helps to avoid gas purity variability from one cylinder to another, which can affect the measurements' reproducibility.

There are four main components of the GC peripherals subsystem (all shown in Figure 3.9): nitrogen generating and purifying, synthetic air generating and purifying, hydrogen generating and purifying, and argon-methane.

#### 3.2.5.1 Nitrogen generating and purifying component

To provide a constant source of high purity (99.9999%) gaseous nitrogen ( $N_2$ ) for the FID, I use a  $N_2$  generator (Parker Balston, model UHPN<sub>2</sub>-1100). Pressurised air for the generator is supplied by an air compressor (C7, Jun-Air, model OF302-25B). To dampen the pressure pulsations from the compressor a two-stage regulator (RE19, Parker Balston, model 425) was installed upstream of the generator. The stability of  $N_2$  delivery pressure (5.4 bar) to the GC is ensured by a two-stage regulator (RE22, same model as RE19) downstream of the generator. In case of maintenance work or generator failure, we have the option to use  $N_2$  from high-pressure (200 bar) cylinders. A manual valve (V29, Swagelok, 40 Series Ball valve) allows selection of either the generator or a cylinder, while a second identical valve (V28) selects between one of two  $N_2$  cylinders. This system allows for rapid selection between cylinders and the generator, without introducing any contaminants into the GC. During testing and evaluation, this setup also allows for very easy comparison between generator and cylinder, or different cylinders. Initially, I used the Omni™ (NuPure Corp.)  $N_2$  purifier both in the heating mode and later at ambient temperature to purify the  $N_2$  gas supplied by the  $N_2$  generator. My tests showed, however, that the quality of generated  $N_2$  was very high, and that no extra

purification was necessary.

<b>FID</b>	<b>Event</b>	<b>Value</b>	<b>Time (min)</b>
	Initial Slope Sensitivity	0.90	Initial
	Initial Peak Width	0.12	Initial
	Initial Area Reject	1.00	Initial
	Initial Height Reject	0.10	Initial
	Initial Shoulders	Off	Initial
	Integration	Off	0.00
	Integration	On	2.53
	Baseline Now		3.10
	Integration	Off	3.20
	Integration	On	3.45
	Integration	Off	4.20
<b>ECD</b>	Initial Slope Sensitivity	0.80	Initial
	Initial Peak Width	0.083	Initial
	Initial Area Reject	1.00	Initial
	Initial Height Reject	0.10	Initial
	Initial Shoulders	Off	Initial
	Integration	Off	0.00
	Integration	On	3.60
	Baseline Now		3.60
	Baseline Now		4.15
	Integration	Off	4.18

**Table 3.3:** Parameters within ChemStation™ for optimal integration of CH<sub>4</sub>, CO and N<sub>2</sub>O peaks.

### 3.2.5.2 Synthetic air generating and purifying component

High-purity synthetic air (so-called ‘Zero Air’) is produced by a Zero Air generator (Parker Balston, model 75-83). The setup is similar to that of the N<sub>2</sub> generator described above, with pressurised air supplied by an identical compressor (C8), which is also used as a source of compressed air for the pneumatic air actuators of the 4-way valves in the O<sub>2</sub> and CO<sub>2</sub> system (V5 and V7 in Figure 3.4). Identical regulators (RE24 and RE25) are used to provide constant pressure to the generator and GC respectively, and a manual system for selecting between the generator or high-pressure cylinders is similarly provided by valves V30 and V31 (Figure 3.9). The Zero Air generator requires a continuous flow which we ensure with a tee-junction and a combined rotameter with needle valve (R4), providing a bypass flow of about 70 mL/min. Thus if for any reason the Zero Air flowrate set at the GC is turned off, the generator will still have a flow through it, preventing damage. The Zero Air either from the generator or from cylinders is purified in two stages. A Sofnocat (Molecular Products Ltd, product number 423) trap (0.1 L) removes residual CO from the incoming air stream by oxidising it to CO<sub>2</sub>.

The second stage consists of a 13X molecular sieve trap (0.2 L), where CO<sub>2</sub> (formed in the first trap) and residual water are removed. The generator usually provides very good performance, however, I did have a problem with a premature catalyst failure after only about a year of operation, which resulted in a very high (~20 pA) FID baseline compared to normal (~8 pA). This is why regular maintenance of the catalyst (usually once in 2 years) is crucial for the generator's long-term successful operation.

### **3.2.5.3 Hydrogen generating and purifying component**

Hydrogen (a fuel gas for the FID) is supplied to the GC by a H<sub>2</sub> generator (Parker Balston, model H<sub>2</sub>-150). The design again allows for easy selection between the generator or H<sub>2</sub> gas cylinders via valves V32 and V33 (Figure 3.9). Incorporating such a design with all of our generators also means that should any generator fail, technical staff on-site could quickly switch the system to use gas cylinders. High purity (5 meg-ohm) deionised water is required for the H<sub>2</sub> generator. I use a Hydrogen Mate™ deionised water generator (Parker Balston, model 72-230, not shown in Figure 3.9). To purify H<sub>2</sub> from the generator or cylinders we use a purifying trap filled with 13X molecular sieve (0.2 L). Normally, when the generator is operational, the generated H<sub>2</sub> does not need any further purification, however, it is necessary when using gas cylinders. After about a year of operation my generator failed due to significant salt formation on the palladium membrane, which did not seem to be a consequence of misuse or bad quality of the deionised water. Such unexpected failures demonstrate even greater importance of the dual design allowing the use of both generators and gas cylinders without major interruptions to the system's operation.

### **3.2.5.4 Argon-methane component**

An argon (95%) and methane (5%) mixture (Ar-CH<sub>4</sub>) (Westfalen, Germany) is used as ECD carrier gas and supplied from high-pressure cylinders (200 bar). In contrast to the three other gas supplies, switching between the two Ar-CH<sub>4</sub> cylinders is achieved by a 3-way computer-controlled solenoid valve, V36 (Parker, Series 9), programmed to switch when the pressure in the cylinder in use drops below 15 bar (cylinder pressure is monitored by pressure transducers (P13 and P14, PMA, model P30)). In addition, to prevent the possibility of both cylinders becoming depleted which could cause irreparable damage to the ECD, a controller independent from our computers is employed which sets off audible (80 dB) and flashing alarms in the measurement container and in the living house, if the summed pressure in both cylinders drops below 40 bar. To flush the regulator of a newly installed Ar-CH<sub>4</sub> cylinder and to eliminate the possibility of small amounts of ambient O<sub>2</sub> from getting

into the tubing and thus the ECD, we employ manual 3-way valves installed at the outlet of the regulators (V34 and V35, Swagelok, 40 Series Ball valve). The quality of the Ar-CH<sub>4</sub> purity varies significantly from one cylinder to another. To reduce this variability I tested the Supelco™ High Capacity Gas Purifier (Surplus Lab Inc.), which in my case did not show any improvements in the ECD baseline stability or reduction in the level of O<sub>2</sub> interference during the gas cylinders' replacements.

### 3.2.6 Data acquisition procedures

In addition to the analysers' signals, our computers acquire data from 29 pressure sensors, 6 digital flowmeters, 10 temperature sensors, and 9 MFCs, all shown in Figure 3.1. These parameters are all displayed in real-time on our computer monitor (Figures 3.11 and 3.12), and all data from these sensors are sent to output files (see Appendix 3 for file structure description). In addition, it is possible to view a graph of data for the past hour for any diagnostic parameter on the computer screen. These data provide information about system performance, and assist in interpreting analyser data quality and troubleshooting. Figure 3.13 shows an example of data from 1 week of some of our diagnostic parameters, showing pressures at 17 different positions in the O<sub>2</sub> and CO<sub>2</sub> system. These weekly diagnostic summary graphs can be automatically generated by custom-written IDL™ (Research Systems, Inc.) routines.

Patterns can be seen in these parameters, which, if all is running well, should correspond with our sampling protocols. For example, approximately once per day a calibration cycle is run for several hours, illustrated most notably in Figure 3.13 by the daily events of relatively high pressure in OXP7 and relatively low pressure in P3. The Figure also shows (bottom panel) that one WT cylinder (shown in red) is at full pressure (160 bar) and ready to be implemented when the current online WT cylinder (in blue), showing a steadily decreasing pressure, is exhausted. Nevertheless, even this diagnostic information had to be pre-approved before it could be released to me (~2 month process), thus the diagnostic parameters were reduced to retrospective 'flagging' of data and long-term preventative maintenance, rather than near-real-time system troubleshooting and correction, as done at most other atmospheric monitoring stations.

The overall ZOTTO measurement system is controlled by a bespoke LabVIEW™ (National Instruments Corp.) programme running on our primary computer. The GC is controlled by a second, dedicated computer using ChemStation™ software, with which all GC parameters and chromatography integration procedures are set (see also Section 3.2.4). The LabVIEW™ programme automatically transfers the GC integration results to our primary computer, processes them, and creates GC data

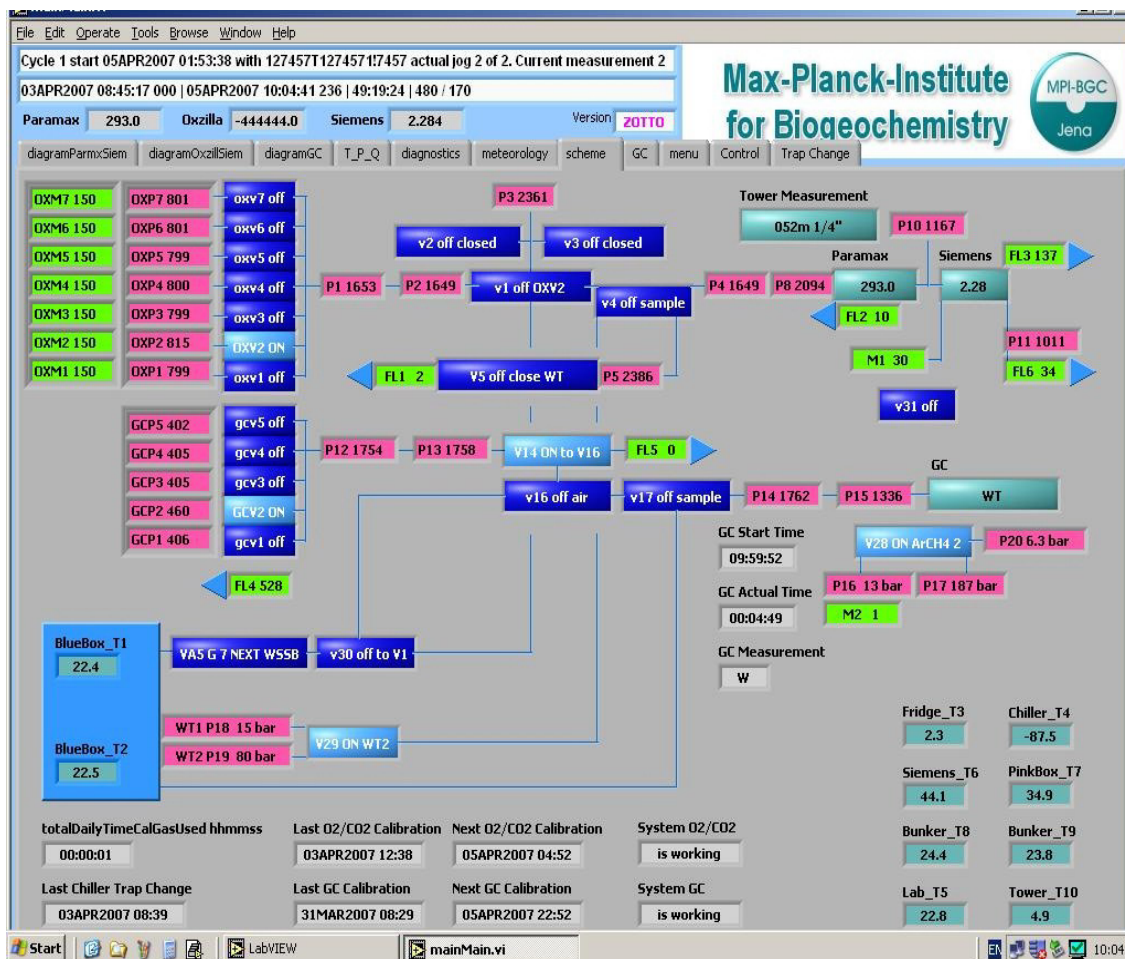


**Figure 3.11:** The screen diagram (generated by a bespoke ZOTTO LabView™ programme) displays all main parts of the measurement system, including diagnostic parameters and their real-time changes. The layout was designed to be similar to the gas-handling schematic in Fig. 3.1. The diagram contains all essential information necessary to monitor the system's operation, e.g., dates of last calibrations and chiller traps changes. The diagnostic data quality indicators (see Appendix 4) are used to identify and troubleshoot most common problems.

output files (see Appendix 3). In the beginning of the GC operation I experienced a very serious problem with the 'communication' between ChemStation™ software and our custom-written LabView™ programme, which often resulted in the GC 'freezing', with no data being collected. The solution was to install a newer version of the ChemStation™ software (version B.01.03), which made it compatible with our Windows XP operating system. However, I discovered that weekly rebooting of the ChemStation™ software (which had to be performed by an operator on-site) was still necessary to avoid any unexpected software failures. Similar regular ChemStation™ rebooting procedures have previously been employed by other colleagues (D. Worthy, Environment Canada, pers. comm.).

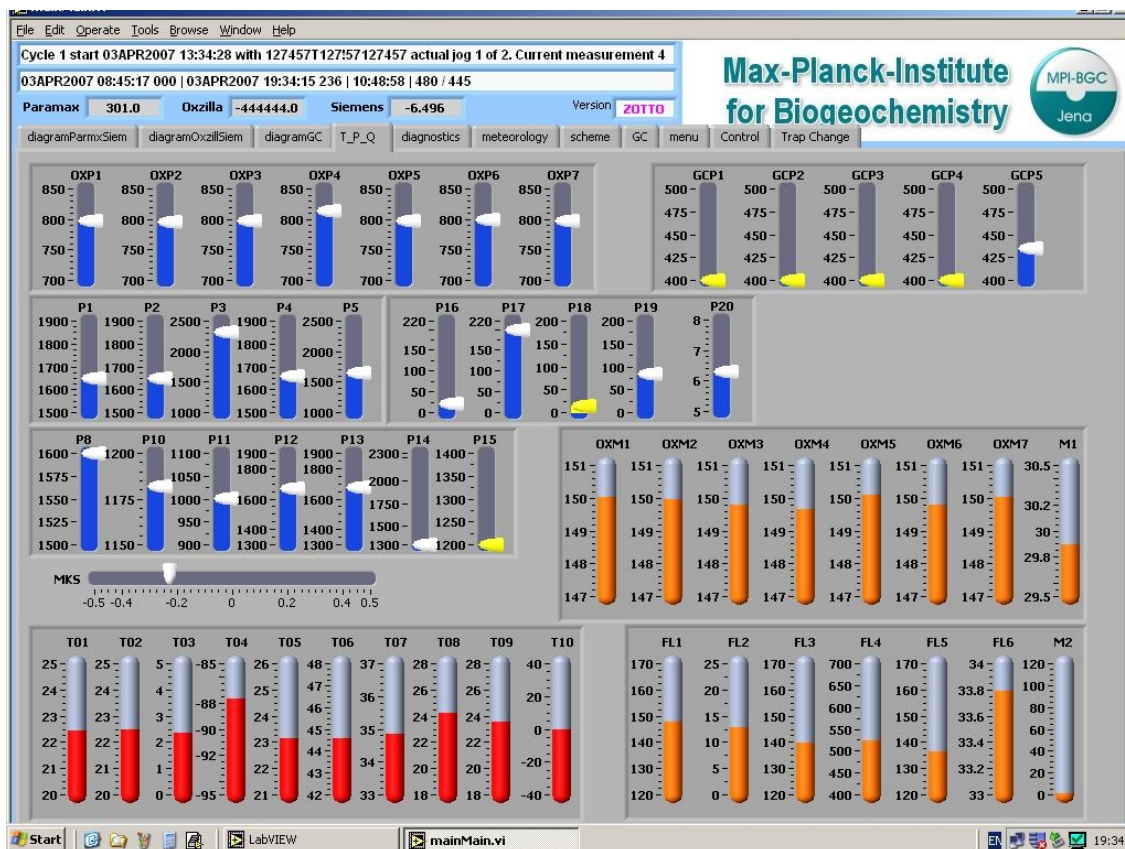


**Figure 3.12:** The diagnostic data quality indicators (see Appendix 4) are used to identify and troubleshoot most common problems. The software is programmed to attract an operator's attention to the inappropriate diagnostic parameters or other problems by flashing (or colour changes) of the relevant windows on the screen.

The O<sub>2</sub> and CO<sub>2</sub>, and GC subsystems function as an integrated whole, sharing equipment such as the cryogenic cooler, refrigerator and 'Blue Box', sharing calibration standards and the 'Target Tank' (defined in Chapter 4, Section 4.5), and having separate but identical air intakes, pumps and tubing from the tower to the analysers. Our LabVIEW™ programme integrates the analytical procedures of all subsystems into a cohesive unit, and creates standardized data output files for all species. The programme outputs 33 different files, organised into 6 sub-directories, and receives input parameters from 8 different 'INI' files (see Appendix 3). The most 'raw' files collect unprocessed data every second, whereas the most processed files incorporate all of our calibration results to provide tower air data of all species in concentration units on the 'S1' calibration scales (defined in Chapter 4, Section 4.2).

The philosophy of the data acquisition procedures is to calculate species' concentrations in real-time, significantly reducing the need for data post-processing. An important component of this philosophy is including automated data quality indicators, so-called 'flags'. These flags are raised for a variety of conditions ranging from

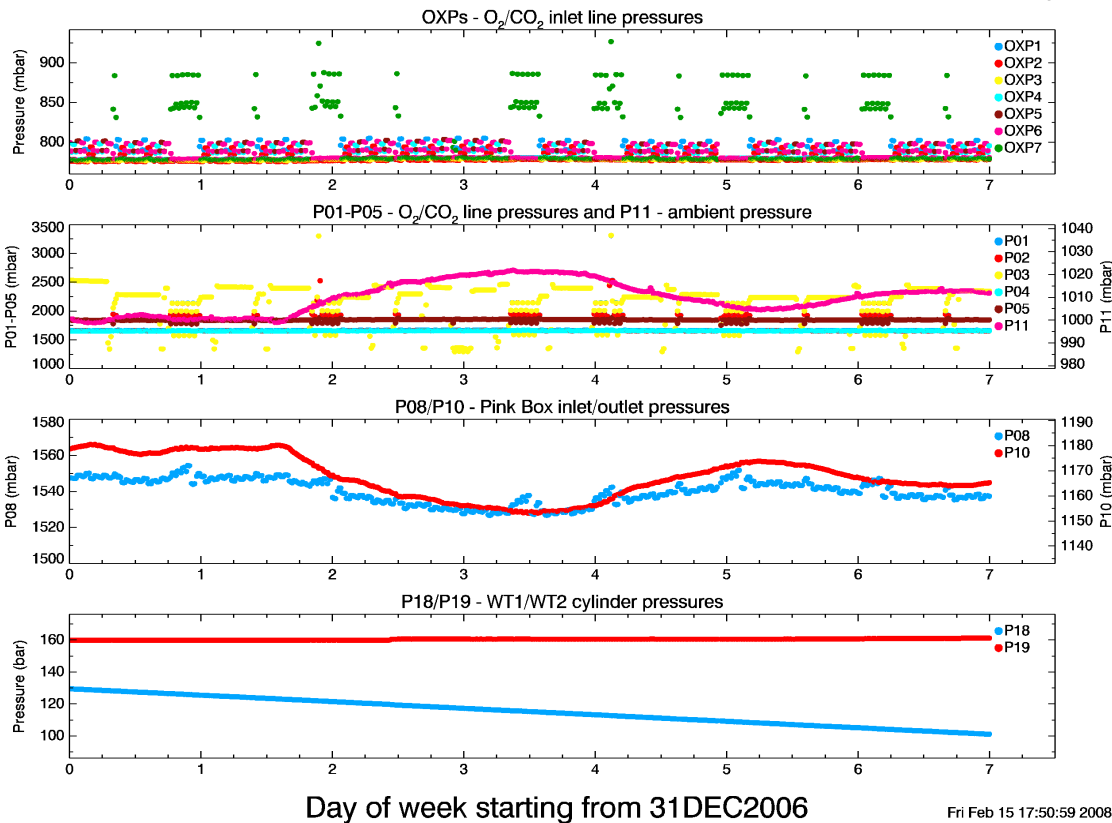


**Figure 3.13:** Example of diagnostic parameters, showing all pressures relevant to the O<sub>2</sub> and CO<sub>2</sub> system over a one-week period starting from 31 December 2006. These diagnostic parameters were only available after a two-month lag, and thus could not be used for real-time troubleshooting.

unacceptable diagnostic parameters, to ‘impossible’ concentration values and unacceptable calibration results (see Appendix 4 for details). As an example, if a calibration is declared by the system as ‘bad’, then ambient air concentrations will continue to be calculated with the previous ‘good’ calibration results (with a note in the data files to this effect). If two consecutive calibrations are declared as bad, a flashing message appears on the computer monitor, alerting the on-site technician to a possible system problem. The system of data flags was developing gradually starting from simply attracting the operator’s attention to unacceptable and most likely problematic values of the diagnostic parameters (yellow flashing in Figure 3.12). Finally, we developed a sophisticated and multi-levelled system of flags (described in detail in Appendix 4), which allows for various levels of data evaluation. The so-called ‘final’ flags, which represent the summary of all possible flags, are written to the final output files (see Appendix 3), and allow any data user to filter the problematic data automatically. However, the data flagging parameters have to be carefully adjusted and periodically checked since their wrong application could potentially lead to discarding of good data.

## CHAPTER 4. Calibration methodology and results

### 4.1 Introduction to Chapter

I present the calibration methodology which was used to define O<sub>2</sub>, CO<sub>2</sub> and GC species concentrations at ZOTTO, and later Cape Verde. I pay special attention to the propagation of the internal (on-site) calibration scales for all measured gases and their internal consistency, which is a crucial prerequisite for maintaining a long-term record of any gas species. Precise O<sub>2</sub> measurements, as the most technically challenging (compared to the other gas species measured at ZOTTO), require several additional features in both calibration methodology and gas handling, which are described in Section 4.2. Section 4.3 discusses the results of my observations of O<sub>2</sub> and CO<sub>2</sub> concentration stabilities in WT cylinders, possible reasons for the observed drifts and their influence on the measurement reproducibility. Section 4.4 provides information on the calibration cylinders for both O<sub>2</sub> and CO<sub>2</sub> and GC species used during the period when the data presented in the following chapters were collected, with special attention paid to O<sub>2</sub> concentration changes. Data reproducibility and comparability results for all measured gas species as a measure of the tower data quality are discussed in Section 4.5. The fractionation of O<sub>2</sub> molecules (relative to N<sub>2</sub>) in air and its influence on the measurements, as well as the ways to minimise it, are the subject of discussion in Section 4.6.

### 4.2 Calibration methodology and scales

The calibration methodology presented below is similar to that for O<sub>2</sub> and CO<sub>2</sub> measurements described in Keeling *et al.* [1998], except that I applied it to continuous (rather than flask-based) measurements and extended it to GC measurements. A similar methodology was also outlined briefly in Manning [2005] for use in the EU CHIOTTO project. This methodology is somewhat different from the ‘traditional’ calibration methodology recommended for high precision CO<sub>2</sub> measurements (e.g. Worthy *et al.*, 2003, Trivett and Koehler, 2000), and for this reason I have described it in detail below. The two key reasons why I have employed a different methodology are because (1) neither a central calibration laboratory (CCL) nor an international calibration scale exist for O<sub>2</sub> measurement, thus the traditional methodology can not be applied for O<sub>2</sub>; and (2) there are several advantages of our methodology, which I describe below.

Calibrations are achieved using a suite of 50 L, 46 L, and 29 L aluminium cylinders (‘industrial’ cylinders, type 6061, Luxfer Gas Cylinders Inc.) containing high



**Figure 4.1:** Thermally insulated enclosure (Blue Box in Figure 3.1) with 15 horizontally placed calibration cylinders. A thick layer of insulation helps to minimise the temperature gradient, which is monitored with two sensors (T1 and T2 in Figure 3.1) at opposite ends of the Blue Box. The regulators are attached to an external manifold (not seen in the photo), which allows adjustments and checking of cylinder delivery pressures without opening the Blue Box.

pressure air with known concentrations of the relevant species. Concentrations of all measured species in the calibration cylinders have been pre-defined at MPI-BGC, measured against primary standards obtained from Scripps Institution of Oceanography (SIO), in the case of  $O_2$ , and from the CCL at NOAA/ESRL/GMD (formerly NOAA/CMDL) in the case of all other species. All calibration cylinders are placed horizontally in a large, thermally insulated enclosure ('Blue Box' in Figures 3.1 and 4.1). In the case of  $O_2$  measurements, such horizontal orientation is a requirement, and it has also been shown to improve the long-term accuracy of  $CO_2$  concentration measurements [Keeling *et al.*, 2007]. Two-stage cylinder regulators (Scott Specialty Gases, model 51-14C; identical to Air Liquide/Alphagaz model 1001) are mounted on a manifold on top of the Blue Box, connected to the cylinders via 1/16" OD nickel tubing (Valco Instruments Co. Inc., 'Nickel 200' TNI140). Installing the regulators on a manifold rather than directly mounted on the cylinders, results in much less frequent opening of the Blue Box, allowing a more stable thermal environment. A multi-position valve (VA5 in Figure 3.1, Valco Instruments Co. Inc., MW/SD-type with micro-electric actuator) selects a given calibration cylinder to be analysed.

I employed three hierarchical levels of calibration: (1) all sample air derived from the tower is directly measured against a reference standard called a 'Working

Tank' (WT1 or WT2 in Figure 3.1 for O<sub>2</sub> and CO<sub>2</sub> analyses, and 'GCWT' for GC analyses); (2) WT and GCWT are both calibrated on a regular basis using four Working Secondary Standards (WSSes); (3) long-term stability of the WSSes is assessed by periodic (3-4 times/year) analysis of a suite of Long-term Secondary Standards (LSSes). Following Keeling *et al.* [1998], I defined the calibration scales resulting from the frequent WSS analyses the 'S1' scales, and any changes to these scales deemed necessary from the LSS analyses result in corrected 'S2' calibration scales.

Calibration curves (described below) for both O<sub>2</sub> and CO<sub>2</sub> analysers are defined relative to WT values, similarly to tower air measurements (described in Section 3.2.3) by having WT analysis jogs bracket each calibration analysis jog, thus the (tower air – WT) differences can easily be converted into concentration units. This procedure of frequent analyses of WT is necessarily employed owing to the relatively variable baseline behaviour of the Servomex O<sub>2</sub> sensor (see Figure 4.2, discussed below, and Figure 3.7). As a by-product, however, very good CO<sub>2</sub> repeatability is achieved (see Table 4.4). For CO<sub>2</sub>, the function of the WT is similar to the 'Zero Tank' commonly used in high precision CO<sub>2</sub> measurements [Manning, 2005; Trivett and Koehler, 2000], except that my WT analyses are much more frequent, and some other methodologies do not incorporate an interpolation between successive Zero Tank analyses, as I do for the successive WT analyses. Calibration curves for all three GC species are defined as ratios relative to bracketing GCWT analysis jogs (similarly to tower air GC measurements), thus the (tower air / GCWT) ratios can easily be converted into concentration units.

Using the WSS cylinders, I calibrate the O<sub>2</sub> and CO<sub>2</sub> analysers every 26 hours, and the GC once every ~7 days. I do not calibrate with multiples of exactly 24 hours to prevent possible aliasing of the calibration results, particularly with respect to possible diurnal temperature cycling in the laboratory container. The WSS cylinders span ranges of concentration for each species that are greater than those expected from ambient air taking into account typical diurnal, seasonal and synoptic variability. It was not easily possible to prepare appropriate ranges for all five species in only four cylinders, thus I use five WSS cylinders (see Section 4.4), three of which are shared. As with tower air measurements, WT or GCWT jogs bracket each WSS jog, resulting in (WSS – WT) or (WSS / GCWT) values. Each WSS is analysed three times in succession for the O<sub>2</sub> and CO<sub>2</sub> calibration, and five times in succession for the GC calibration (to improve the precision of the calibration cylinder measurements). Prior to the first analysis (jog), I purge the cylinder regulator and tubing for 8 minutes at 250 mL/min (through valve V2

via the second outlet on the four-way valve, V5; see Figure 3.1 and 3.4) followed by 8 minutes at 150 mL/min (through valve V1 via V5; identical to the analysis flowrate) for the O<sub>2</sub> and CO<sub>2</sub> system, and for 4 minutes at 250 mL/min for the GC system (through valve V2). Typically, this purging is still not sufficient and I often find that results from the first WSS jog are significantly different from subsequent jogs, thus I discard the first WSS jog, and average the remaining ones to define the analysers' response to the given WSS. Longer purging times do not appear to prevent the first jog from being dissimilar to subsequent jogs. Similar observations have been found by Keeling *et al.* [1998] whose first measurement of a reference tank was reported to be typically 1-2 per meg lower than the subsequent measurements, presumably owing to residual disequilibria in the high-pressure cylinder lines. We also observed such differences for the GC species and therefore we always discard the first cylinder measurement for all measured species at ZOTTO. For the O<sub>2</sub> and CO<sub>2</sub> system, I additionally flush the WSS through V8 (via the second outlet on the four-way valve, V7 in Figures 3.1 and 3.4) during all WT jogs to maintain pressure and flow equilibrium, as discussed above (Section 3.2.3). Figure 4.2 shows a typical calibration for O<sub>2</sub> and CO<sub>2</sub>. GC calibrations look essentially identical, except with five jogs of each WSS instead of three.

Using the averaged data for WSS measurements (in uncalibrated analyser units, and differenced from the WT jogs) and the pre-defined concentrations for these cylinders from MPI-BGC (see Section 4.4), I can compute calibration curves (also called analyser response curves). For all species, I fit linear least squares fits to the averaged (WSS – WT) values, using a linear fit for O<sub>2</sub>, CH<sub>4</sub>, and CO, and a quadratic fit for CO<sub>2</sub> and N<sub>2</sub>O. Using these calibration curves, the tower air measurements are reported in concentration units ('ppm' for CO<sub>2</sub>, 'ppb' for CH<sub>4</sub>, CO and N<sub>2</sub>O and 'per meg' for O<sub>2</sub>; see Section 4.2.1 for O<sub>2</sub> units description), and are referred to as being on the 'S1' calibration scales. Each time a calibration cycle is completed, the new calibration curve coefficients are automatically updated in the LabVIEW™ program (provided that they are considered within acceptable tolerances (see Appendix 4)).

Examining my WSS calibration results, the curve fits gave average 'r-squared' values of 0.989, 0.9999, 0.99999, 0.9991, and 0.995 for O<sub>2</sub>, CO<sub>2</sub>, CH<sub>4</sub>, CO, and N<sub>2</sub>O respectively (103 calibrations for O<sub>2</sub> and CO<sub>2</sub> and 16 calibrations for all GC species, collected over 4 months from February to June 2007). In 2008, upon return of the WSS cylinders to Germany after all measurements from the tower had stopped, I learnt that the MPI-BGC declared values for O<sub>2</sub> for two of the WSS cylinders were incorrect by ~50 per meg (see Section 4.4.2 for details; 'per meg' unit defined in Section 4.2.1 below), which explained the poor r-squared result for O<sub>2</sub>.

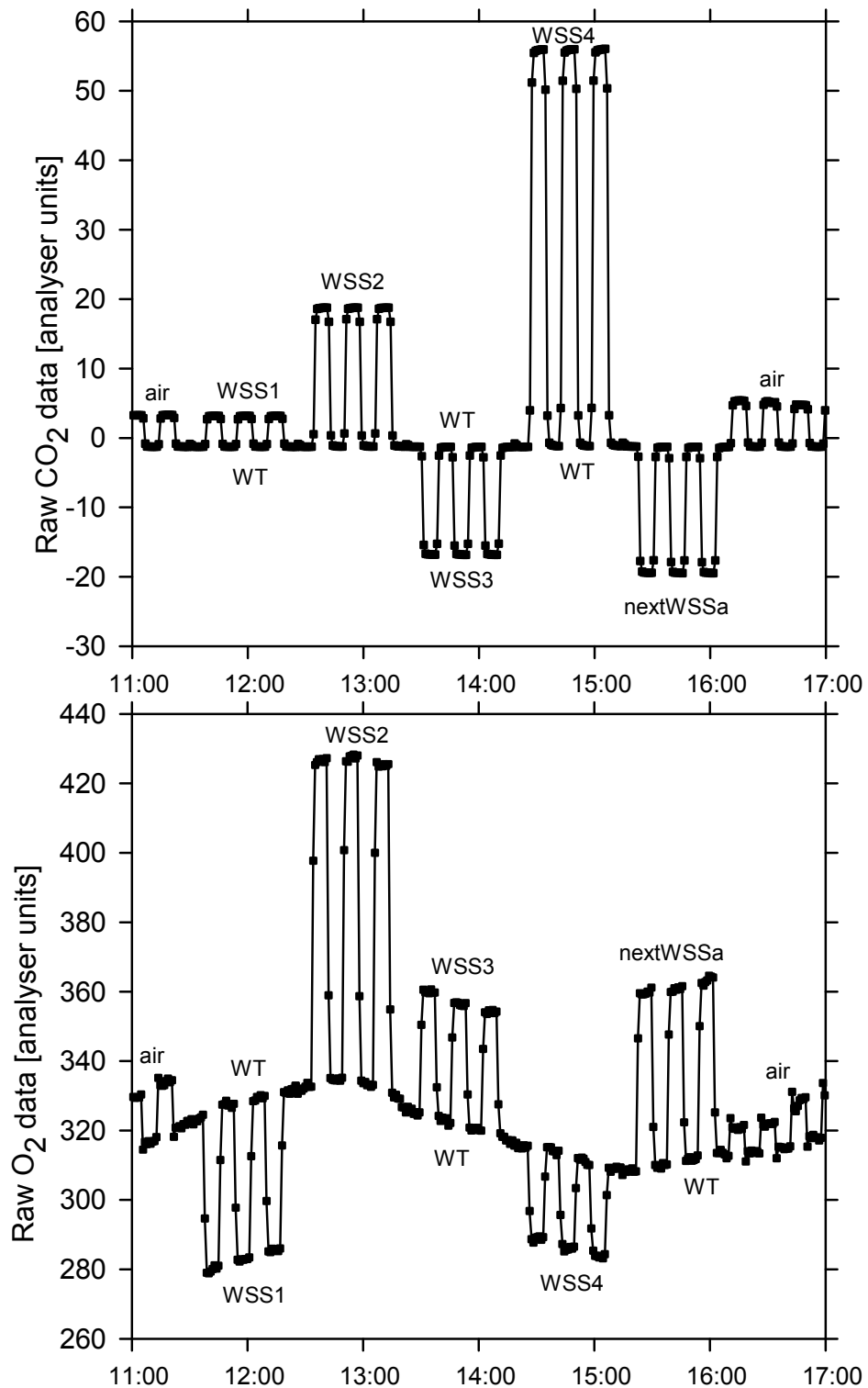


**Figure 4.2:** Example of a WSS calibration cycle, for O<sub>2</sub> and CO<sub>2</sub>, from 03 March 2007. Data are shown in uncalibrated analyser units and each point is a 30 sec average of 1 sec data. Four standards (WSS1-4) are used to define calibration curves for both O<sub>2</sub> and CO<sub>2</sub> on the S1 scales. The fifth standard (nextWSSa) is being analysed for 2-3 months before it will replace the existing WSS1 (see Section 4.2.2 for details). As shown, I switch frequently between a given calibration standard and Working Tank (WT) to minimise the influence of baseline drift on the measurements, which can be clearly seen in the O<sub>2</sub> analyser signal.

The calibration curve coefficients for CO (see Figure 4.3, lower panel) and N<sub>2</sub>O

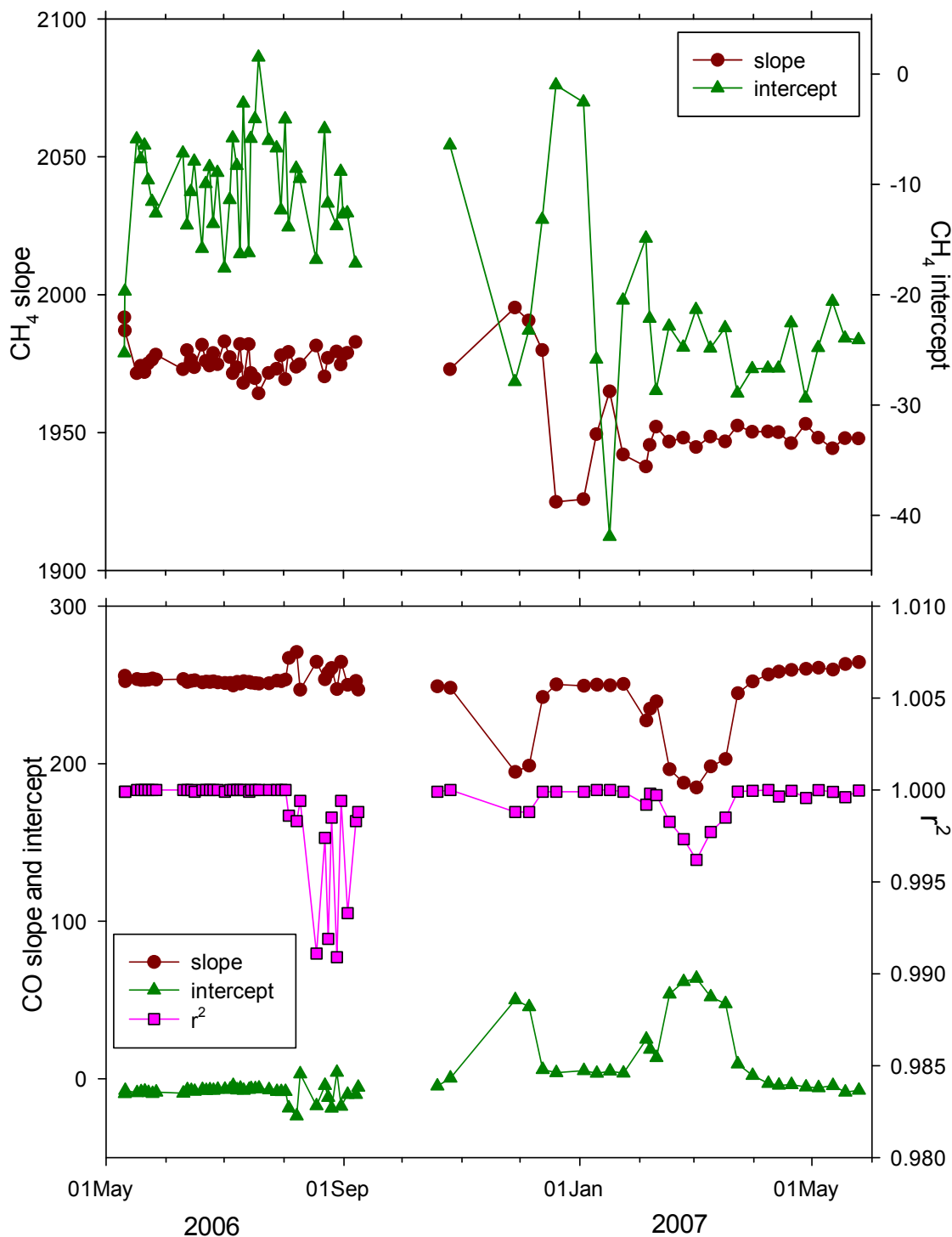


**Figure 4.3:** CH<sub>4</sub> (upper panel) and CO (lower panel) calibration coefficients (slope and intercept) shown from May 2006 to June 2007. For CO the variations of the calibration linearity expressed as the least square fit ( $r^2$ ) to four-point calibrations are also shown. The large gap in the measurements in Sept-Oct 2006 is due to the tower construction.

(not shown) were relatively variable in February/March 2007, and more stable in April/May. The GC was shut down for modifications during my visit to ZOTTO in January-February 2007, and the observed feature in the CO calibration coefficients suggests that the methaniser (as well as the ECD in the case of N<sub>2</sub>O) might require

several weeks to stabilise after such interruptions. The linearity of the FID response to CO was also lower than usual during this period as shown by the  $r^2$  statistic (Figure 4.3, lower panel). The upper panel of Figure 4.3 shows CH<sub>4</sub> calibration coefficients that do not show the prominent feature seen in CO calibrations in February/March 2007. This also provides evidence that the methaniser's response might have been the cause of the variability seen in CO calibration coefficients. After the GC was restarted in October 2006, and after an unsettled period spanning several months, a clear shift downwards was observed in the CH<sub>4</sub> slope and intercept. The cause of these changes is unknown, although they are probably related to the instrument shut down and various modifications carried out at the same time.

Regarding the frequency of WSS calibrations, the variation of the N<sub>2</sub>O calibration coefficients, even under the most stable conditions, clearly demonstrated the need to calibrate N<sub>2</sub>O more frequently than once every 7 days. For all other species, the existing frequency appears to be sufficient. For O<sub>2</sub> and CO<sub>2</sub>, a decrease in calibration frequency by a factor of two (to once every 52 hours) would introduce additional inaccuracies of only  $0.1 \pm 0.8$  ppmEquiv (unit defined in Section 4.2.1 below) and  $0.006 \pm 0.005$  ppm respectively. These values were arrived at by recalculating TT measurements over a 2-month period on the assumption that the calibration frequency was reduced to the above frequency. Additional inaccuracy introduced by the reduced calibration frequency was calculated as the difference between the TT measurements based on once every 26 hours and 52 hours calibrations respectively. In an effort to reduce the rate of depletion of the calibration standards, such a change could be considered.

#### 4.2.1 Definition of the O<sub>2</sub> units

In the particular case of O<sub>2</sub>, I report measurements as changes in the O<sub>2</sub>/N<sub>2</sub> ratio in 'per meg' units following Keeling and Shertz [1992]. Given that N<sub>2</sub> changes are typically much smaller than O<sub>2</sub> changes, the O<sub>2</sub>/N<sub>2</sub> ratio can be used to quantify changes in O<sub>2</sub> concentration. From an analytical perspective, the Servomex sensor measures O<sub>2</sub> mole fractions, which are expressed in 'ppmEquiv' units. The 'ppmEquiv' rather than 'ppm' unit is purposefully used to indicate that one cannot consider O<sub>2</sub> values in mole fraction in the same way as typically used for trace gases (see below).

I convert the Servomex signal from mole fraction to per meg units using a similar equation (see Appendix 1 for derivation) as given in Stephens *et al.* [2003],

$$\delta(O_2 / N_2) = \frac{\delta X_{O_2} + (X_{CO_2} - 363.29)S_{O_2}}{S_{O_2}(1 - S_{O_2})}, \quad (4.1)$$

where  $\delta(O_2 / N_2)$  is the O<sub>2</sub>/N<sub>2</sub> ratio in per meg units and  $\delta X_{O_2}$  is the O<sub>2</sub> mole fraction of the air sample as determined by the Servomex sensor, multiplied by 10<sup>6</sup>, and relative to an arbitrary ‘zero’ defined in the SIO calibration scale. Changes in CO<sub>2</sub> concentration influence the O<sub>2</sub> mole fraction but not O<sub>2</sub>/N<sub>2</sub> ratios, thus we correct for this influence as shown in the equation, where  $X_{CO_2}$  is the CO<sub>2</sub> mole fraction of the air sample (in ppm), and 363.29 is an arbitrary CO<sub>2</sub> reference value (in ppm) implicit in the definition of the SIO O<sub>2</sub>/N<sub>2</sub> per meg scale.  $S_{O_2}$  is the standard mole fraction of O<sub>2</sub> in air, given as 0.20946 [Machta and Hughes, 1970].

From this equation, if one considers a change in O<sub>2</sub> mole fraction, keeping CO<sub>2</sub> constant, it can be seen that a 1  $\mu\text{mol mol}^{-1}$  change in O<sub>2</sub> mole fraction is equivalent to a 6.04 per meg change in O<sub>2</sub>/N<sub>2</sub> ratio. This factor should not be confused with the factor of 4.8, which is sometimes mistakenly used as a ‘conversion factor’ from ppm to per meg units. As stated by Keeling *et al.* [1998], “4.8 per meg is equivalent to the same number of molecules as 1  $\mu\text{mol mol}^{-1}$  in a trace gas abundance” (for example, CO<sub>2</sub>, but not O<sub>2</sub>, which is obviously not a trace gas).

#### 4.2.2 Propagation of the S1 scale

The WSSes are consumed relatively rapidly (each having a lifetime of approximately 2 years), thus it is important to have a methodology for replacing them. I follow the same procedures given in Keeling *et al.* [1998] for flask sample analyses, extended to all five measured species, which allow the S1 scales to be propagated indefinitely into the future with a high degree of internal consistency. Two to three months before a WSS cylinder requires replacement, an additional fifth (and sometimes sixth) cylinder is analysed immediately after the four WSSes in each calibration cycle (Figure 4.2), following identical analytical procedures as described above. The calibration curve coefficients are determined as usual with the four WSSes, while the additional cylinders’ (positions ‘Next WSSa’ and ‘Next WSSb’ in the Blue Box) concentrations are determined based on these calibration coefficients. After 2-3 months, results for the new cylinder are compiled, ‘declared’ concentrations, in S1 units, are defined for the cylinder, and the cylinder takes the place of one of the four WSSes in all future calibration cycles.

Owing to differences in the frequency of WSS calibrations between the O<sub>2</sub> and CO<sub>2</sub>, and GC systems, our LabVIEW™ program has been made versatile so that either or both systems can be in a transition stage of analysing 1 or 2 next WSSes, and the transition stage for the GC system is necessarily made longer owing to less frequent WSS calibrations. I never replace two WSSes at the same time, so that any unexpected

calibration scale shifts upon WSS replacement can immediately be attributed to a given cylinder.

Additional details on the practicalities of phasing in new WSS cylinders are given in Appendix 2.

Although being internally consistent by strictly following the above procedures, it is still possible that the S1 scales will drift over time. I examine and correct for such possible drift by periodic (3-4 times/year) analyses of an additional suite of cylinders named LSSes, again following procedures similar to Keeling *et al.* [1998]. Any corrections deemed necessary from the LSS analyses result in revised 'S2' calibration scales, and these scale corrections are applied retrospectively to all tower air measurements. Thus far, I have not applied any S2 scale corrections, because no LSS cylinders were available at ZOTTO until October 2006.

There is a further possible scale correction which may become necessary in the longer term, if one of my S2 scales is found to have shifted away from the CCL scales or the SIO S2 scale, or if the CCL or SIO S2 scales themselves are retrospectively revised. Procedures for applying such corrections, resulting in S3 scales, have yet to be determined.

### **4.3 Stability of WT concentrations**

A secondary result from the WSS calibrations is information about the stability of the measured gas species in the WT and GCWT cylinders. Figure 4.4 shows these results from 2007 for O<sub>2</sub> and CO<sub>2</sub>, for which I have the most calibration data. As seen in Figure 4.4, O<sub>2</sub> concentrations in the WTs become depleted as they are consumed and the cylinder pressure decreases. This effect has been observed previously [Manning, 2001], and is most likely owing to preferential desorption of N<sub>2</sub> relative to O<sub>2</sub> from the cylinders' interior walls. The average O<sub>2</sub> depletion over the lifetime of the WT cylinders (excluding ND21972) was about 5 ppmEquiv, which is about 5 times greater than that observed by Manning [2001]. Possible reasons for this faster depletion rate include: (1) a 50% higher WT flowrate in my system (150 mL/min compared to 100 mL/min); (2) my cylinders were brand new, and thus may have been undergoing interior wall 'conditioning' processes such as corrosion or other surface reactions; and (3) relatively 'wet' cylinders prepared by MPI-BGC possibly resulting in enhanced reaction processes. Regarding (3), I note that the cylinder which showed the lowest depletion rate, D420482, was filled at ZOTTO and contained 0.5 ppm H<sub>2</sub>O, compared with 3.5–5 ppm H<sub>2</sub>O in MPI-BGC filled WTs. I examined other WTs used in 2006 (not shown in Figure 4.4), and found consistent results, in terms of higher water content leading to

greater O<sub>2</sub> depletion. Hypothesis (2), however, could also explain the improved results with D420482, since this cylinder had already been filled and used one time previously, in 2006. I also considered the fact that, despite exclusively using Luxfer aluminium cylinders, some were manufactured in the UK and others in the US. The UK plant is known to use a different cleaning process, and may have different tolerances on the surface roughness of the interior walls. My results, however, including the WTs used in 2006, found no correlation in depletion rates based on source of manufacture. I also examined data from a TT cylinder over a 7-month period, which, in contrast to WTs, is not used continuously and thus has a much longer lifetime. The rate of O<sub>2</sub> depletion with respect to decreasing cylinder pressure, however, was of similar magnitude as that for WTs, which tentatively suggests that the above-mentioned preferential desorption from the cylinder walls (which is pressure but not time dependent) could be the prevailing factor leading to the observed O<sub>2</sub> depletion rates, rather than surface reaction processes.

For cylinder ID ND21972 the observed O<sub>2</sub> depletion is much more pronounced, decreasing by over 20 ppmEquiv over the cylinder lifetime. In addition, and of greater impact on the precision of the tower air measurements, the average of the absolute difference between two consecutive WT measurements is 1.8 ppmEquiv for ND21972, compared to 0.5 ppmEquiv for all other WTs. Thermal fractionation effects could cause O<sub>2</sub> depletion in a cylinder similar to a Rayleigh-type distillation [Keeling *et al.*, 2007], and could occur, for example, had the Blue Box doors been inadvertently left open and the front of the box was a different temperature than the back. However, Blue Box temperature data, collected at both front and back, do not support such a possibility. The most likely cause for the poor performance of ND21972 would seem to be from a leak at the cylinder head valve fitting. Keeling *et al.* [1998] state that a small leak would result in O<sub>2</sub> enrichment in the cylinder, rather than the depletion I observed. However, such an enrichment applies only under conditions where the leak is through an orifice with characteristic diameter smaller than the mean free path between molecular collisions (Knudsen diffusion). Thus, particularly because no other solution appears plausible, I hypothesise that a larger leak may have resulted in the dramatic O<sub>2</sub> depletion and increased scatter observed for cylinder ND21972.

As shown in Figure 4.4, CO<sub>2</sub> data show remarkable precision and stability over each WT's lifetime, with slight evidence for a small CO<sub>2</sub> decrease as the cylinder is

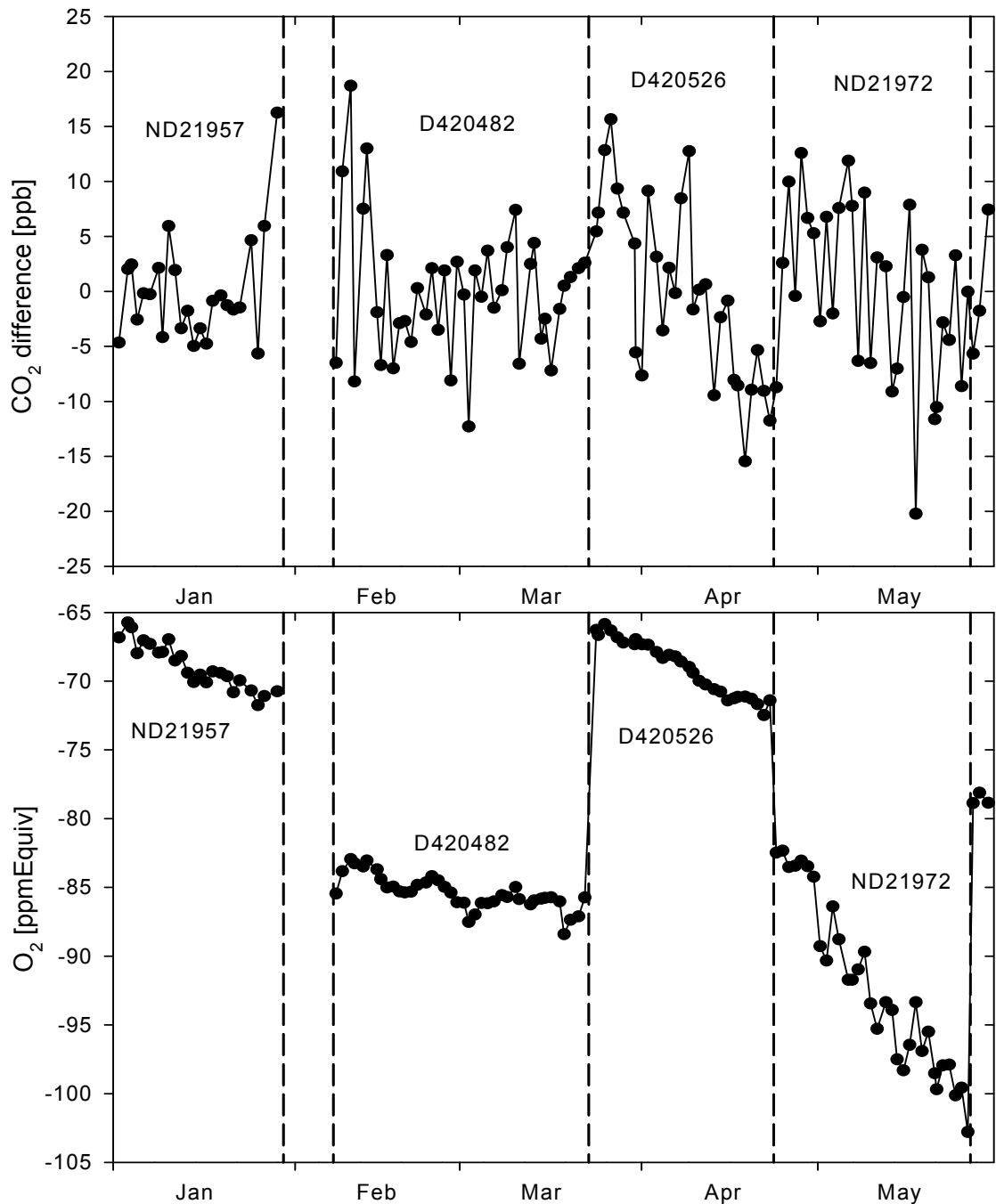


**Figure 4.4:** WT concentrations for CO<sub>2</sub> (upper panel) and O<sub>2</sub> (lower panel), shown from January to June 2007. Each point shows the revised WT concentration which is recalculated at the end of each WSS calibration cycle. In order to highlight small changes, CO<sub>2</sub> results are shown as differences from the mean concentration over the lifetime of each WT cylinder, and displayed in ppb. O<sub>2</sub> concentrations are shown in ppmEquiv (see section 4.2.1 for units description). The vertical dashed lines indicate when a new WT cylinder was brought online, with cylinder IDs indicated on the Figure.

depleted, but not for all cylinders. This is in contrast to other workers, who frequently find CO<sub>2</sub> concentration increases as the cylinder is depleted, typically of 50 ppb, and sometimes much greater [Keeling *et al.*, 2007]. It is important to note that the residual pressure at which we remove our cylinders (both calibration and WTs) from the system is 15 bar, which means that the lifetime of any given cylinder spans from about 150 bar

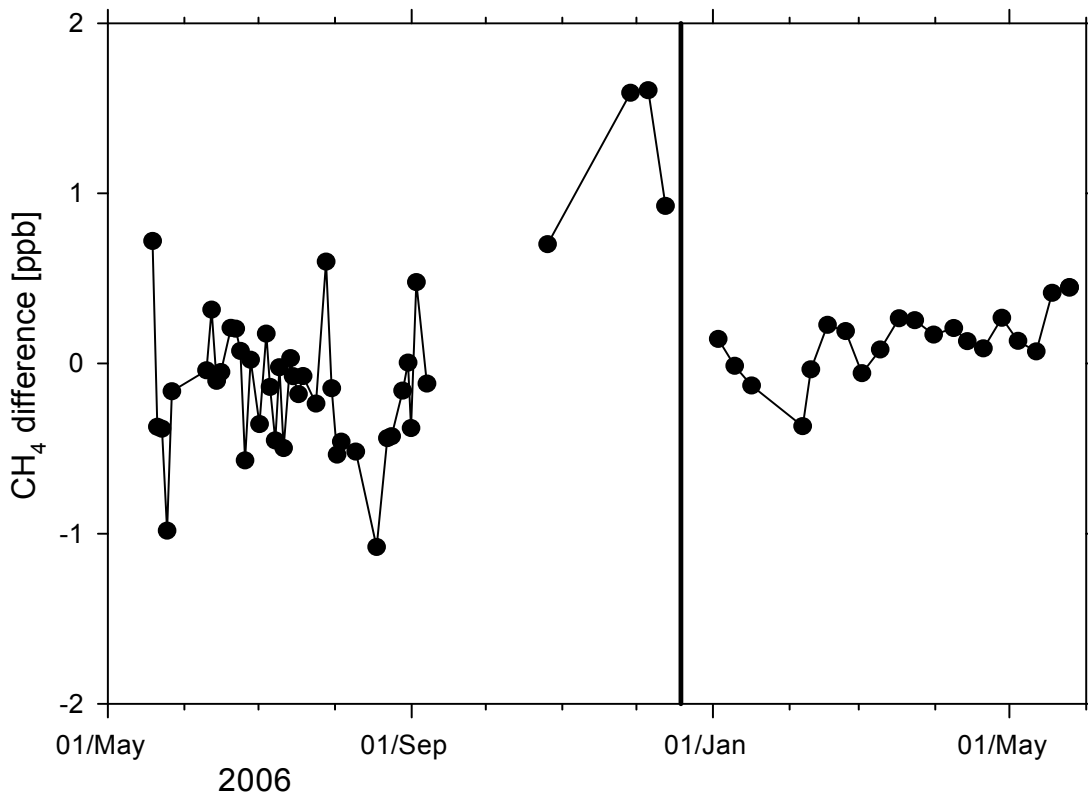


**Figure 4.5:** GCWT concentrations for CH<sub>4</sub> shown from May 2006 to June 2007. Each point shows the GCWT concentration which is recalculated at the end of each WSS calibration cycle. The solid vertical line indicates when a new GCWT cylinder was brought online. The CH<sub>4</sub> concentrations are shown as differences from the mean concentrations over the lifetime of the cylinders, and displayed in ppb. The second cylinder was not finished when the measurements were halted thus its mean concentration was calculated using all available measurements from 19 December 2006 to 01 June 2007.

(when a cylinder is full) to 15 bar. Measurements from cylinders with lower pressures typically result in concentration drifts and much noisier (than typical) measurements of O<sub>2</sub>/N<sub>2</sub> ratios. Langenfelds *et al.* [2005] also reported drifts of up to 0.1 ppm of CO<sub>2</sub> in cylinders with pressures lower than 8 bar. My results support the conclusion of Keeling *et al.* [2007], that the measures we have taken to eliminate thermal and gravitational fractionation for O<sub>2</sub>, placing cylinders horizontally in a thermally insulated enclosure, also give improved CO<sub>2</sub> stability.

Interestingly, cylinder ND21972 also shows comparatively worse stability for CO<sub>2</sub>, with the average of the absolute difference between two consecutive WT measurements being 9.1 ppb, compared to 5.8 ppb for all other WTs. If one assumes that the increase in scatter in O<sub>2</sub> concentrations for ND21972 is due to mass-dependent fractionation (clearly an oversimplification, but nevertheless illustrative), then one would expect an increase in the average CO<sub>2</sub> scatter of ~8.8 ppb, which, although higher, is of the same approximate magnitude as the observed average increase of 3.3

ppb. The CO<sub>2</sub> data also provide further evidence that thermal fractionation effects could not have caused the 20 ppmEquiv O<sub>2</sub> depletion in this cylinder. Keeling *et al.* [2007] have measured the relative thermal sensitivities in air for (CO<sub>2</sub>/N<sub>2</sub>) / (O<sub>2</sub>/N<sub>2</sub>), and found values between 7 and 11 ppb CO<sub>2</sub>/ppmEquiv O<sub>2</sub> (depending on cylinder pressure). Thus, a 20 ppmEquiv O<sub>2</sub> depletion, if due to thermal fractionation, should be accompanied by a CO<sub>2</sub> depletion of at least 140 ppb, in contrast to the observed depletion of less than 10 ppb. These data for relative thermal sensitivities also provide evidence that the Blue Box is performing its function as a thermal insulator, since the average WT O<sub>2</sub> depletion of ~5 ppmEquiv, if due to temperature effects, would have a corresponding CO<sub>2</sub> depletion of at least 35 ppb, many times greater than that observed (see Figure 4.4).

Unfortunately, I could not perform similar investigations on the stability of the GC species concentrations in the depleting GCWTs since we had only used up about 1.2 cylinders over the period of measurements presented in this thesis. However, Figure 4.5 shows CH<sub>4</sub> concentrations (calculated from the calibration curves) in two GCWT cylinders as differences from the average cylinder concentrations over their lifetime. The observed increase in CH<sub>4</sub> concentrations in Oct-Dec 2006 cannot be directly contributed to the pressure depletion in the first GCWT since it follows the gap in the measurements owing to the tower construction and could be a technical artefact. I do note, however, that the second GCWT shows tentative evidence of increasing CH<sub>4</sub> concentrations as the cylinder becomes depleted. Further research (based on longer periods and several GCWTs) is needed.

#### **4.4 ZOTTO calibration cylinders**

Here I present an overview of the actual calibration cylinders used to define the tower air concentrations for all measured gas species from Oct 2005 to June 2007.

##### **4.4.1 CH<sub>4</sub>, CO<sub>2</sub>, N<sub>2</sub>O and CO concentrations**

The concentrations of all ZOTTO GC species and CO<sub>2</sub> for all five WSS cylinders initially used to define the ZOTTO S1 scales and consequently all tower air data are summarised in Table 4.1. Target Tank data are also shown. All cylinder concentrations shown in Table 4.1 were measured on an Agilent 6890 GC at MPI-BGC in Sept-Oct 2005, by Dr. Armin Jordan.

All calibration cylinders were re-analysed at MPI-BGC in Dec 2007 – Feb 2008. The updated concentrations of all GC species and CO<sub>2</sub> are shown in Table 4.2. Although some of the differences between the second and the first analyses (‘Δ’

columns in Table 4.2) are not negligible, they either are within expected laboratory imprecision, or are due to clearly documented reasons as described below.

Cylinder ID	Used as	H <sub>2</sub> O (ppm)	CH <sub>4</sub> (ppb)	CO <sub>2</sub> _GC (ppm)	N <sub>2</sub> O (ppb)	CO (ppb)
D420534	WSS1	3.3	1972.01	393.53	319.22	297.22
D420465	WSS2	6.7	2164.22	409.67	324.75	395.06
ND21971 <sup>a)</sup>	WSS3	6.3	-	373.27	-	-
ND21969	WSS4	2.5	1869.88	472.30	318.81	209.44
ND21968 <sup>b)</sup>	WSS5	2.7	1774.60	-	314.34	113.40
D420530	TT <sup>c)</sup>	-	1997.22	385.69	321.28	199.92

<sup>a)</sup> This cylinder was only used for O<sub>2</sub> and CO<sub>2</sub> calibrations.

<sup>b)</sup> This cylinder was only used for GC calibrations.

<sup>c)</sup> The purpose of this cylinder (TT, or Target Tank) is explained in Section 4.5 below.

**Table 4.1:** Initially assigned calibration cylinders concentrations used to define S1 scales for CH<sub>4</sub>, CO<sub>2</sub>, N<sub>2</sub>O and CO.

For CO<sub>2</sub>, prior to 2006, a quadratic fit was used at MPI-BGC for the GC calibration to assign the CO<sub>2</sub> concentration for the cylinders above. However, due to good linear response of the FID within the ambient ranges of CO<sub>2</sub> concentration, a linear fit was introduced in 2006. All previously obtained cylinder concentrations were updated, resulting in a small correction to CO<sub>2</sub> concentrations. In addition, changes in CO<sub>2</sub> scale from NOAA X2005 to NOAA X2007 lead to a small change, mainly at

ID	CH <sub>4</sub>	Δ <sup>a)</sup>	CO <sub>2</sub> _GC	Δ <sup>a)</sup>	N <sub>2</sub> O	Δ <sup>a)</sup>	CO	Δ <sup>a)</sup>
WSS1	1971.70	-0.31	393.60	0.07	318.90	-0.32	297.40	0.18
WSS2	2163.9	-0.32	409.78	0.11	323.78	-0.97	394.50	0.56
WSS3	-	-	373.27	0.00	-	-	-	-
WSS4	1869.90	0.02	472.25	-0.05	318.27	-0.54	211.80	2.36
WSS5	1775.0	0.4	-	-	314.00	-0.34	114.23	0.83
TT	1996.7	-0.52	385.77	0.08	320.30	-0.98	199.20	-0.72

<sup>a)</sup> The Δ columns are calculated as the difference between the second MPI-BGC analyses (Dec 2007 – Feb 2008; shown in preceding column) and the first analyses (Sept – Oct 2005; shown in Table 4.1).

**Table 4.2:** Calibration cylinders concentrations after re-analyses in Dec 2007- Feb 2008.

concentrations over 440 ppm of CO<sub>2</sub>. The actual change in the ZOTTO WSS concentrations due to either drift or laboratory imprecision was small (about 0.02 ppm). At the end of 2005, a 'LoFlo' CO<sub>2</sub> analyser was added to the GASLAB at MPI-BGC, however, the WSS cylinders shown above were not analysed on it, therefore, there are no comparison results available. Now there exists, however, a systematic difference between the Loflo and the GC measurements for LSS cylinders (not shown in the tables) of about 0.05 ppm (A. Jordan, MPI-BGC, pers. comm., 2008). Due to only small differences in CO<sub>2</sub> concentrations for all calibration cylinders, I have presented the CO<sub>2</sub> data in this thesis on the 'old' NOAA X2005 scale without applying the retrospective corrections to all tower data.

The  $\Delta$  CH<sub>4</sub> values for all cylinders lie within the reproducibility and comparability limitations for both ZOTTO and GASLAB GC systems. There have been no scale changes, and all data are on the NOAA 2004 scale.

Large  $\Delta$  N<sub>2</sub>O values (~0.3 to 1.0 ppb at ambient concentration range) were observed for all WSS cylinders, mainly due to the change at MPI-BGC of the N<sub>2</sub>O calibration scale from the CSIRO to the NOAA X2006 scale. All N<sub>2</sub>O data shown in this thesis were updated to the NOAA X2006 scale using a concentration dependent correction function. In addition, however, there is an average increase of 0.15 ppb for all ZOTTO calibration cylinders. The reasons are still unclear, and are either related to the laboratory imprecision at MPI-BGC or actual concentration drift in the cylinders, which may require relevant corrections to be applied to tower air data.

The  $\Delta$ CO values are generally small except for the cylinder WSS4, for which the change exceeds our inter-laboratory comparability goal ( $\pm 2$  ppb). The reason for such a large change is unclear and may require a future update of the ZOTTO CO calibration scale, and relevant corrections of tower air data. There have been no scale changes for CO concentrations, and all data shown are on the NOAA 2000 scale.

#### **4.4.2 O<sub>2</sub> concentrations**

In contrast to the species described above, I have experienced various serious problems with the ZOTTO O<sub>2</sub> calibration scale. Initially, the problem arose in 2005 when despite the expected very high linear response of Servomex O<sub>2</sub> analyser [*Manning et al.*, 1999], I could not obtain linear fits with  $r^2$  of better than 0.98 (four-point fits with the four WSS cylinders). I conducted an extensive study on all of the WSS cylinders looking for any possible problems related to dew points, O-rings and head valve sealing materials, origin of the cylinders, as well as various communications with MPI-BGC asking for verification and checking of the assigned values. However, no correlations or errors

were found. Surprisingly, in October 2006 the first analyses of four newly-obtained LSS cylinders at ZOTTO gave an excellent linear fit (quantify with the  $r^2$  value), providing further evidence of errors in the assigned WSS concentrations. In the absence of further information, but convinced that there were errors in the assigned WSS  $O_2$  concentrations, I applied corrections to the assigned concentrations (and TT) based on my analyses of LSSes in Oct 2006 (see Table 4.3). These corrections were somewhat arbitrary and ad-hoc, in the sense that different quantitative corrections to the four WSSes were possible that could give similarly improved  $r^2$  and LSS results. My results suggested that perhaps two of the assigned WSS concentrations were in error, while the other two were correct. Nevertheless, unable to distinguish between the ‘good’ and ‘bad’ pair, I decided to treat all four WSSes equally, and applied corrections to all.

ID	$O_2$ (2005)	$O_2$ (Oct 2006) corrected from LSSes	$O_2$ (2008)	$\Delta O_2^{b)}$	$\Delta O_2^{c)}$
WSS1	-690 <sup>a)</sup>	-660.07	-649.9	40.1	10.1
WSS2	-137	-157.39	-142.2	-5.2	15.2
WSS3	-438	-401.76	-378.2	59.8	23.6
WSS4	-464	-482.23	-467.5	-3.5	14.7
TT	-453	-452.68	-450.1	2.9	2.6

<sup>a)</sup> All values in table are in per meg.

<sup>b)</sup> MPI-BGC difference between the re-analyses in 2008 and the first analyses in 2005.

<sup>c)</sup> Difference between the re-analyses in 2008 at MPI-BGC and the provisionally corrected  $O_2$  scale based on LSS analyses at ZOTTO (as described in the text).

**Table 4.3:** Summary of  $O_2$  cylinder (WSS and TT) concentrations.

In late 2007, these cylinders were returned to MPI-BGC, and the root of the problem became more clear. In Figure 4.6, I show the  $O_2$  differences (in per meg) between the 2005 and 2008 MPI-BGC analyses for all WSS cylinders and a ‘Target Tank’ (TT, defined in Section 4.5 below). The very large differences for cylinders WSS1 and WSS3 were caused by either analytical artefacts or poor cylinder handling procedures during the process of cylinder concentration assignment at MPI-BGC. Further supporting evidence for this conclusion was obtained in 2008, from an examination of the 2005 raw data files from the MPI-BGC mass spectrometer, showing anomalous behaviour during the analysis of these two cylinders. However, even the second set of measurements cannot be considered very robust since they are based only

on two sets of measurements conducted on two consecutive days and with unclear (unreported) cylinder handling protocols.

According to Keeling *et al.*'s [2007] long-term observations of the stability of O<sub>2</sub> concentrations in 18 calibration cylinders, we can clearly state that the actual drift in O<sub>2</sub> concentrations within high-pressure cylinders should typically be within a 5-10 per meg range. One, however, should also take into consideration the cylinder handling and analysis techniques, which must include repeated measurements of O<sub>2</sub> concentrations (5 or 6 sets of measurements over at least a 2-month period) that were neglected in this case. Based on these concentration differences, the ZOTTO S1 O<sub>2</sub> scale had to be retrospectively re-defined resulting in the necessity to re-calculate all tower O<sub>2</sub> data for a one-year period. Subsequent O<sub>2</sub> data shown in my thesis have all been corrected, by assuming that the 2008 MPI-BGC WSS determinations were correct.

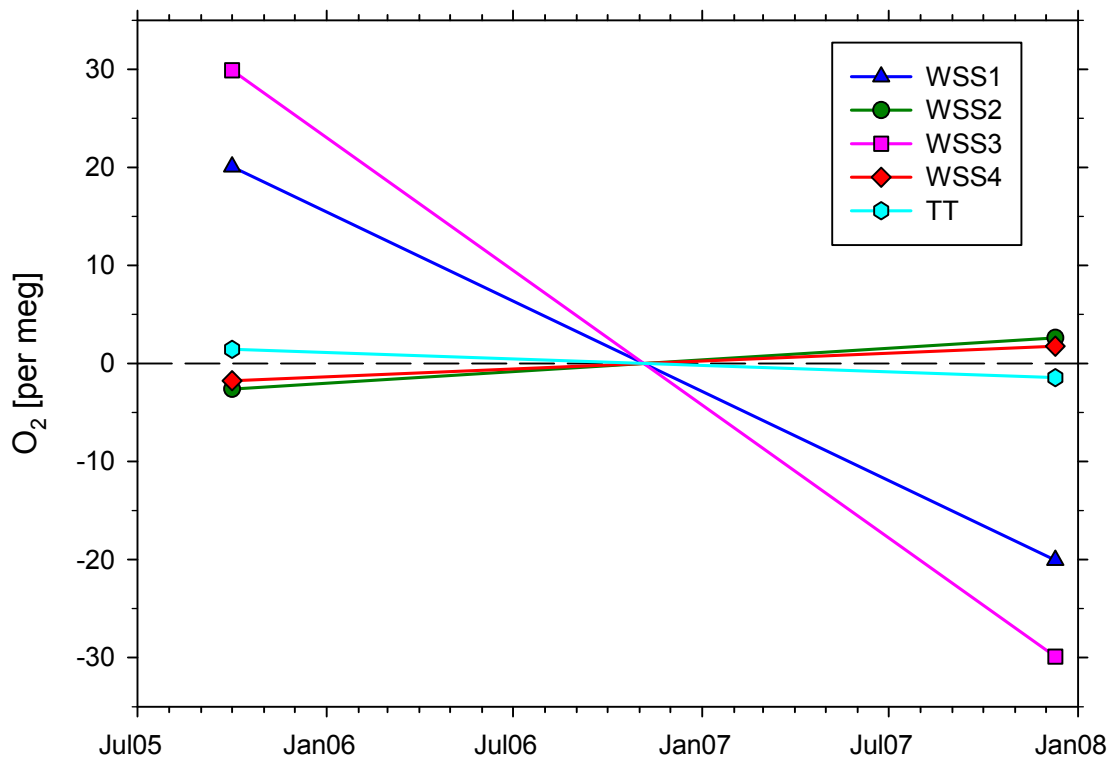


**Figure 4.6:** Changes in O<sub>2</sub> concentrations (in per meg) for WSS and TT cylinders are shown as a difference from their average values (calculated from measurements in 2005 and 2007-08). Two cylinders (D420534 and ND21971) show very large changes of ~60 and ~40 per meg, which are due to analytical errors, most probably in the 2005 measurements, rather than concentration drift. The other three cylinders show drift/imprecision as would be typically expected.

#### 4.5 Data evaluation results: repeatability and comparability

The primary tool used for evaluating our concentration data during routine operation is a cylinder called the 'Target Tank' (TT), whose concentrations have been

defined at MPI-BGC (see Section 4.4) before being shipped to ZOTTO. The first level of evaluation is done in real-time by analysing the TT approximately once every 10 hrs on the O<sub>2</sub> and CO<sub>2</sub> system, and once every 13 hrs on the GC system, where the analysis and data processing protocols are identical to that for a WSS cylinder. Using the most recent ‘good’ WSS calibration results, the TT data are converted into concentration units by our custom LabVIEW™ program, and if these results are outside given tolerances from the ‘declared’ MPI-BGC values, a flag is raised on all subsequent tower air measurements, indicating that these data may be suspect (see also Appendix 4).

Gas species	Repeatability			Comparability	
	Goal	Achieved <sup>(b)</sup>	from Airlines <sup>(c)</sup>	Goal	Achieved <sup>(d)</sup>
CO <sub>2</sub> (ppm)	±0.05	±0.0032±0.0007	±0.03	±0.10 <sup>(e)</sup>	0.06±0.08
O <sub>2</sub> (per meg) <sup>(a)</sup>	±5	±1.5±0.2	±1.2	±10	-1.9±6.0
CH <sub>4</sub> (ppb)	±1.0	±0.6±0.4	±0.7	±2.0 <sup>(e)</sup>	0.1±0.5
CO (ppb)	±1.0	±1.7±1.3	±1.4	±2.0 <sup>(e)</sup>	-3.3±3.3
N <sub>2</sub> O (ppb)	±0.1	±0.3±0.2	±0.3	±0.2	-0.6±0.4

<sup>(a)</sup> See Section 4.2.1 for definition of per meg unit.

<sup>(b)</sup> Average standard deviations of two successive measurements from a given cylinder (TT), determined from over 500 TT measurements collected over a 6 month period from November 2006 to May 2007 for CO<sub>2</sub> and O<sub>2</sub>, and from over 250 TT measurements over a 4 month period from February to June 2007 for CH<sub>4</sub>, CO, and N<sub>2</sub>O. Uncertainties are given on these average standard deviations, illustrating the fact that analytical repeatability varies over time.

<sup>(c)</sup> Typical standard deviations of two successive sample air measurements from the tower, during selected periods when ambient concentrations were relatively stable. These values, which incorporate both ambient variability and analytical imprecision, are used to validate the repeatability results achieved from the TT analyses. Data from all 5 heights were used to compute the values shown, using a period in May 2007 (3 days) for GC results, and two periods in December 2006 (5 days) and April 2007 (6 days) for O<sub>2</sub> and CO<sub>2</sub> results.

<sup>(d)</sup> Average differences between my determinations of TT, and the ‘declared’ values determined at MPI-BGC against primary calibration standards before the cylinder was shipped to ZOTTO. These data were computed over the same time periods as given in <sup>(b)</sup>, and the uncertainties represent the 1σ standard deviations of the (ZOTTO – MPI-BGC) average differences. The MPI-BGC primary standards have been obtained from Scripps Institution of Oceanography, in the case of O<sub>2</sub>, and from the WMO Central Calibration Laboratory (NOAA/ESRL/GMD, formerly NOAA/CMDL), in the case of all other species.

<sup>(e)</sup> These values are the same as the WMO-specified inter-laboratory comparability goals [Expert Group Recommendations *Miller*, 2007]. In the case of O<sub>2</sub> and N<sub>2</sub>O, the WMO goals (1 per meg and 0.1 ppb respectively) are not achievable by any pair of laboratories, therefore we have set slightly less stringent goals (equivalent to the CarboEurope goals).

**Table 4.4:** Repeatability and comparability goals and achievements for all gas analysers at ZOTTO.

The next level of evaluation is to answer the questions, how precise, and how accurate are the concentration measurements of tower air, when defined with the ZOTTO calibration scales computed with WT, WSS, and LSS cylinders? These questions can also be answered using results from the TT analyses.

In Table 4.4 I present results on the repeatability and comparability achievements for measurements made at ZOTTO and compare them with the goals set in the European Commission-funded ‘*CarboEurope-IP*’ and WMO programmes (the full definitions of ‘repeatability’ and ‘comparability’ terms are given in detail in Miller [Expert Group Recommendations 2007]). The goals are based on a consideration of requirements for the data to be scientifically useful, as well as what is considered realistically achievable from an analytical and sampling standpoint.

I consider repeatability, defined as the closeness of agreement between results of successive measurements of the same measure, to be a proxy for the precision of my measurement system. However, the nature of continuous ambient air measurements is such that it is not possible to make successive measurements of the same measure, in contrast to flask or high pressure cylinder analyses, where clearly the repeatability can be both easily determined and improved by analysing multiple sample aliquots. Thus, the best estimate I can give for repeatability at ZOTTO is to report the average standard deviation from the mean of two consecutive analyses from a given high pressure cylinder over a given time interval. To report the standard deviation from a larger number of analyses would bias the results more favourably but is inappropriate, since this is not an option with ambient air measurements from the tower. I also examine how this standard deviation varies over time, since it is an inherent characteristic of any analytical system that the repeatability performance will not be constant. I use the TT cylinder because it is independent from the procedures used to establish the S1 calibration scales.

As shown in Table 4.4, the ZOTTO analytical system is within the repeatability goals for CO<sub>2</sub>, O<sub>2</sub>, and CH<sub>4</sub>, but not for CO and N<sub>2</sub>O. In the case of CO<sub>2</sub>, the achieved repeatability was more than an order of magnitude better than the goal. In the case of CO, I previously obtained repeatability values of about ±0.7 ppb (November/December 2006), but this performance degraded after February 2007, when changes were made to the GC setup which improved CH<sub>4</sub> repeatability, but conversely resulted in worse CO repeatability. In the case of N<sub>2</sub>O, clearly work must be done to improve these results, and there are several clear steps to be taken in future which will result in such improvements.

Additional sources of uncertainty may be introduced by air intake system (e.g. pumps, refrigerator traps, air intakes on the tower, and potentially very long lengths of Synflex tubing) which are not apparent from cylinder analyses. Thus, as a check on the TT-derived values, I calculated typical standard deviations of two consecutive sample air measurements (from all 5 heights on the tower), during selected periods when ambient concentrations were relatively stable, shown in the 'from Air lines' column of Table 4.4. The consecutive air measurements were 16 minutes apart for O<sub>2</sub> and CO<sub>2</sub>, and 12 minutes apart for the GC species, and incorporated ambient variability as well as analytical imprecision. With the exception of CO<sub>2</sub>, the results were very similar to the TT-derived results, suggesting that the methodology of quoting repeatability from TT analyses is valid, and that effectively no additional analytical imprecision was introduced from the air intakes, pumps, etc. The value for CO<sub>2</sub> was much worse (but still within the goal), which suggests that the analytical precision which can be obtained for CO<sub>2</sub> is much greater than ambient variability, even under stable ambient conditions.

In the case of O<sub>2</sub>, although the results were very good, two observations were puzzling. First, air line data from the 300 m height gave slightly worse repeatability than the other heights. In terms of ambient variability, this height should be the most stable. In terms of analytical artefacts, a major difference in November/December 2006 was that I sampled from 300 m with a ¼ inch OD Synflex line, at a flowrate of 150 mL/min (compared to 12 mm OD tubing from 227 and 92 m, at a flowrate of 15 Lpm), leading to a relatively long residence time (32 min) of sample air in the Synflex tubing. In February 2007, suspecting that this was the cause of the worse repeatability, I switched to using 12 mm OD tubing from the 300 m height, at a flowrate of 3 L/min, reducing the residence time to <2 min. The repeatability performance, however, did not improve. With this new arrangement, if there were still a tubing length or residence time-induced artefact, for example owing to absorption/desorption characteristics of O<sub>2</sub> from the inner walls of the tubing, I would expect it to scale proportionally with the other tower heights. But I found no differences in O<sub>2</sub> data repeatability between the 52 m and 227 m heights.

The second observation, also from the 300 m height only, was that during several extremely cold periods (less than -30°C) in November/December 2006 (Figure 5.9), O<sub>2</sub> data showed unusually high scatter. I was not able to find any correlations in the data or diagnostic parameters to explain these observations. One possible cause, however, is that the fan on the aspirated inlet may have stopped working, for example owing to ice blockage. This hypothesis is further supported by the fact that the O<sub>2</sub> scatter decreased again only after the temperature warmed back up to approximately

0°C. The long air residence time inside this 300 m line, especially under such extreme weather conditions, might have also contributed to the problem. In addition, I did not observe such scatter during subsequent cold periods in 2007 (Figure 5.10), when I had changed to using a 12 mm OD sampling line, with no aspirated inlet.

The average calculated concentrations of all TT measurements over a given time interval, compared to the MPI-BGC ‘declared’ concentrations provides a measure of the comparability of the ZOTTO calibration scales over that time interval (see Table 4.4). MPI-BGC has very well established links to the international carbon cycle community (including CarboEurope) through its participation in several intercomparison programs (e.g. CarboEurope Cucumbers (<http://cucumbers.uea.ac.uk/>) and GOLLUM (<http://gollum.uea.ac.uk/>)), and acquisition of primary calibration standards from the WMO-certified CCL. This provides indirect linkage of the ZOTTO measurements to these communities, thus I consider the comparability to MPI-BGC to be the closest proxy possible to estimate the accuracy of the ZOTTO data.

The system’s comparability results (Table 4.4) were similar to those for repeatability, that is, within the goals for CO<sub>2</sub>, O<sub>2</sub>, and CH<sub>4</sub>, but not for CO and N<sub>2</sub>O. The values shown are average offsets from MPI-BGC, with associated 1σ standard deviations, computed over the same periods as for the repeatability results, which are 6 and 4 months respectively for O<sub>2</sub> and CO<sub>2</sub>, and GC species.

An interesting observation with the CO results, is that during the 4 month period used to compute the values in Table 4.4, for the first half of the period the repeatability was about a factor of two better than the average, whereas for the second half comparability was about a factor of two better than the average. In the first half of the period, I also found atypical CO calibration curve coefficients. In hindsight, it appears that the FID methaniser required up to two months to stabilise after the system had been shutdown for modifications in February 2007 (see also Section 4.2 above). Thus, the CO peak integration parameters, established in February 2007, were optimised for a non-steady state system. When the methaniser’s performance stabilised, the repeatability became worse, because the integration parameters were not optimised for those conditions, whereas the comparability became better since the methaniser was performing more consistently. With this knowledge, I am confident of improving both repeatability and comparability for CO to the stated goals in future.

Improvements for N<sub>2</sub>O are less straightforward, however, it is well known that the ECD requires a very long time to stabilise after any ‘down-time’ or other interruptions to routine operation (A. Jordan, MPI-BGC, pers. comm., 2005), of similar duration to my findings for the methaniser. This fact has made it very difficult to

optimise ECD settings when visiting the site only two times per year. One obvious step, which would lead to improvements in N<sub>2</sub>O comparability (but not repeatability), is to increase the frequency of WSS calibrations.

On the one hand the comparability (accuracy) results reported above are conservative, since, for example, if the concentration of any species were drifting in the TT cylinder, the results would be negatively influenced. In fact, as stated above (Section 4.3), I found that O<sub>2</sub> became depleted over time in the TT, in a similar fashion as in the WTs. On the other hand, it is a clear weakness that the ZOTTO calibration scales were compared to only one international laboratory (MPI-BGC). Unfortunately, I was unable to join the European intercomparison programmes because of the remoteness of the ZOTTO site, and the difficulty of importing/exporting equipment in/out of Russia. There is, however, one other source of comparability, which could provide additional information, albeit also only to MPI-BGC. According to the calibration methodology described in Section 4.2 above, two new WSS calibration standards from MPI-BGC will be incorporated into the system each year, with their concentrations to be determined on the internal S1 calibration scales. These standards, however, will have been previously analysed at MPI-BGC, thus the measurements from these standards during the transition period (before they are incorporated as new WSSes) can be used as an additional comparability tool. This procedure has the advantage of examining for drifts in comparability between the field station and MPI-BGC over the long-term based on the continually revised calibration scales at both locations.

#### **4.6 O<sub>2</sub> fractionation issues**

Atmospheric O<sub>2</sub> sampling problems caused by the introduction of artefacts from various O<sub>2</sub> fractionation mechanisms have been discussed previously [e.g. *Keeling et al.*, 2007; *Stephens et al.*, 2007; *Blaine et al.*, 2006; *Langenfelds et al.*, 2005]. Here I present only a short overview of additional findings observed at ZOTTO. To minimise fractionation at the air intakes on the tower which can occur at low flowrates ( $\sim < 0.5$  L/min; [*Manning*, 2001]), we fitted aspirated inlets on all low-flow (150 mL/min) intakes, following *Blaine et al.* [2006]. The higher flow intakes do not require aspirated inlets, however, a ‘tee’ junction is required to divide the flow, siphoning off only 150 mL/min to the analysers. The phenomena of O<sub>2</sub> fractionation (relative to N<sub>2</sub>) at tee junctions has been well established in experimental testing [e.g. *Manning*, 2001]. Effective elimination of such fractionation and an understanding of the underlying mechanisms have remained elusive. What is known, however, is that the degree of

fractionation is most sensitive to temperature variations and pressure pulsations at the tee, and is dependent on the flow ratio (ratios closer to 1:1 result in less fractionation).

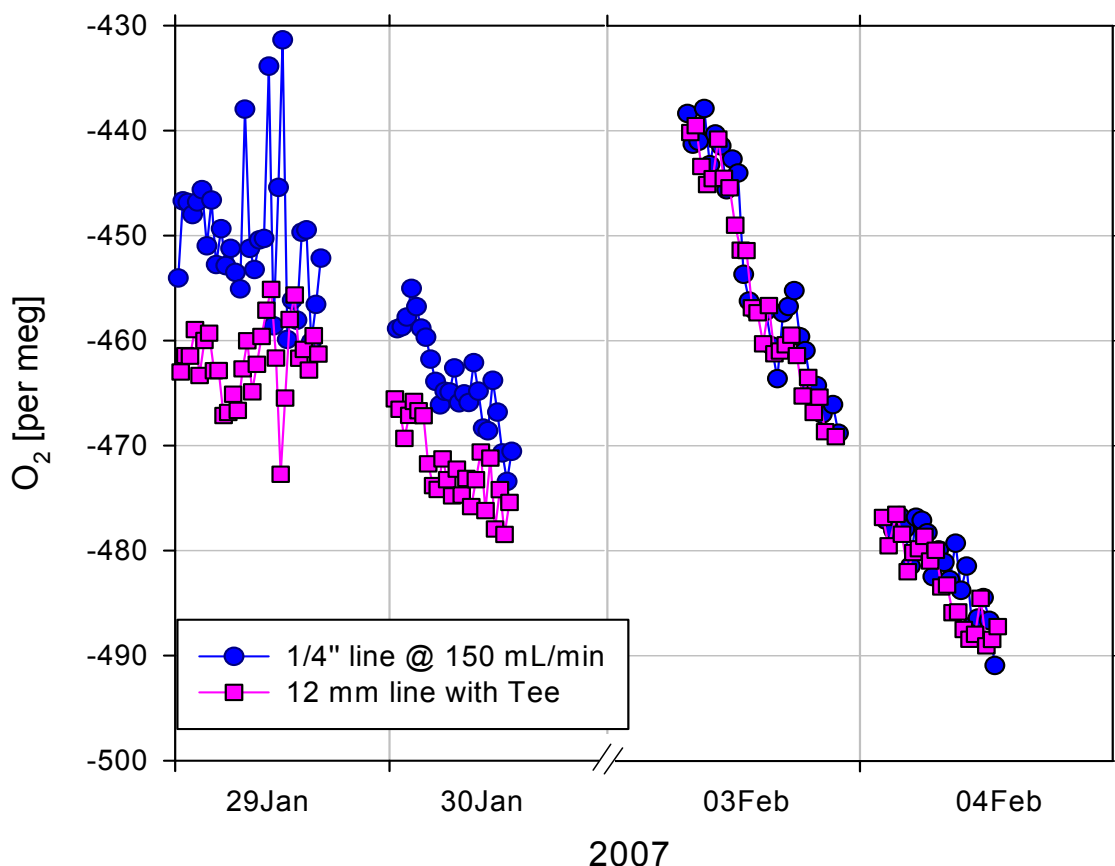


**Figure 4.7:** Results from fractionation tests are shown by comparing  $O_2$  data from two lines at 52 m:  $\frac{1}{4}$ " OD line (blue colour) with a flowrate of 150 mL/min and 12 mm line (pink colour) which incorporates a tee, buffer volume and a purge pump, and at an initial flowrate of  $\sim 15$  L/min. Several different set-ups were tested aiming to reduce the visible offset in the data, with four set-ups shown here and described in the text. The noisy data on 29 Jan 2007 from the  $\frac{1}{4}$ " OD line are thought to be caused by a temporary fan failure (installed as a part of the aspirated inlet) due to very cold ( $\sim -35^\circ\text{C}$ ) weather conditions. The  $O_2$  data collected on 03 and 04 Feb showed minimum offset ( $\sim 1$ -2 per meg) between the two lines (see text for more details).

To minimise these effects, I installed all tees inside the temperature-controlled laboratory, away from any direct heat sources, and isolated them from pressure pulsations induced by the pumps (OXC3, 4, 5 and 7 in Figure 3.1) by installing cylindrical buffer volumes (3.1 L). Comparison tests in 2007 of sampling lines with and without a tee from the 52 m height (see Figure 4.7), however, showed that the buffer volumes were not effective at removing all fractionation, with residual fractionation between the two lines of 10-15 per meg (the line with the tee gave lower  $O_2$  concentrations; test (i) in the Figure; flowrate of the line with the tee was 15 L/min, giving a flow ratio at the tee junction of 99:1). Reducing the 12 mm OD line flowrate to 3 L/min (flow ratio = 19:1) appeared to result in a reduction in fractionation (to 5-10 per meg), but did not eliminate it (test (ii)). Thus I installed a ‘dip-tube’ into the tee,

following Stephens *et al.* [2007]. A dip-tube is a piece of tubing of a smaller OD than the inlet tube (in our tests we used 1/8" and 1/16" dip-tubes) extending upstream of the tee junction. I found that a 1/8 inch OD dip-tube, extending 12 cm upstream of the tee inside the 12 mm OD Synflex tubing gave no noticeable improvement (not shown in Figure). However, dip-tubes extending 32 cm, of either 1/8 or 1/16 inch OD tubing, appeared to eliminate fractionation to within 1-2 per meg (see Figure 4.7, tests (iii) and (iv) respectively, both at 3 L/min flowrate). In the case of the 1/8 inch OD, 32 cm-length dip tube my results were different from those observed by Stephens *et al.* [2007], who found that a dip-tube of this length and OD still gave large fractionation. The fact that Stephens *et al.* [2007] had a much greater flow ratio at the tee junction of 200:1 may possibly explain these differences. My 1/16 inch OD results (32 cm length) agree with this earlier study. According to Stephens *et al.* [2007], the positioning of the 1/8 inch OD dip-tube inside the housing tubing is also important, however, the 1/16 inch OD dip-tube proved to be insensitive to its radial positioning. My dip-tubes were all installed in the centre of their housing tubing, and I did not test the influence of the dip-tubes' positioning.

Although not tested, I suspect that the temperature stability of this arrangement is important, to ensure that no radial gradients in O<sub>2</sub> concentration can develop inside the 12 mm tubing. Finally, I caution other workers that in my successful tests with the 32 cm long dip-tubes, the buffer volumes were still present, and I did not test at the original higher flowrates (12-15 L/min). In both my study and the study of Stephens *et al.* [2007], tests were done somewhat hurriedly in the field, precluding more comprehensive testing and conclusions that could be obtained from a full-scale laboratory analysis. To my knowledge, however, no such laboratory tests have yet been carried out.

## **CHAPTER 5. Seasonal, synoptic and diurnal scale variability of biogeochemical trace gases and O<sub>2</sub> in central Siberia**

### **5.1 Introduction to Chapter**

This chapter presents semi-continuous atmospheric measurements of CO<sub>2</sub>, O<sub>2</sub>, CH<sub>4</sub> and CO concentrations collected from a 300-m tall tower in central Siberia between November 2005 and June 2007. The importance of GHG measurements in light of changing climate, particularly in such a vulnerable ecosystem as the Siberian taiga, was discussed in Chapter 1, Sections 1.3 and 1.4. The data shown and discussed in this chapter represent a unique multi-species dataset from a very remote location in the middle of the Siberian taiga, and one of the first datasets of atmospheric O<sub>2</sub> measurements within the interior of a continent. In this chapter I discuss concentration variations of all species measured at ZOTTO (except N<sub>2</sub>O, for which only 3.5-months of wintertime data were available) on different temporal and spatial scales, including relationships between them by taking advantage of our multi-species measurement approach (also discussed in Chapter 2).

Section 5.2 gives an overview of the ZOTTO site and its main geographic and climatic characteristics; it also discusses previous carbon cycle studies performed in the vicinity. Seasonal variations of CO<sub>2</sub>, O<sub>2</sub> and Atmospheric Potential Oxygen (APO) at ZOTTO are the subject of discussion in Section 5.3. Most of the material presented in this section has been published in Kozlova *et al.* [2008]. To facilitate discussion on horizontal air mass transport I use O<sub>2</sub> and CO<sub>2</sub> data from Shetland Islands (SIS), Scotland (60.28°N, 1.28°W) collected by MPI-BGC, situated at a similar latitude as ZOTTO. In addition to the observations themselves, their comparisons with global transport model (TM3) simulations are presented and results are discussed in Section 5.3.1. Section 5.4 is devoted to discussion on important revisions that were retrospectively applied to the ZOTTO O<sub>2</sub> calibration scale and subsequently to all O<sub>2</sub> data used in this thesis. This section also summarises advantages and disadvantages of flask sample collections, and suggests a way to correct the existing O<sub>2</sub> datasets from pressurised flasks by using concurrent Ar/N<sub>2</sub> measurements (Section 5.4.1). Section 5.4.2 presents updated (in comparison to Kozlova *et al.* [2008]) results obtained from the study on seasonal variations of CO<sub>2</sub>, O<sub>2</sub> and APO based on the revised O<sub>2</sub> calibration scale. This section highlights similarities and differences between the revised and unrevised datasets and the impact that this scale revision has had on the conclusions of the study, including the comparison with the TM3 model simulations (Section 5.4.3).

Seasonal variations of CH<sub>4</sub> and CO concentrations at ZOTTO are analysed in Section 5.5. In addition, I use CO data from SIS and CH<sub>4</sub> and CO data for the ‘marine

boundary layer reference' from the GLOBALVIEW database to facilitate discussion on seasonal variations observed in atmospheric concentrations of these trace gases at ZOTTO. Synoptic variations of CO<sub>2</sub>, O<sub>2</sub>, CH<sub>4</sub> and CO are the topic of discussion in Section 5.6, with special attention given to local meteorological phenomena ('cold events') and emission ratios of all measured species during pollution events observed at ZOTTO (Sections 5.6.1 and 5.6.2 respectively). Difficulties associated with using O<sub>2</sub>/CO<sub>2</sub> ratios as an identifier for types of burned fossil fuels are also summarised here (Section 5.6.2). Finally, diurnal variations of CO<sub>2</sub> and O<sub>2</sub> are briefly discussed in Section 5.7. This Section also contains a discussion on vertical profiles of CO<sub>2</sub> and CH<sub>4</sub> with some surface carbon flux estimates.

## 5.2 The ZOTTO site

The ZOTTO site is situated in a region characterised by a strong continental climate. The average January temperature is -26°C with observed minima of -56°C; the average July temperature is 21.8°C with a highest recorded temperature of 36°C; average annual precipitation is between 500-600 mm [Schulze *et al.*, 2002]. The tower base (60.80°N, 89.35°E, elevation 114 m a.s.l.) is situated about 30 km to the west of the Yenisei River. The nearest village, Zotino, with a population of about 500 people, lies about 25 km northeast of the tower, on the bank of the Yenisei. The nearest city of appreciable size is Krasnoyarsk, population ~1 million, 600 km to the south. The river divides the region into two distinct parts, with *Pinus sylvestris* forests and bogs to the west, and dark coniferous taiga dominated by *Pinus sibirica* to the east. The western region (where the tower is built) consists of a fluvial sand plateau (50-100 m above the river level), and is intercepted by numerous lakes and ponds due to the presence of clay lenses. The soil type is podzolic, characterised by low pH<sub>H2O</sub> (4.7-5.3), low nitrogen (2-3 tN ha<sup>-1</sup>), and low soil carbon content (<35 tC ha<sup>-1</sup> in the uppermost 1-m layer) [Schulze *et al.*, 2002].

Several studies were previously conducted close to the ZOTTO site. Eddy covariance flux measurements of CO<sub>2</sub>, H<sub>2</sub>O and energy exchanges were made in a nearby pine forest [Lloyd *et al.*, 2002b; Shibistova *et al.*, 2002b], dark taiga [Röser *et al.*, 2002] and bogs [Kurbatova *et al.*, 2002]. These measurements were accompanied by process studies on soil respiration [Shibistova *et al.*, 2002a] and detailed forest inventories [Schulze *et al.*, 2002; Wirth *et al.*, 1999]. These studies indicated that the local forest and bog ecosystems constitute a moderate carbon sink (typical growing season net ecosystem exchange (NEE) for forests from -300 to -150 g C m<sup>-2</sup> and for bogs about -50 g C m<sup>-2</sup>) with relatively large interannual variability. Additional

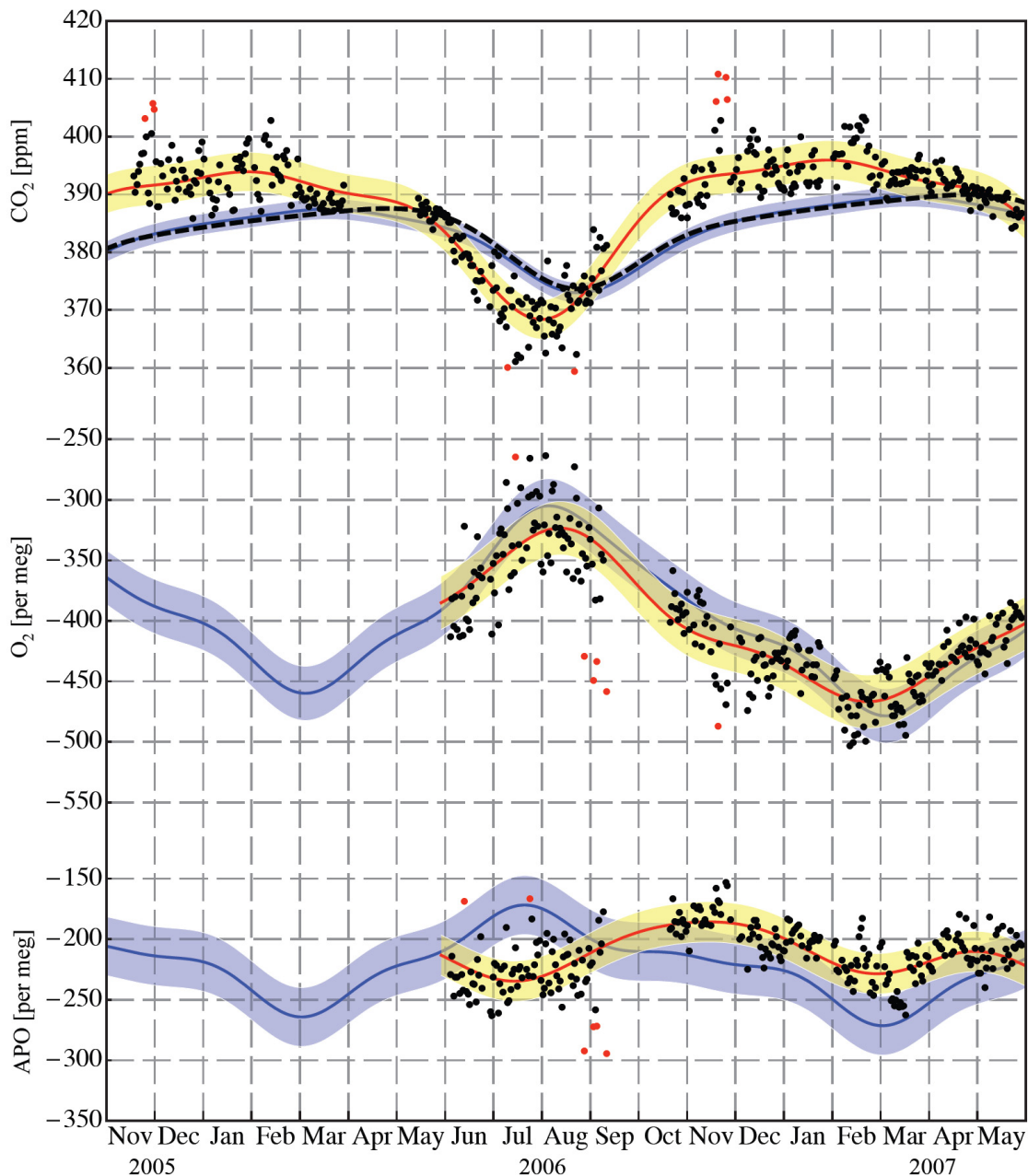
measurement programs included several years of monthly atmospheric vertical profile sampling up to 3000 m by light aircraft establishing a seasonal climatology of the major GHGs and their isotopic composition in central Siberia [Levin *et al.*, 2002; Lloyd *et al.*, 2002a]. Atmospheric chemistry measurements of shorter lived gas species have been performed in neighbouring regions along the Trans-Siberian Railroad (TROICA project) [e.g. Tarasova *et al.*, 2006]. The observations have been accompanied by a series of modelling studies on various scales: global atmospheric inversion calculations of CO<sub>2</sub> documenting the large interannual variability of Siberian ecosystems, partly attributable to variations in fire emissions [Rödenbeck *et al.*, 2003]; continental scale forward simulations with mesoscale models investigating the large-scale transport patterns over the area [e.g. Karstens *et al.*, 2006; Chevillard *et al.*, 2002] and high-resolution model simulations for the determination of diurnal cycle variations in the ZOTTO area caused by the Yenisei river [van der Molen and Dolman, 2007].

The construction of the ZOTTO site and tower itself, and preparation of all scientific equipment and related permissions from the Russian authorities, took several years to complete. In August 2005 the scientific equipment was shipped to Russia and the tower was built up to 52 m height; further construction had to be halted due to the approaching winter. By the end of November 2005 all equipment installations in the laboratory container were completed as well as the installation of temporary sampling lines that allowed us to start the testing phase of the measuring system, up to 52 m.

By the end of September 2006, the construction of the tower was completed up to 300 m and the end of October 2006 is considered the official start of the measurements (with approval from the Russian Gostech Commission). Since then, both the O<sub>2</sub> and CO<sub>2</sub>, and GC subsystems were collecting measurements from five heights on the tower until 01 June 2007, when the measurements were stopped.

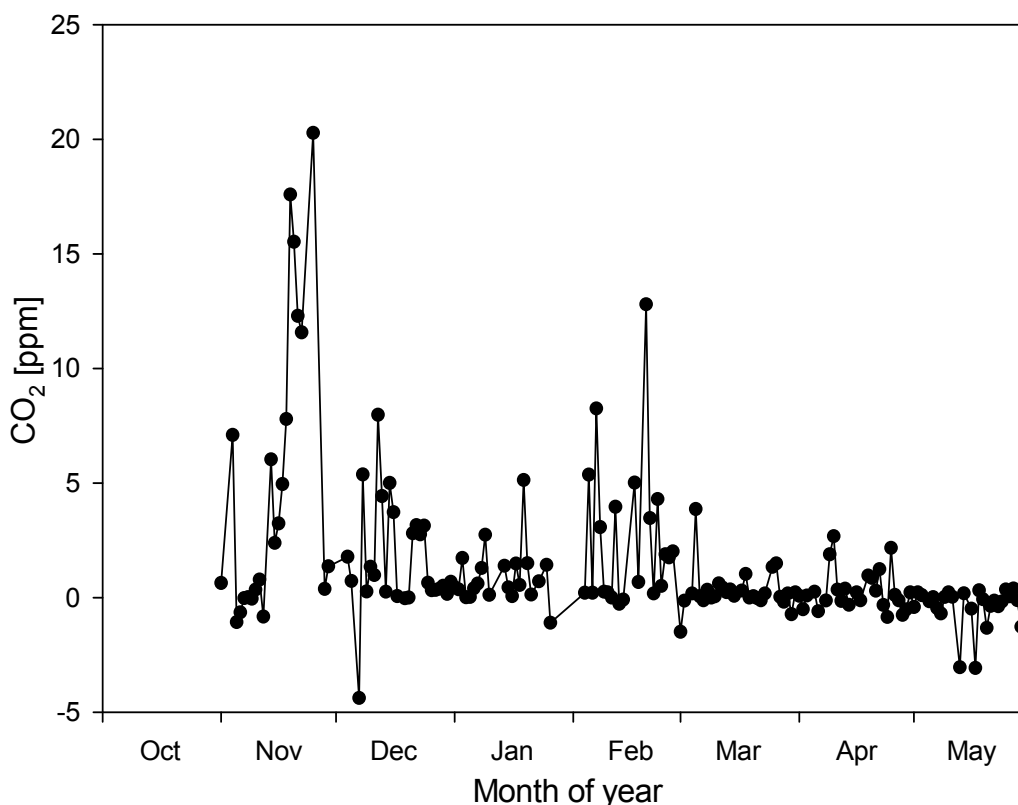
### **5.3 Seasonal variations of CO<sub>2</sub>, O<sub>2</sub> and APO**

Figure 5.1 shows the seasonal cycles of CO<sub>2</sub>, O<sub>2</sub> and APO as observed at ZOTTO. Here I only present data from the 52 m height, since they are available for a longer period (including before the tower was fully constructed). A quantitative comparison with ‘background’ observations elsewhere can be obtained by means of a data selection procedure where only daytime values between 11:00 and 17:00 are selected (local standard time, UTC + 7 hr), and averaged, excluding the 25% highest and 25% lowest values to obtain trimmed daily averages (black points in Fig. 5.1). This minimises the impact of incomplete vertical mixing during stable atmospheric conditions, in particular during the night.



**Figure 5.1:** Seasonal cycles of  $\text{CO}_2$ ,  $\text{O}_2$  and APO from 52 m height of the ZOTTO tower. The y-axis scales of all three panels have been adjusted so that visually, changes in  $\text{CO}_2$  (ppm), and  $\text{O}_2$  and APO (per meg), are directly comparable on a mole to mole basis. Black and red points on all three panels show trimmed daytime averages of measurements between 11:00 and 17:00 (local standard time: UTC + 7 hr). The fit functions (red lines) were computed iteratively from the trimmed daytime averages. Convergence was achieved after 4 ( $\text{CO}_2$  and APO) and 3 ( $\text{O}_2$ ) iterations, identifying a total of 9 ( $\text{CO}_2$ ) and 6 ( $\text{O}_2$ , APO) outliers of daily averages (red points). Outliers are defined as  $>3$  standard deviations from the average. Yellow bands on all panels denote  $\pm 1$  standard deviation of the residuals of the trimmed daytime averages from the fit functions. For comparison, the blue lines and bands show similar fit functions and  $\pm 1$  standard deviation of the residuals from flask measurements ( $\sim$ weekly frequency) from SIS (60.28°N, 1.28°W). The black dashed line on the  $\text{CO}_2$  panel shows the ‘marine boundary layer reference’ concentration at 60°N as given in the GLOBALVIEW- $\text{CO}_2$  database [2007] (linearly extrapolated after 01 Jan 2007 with constant annual growth rate).  $\text{CO}_2$  data are reported on the NOAA/WMO X2005 scale, and  $\text{O}_2$  and APO data are reported on the SIO scale but with the caveats as mentioned in the text.

Figure 5.2 presents the interpolated differences between the daily trimmed averages from 52 and 300 m of the ZOTTO tower. As expected, the largest discrepancies are observed over the wintertime, especially under very cold and calm conditions when vertical mixing is suppressed (see discussion on ‘cold events’ in Section 5.6.1). In contrast to the wintertime, the same comparison with the spring data (starting from March onwards) showed very small differences between the two heights, with only a few outliers.



**Figure 5.2:** CO<sub>2</sub> concentration interpolated differences (in units of ppm) between two sampling lines (52 m minus 300 m) from Oct 2006 to Jun 2007. As measurements at both heights were not simultaneous, the 300 m measurements were interpolated to the time stamp of the measurements at 52 m.

Finally, a 3-harmonic function was fitted to a base period of one year plus a linear trend to the trimmed daily averages (red lines in Fig. 5.1). The fitting procedure was iteratively repeated, removing daily averages lying outside 3 standard deviations from the fit functions. This procedure removed outliers that were considered to be caused by local effects and that, despite being relatively sparse, do not represent the large-scale seasonal variation that the fitting function should capture. The yellow bands represent  $\pm 1$  standard deviation of the residuals of the daily averages from the fit functions. Since for O<sub>2</sub> and APO the data records are not long enough to reliably determine a long-term trend, I used the linear trends of  $-18.6$  per meg yr<sup>-1</sup> (O<sub>2</sub>) and  $-7.2$  per meg yr<sup>-1</sup> (APO) from observations during a similar time period at SIS (60.28°N,

1.28°W), the same latitude as ZOTTO. For comparison, I also display the fit functions (blue lines in Fig. 5.1) obtained by a similar data selection procedure from weekly flask measurements collected at SIS (with  $\pm 1$  s standard deviation of the residuals shown as light blue bands). In the case of CO<sub>2</sub>, I also plot the ‘marine boundary layer reference’ at 60°N as defined and given in the GLOBALVIEW-CO<sub>2</sub> database [2007] (black dashed line).

The CO<sub>2</sub> daytime data in Figure 5.1 exhibit the expected seasonal cycle, with the spring/summer decline caused by net land biotic photosynthesis and the autumn/winter release caused by net respiration. Clearly, the presently available short record does not permit a rigorous determination of the amplitude of the CO<sub>2</sub> seasonal cycle in the atmospheric boundary layer (ABL) in central Siberia. Nevertheless, from the fitting function I estimated an amplitude of about 26.6 ppm, which is consistent with previous results from aircraft observations averaged over the ABL (~22 ppm), performed a few km away from ZOTTO [Lloyd *et al.*, 2002a]. Comparing SIS and ZOTTO data I observed a seasonal amplitude of 15.4 ppm at SIS, 11.2 ppm smaller than at ZOTTO. In July, between these two stations there existed a west-east gradient of about -7 ppm, most likely reflecting the summertime continental uptake of CO<sub>2</sub>. This gradient is consistent with results from regional model simulations for this time of year [Karstens *et al.*, 2006; Chevillard *et al.*, 2002].

The CO<sub>2</sub> minimum at ZOTTO occurred at the end of July, which was also found by Lloyd *et al.* [2002a]. At SIS the minimum occurred at the end of August with a much more gradual autumn increase, as expected due to the more maritime character of this station. At ZOTTO, CO<sub>2</sub> increased rapidly until the end of October, then continued to increase relatively slowly, reaching a maximum in late January, compared to the later maximum at SIS in late March. The SIS maximum is about 7 ppm lower than that observed at ZOTTO, most likely reflecting both anthropogenic and land biotic CO<sub>2</sub> sources from the European continent in the ZOTTO signal. The linear trend in the ZOTTO CO<sub>2</sub> record determined in the fitting procedure yielded an increase rate of 2.02 ppm yr<sup>-1</sup>, which is similar to the trends observed at SIS (2.17 ppm yr<sup>-1</sup>) and from the marine boundary layer reference (2.0 ppm yr<sup>-1</sup>).

The seasonal cycle of O<sub>2</sub> is roughly anti-correlated with the cycle of CO<sub>2</sub> as expected from the coupling of the two gases in land biotic photosynthesis and respiration. In July, assuming simplistically that the observed 7 ppm CO<sub>2</sub> west-east decline is entirely due to land biotic uptake, I would expect to see ZOTTO O<sub>2</sub> concentrations elevated by ~37 per meg compared to SIS. Instead, I observed ZOTTO O<sub>2</sub> in July to be ~20 per meg lower than SIS. The main reason for this discrepancy can

be attributed to the larger oceanic component in the SIS O<sub>2</sub> seasonal cycle. In addition, it is possible that the west-east land biotic CO<sub>2</sub> sink is even greater than implied by the -7 ppm July concentration gradient, because it may be partially offset by fossil fuel emissions in Europe and Russia. If so, such fossil fuel emissions would result in a corresponding O<sub>2</sub> uptake at a greater O<sub>2</sub>:CO<sub>2</sub> ratio than that released from land biotic exchanges, thus also contributing to a lower O<sub>2</sub> signal at ZOTTO. The air flow over the Eurasian continent, however, is not completely zonal, which complicates this interpretation, with possibly different source and sink patterns influencing ZOTTO compared to SIS. In the next subsection I investigate this assumption further by using a three-dimensional atmospheric transport model (TM3).

I calculated an approximate seasonal O<sub>2</sub> amplitude of 134 per meg, corresponding to 28.1 ppm of CO<sub>2</sub> (on the basis that mole for mole, a 1 ppm change in CO<sub>2</sub> corresponds to a 4.77 per meg change in O<sub>2</sub>). The O<sub>2</sub> maximum at ZOTTO almost coincided with the CO<sub>2</sub> minimum, in early August. In the winter months, ZOTTO O<sub>2</sub> and CO<sub>2</sub> are not as well anti-correlated, as O<sub>2</sub> continued to decrease relatively steadily to a minimum in February, in contrast to the comparatively stable CO<sub>2</sub> from November onwards. As an atmospheric O<sub>2</sub> marine reference does not exist, I used SIS O<sub>2</sub> data as a proxy reference, and found a seasonal amplitude of 163 per meg, about 29 per meg greater than at ZOTTO. In summertime, in contrast to ZOTTO, SIS O<sub>2</sub> and CO<sub>2</sub> cycles are slightly out of phase: the O<sub>2</sub> maximum occurred in the beginning of August while the CO<sub>2</sub> minimum occurred one month later. In the winter months, SIS O<sub>2</sub> and CO<sub>2</sub> show stronger anti-correlation than at ZOTTO, although with CO<sub>2</sub> still lagging O<sub>2</sub> by one month.

These observations are interpreted as follows: in summertime at ZOTTO, CO<sub>2</sub> and O<sub>2</sub> changes are dominated by strong, anti-correlated land biotic exchanges, whereas at SIS, changes in O<sub>2</sub> are influenced by both land and ocean exchanges, with different phasing, with only the former influencing CO<sub>2</sub> changes. In the winter months, at SIS the situation is much the same as in summer (but reversed), whereas at ZOTTO, with little activity from the land biosphere, there is a greater influence from the (attenuated) O<sub>2</sub> seasonal signal derived from the distant oceans. In the very cold, snow-covered environment at ZOTTO, land biotic respiration is minimal during the winter months, as shown by the very broad CO<sub>2</sub> maximum.

I also present results of APO, Atmospheric Potential Oxygen, which reflects the weighted sum of O<sub>2</sub> and CO<sub>2</sub> concentrations, where the weighting is adjusted so that APO is essentially invariant with respect to O<sub>2</sub> and CO<sub>2</sub> exchanges with land biota [Manning and Keeling, 2006; Stephens et al., 1998]. APO (in per meg) is defined as:

$$APO = \delta(O_2 / N_2) + \frac{\alpha_B}{S_{O_2}} (X_{CO_2} - 350), \quad (5.1)$$

where  $\alpha_B$  corresponds to a typical average O<sub>2</sub>:CO<sub>2</sub> molar exchange ratio for land biotic photosynthesis and respiration in units of moles of O<sub>2</sub> produced per mole of CO<sub>2</sub> consumed (taken as 1.10 [Severinghaus, 1995]), and 350 is an arbitrary reference CO<sub>2</sub> concentration used in the SIO definition of APO.

The seasonal amplitude of APO at ZOTTO (bottom panel of Fig. 5.1) is about 51 per meg, compared to a much larger amplitude of 95 per meg at SIS, reflecting a strong attenuation of the oceanic signal in the continental interior. What is surprising, however, is the lag of 4 months in the ZOTTO APO minimum and maximum in comparison to SIS. A lag is to be expected as the oceanic signal propagates into the continental interior, but not of such long duration. This finding is not very robust, however, with only one year of data and because of the large gap in observations during the tower construction in September and October that very plausibly may have masked a significantly earlier APO maximum. In addition, the ‘signal to noise ratio’ is low when considering the APO amplitude and as a result, for example, the fitted curve exhibits double maxima/minima which are unlikely to be real, and with the seasonal minimum in particular not very distinct. Clearly, additional years of data collection are required in order to derive a more robust APO seasonal cycle.

### 5.3.1 Comparison with TM3 model simulations

By definition, the APO seasonal cycle should be primarily driven by seasonal air-sea fluxes of O<sub>2</sub>, plus a small component from thermally driven air-sea fluxes of N<sub>2</sub>. Thus the dilution of the APO seasonal amplitude over the continents by atmospheric mixing provides a convenient way to evaluate models of atmospheric transport [Blaine, 2005; Heimann, 2001]. Simulations of the global distribution of atmospheric CO<sub>2</sub>, O<sub>2</sub> and N<sub>2</sub> (from which APO can be derived) were performed in the TRANSCOM atmospheric transport model intercomparison activity [Blaine, 2005; Gurney *et al.*, 2000]. Here, I compare the simulation results of the TM3 model [Heimann and Koerner, 2003] with ZOTTO observations as an illustrative example.

The CO<sub>2</sub> concentration was obtained as a composite from simulations using three surface flux fields: (1) fossil fuel emissions [Andres *et al.*, 1996], (2) seasonal land biosphere exchange fluxes from a steady-state run of the CASA model [Randerson *et al.*, 1999], and (3) air-sea CO<sub>2</sub> fluxes from pCO<sub>2</sub> observations [Takahashi *et al.*, 1999].

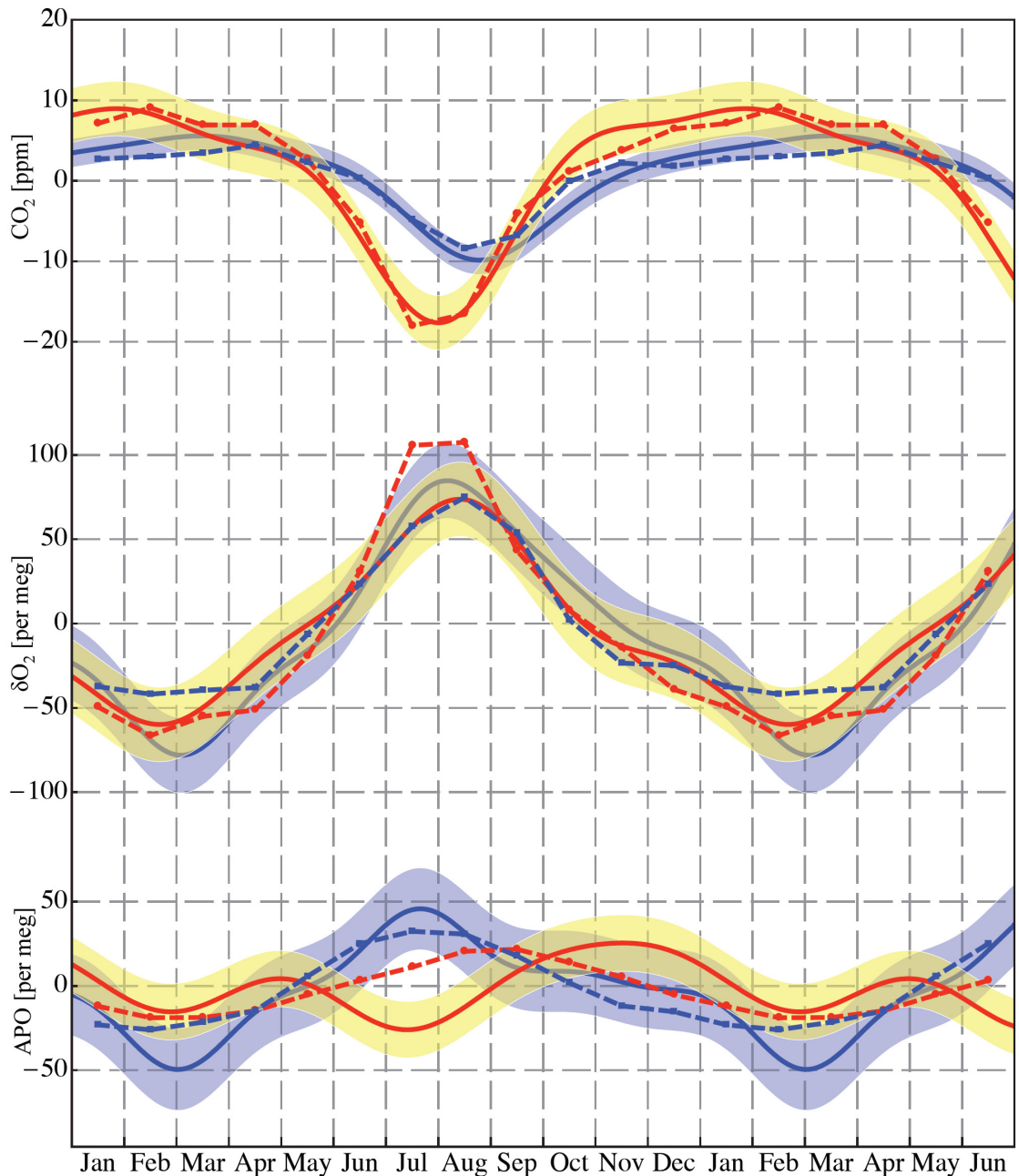


**Figure 5.3:** Seasonal cycles of  $\text{CO}_2$ ,  $\text{O}_2$ , and APO from model results (dashed lines) and fit functions to the observations (solid lines) at ZOTTO (red lines) and SIS (blue lines). Seasonal cycles were obtained by subtracting the linear trends and annual means from the fit functions of the observations and the model results. The yellow (ZOTTO) and light blue (SIS) bands denote  $\pm 1$  standard deviation of the residuals of the daytime averages from the fit functions (as for Fig. 5.2). For visual clarity, the first 6 months are repeated, and all species can be compared visually on a mole to mole basis.

The corresponding  $\text{O}_2$  composite was derived from (1) the fossil fuel  $\text{CO}_2$  simulation using an  $\text{O}_2:\text{CO}_2$  molar ratio of 1.4, (2) the land biosphere  $\text{CO}_2$  simulation using an  $\text{O}_2:\text{CO}_2$  molar ratio of 1.1, and (3) a simulation with the air-sea fluxes of  $\text{O}_2$  from the compilation of Garcia and Keeling [2001]. The  $\text{N}_2$  simulation included only the air-sea fluxes of  $\text{N}_2$  calculated from air-sea heat fluxes [Gibson *et al.*, 1997] and the  $\text{N}_2$  solubility temperature dependence [Weiss, 1970]. Modelled APO concentrations were then computed according to the equation 5.1 above. In most respects the model

simulation protocol corresponds to that given in Battle *et al.* [2006], except that any annual mean uptake or release by the land biosphere (of O<sub>2</sub> and CO<sub>2</sub>) or oceans (of O<sub>2</sub> and N<sub>2</sub>) was neglected. These annual mean flux components are not well constrained and are relatively small compared to the seasonal exchanges.

Figure 5.3 compares modelled and observed seasonal cycles of CO<sub>2</sub>, O<sub>2</sub>, and APO at ZOTTO and SIS. Both SIS (model: blue dashed line; observations: blue solid line and blue band) and ZOTTO (model: red dashed line, observations: red solid line and yellow band) show good agreement for amplitude and phasing for CO<sub>2</sub>. For the O<sub>2</sub> seasonal amplitude, the model underestimates SIS by 43 per meg but overestimates ZOTTO by 43 per meg. The O<sub>2</sub> phasing is in good agreement at both stations between model and observations. For APO, the model underestimates the seasonal amplitudes by 36 per meg and 9 per meg at SIS and ZOTTO respectively. Observations and model results for APO from both stations do not show distinct annual minimums; therefore for phasing analysis, I only examined their annual maximums. SIS gave good agreement, whereas at ZOTTO, the observations annual maximum lags the model maximum by two months.

The model/observations discrepancy in the APO seasonal amplitude at SIS could be explained as a result of the discrepancy in O<sub>2</sub>. Although Battle *et al.* [2006] generally found TM3 modelled APO results in the northern hemisphere to slightly underestimate the APO seasonal amplitude by about 10-20%, the exception was Cold Bay, Alaska, USA (55.20°N, 162.72°W) where the modelled amplitude was about 25 per meg greater than observations. Battle *et al.* [2006] explained this discrepancy based on the existence of a large seasonal oceanic O<sub>2</sub> outgassing in the vicinity of Cold Bay [García and Keeling, 2001], and previous evidence that the TM3 model overestimates tracer concentrations near source regions [Denning *et al.*, 1999]. SIS is also in close proximity to regions of large air-sea O<sub>2</sub> fluxes [Plate 3, García and Keeling, 2001], therefore the model result of a large underestimation of the SIS APO seasonal amplitude is possibly inconsistent with Battle *et al.* [2006] and Denning *et al.* [1999].

The ZOTTO model/observations seasonal amplitude discrepancies appear at first inconsistent, with opposite discrepancies between O<sub>2</sub> and APO. Closer analysis of Figure 5.3, however, reveals that the O<sub>2</sub> seasonal amplitude discrepancy resulted in the large phasing discrepancy in APO, giving large model/observation differences from June–August, in the time of the O<sub>2</sub> maximum. These differences appear to be the result of phasing differences in land and ocean signals as observed at ZOTTO where ocean signals have a significant lag. None of the stations used in Battle *et al.* [2006] are mid-continental stations, precluding comparisons with ZOTTO. Blaine [2005] and Stephens

*et al.* [1998] modelled APO simulations at Niwot Ridge, Colorado (40.05°N, 105.63°W), a mid-continental site in the USA, and both found the model to give a small underestimation in the APO seasonal amplitude, similar to ZOTTO findings, and with an annual maximum about one month earlier than the observations. The APO phasing discrepancy at ZOTTO, while larger, is consistent with these results. But such a comparison is further convoluted because Niwot Ridge is a high altitude station (3749 m asl), which will affect both the phasing of the observed seasonal cycle and the performance of the transport model.

The reasons for the model/observation differences at ZOTTO are likely to be related to the more complex source/sink patterns of O<sub>2</sub>, which contain a significant contribution from the distant oceans, resulting in O<sub>2</sub> (and APO) concentrations at ZOTTO being more sensitive to errors in model transport, in contrast to the CO<sub>2</sub> signal which is dominated by continental sources closer to ZOTTO. Alternatively, the O<sub>2</sub> air-sea flux fields which are input to the model could contain errors, and either these, or seasonal changes in vertical transport, are more likely to explain the O<sub>2</sub> and APO amplitude discrepancies observed at SIS. As discussed above, however, an important caveat in the findings is the untimely 2-month gap in the ZOTTO data record and the low signal to noise ratio in the APO seasonality which most likely influenced our APO observations.

## **5.4 ZOTTO O<sub>2</sub> calibration scale and seasonal cycle revisions**

Section 4.4.2 summarises the reasons for the retrospective O<sub>2</sub> S1 calibration scale corrections applied to all O<sub>2</sub> data in 2008 after reanalyses of all WSSes. The O<sub>2</sub> (and thus APO) data were subsequently published in Kozlova *et al.* [2008] and discussed in Section 5.3 above. In 2009, additional data analyses, namely a detailed comparison with flask samples, was performed and resulted in additional corrections to the published data.

### **5.4.1 Ar/N<sub>2</sub> correction of O<sub>2</sub> data**

The quality of O<sub>2</sub>/N<sub>2</sub> flask sample measurements is largely influenced by pressure disturbances occurring during the sampling process; to minimise these the flasks are initially ‘conditioned’ to ~2 bar (absolute) which is similar to the pressure at which the flasks are filled. If the ‘conditioning’ is not done, or ‘lost’ (owing to leakages in the valves prior to sampling or loss of pressure during the sampling process) large pressure changes that occur during the filling procedures might have a sizeable impact on O<sub>2</sub>/N<sub>2</sub> ratios of an air sample. However, the biggest problem that has been so far experienced with the ZOTTO flasks is leaking flask valves that mainly affect the O<sub>2</sub>/N<sub>2</sub>

ratios of sampled air via fractionation effects. The above-ambient pressure inside the flasks increases the magnitude of such leaks which would have been negligible were the flasks filled to atmospheric pressure. The number of rejected O<sub>2</sub> flask samples (prior to data analyses) collected at several locations within the MPI-BGC network is very large, with an average of about 40%. This value, however, is usually not reported when comparisons between flask and continuous data are made. In addition, as large standard deviations between the remaining flasks and continuous measurements are masked by calculations of standard errors ( $\frac{stdev}{\sqrt{n}}$ , where  $n$  is the number of samples) determined from large datasets, this very problematic issue remains practically unknown and thus unaddressed. In contrast to the pressurised MPI-BGC flask network the number of rejected flask samples in the O<sub>2</sub> flask sampling network run by SIO is only ~15%, which also includes post-analysis rejections (R. Keeling, SIO, pers. comm., 2009). When applied to the flasks collected at ZOTTO these problems were amplified due to their extended storage prior to analyses.

Despite the limitations mentioned above, flask sample collection represents an independent tool for evaluating the calibration scale accuracy at a remote location, which is particularly important for newly established measurement programs. The retrospective recalculation of all ZOTTO WSS calibrations performed in 2008 was made with the assumption that the initial values assigned to all WSS cylinders at the beginning of ZOTTO measurements in 2005 were erroneous and no additional effects were accounted for. To address the limitation of this method I performed an additional analysis of the flask sample measurements from ZOTTO. Following Langenfelds *et al.* [2005], I applied an Ar/N<sub>2</sub> correction to all flask O<sub>2</sub> measurements according to equation:

$$O_2 / N_{2cor} = O_2 / N_{2meas} - 0.4 \times (Ar / N_{2meas} - Ar / N_{2ambient}), \text{ where} \quad (5.2)$$

$O_2 / N_{2cor}$  is the corrected O<sub>2</sub>/N<sub>2</sub> ratio of the sample (presumed to be equal or close to the ambient O<sub>2</sub>/N<sub>2</sub> ratio at the time of the sample collection);  $O_2 / N_{2meas}$  is the measured O<sub>2</sub>/N<sub>2</sub> ratio of the sample at the time of the sample analysis; ‘0.4’ is a scaling factor of the Ar/N<sub>2</sub> mass dependent fractionation with respect to O<sub>2</sub>/N<sub>2</sub>;  $Ar / N_{2meas}$  is the measured Ar/N<sub>2</sub> ratio of the sample at the time of the sample analysis; and  $Ar / N_{2ambient}$  is the (assumed constant) ambient Ar/N<sub>2</sub> ratio at ZOTTO.

In other words, if any O<sub>2</sub>/N<sub>2</sub> fractionation occurred over a flask’s storage period, it is assumed that its effect would be 2.5 times more prominent when applied to Ar/N<sub>2</sub>

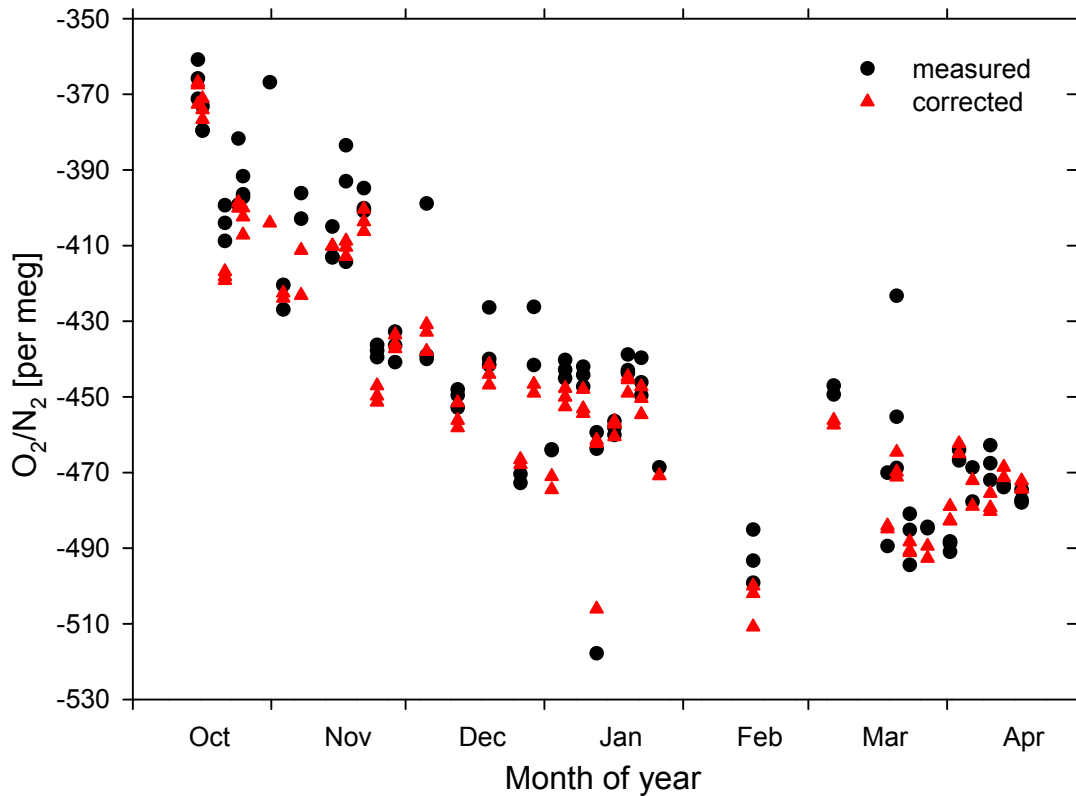


**Figure 5.4:** Measured (black circles) and corrected (red triangles)  $O_2/N_2$  ratios from flask samples collected at ZOTTO from Oct 2006 to May 2007. Total amount of flasks collected: 120. Number of flasks used for analysis: 93 and 79 after and before the  $Ar/N_2$  correction respectively. Initially rejected flask samples (lost pressure, failed measurements or very high  $Ar/N_2$  ratios): 22 (18.3%). Flask samples rejected at a later stage as not meeting the data selection criterion (maximum standard deviation of a triplet/duplicate set  $\leq 10$  per meg): 5 and 19 after and before the  $Ar/N_2$  correction respectively. Total percentage of air samples excluded after and before the correction: 27 (22.5%) and 41 (34.2%).

ratios. Thus the approach enables one to quantify the long-term storage effects often observed in pressurised flasks. Nevertheless, the approach relies on the assumption that all changes in ambient  $Ar/N_2$  are negligible. This assumption is based on the fact that seasonal variations in  $Ar/N_2$  atmospheric ratios are usually small, from just a few per meg to a maximum range of 10-20 per meg [Keeling *et al.*, 2006], with other variations being much smaller than seasonal ones. In applying equation 5.2 to ZOTTO data, I assumed an ambient  $Ar/N_2$  ratio of 13 per meg which is the average value for the samples collected at Alert, Canada (R. Keeling, pers. comm., 2009). I chose the Alert, station since it is the station in the SIO network with closest characteristics to ZOTTO, namely a high latitude station in the northern hemisphere. As ZOTTO is situated in the middle of a large continent and any changes in  $Ar/N_2$  ratios are normally associated with changes in their oceanic fluxes, it is unlikely that any significant errors would be introduced from seasonal variations of  $Ar/N_2$ . Although no measurements of  $Ar/N_2$  ratios exist in the area close to ZOTTO, the model simulations (from 9 different models)

for the continental interiors of Eurasia showed maximum seasonal peak-to-peak amplitudes of 5-10 per meg (Fig.3.13 [Blaine, 2005]).

Figure 5.4 shows measured and corrected O<sub>2</sub>/N<sub>2</sub> ratios in flask samples from October 2006 to May 2007. The main feature seen in the Figure is the reduced measurement scatter (between triplicates/duplicates) after applying the Ar/N<sub>2</sub> correction. The mean standard deviations of the triplicates /duplicates were 6.4 per meg and 3.4 per meg before and after the correction respectively. These results show that at least half of the observed scatter between the triplicates is caused by O<sub>2</sub>/N<sub>2</sub> fractionation problems, and provides much confidence for the correction procedure itself. The corrected mean values of the triplicates show slightly lower values than those of the uncorrected data.

Another important consequence of the Ar/N<sub>2</sub> correction is that the number of flasks which were rejected based on the selection criterion (see Fig. 5.4 caption) was reduced from 19 (before) to 5 (after) the correction. This is the direct consequence of the smaller mean standard deviation of the samples as more flasks met the selection criterion. This is particularly important for a small dataset of samples (e.g., ZOTTO). A similar improvement was obtained when the same correction was applied to the SIS O<sub>2</sub> dataset, which was characterised by large scatter and a significant number of rejected samples prior to correction. Unfortunately, the initial loss of ZOTTO flask samples (18.3%; those which could not even be considered for Ar/N<sub>2</sub> corrections) is still very high and is mainly the result of bad flask handling and faulty valves leading to significant pressure losses.

To define the correction applicable to the continuous measurements at ZOTTO I calculated the linearly-interpolated differences between the latter and the corrected flask samples. This resulted in subtracting a value of 27.6 per meg from all continuous O<sub>2</sub> data from October 2006 to June 2007. Naturally, this method has introduced additional uncertainty to all O<sub>2</sub> data accuracy which is dominated by the standard deviation of the correction itself (~±14 per meg). However, for the purposes of the studies based on this dataset, this correction can be considered to be acceptable as this standard deviation is only slightly larger than the inter-laboratory comparability goal for O<sub>2</sub> measurements (±10 per meg).

Since one of the biggest problems complicating the interpretation of the flask samples measurements, i.e. O<sub>2</sub>/N<sub>2</sub> fractionation, was at least partially addressed and corrected with the method above, I decided to use the corrected data from the flask samples as a proxy for an independent O<sub>2</sub> scale revision at ZOTTO. As the original measurements of ZOTTO O<sub>2</sub> WSS concentrations in 2005 were compromised it is

possible that their retrospective corrections in 2008 did not fully represent the processes occurring in the cylinders (and the analysis system itself) over the 3-year period (2005-2008). In addition, the field tests on the O<sub>2</sub>/N<sub>2</sub> fractionation at Tee junctions (see Chapter 4, Section 4.6) showed that there existed some offsets between different types of sampling lines at ZOTTO (see Chapter 3, Section 3.2.1) thus possibly contributing to the observed differences between the flask and continuous measurements. No flasks were collected over the summer of 2006, which prevented me from extending the above correction to this period as well. In addition, owing to the faulty O<sub>2</sub> sensor, the 2006 summer months were characterised by much noisier O<sub>2</sub> data. After a careful analysis of the TT measurements from May to September 2006 I found that the ZOTTO values were consistently lower than the declared value by ~9.5 per meg. Nevertheless, it was impossible to make final conclusions without the MPI-BGC reanalysis results of this TT cylinder, which proved to be almost identical to the initially assigned values. This provided me with more evidence that the O<sub>2</sub> concentration of this cylinder was very stable over the whole period of the measurements, and allowed me to make a one-time adjustment to the air data. The latter should not, however, become a routine procedure for correcting continuous measurements but rather an exceptional case prompted by the combination of calibration and technical problems at a newly established site. Nevertheless, the observed differences in the instrument responses between the old and the new models of O<sub>2</sub> sensors suggests that there could be possible offsets in the air data as well. Since no flask samples were collected at ZOTTO over summer 2006, the TT comparison represents the only external estimate for the system's comparability with MPI-BGC.

As retrospective corrections to the O<sub>2</sub> data led to changes in the results of their comparison with TM3, I devoted a dedicated section to their discussion, highlighting all similarities and differences from the previous analyses (see Section 5.4.3 below). In addition, the same Ar/N<sub>2</sub> correction procedure was applied to all flask samples collected at SIS, and all subsequent changes in their comparison with ZOTTO data as well as their agreement with TM3 are presented here as well. Unfortunately, the short length of the O<sub>2</sub> record from ZOTTO does not provide me with the ultimate evidence in support (or against) the analyses that helped me to estimate the corrections described above. Nevertheless, all the consequent analyses that were necessary to correct the data with the highest possible degree of confidence, have additionally demonstrated the challenge of making high-precision atmospheric measurements at such remote location as well as the necessity of the extreme care and meticulous measures to be taken when transferring the O<sub>2</sub> scale from the laboratory to the remote field site. Also, additional field testing of

the sampling lines and analysers proved to be necessary to provide the integrity and credibility of the long-term O<sub>2</sub> calibration scale.

#### **5.4.2 Seasonal variations of CO<sub>2</sub>, O<sub>2</sub> and APO from the revised data records at SIS and ZOTTO**

Section 5.4.1 above describes the revisions (and the reasons why they were applied) that were made to the ZOTTO O<sub>2</sub> calibration scale in 2009. This section provides a brief summary on how the results and conclusions from the previous seasonal cycle analyses (Section 5.3) have changed since those revisions were made to the ZOTTO and SIS O<sub>2</sub> data records.

Figure 5.5 shows the seasonal cycles of CO<sub>2</sub>, O<sub>2</sub> and APO at ZOTTO (red fitted curves and yellow bands) and SIS (blue fitted curves and bands). The data selection, curve fitting and presentation of the data are identical to those shown in Fig. 5.1 and discussed in Section 5.3. No changes were made to ZOTTO CO<sub>2</sub> data (top panel in Fig. 5.5). The Ar/N<sub>2</sub> correction was applied to all flask samples at SIS resulting in significantly smoother fitted curves with smaller error bands for O<sub>2</sub> and APO. In addition, the SIS fitted curves shown in Fig. 5.5 were calculated based on longer datasets (up to Sept 2009) than those in Fig. 5.1. Because of this the average CO<sub>2</sub> seasonal amplitude at SIS has slightly changed from 15.5 ppm to 15.4 ppm. The Ar/N<sub>2</sub> correction to SIS O<sub>2</sub> data has made a large impact on the number of flask samples that were included in the fitting procedure due to the reduced scatter, and resulted in a reduction of the O<sub>2</sub> seasonal amplitude from 163 to 127 per meg. In addition to the amplitude change, the O<sub>2</sub> seasonal maximum has shifted to late August (from late July – early August in Fig. 5.1), which coincides with the summer CO<sub>2</sub> minimum at SIS. The O<sub>2</sub> minimum also occurs later now, in the middle of March rather than late February – early March as seen in Fig. 5.1. The changes in O<sub>2</sub> amplitude and phasing have influenced those of APO. In Fig. 5.5 the revised APO amplitude is 56 per meg (compared to 95 per meg in Fig. 5.1). Such a large reduction in the APO amplitude at SIS is the direct consequence of the decreased O<sub>2</sub> amplitude.

After the revision, ZOTTO O<sub>2</sub> seasonal amplitude has increased from 134 to 190 per meg. Consequently, the July O<sub>2</sub> concentrations at ZOTTO are about 40 per meg above the SIS O<sub>2</sub> (whose maximum has shifted to August), which corresponds and can be attributed to about 8 ppm of CO<sub>2</sub> uptake by terrestrial biota over Eurasia. This means that the observed west-east gradient of 7 ppm (difference between July CO<sub>2</sub> concentrations at SIS and ZOTTO) can be explained by the continental uptake by terrestrial biota. The late February – beginning of March O<sub>2</sub> minimum at ZOTTO is

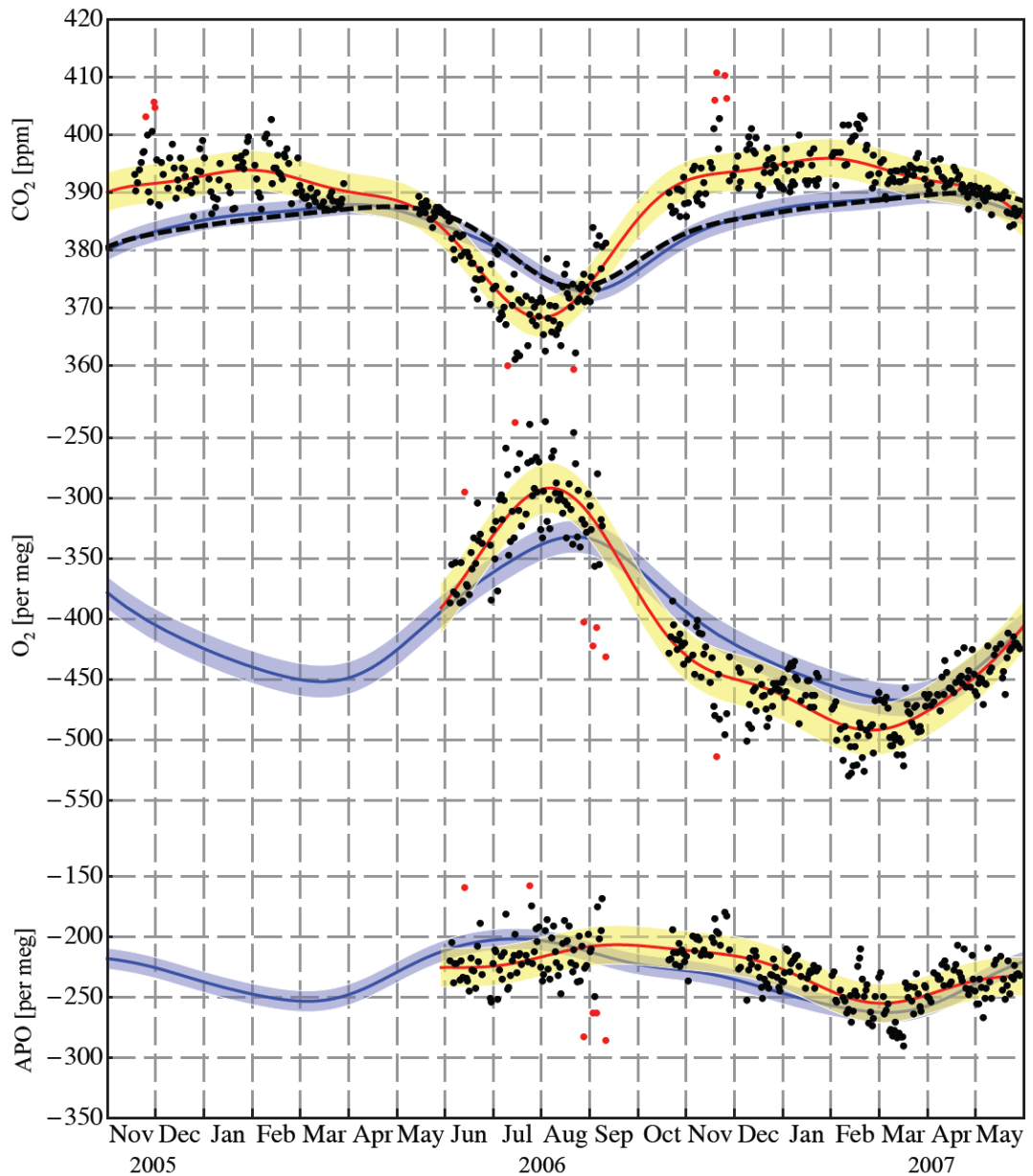


**Figure 5.5:** Seasonal cycles of  $\text{CO}_2$ ,  $\text{O}_2$  and APO from 52 m height of the ZOTTO tower based on the revised  $\text{O}_2$  dataset. The y-axis scales of all three panels have been adjusted so that visually, changes in  $\text{CO}_2$  (ppm), and  $\text{O}_2$  and APO (per meg), are directly comparable on a mole to mole basis. Black and red points on all three panels show trimmed daytime averages of measurements between 11:00 and 17:00 (local standard time: UTC + 7 hr). The fit functions (red lines) were computed iteratively from the trimmed daytime averages. Yellow bands on all panels denote  $\pm 1$  standard deviation of the residuals of the trimmed daytime averages from the fit functions. For comparison, the blue lines and bands show similar fit functions and  $\pm 1$  standard deviation of the residuals from flask measurements ( $\sim$ weekly frequency) from SIS (60.28°N, 1.28°W). The black dashed line on the  $\text{CO}_2$  panel shows the ‘marine boundary layer reference’ concentration at 60°N as given in the GLOBALVIEW- $\text{CO}_2$  database [2007] (linearly extrapolated after 01 Jan 2007).  $\text{CO}_2$  data are reported on the NOAA/WMO X2005 scale, and  $\text{O}_2$  and APO data are reported on the SIO scale with the corrections as discussed in the text.

now also lower than the SIS  $\text{O}_2$  record (whose minimum lags the ZOTTO  $\text{O}_2$  minimum by  $\sim 2$ -3 weeks) by about 29 per meg, which could be the result of the continental fossil

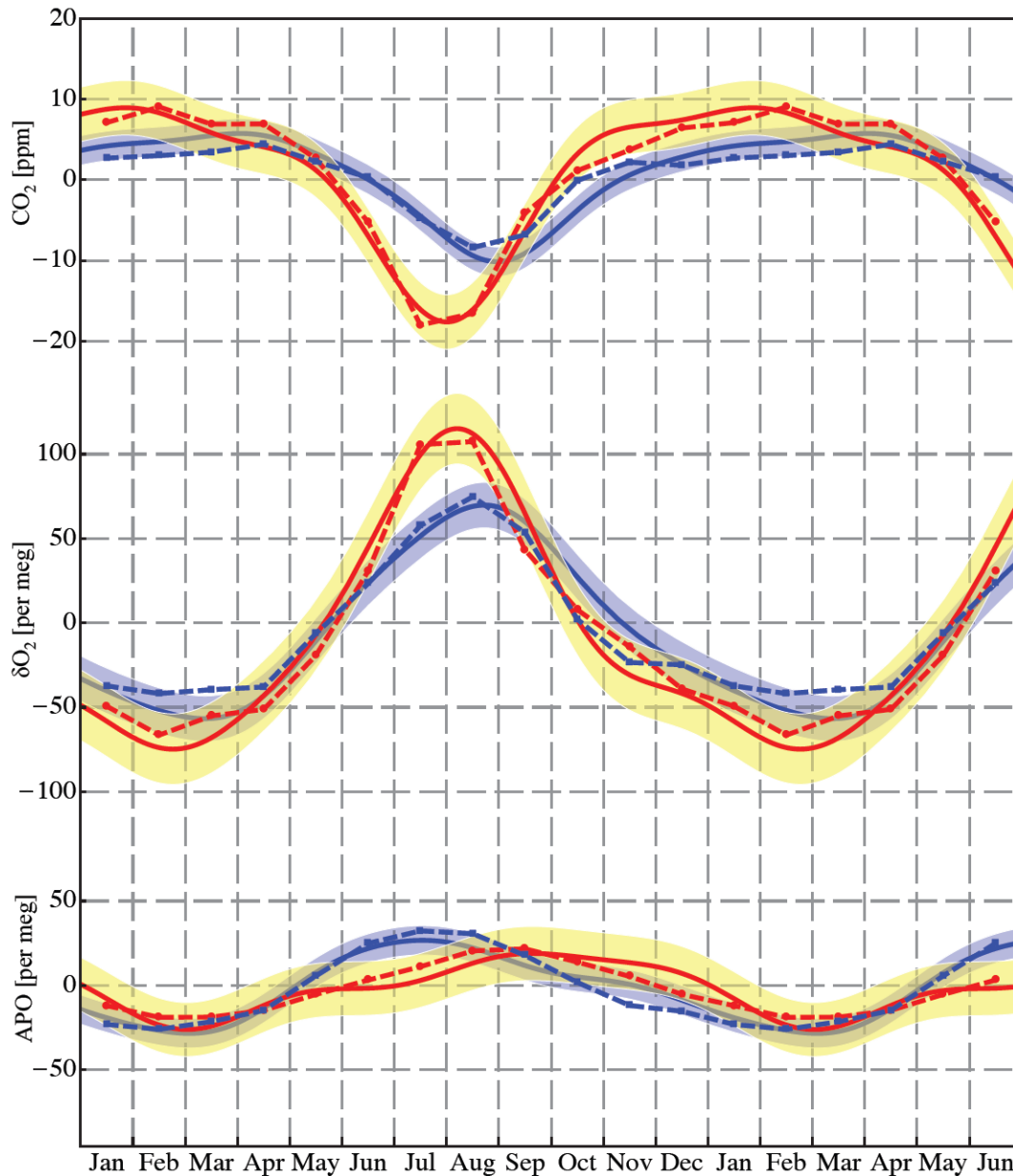


**Figure 5.6:** Seasonal cycles of  $\text{CO}_2$ ,  $\text{O}_2$ , and APO from model results (dashed lines) and fit functions to the revised observations (solid lines) at ZOTTO (red lines) and SIS (blue lines). Seasonal cycles were obtained by subtracting the linear trends and annual means from the fit functions of the observations and the model results. The yellow (ZOTTO) and light blue (SIS) bands denote  $\pm 1$  standard deviation of the residuals of the daytime averages from the fit functions (the same as for Fig. 5.5). For visual clarity, the first 6 months are repeated, and all species can be compared visually on a mole to mole basis.

fuel  $\text{O}_2$  sink. Despite the larger  $\text{O}_2$  amplitude (and no changes in  $\text{CO}_2$ ) the APO seasonal amplitude at ZOTTO has decreased from 51 to 45 per meg which reflects the significant differences in phasing between  $\text{O}_2$  and APO. The APO seasonal cycle still suffers from a 2-month gap in the observations in Sept-Oct 2006, and it has become much more apparent from the revised dataset that my previous hypothesis about the ‘missed’ APO maximum (due to tower construction) that might have occurred over this period is

plausible. Nevertheless, the 2-month lag between the APO maxima at SIS and ZOTTO (assuming that the latter occurred in Sept) is still not well understood. The APO minimum is also much better defined in Fig. 5.5; its timing coincides with the O<sub>2</sub> maximum at ZOTTO.

### 5.4.3 Comparison with TM3 model simulations

The model simulations shown in Figure 5.6 are identical to those in Figure 5.3. Thus all changes in model-observations comparisons are a result of the revisions made to both SIS and ZOTTO observations. No changes in comparison results have occurred for CO<sub>2</sub> records at either station. The revision of SIS O<sub>2</sub> dataset has resulted in significant improvement in the agreement between the observed (163 and 127 per meg before and after revision respectively) and modelled (120 per meg) O<sub>2</sub> amplitudes. A discrepancy of about 15 per meg still exists at the minima of the observed and modelled fitted curves in February – March, which was also the case before the revision. However, these discrepancies do not appear in the APO model-observations comparison, which has also improved, similarly to O<sub>2</sub>, after the SIS flask sample revision.

In the case of ZOTTO, the agreement between the observed and modelled O<sub>2</sub> seasonal phasing and amplitudes (middle panel in Fig. 5.6) has dramatically improved with the revised dataset. As the observed O<sub>2</sub> amplitude has increased to 190 per meg it has become more comparable to the model estimate of 177 per meg. Although, the agreement between the observed and modelled fitted curves has improved over the whole studied period, it is most apparent in both phasing and amplitude at the end of July – beginning of August, when the maximum of the revised O<sub>2</sub> seasonal amplitude occurs. The same tendency has been observed for the revised APO data – model comparison (bottom panel in Fig. 5.6). The biggest improvement on the model-observations agreement has been observed on the phasing of the observed and modelled APO amplitudes. Both APO fitted curves exhibit clear minima in February - March. The APO maximum is predicted (by the model) to occur in late August – beginning of September, which is about 2 months after the modelled SIS APO maximum (middle of July). The observed and modelled APO amplitudes at ZOTTO (45 and 42 per meg) also show smaller discrepancies compared to their estimates before the revision (51 and 42 per meg respectively).

## 5.5 Seasonal variations of CH<sub>4</sub> and CO

The importance of continuous monitoring of CH<sub>4</sub> concentrations at ZOTTO has been discussed already in Chapter 1, Section 1.5.3. So far, very few continuous CH<sub>4</sub>

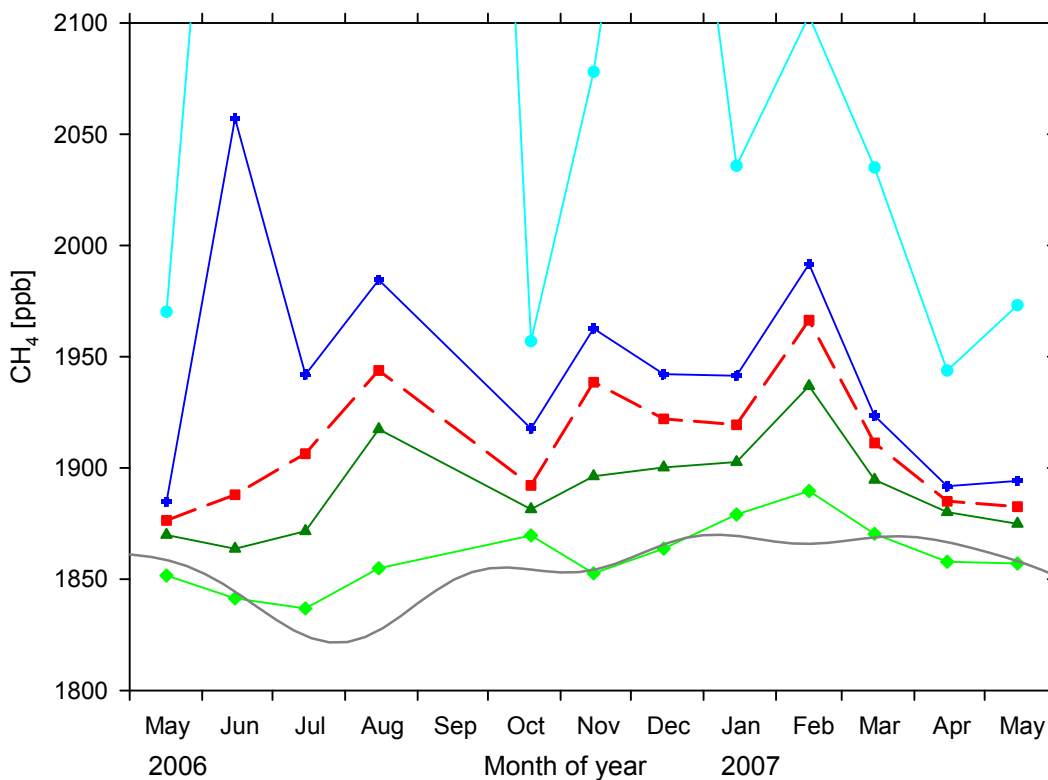


**Figure 5.7:** Seasonal variations of CH<sub>4</sub> concentrations at ZOTTO from May 2006 to June 2007 shown as monthly statistics: minimum (light green diamonds and line), 25<sup>th</sup> percentile (dark green triangles and line), median (red squares and dashed line), 75<sup>th</sup> percentile (blue crosses and line) and maximum (cyan circles and line). A marine boundary layer reference is shown with grey solid line and represents weekly average CH<sub>4</sub> concentrations from the GLOBALVIEW database at ~58°N [GLOBALVIEW-CH<sub>4</sub>: Cooperative Atmospheric Data Intergration Project - Methane. CD-ROM]. All monthly statistics are displayed at the middle of the respective month.

measurements have been made at high-latitudes, close to wetlands, one of the largest natural sources of CH<sub>4</sub>. Existing flask sampling programs mainly include the background and coastal stations, leaving the high latitudes and continental interiors under-represented in the global observation network. In spite of this under-representation, some studies [e.g. *Worthy et al.*, 1998] showed the importance of extending similar observational efforts to the mid-continent. *Worthy et al.* [1998] reported significant differences in seasonal variations (based on 7 years of measurements) of CH<sub>4</sub> concentrations as observed at Fraserdale (Canada) compared to Cold Bay (Alaska) despite the fact that both sites are situated at a similar latitude. The former location is characterised by higher (~15 ppb) CH<sub>4</sub> concentrations throughout the year, representing a continental CH<sub>4</sub> emission offset. In addition, a very distinctive second maximum was observed in the Fraserdale CH<sub>4</sub> concentration record in late summer, which was attributed to emissions from large areas of wetlands in the vicinity of the site.

The ZOTTO CH<sub>4</sub> concentration record is, unfortunately, only one-year long, which clearly prevents such in-depth data analyses as performed by Worthy *et al.* [1998]. Nevertheless, some interesting and important features can already be investigated and discussed.

Figure 5.7 shows monthly means of CH<sub>4</sub> concentrations from May 2006 to June 2007. The figure illustrates the statistical distribution of monthly means by presenting their minimum, 25<sup>th</sup> percentile, median, 75<sup>th</sup> percentile and maximum values. To calculate monthly means, I used all CH<sub>4</sub> measurements from the 52 m height as it provides the longest data record. The data selection procedure is different from that used for CO<sub>2</sub> and O<sub>2</sub> analyses in Sections 5.3 and 5.4.2 as the ZOTTO observation records of CH<sub>4</sub> and CO were significantly influenced by very high summertime concentrations from fires.

In Sections 5.3 and 5.4.2, I presented flask sample measurements from SIS as a marine reference site situated at a similar latitude to ZOTTO. In this section, I use a ‘marine boundary layer’ reference (grey solid line in Figure 5.7) as given in the GLOBALVIEW database [*GLOBALVIEW-CH<sub>4</sub>: Cooperative Atmospheric Data Integration Project - Methane. CD-ROM*] at 58°N instead of the SIS data, as the latter show very large scatter that might have been caused by complex local CH<sub>4</sub> sources and thus prohibiting its usage as a marine reference. Figure 5.7 shows high variability of CH<sub>4</sub> concentrations, with summertime monthly maxima off the scale, reaching up to ~2300 and 3400 ppb in July and August 2006 respectively. December and February monthly means were also characterised by very high maxima of ~2300 and 2100 ppb respectively. In summertime, high CH<sub>4</sub> concentrations were the result of emissions from large boreal fires, some of which were very close to ZOTTO. Section 6.6 discusses emission ratios of trace gases, including CH<sub>4</sub>/CO<sub>2</sub>, observed at ZOTTO during fires in summer 2006. All fire events studied were characterised by high concentrations of CH<sub>4</sub> that masked contributions from other sources (e.g. wetlands) during mid and late summer 2006. High CH<sub>4</sub> concentrations in wintertime can be attributed to local (or distant) pollution events (two of which are analysed in more detail in Section 5.6.2 below) which are characterised by high CH<sub>4</sub>/CO<sub>2</sub> emission ratios.

In contrast to their maxima, monthly minima of CH<sub>4</sub> observations are very close to the concentrations of the marine boundary layer throughout the year. Both records (ZOTTO monthly minima and marine boundary reference) showed no significant increase in CH<sub>4</sub> over the 12-month period studied. Similarity of these two records can be explained by the fact that ZOTTO monthly minima characterise clean background air, mostly free of any local effects, thus making them comparable with the marine

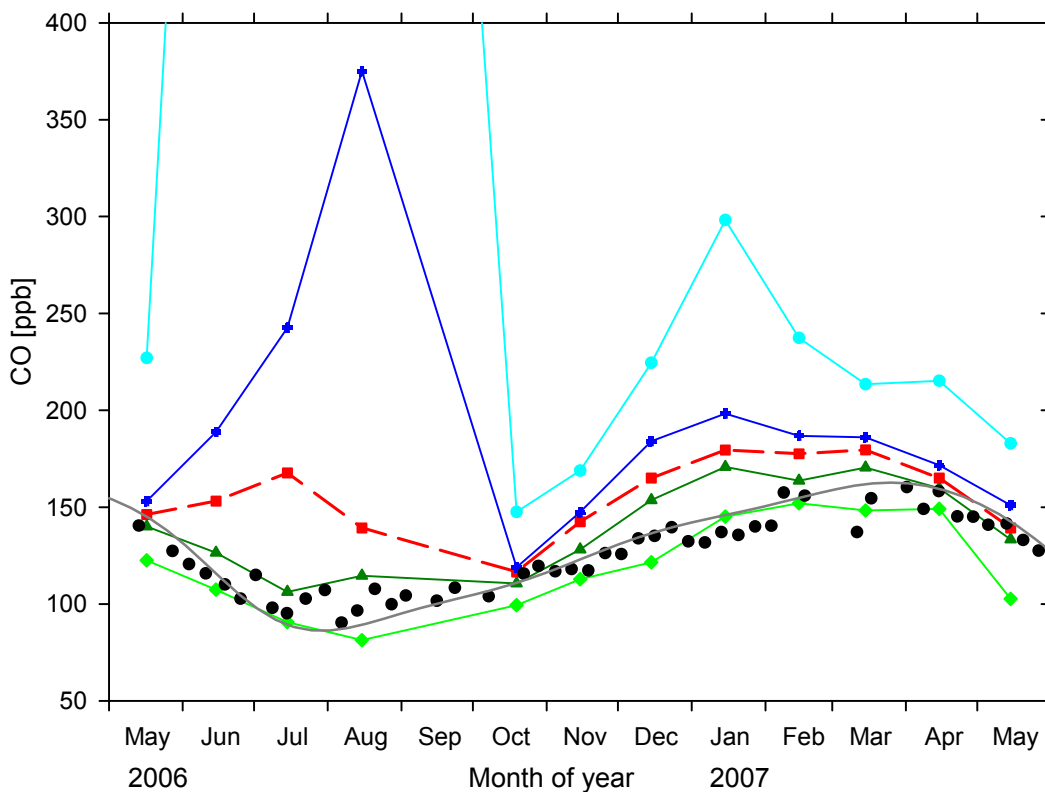


**Figure 5.8:** Seasonal variations of CO concentrations at ZOTTO from May 2006 to June 2007 shown as monthly statistics: minimum (light green diamonds and line), 25<sup>th</sup> percentile (dark green triangles and line), median (red squares and dashed line), 75<sup>th</sup> percentile (blue crosses and line) and maximum (cyan circles and line). Black circles represent the weekly averages of CO concentrations at SIS. A marine boundary layer reference is shown with grey solid line and represents weekly average CO concentrations from the GLOBALVIEW database at ~58°N [*GLOBALVIEW-CO: Cooperative Atmospheric Data Intergration Project - Carbon Monoxide. CD-ROM*].

boundary layer reference. Owing to high variability of CH<sub>4</sub> concentrations, it is difficult to reliably estimate the seasonal cycle of CH<sub>4</sub> for this particular year at ZOTTO. It is clear, however, that both fires and pollution significantly contributed to seasonal variability of CH<sub>4</sub> in the area around ZOTTO. Nevertheless, the ZOTTO minima curve shows a well-defined minimum in July 2006 despite very large overall variability (seen in other data percentiles) caused by fires. This is in good agreement with the minimum of the marine boundary reference in late July. With regard to seasonal maxima, the ZOTTO minima curve shows two in Oct 06 and Feb 07, which is somewhat similar to the seasonal patterns of the marine boundary layer reference.

A longer data record would considerably facilitate its interpretation, however, the discussion above clearly demonstrates that even the short record available can provide insightful information thus emphasising the importance of CH<sub>4</sub> measurements at ZOTTO.

Figure 5.8 shows variations of CO concentrations as observed at ZOTTO from May 2006 to June 2007. Data selection and presentation are identical to those in Figure

5.7 except that I also plotted weekly averages of CO concentrations at SIS (black circles) in addition to the marine boundary layer reference [*GLOBALVIEW-CO: Cooperative Atmospheric Data Integration Project - Carbon Monoxide. CD-ROM*]. In contrast to CH<sub>4</sub>, CO concentrations at SIS do not exhibit large variability and thus are more suitable as reference values for the 60°N latitude. In addition, CO concentrations at SIS appear to be very similar to those of the marine boundary layer reference, both in phasing and amplitude, with an offset of less than 10 ppb (with higher values at SIS) throughout the period studied. The latter provides me with additional confidence for using both of these records as marine references.

Similar to CH<sub>4</sub>, monthly minima of CO concentrations at ZOTTO show very good agreement to those at SIS and the marine boundary layer reference. Both of the latter show a distinctive seasonal minimum in mid July, with the ZOTTO minimum lagging by ~1 month. All three curves show an approximate 4-month period in winter – beginning of spring with consistently high CO concentrations (Jan-Apr 2007) and a subsequent rapid decrease in May. This is as expected since seasonal variations of CO concentrations are mainly driven by the availability of OH radicals that is directly proportional to sunlight and amount of water vapour, both of which increase in spring. Good agreement between the three records above shows robustness of the selected method of using the minima of the ZOTTO monthly means as proxies for background CO concentrations. A small offset (with lower values at ZOTTO) is most probably caused by the fossil fuel CO emissions in Europe. The offset is more apparent in the late winter – beginning of spring (Feb-Apr) with a 3-month plateau in ZOTTO CO concentrations. Section 5.6.2 below presents results from a study of the CO/CO<sub>2</sub> emission ratios from wintertime pollution events at ZOTTO, characterised by considerably lower ratios (and thus CO concentrations) than those reported for western Europe.

Similarly to CH<sub>4</sub>, CO concentrations were highly variable during the summer of 2006 owing to large fires in the vicinity of ZOTTO. The monthly maxima for July and August (off scale in Fig. 5.8) were as high as ~1700 and 1300 ppb respectively. In comparison to the very high concentrations from summer fires the maximum CO concentration in January 2007 was quite low (about 300 ppb), illustrating the dominance of the fire related CO emissions to the seasonal cycle at ZOTTO. Section 6.6 presents results from a study of several fire events in summer 2006, and their comparison with simulations from a regional model. Interestingly, the very high variability of CO concentrations in summertime did not influence the lowest percentile of their monthly means so that they exhibited the expected seasonal minimum, which

provides additional evidence of the background nature of these measurements. I estimated a seasonal cycle of about 71 ppb (with a minimum of ~81 ppb in July and a maximum of ~152 ppb in Feb) at ZOTTO (from the monthly minima shown in Fig. 5.8 (light green)), which is consistent with those observed at SIS and marine boundary layer reference. No significant annual trend was determined from the available dataset.

## 5.6 Synoptic variations

Synoptic variability of trace gas concentrations normally occurs on a rather short temporal scale ranging from a couple of days to weeks and reflecting smaller scale meteorological conditions of a region, including pollution. This is in contrast to ‘background’ measurements which typically represent processes on seasonal temporal scales and continental to hemispheric spatial scales. The multi-species semi-continuous measurements at ZOTTO represent perfect prerequisites for studying such synoptic conditions and meteorological peculiarities of the region.

Owing to short lengths of the concentration records from all five tower heights this discussion is based on analyses of wintertime data. The so-called ‘cold events’ represent one of the most distinguishing synoptic features over the winter of 2006-7. These were the synoptic variations observed in the concentration records of all trace gases and O<sub>2</sub> under very cold (<-30°C), low wind and high pressure conditions at ZOTTO. The first and one of the longest ‘cold events’ was discussed in Kozlova *et al.* [2008], however, several similar periods were observed throughout the winter of 2006/07 and are discussed below.

The second part of this section provides a couple of examples of pollution events detected from the ZOTTO measurements and discusses their O<sub>2</sub>/CO<sub>2</sub>, CO/CO<sub>2</sub> and CH<sub>4</sub>/CO<sub>2</sub> emission ratios, taking into account local meteorological conditions. These discussions are facilitated by back trajectory analyses.

### 5.6.1 ‘Cold events’

Figure 5.9 shows vertical gradients of CO<sub>2</sub> and O<sub>2</sub> over a period of ‘cold events’ on 17-27 November 2006. Very low and decreasing temperatures and wind speeds dominated the whole period (see Figures 6.2b. and 6.3b.). Radiosonde data from the meteorological station at Bor (61.60°N, 90.00°E, ~95 km from ZOTTO) show the development of a strongly stratified temperature inversion layer (Figure 6.10). As seen in Figure 5.9, CO<sub>2</sub> concentrations increased at all three lower levels of the tower while at the top (227 and 300 m) a concurrent decrease in CO<sub>2</sub> concentration was observed. On 20-21 November, the highly stratified air column appeared to break down resulting in a decrease in CO<sub>2</sub> concentrations at the lower heights (52 and 92 m) towards the

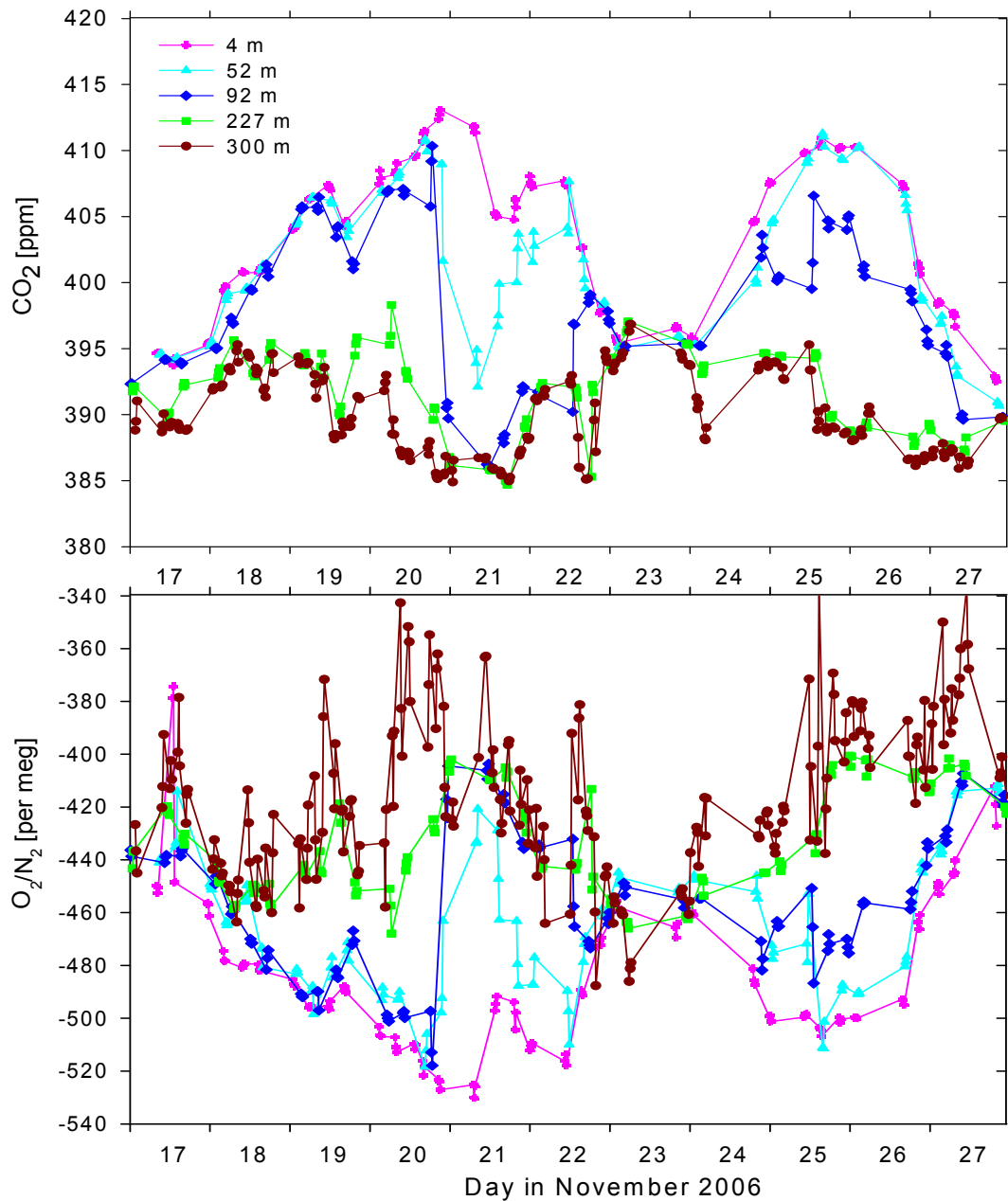


**Figure 5.9:** CO<sub>2</sub> (top panel) and O<sub>2</sub> (bottom panel) variations as measured at five heights of the tower (see legend for height definitions) over a period of ‘cold events’ in Nov 2006. The y-axis scales have been adjusted so that visually, changes in CO<sub>2</sub> (ppm) and O<sub>2</sub> (per meg) are directly comparable on a mole to mole basis. Each data point represents a 4-min average, 16 min apart.

values observed at the top. CH<sub>4</sub> vertical gradients on 18-21 November (data not shown) exhibited a similar pattern: CH<sub>4</sub> concentrations at 227 and 300 m decreased while a concurrent increase occurred at 4, 52 and 92 m, however, with a 1-2 day lag relative to CO<sub>2</sub>. In Figure 5.9, no CO<sub>2</sub> vertical gradient can be seen on 23 November, when temperature increased, followed by the second cold period which resulted in a similar gradient.

O<sub>2</sub> concentrations observed over this period mirror those of CO<sub>2</sub>. However, O<sub>2</sub> measurements at 300 m appear to be much more variable than those at the other heights. This variability does not seem to be caused by any natural factors but rather believed to be an artefact (only observed under very cold conditions) that was most probably caused by a long residence time of air (~30 min) inside the 320-m long Synflex tubing. Similar variability was observed during the following ‘cold events’ under similar weather conditions (not shown). The problem was finally solved in February 2007 when I switched to using a different sampling line of a larger diameter allowing for higher flowrate and thus shorter air residence time inside the tubing (see also Chapter 4, Section 4.6).

The build-up of CO<sub>2</sub> at the lower levels can not be explained by local anthropogenic emissions (diesel generators and wood burning) since concurrent CO measurements did not show any significant increase. Previous workers have observed haze formation under very low wind and cold conditions during winter at ZOTTO (E.-D. Schulze, MPI-BGC, pers. comm., 2007). During these events, the air column from the bottom to the top of the tower may be divided into two separate layers, each with independent air circulation patterns. While at the lower levels CO<sub>2</sub> could increase as the result of local respiration, which can occur even under very cold conditions [Zimov *et al.*, 1993], and/or diffusion of CO<sub>2</sub> through the soil after frost, the upper levels of the tower could show a concurrent decrease since mixing with the higher CO<sub>2</sub> concentration at the bottom is restricted. Unfortunately, we did not have *in situ* soil temperature measurements during the winter of 2006/07, however, at the nearby flux tower site (60.73°N, 89.15°E) the soil temperature at 10 cm depth never decreased to less than -10°C during 6 years (1998-2004) of measurements [Shibistova *et al.*, 2002a], which could confirm the potential contribution of soil respiration to the CO<sub>2</sub> build-up near the ground. Figure 5.9 shows that the CO<sub>2</sub> concentrations increased at the lower levels faster than they decreased at the top. The vertical integral of CO<sub>2</sub> concentrations over the height of the tower showed an increase of about 3000 ppm m during the 3-4 day build-up phase of both cold events. If I assume that this increase is entirely due to a local ground source, then this corresponds to a source flux of about 0.36 – 0.48 μmol C m<sup>-2</sup> s<sup>-1</sup> (0.03 - 0.04 mol C m<sup>-2</sup> d<sup>-1</sup>). Early wintertime CO<sub>2</sub> respiration fluxes of similar magnitude were observed at a nearby flux tower site in 1999 [Shibistova *et al.*, 2002b] and from soil respiration flux measurements in north-eastern Siberia [Zimov *et al.*, 1993].

An initial build-up of CH<sub>4</sub> occurred similarly at all heights on November 17-18, with the development of a concentration gradient beginning only on 19 November (not

shown). This contrasting behaviour between CO<sub>2</sub> and CH<sub>4</sub> demonstrates that the two gases do not have identical local source patterns, with CH<sub>4</sub> likely having a more heterogeneous source distribution. This would be expected if the observed CH<sub>4</sub> concentration increases resulted primarily from CH<sub>4</sub> outgassing from the waterlogged bogs surrounding the ZOTTO site.

In an attempt to understand the observed phenomena, I performed an analysis of O<sub>2</sub>/CO<sub>2</sub> exchange ratios over the 10 day period shown in Figure 5.9. Interestingly, at lower levels (4, 52 and 92 m) the O<sub>2</sub>/CO<sub>2</sub> ratios were very low (0.93±0.04, 0.87±0.04 and 0.90±0.03). In contrast, the top levels of the tower were characterised by higher ratios of 1.19±0.05 and 1.29±0.11 respectively. As expected, the 300 m estimate has the largest uncertainty owing to the high O<sub>2</sub> variability discussed above. These results point favourably towards the hypothesis of having two separated air layers characterised by different gas exchange ratios. A hypothesised additional consequence of these unusual meteorological conditions is a gravitational separation of gases over the air column based on their molecular mass differences [Adachi *et al.*, 2006] that occur only under very cold conditions. As the CO<sub>2</sub> molecule is heavier than air, higher CO<sub>2</sub> concentrations would be expected closer to the ground, resulting in lower O<sub>2</sub>/CO<sub>2</sub> ratios as I observed. In addition, estimates of O<sub>2</sub>/CO<sub>2</sub> ratios from the three lower levels of the tower are too low for any known process involving O<sub>2</sub> and CO<sub>2</sub> exchanges; whilst under the latter hypothesis they could have been the result of the molecular separation at very cold temperatures.

Further investigation of wintertime data showed that such ‘cold events’, although observed under quite specific meteorological conditions, were not uncommon at ZOTTO. Figure 5.10 shows vertical gradients of CO<sub>2</sub> and O<sub>2</sub> over another 10 days of very cold weather conditions in Feb 2007. Temperatures as low as -40°C, with a clear increasing trend towards the end of the month (up to -22°C on 24 Feb), were recorded at Bor station (bottom plot in Fig. 5.10). Interestingly, the increasing trend in temperature was mirrored by CO<sub>2</sub> concentrations which demonstrated strong vertical gradients and significant increases at the bottom of the tower and concurrent depletion at the top only when temperatures were below -30°C. As soon as air temperatures warmed up to about -22°C the vertical gradients decreased dramatically. Similar patterns were observed in O<sub>2</sub> concentrations as well. This was most probably due to the fact that the temperature increase was accompanied by higher wind speeds (an increase from close to zero to ~2-4 m/s was recorded at Bor) resulting in stronger mixing and thus smaller concentration gradients.

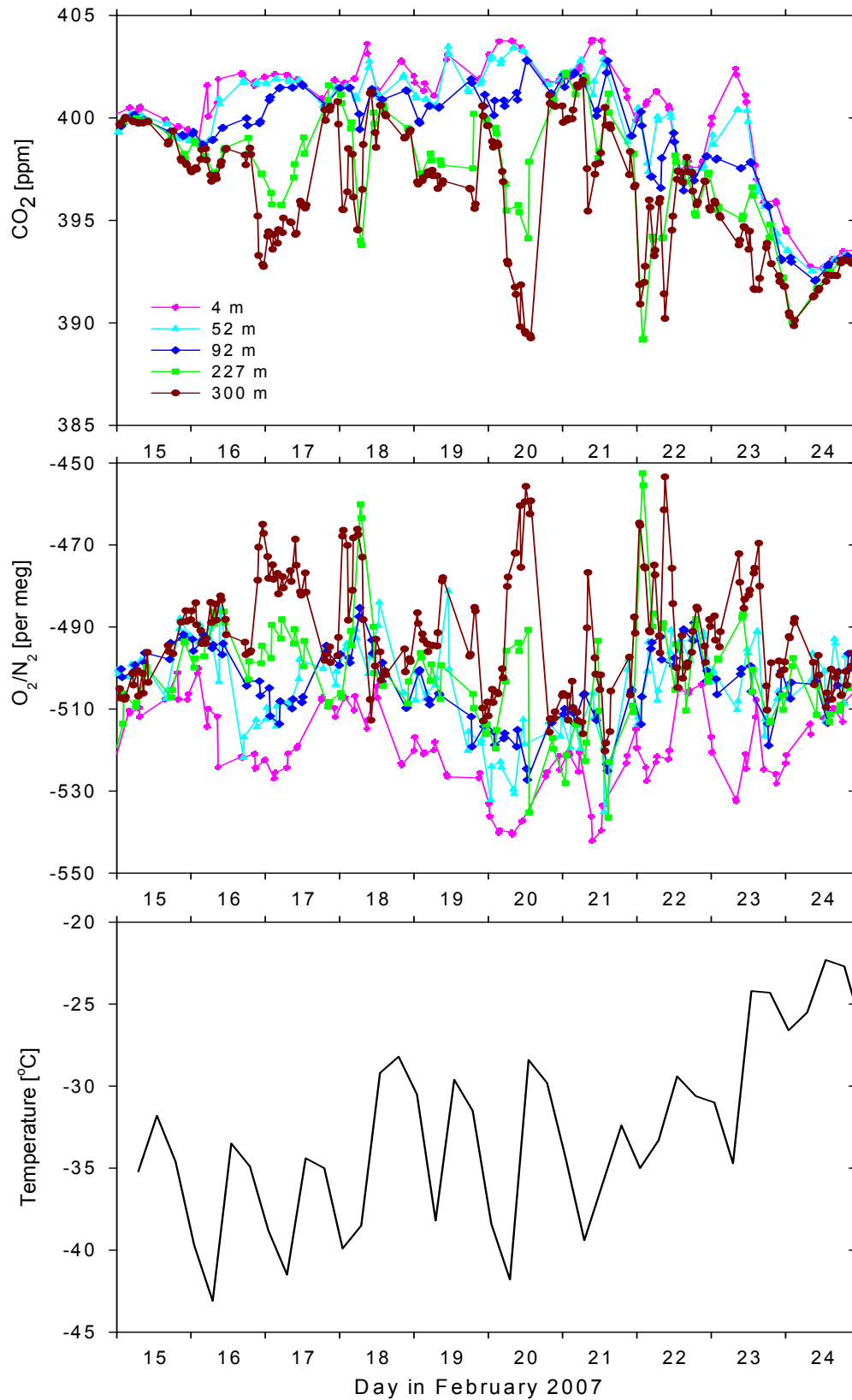


**Figure 5.10:** CO<sub>2</sub> (top panel), O<sub>2</sub> (middle panel) and temperature variations (at Bor station) over a period of ‘cold events’ in February 2007. Changes in CO<sub>2</sub> (ppm) and O<sub>2</sub> (per meg) are directly comparable on a mole to mole basis. For CO<sub>2</sub> and O<sub>2</sub> each data point is a 4-min average, 16 min apart.

Figure 5.11 shows O<sub>2</sub> and CO<sub>2</sub> correlation plots over the same period of ‘cold events’

for each height separately (plots a. through e.). An apparent separation of the data points into two distinct clusters seen in all plots precludes any robust estimates of  $O_2/CO_2$  ratios. The different clusters probably reflect the vertical distribution of  $O_2$  and  $CO_2$  concentrations over periods of very strong stratification and those with stronger vertical mixing. Figure 5.10 shows that the magnitudes of the  $CO_2$  depletion/accumulation cycles at the top/bottom levels were not constant but rather alternating. This pattern appears to be roughly in correlation with diurnal temperature variations (Fig. 5.10, bottom panel), with two minima in  $CO_2$  concentrations at 227 and

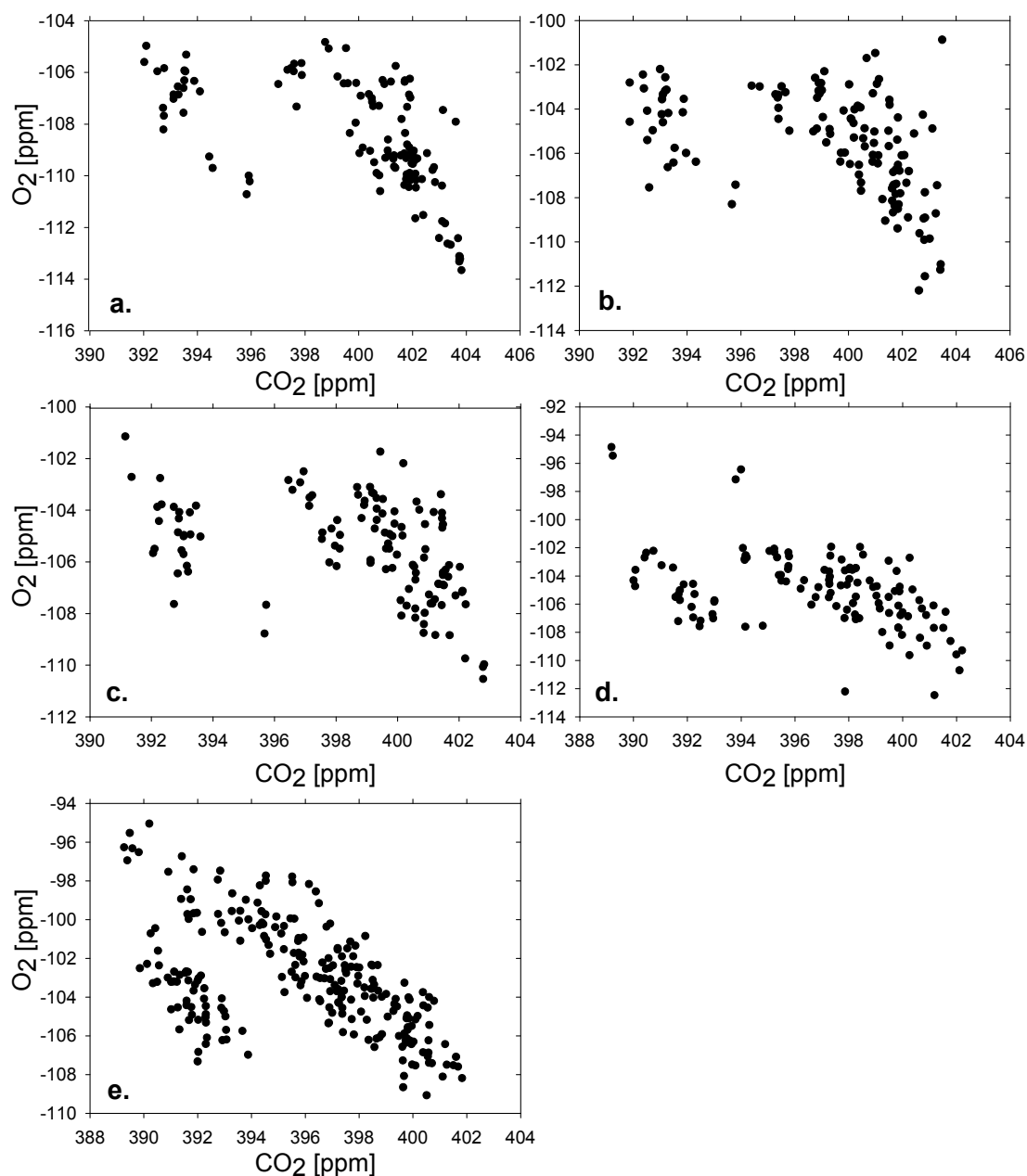


**Figure 5.11:**  $O_2$  (y-axis) and  $CO_2$  (x-axis) concentration correlations as observed from five levels of the ZOTTO tower: 4, 52, 92, 227 and 300 m (a. through e. respectively) from 15 to 25 Feb 2007. Both  $O_2$  and  $CO_2$  are in units of ppm.

300 m (16-17 and 20 Feb), which also correspond to the coldest temperatures over this period.

Figure 5.12 shows CH<sub>4</sub> and CO variations over the same ‘cold events’ in Feb 2007. The concentrations of both gases follow the same pattern as that for CO<sub>2</sub> except on 18 Feb, when large upward excursions were observed at 4, 227 and 300 m in both concentration records. The observed vertical distribution of CH<sub>4</sub> and CO undermines

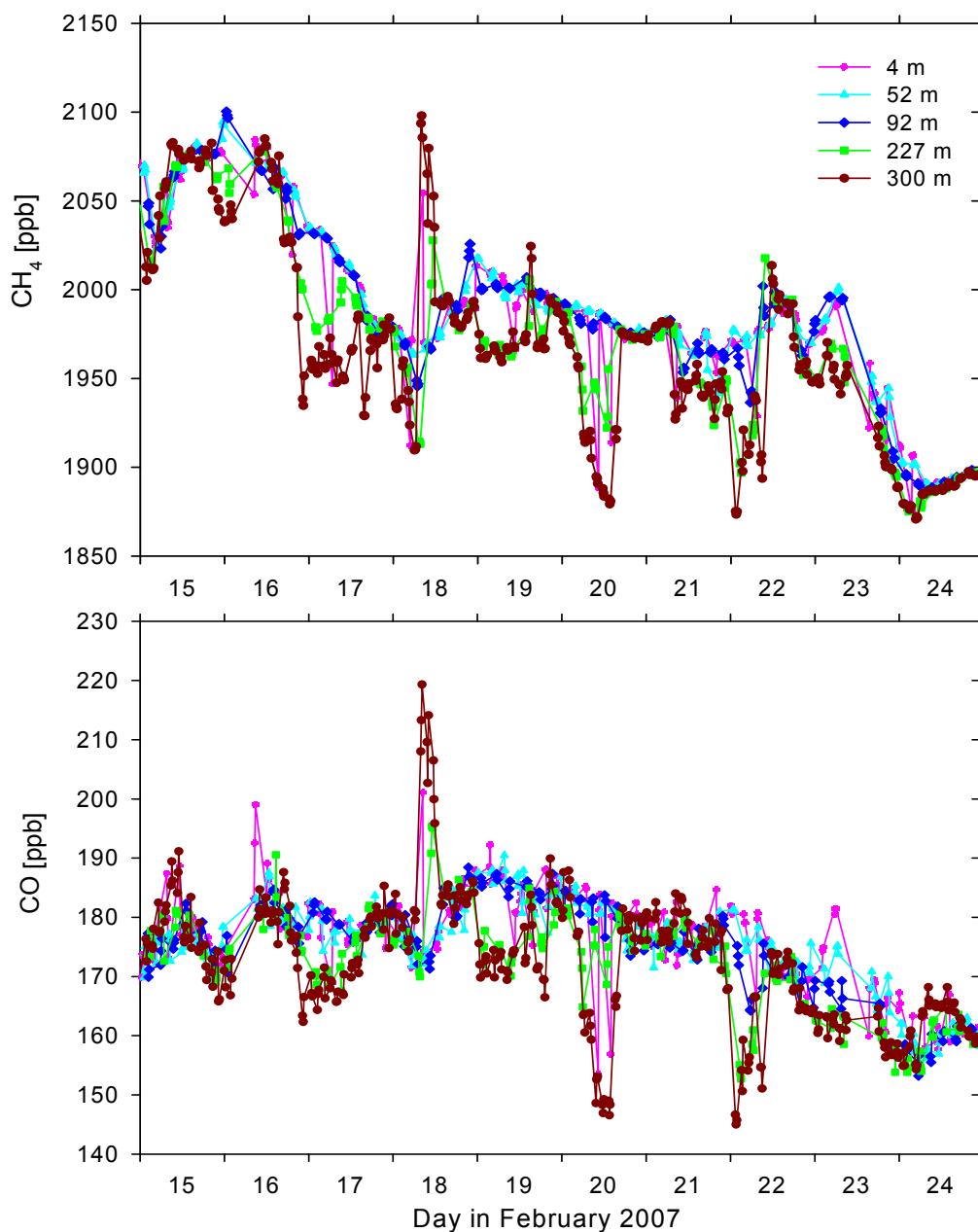


**Figure 5.12:** CH<sub>4</sub> (top panel) and CO (bottom panel) concentrations over a period of ‘cold events’ from 15 to 25 Feb 2007. Data points are 12-min apart.

the hypothesis of their gravitational separation. If gravitational separation were indeed the cause of the observed vertical gradients of CH<sub>4</sub> they would have been the opposite from those observed because of the CH<sub>4</sub> molecule being lighter than air, whilst the CO

molecule having almost the same molecular mass as air should have been largely unaffected by the phenomena. In addition, no vertical gradients were observed in N<sub>2</sub>O concentrations (not shown), but the same decreasing trend was clearly seen towards the end of the month. However, as presumably only very small vertical gradients in N<sub>2</sub>O concentrations would have been expected they might have remained unnoticed because of the limited measurement precision.

Another series of ‘cold events’ was observed from 07 to 10 Jan 2007 (not shown). Results of an analysis of the O<sub>2</sub>/CO<sub>2</sub> exchange ratios exhibited similar patterns to those for the February events with, however, less distinctive separations in clusters. CH<sub>4</sub> concentrations also followed the February ‘cold events’ patterns, whereas CO concentrations did not exhibit any significant vertical gradients.

In conclusion, it appears that during periods of ‘cold events’ vertical distributions of trace gases and O<sub>2</sub> were largely the result of a combination of local meteorological conditions such as very low temperatures and wind speeds, high atmospheric pressure and suppressed vertical mixing resulting in the formation of separate air layers with different characteristics and air circulation patterns. A hypothesis of the gravitational separation within the vertical air column, although

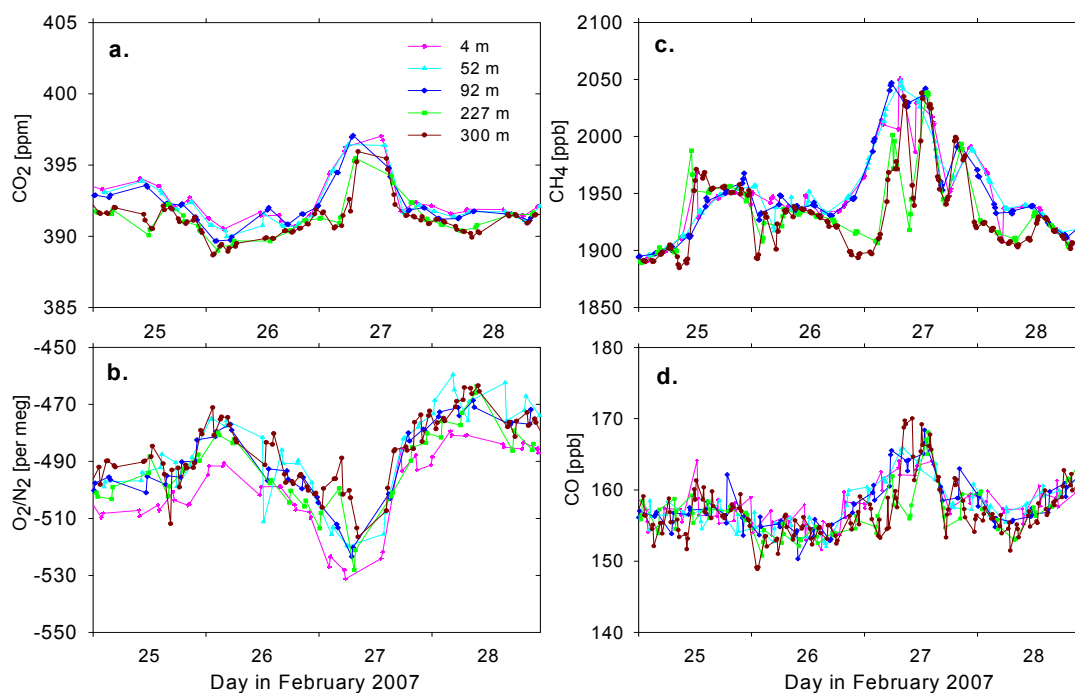


**Figure 5.13:** CO<sub>2</sub>, O<sub>2</sub>, CH<sub>4</sub> and CO concentrations during a pollution event on 27 Feb 2007 (a. through d. respectively).

helpful in explaining some of the features of the ‘cold events’ (e.g. high CO<sub>2</sub> concentrations near the ground and vertical distribution of O<sub>2</sub>/CO<sub>2</sub> ratios) can not provide the exhaustive explanations for the others (e.g., CH<sub>4</sub> and CO vertical gradients).

Nevertheless, the hypothesis might still have some validity if one presumes that there may exist some additional unidentified processes contributing to the observed phenomena.

### 5.6.2 Pollution events

The multi-species approach to ZOTTO measurements can also be a useful tool for identifying pollution signatures of air masses arriving at ZOTTO.

Figure 5.13 shows CO<sub>2</sub>, O<sub>2</sub>, CH<sub>4</sub> and CO concentrations during a pollution event in February 2007. The CO<sub>2</sub> accumulation is not very large but clearly defined and mirrored by depletion in O<sub>2</sub> concentrations. Table 5.1 summarises the average ratios calculated for different gas species (O<sub>2</sub>/CO<sub>2</sub>, CO/CO<sub>2</sub> and CO<sub>2</sub>/CH<sub>4</sub>) for this period. The O<sub>2</sub>/CO<sub>2</sub> ratios were calculated together for all heights, whereas the other ratios were estimated separately for the top and bottom levels mainly owing to evidence of CH<sub>4</sub> vertical gradients (Fig. 5.13c.). All ratios were calculated using differences between concentrations during the pollution plume and average background values (before and after the event). The uncertainties are reported as standard errors and were calculated with standard procedures of error propagation.

Height (m)	O <sub>2</sub> /CO <sub>2</sub> (ppm/ppm)	CO/CO <sub>2</sub> (ppb/ppm)	CH <sub>4</sub> /CO <sub>2</sub> (ppb/ppm)
All	1.46±0.17	-	-
4+52+92	-	1.43±0.16	12.23±1.49
227+300	-	2.21±0.42	26.25±4.67

**Table 5.1:** Emission ratios for a pollution event on 25-27 February 2007.

The O<sub>2</sub>/CO<sub>2</sub> exchange ratios for this event are quite high indicating the possibility of pollution from fossil fuel burning. However, a 72-hour back trajectory analysis indicates that the air masses responsible for the elevated CO<sub>2</sub> concentrations arrived from the Kara Sea via Yamalia bypassing any large cities on their way to ZOTTO. The CO/CO<sub>2</sub> ratios at the bottom and top levels of the tower are statistically different, with both being much lower than those previously reported for European emissions (11.0±1.1 ppb, [*Gamnitzer et al.*, 2006]). The latter estimate, however, was based on a <sup>14</sup>C derived fossil fuel CO<sub>2</sub> estimate, whereas I used the ambient CO<sub>2</sub> concentrations above background values (as measured at the tower) for these calculations. The vertical gradients are especially large for CH<sub>4</sub>/CO<sub>2</sub> ratios (as expected from Fig. 5.13c.), with the top level estimate being double than that at the bottom.

Figure 5.14 illustrates another pollution event in December 2006 which was observed in concentration variability of all gas species measured at ZOTTO (plots a. through d.). The maximum CO<sub>2</sub> and consequently minimum O<sub>2</sub> concentrations were

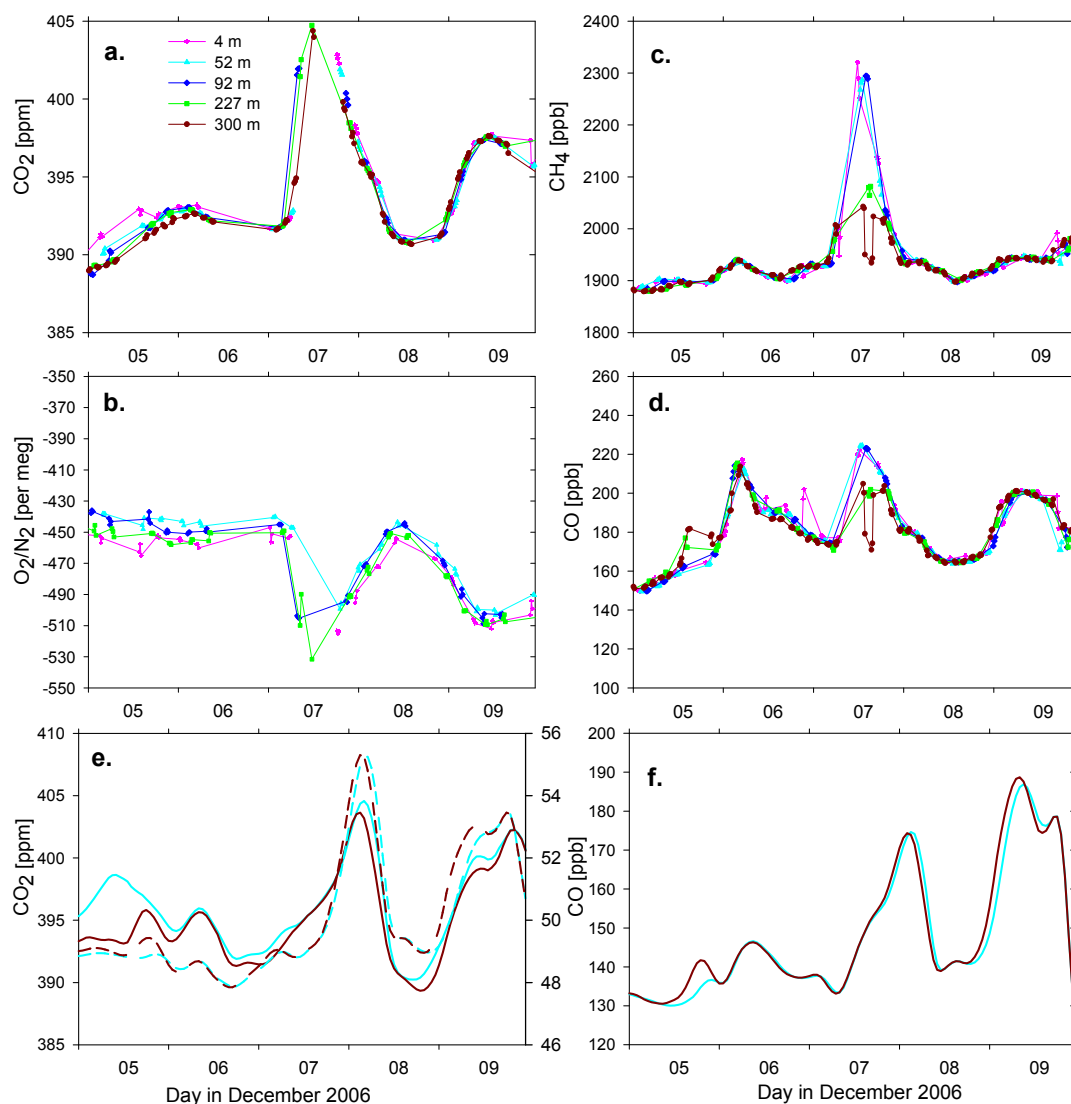


**Figure 5.14:** CO<sub>2</sub>, O<sub>2</sub>, CH<sub>4</sub> and CO variations as measured at five levels of the ZOTTO tower (a. through d.). Changes in CO<sub>2</sub> (ppm) and O<sub>2</sub> (per meg) are directly comparable on a mole to mole basis. e. REMO total CO<sub>2</sub> simulations at 52 and 300 m (solid cyan and dark red lines) and fossil fuel CO<sub>2</sub> at 52 and 300 m (dashed cyan and dark red lines). Both right and left y-axes are in ppm of CO<sub>2</sub>: left y-axis denotes total CO<sub>2</sub> and right y-axis denotes fossil fuel CO<sub>2</sub>. f. REMO total CO simulations at 52 and 300 m (solid cyan and dark red lines).

observed on 07 Dec, with no significant vertical gradients for either species.

Conversely, CH<sub>4</sub> and CO concentrations exhibited clear vertical gradients with lower values at the top of the tower.

O<sub>2</sub>/CO<sub>2</sub> exchange ratios are often used as indicators for polluted air masses and types of burned fossil fuels (as different types of fossil fuels are characterised by distinctive and well defined O<sub>2</sub>/CO<sub>2</sub> ratios). Such studies have been performed for many stations where *in situ* O<sub>2</sub> measurements are made concurrently with CO<sub>2</sub>. Nevertheless, this approach, although being a useful additional tool to distinguish the O<sub>2</sub>/CO<sub>2</sub> signatures from different processes, is likely to not be entirely reliable and

straightforward, at least not on its own. One of the difficulties of this approach is the data selection criteria, which are rarely properly documented. However, the latter is a very important part of any O<sub>2</sub>/CO<sub>2</sub> ratio analysis, particularly since different data selection criteria can significantly alter the results and conclusions of such studies. Another important but often unreported crucial constituent of O<sub>2</sub>/CO<sub>2</sub> exchange ratio analyses is uncertainty estimates. To illustrate these statements, I used the O<sub>2</sub> and CO<sub>2</sub> concentration data over the pollution event shown in Figure 5.14 to calculate the O<sub>2</sub>/CO<sub>2</sub> exchange ratios with different data selection criteria below.

Figures 5.14a. and b. show mirrored concentrations of CO<sub>2</sub> and O<sub>2</sub> with a very well defined CO<sub>2</sub> peak (O<sub>2</sub> depletion) on 07 Dec 2006. To calculate the O<sub>2</sub>/CO<sub>2</sub> exchange ratios I estimated the average background values for both gases (using data before and after the event) and subtracted them from the concentrations of both species during the pollution event. In the first case, I used all data points (from all heights) for both O<sub>2</sub> and CO<sub>2</sub> from the very beginning of the peak (~5 am 07 Dec) to its end (~9 am 08 Dec). Altogether, I used 76 data points for each of O<sub>2</sub> and CO<sub>2</sub>. The resulting O<sub>2</sub>/CO<sub>2</sub> ratio was 1.21±0.04 with a high degree of correlation between the species (R<sup>2</sup>=0.91). This ratio is higher than that expected from the processes of photosynthesis and respiration (1.10±0.05, [Severinghaus, 1995]) but lower than the average ratios characterising burning of fossil fuels (except coal). Most likely this ratio represents a combined signature of several processes but it is difficult to make their further differentiation using these results alone.

Next, I selected only the innermost ~25% of all CO<sub>2</sub> and O<sub>2</sub> concentration values around their maxima and minima during the pollution plume. The estimated ratio was 1.47±0.25, with much lower correlation between the gas species (R<sup>2</sup>~0.66) and number of data points used (20). In this case, the O<sub>2</sub>/CO<sub>2</sub> ratios covered a range from 1.22 to 1.72, which could be attributed to the burning of liquid fossil fuels (e.g. petroleum, with an average of ~1.4).

When selecting mainly maxima and minima CO<sub>2</sub> and O<sub>2</sub> concentrations from all heights, another 3 points were removed resulting in a total of 17 data points or 22% of the original dataset. The O<sub>2</sub>/CO<sub>2</sub> ratio with the latter data selection criterion was estimated to be 2.06±0.34 ( R<sup>2</sup>~0.72). The mean of this estimate (2.06) could be attributed to the process of natural gas burning. Nevertheless, significant errors of this estimate make it difficult to define the contributing processes with a high level of confidence.

This short exercise demonstrates the importance of data selection criteria and their error estimates when defining O<sub>2</sub>/CO<sub>2</sub> exchange ratios for various processes. Thus,

for purposes other than very rough estimates, any extensive scientific study which incorporates investigations on the O<sub>2</sub>/CO<sub>2</sub> exchange ratios (for example, relating the ratios to the type of burned fossil fuels) should document all data selection criteria as well as other statistical information (e.g. error estimates).

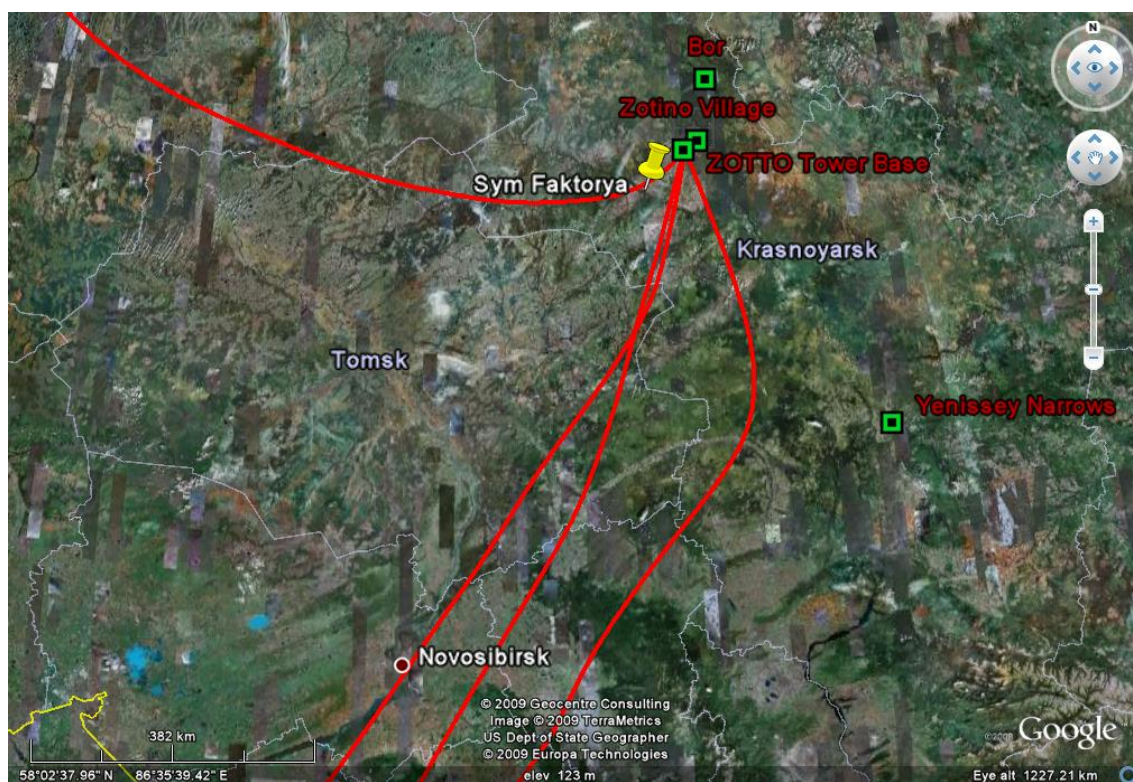


**Figure 5.15:** 72-hour back trajectories [Draxler and Hess, 1998] (at 300 m above the ground) show the origin of air masses that arrived at ZOTTO during the pollution event on 07 Dec 2007 (from north-west) and before and after the event (all three from South).

Figure 5.15 shows back trajectories of air masses arriving at ZOTTO during (from north-west) and before and after (from south) the event on 07 Dec 2006. Interestingly, despite the fact that the air masses that arrived at ZOTTO before and after 07 Dec had travelled over large densely inhabited areas (e.g. the large city of Novosibirsk), it appears that the air which is characterised by the elevated concentrations of all trace gases (Figure 5.14) arrived at ZOTTO from a completely different direction, and had flown over the small nearby city of Sym-Faktorya.

Table 5.2 summarises emission ratios (except for O<sub>2</sub>/CO<sub>2</sub>) for the event shown in Figure 5.14. To calculate these ratios I used only the highest innermost concentrations (over the pollution peak) of all gas species. Similar to the pollution event in February 2007, I calculated separate estimates for the bottom and top levels of the tower as some of the species (mainly CH<sub>4</sub> and CO) showed different patterns in their vertical gradients.

Height (m)	CO/CO <sub>2</sub> (ppb/ppm)	CH <sub>4</sub> /CO <sub>2</sub> (ppb/ppm)	REMO CO/CO <sub>2</sub> (ppb/ppm)
4+52+92	3.70±0.24	25.75±2.74	-
227+300	1.46±0.31	9.61±0.94	2.91±0.34

**Table 5.2:** CO/CO<sub>2</sub> and CH<sub>4</sub>/CO<sub>2</sub> emission ratios from observations for the bottom and top levels of the ZOTTO tower. Modelled CO/CO<sub>2</sub> ratios are also calculated, using the total CO and CO<sub>2</sub> REMO simulations (see text for further details).

The separate estimates of CO/CO<sub>2</sub> and CH<sub>4</sub>/CO<sub>2</sub> ratios for the bottom and top levels of the tower might be useful for their interpretation. The ratios summarised in Table 5.2 show that for the event of 07 Dec 2006 both CO/CO<sub>2</sub> and CH<sub>4</sub>/CO<sub>2</sub> ratios were significantly higher at the lower heights, which might be an indication of strong influence from local CO and CH<sub>4</sub> emissions. This hypothesis is confirmed by the back trajectory analysis (Fig. 5.15) which showed that this pollution event was most likely caused by a relatively local source (Sym-Faktorya is <100 km away from ZOTTO).

Under low wind conditions (~1 m/s on 07 Dec) in wintertime, local emissions might accumulate near the ground with only very limited vertical mixing occurring during daytime. The trace gas concentrations at 200-300 m above the ground, on the contrary, are representative of much larger areas, and in the case of this particular pollution event could have arrived from a different direction thus possibly incorporating fossil fuel emission signatures from large cities to the south of ZOTTO (Fig. 5.15).

In contrast to the December event, the estimates presented in Table 5.1 show that CO/CO<sub>2</sub> and CH<sub>4</sub>/CO<sub>2</sub> ratios were twice as high at the top of the tower on 27 Feb 2007. This might support the argument that the polluted air masses had travelled over some distance before arriving at ZOTTO. The air back trajectory (not shown) demonstrated that the air masses that arrived at ZOTTO on 27 Feb 2007 originated in the north.

As the wintertime vertical mixing within the ABL is not very strong the concentration signatures at the top and bottom levels of the tower might represent different air masses. Consideration of this fact and thus estimating the gas emission ratios separately for those levels might be helpful for interpretation of wintertime pollution events.

In this study I found CO/CO<sub>2</sub> ratios (Tables 5.1 and 5.2) that were significantly lower than those reported by Gamnitzer *et al.* [2006]. As mentioned above, the latter were based on <sup>14</sup>C anthropogenic CO<sub>2</sub> estimates which were unavailable for ZOTTO. Nevertheless, as photosynthetic and respiration activities of the terrestrial biosphere are

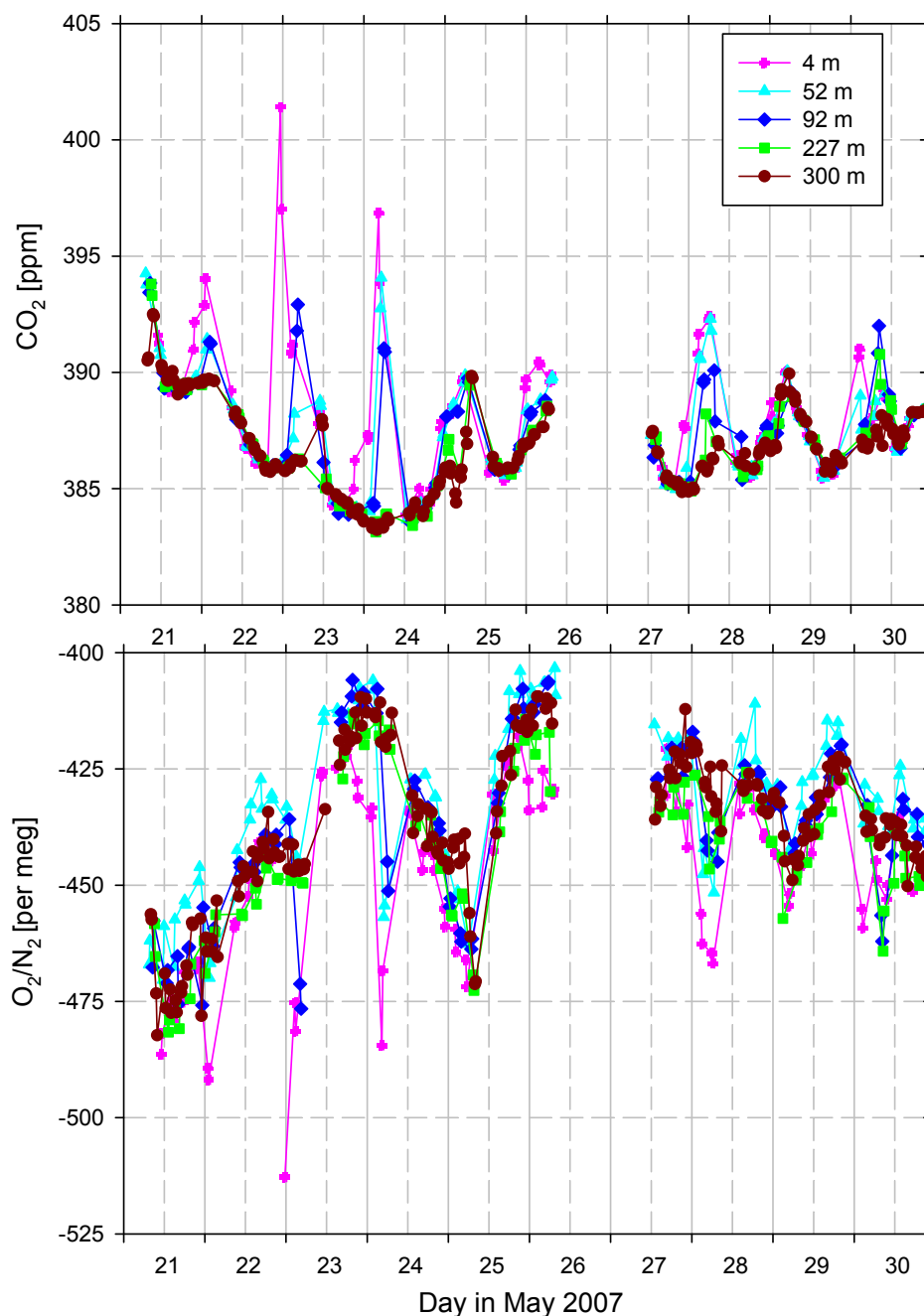


**Figure 5.16:** Diurnal variations of  $\text{CO}_2$  and  $\text{O}_2$  concentrations from 21 to 31 May 2007. Changes in  $\text{CO}_2$  (ppm) and  $\text{O}_2$  (per meg) are directly comparable on a mole to mole basis. Each data point represents a 4-min average, 16 min apart. Dashed vertical gridlines correspond to 12:00 (local standard time) of each day; solid vertical gridlines correspond to 00:00.

minimal in wintertime, the observed changes in  $\text{CO}_2$  concentrations are mainly determined by the burning of fossil fuels. Thus, I assume that no significant errors were introduced to my  $\text{CO}/\text{CO}_2$  estimates by using total  $\text{CO}_2$  concentrations as proxies for anthropogenic  $\text{CO}_2$ .

In addition to the observation-based estimates, I calculated  $\text{CO}/\text{CO}_2$  ratios using total  $\text{CO}$  and  $\text{CO}_2$  concentration simulations from a high-resolution regional model (REMO). All details on the model simulations (see summary in Table 6.1) as well as

their detailed comparison with observations are presented in Chapter 6. In this section, I only use the results from CO and CO<sub>2</sub> simulations to calculate the modelled CO/CO<sub>2</sub> ratios during the pollution event on 07 Dec 2006. Figure 5.14e. shows the modelled total and fossil fuel CO<sub>2</sub> at 52 and 300 m. In contrast to the ZOTTO measurements, there are no vertical gradients in the modelled concentrations. The fossil fuel CO<sub>2</sub> (right y-axis) was plotted to demonstrate the anthropogenic origin of the CO<sub>2</sub> peak on 07 Dec, which is also clearly seen in the total CO<sub>2</sub> simulations. Figure 5.14f. shows total CO simulations at 52 and 300 m for the same period, which are practically indistinguishable. The modelled CO/CO<sub>2</sub> ratio (see Table 5.2) for 300 m height is  $2.91 \pm 0.34$ , which is in good agreement with the ratios calculated from the observations.

## 5.7 Diurnal variations

Figure 5.16 shows diurnal variations of CO<sub>2</sub> and O<sub>2</sub> concentrations from 21-31 May 2007. The data exhibit clear though not large diurnal anti-correlated changes in CO<sub>2</sub> and O<sub>2</sub>. The highest CO<sub>2</sub> concentrations (lowest O<sub>2</sub>) were observed at 4 m, as expected. The vertical gradients were most pronounced when stable atmospheric conditions (low wind speed) prevailed, which was the case for most of the time period shown. The gradients were rather small probably because of relatively cold weather conditions, with ambient temperatures often below freezing in the first half of May (not shown). Only after 16 May did the air temperature begin to rise and with above zero values in the night. As seen in the figure, CO<sub>2</sub> concentrations gradually increased during the night, reaching a maximum between 03:00-06:00. Sunrise (about 04:00) caused ground-level warming and hence mixing of the stratified air column, usually becoming well mixed by 12:00. Changes in O<sub>2</sub> concentration almost always mirrored CO<sub>2</sub> with maxima shortly after midday and minima in the night (from 00:00 to 03:00).

Typical night-time vertical profiles of CO<sub>2</sub> and CH<sub>4</sub> concentrations are shown in Figures 5.17a and b respectively (solid circles), shown for 07-08 May 2007. The concentrations at the top two levels were nearly constant, and steadily increased from 92 m down to 4 m, suggesting that the measurements from both 227 and 300 m were representative of the ABL. I also show typical afternoon profiles (solid triangles), when the air column was well mixed, from the same time period.

I estimated night-time CO<sub>2</sub> respiration fluxes by examining twenty events in April and May 2007 which exhibited clear night-time vertical gradients and stable CO<sub>2</sub> concentrations at the top level of the tower throughout the afternoon. Fluxes were calculated by integrating between the CO<sub>2</sub> concentration before the night-time build-up (afternoon values) and the maximum night-time concentration (before vertical mixing

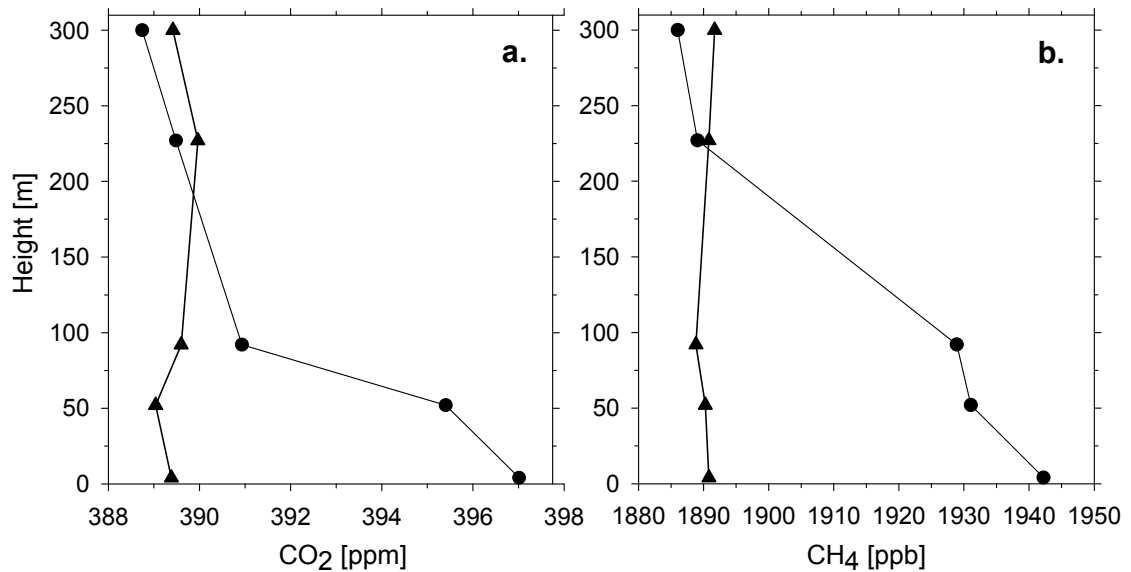


**Figure 5.17:** Vertical concentration gradients of (a) CO<sub>2</sub> and (b) CH<sub>4</sub> up to 300 m observed on 7-8 May 2007. The solid circles show early morning concentrations when the air column was stratified, where each data point is an average over the time period 05:00 to 07:00. The solid triangles represent afternoon averages from the previous day (14:00-16:00 for CO<sub>2</sub> and 18:00-20:00 for CH<sub>4</sub>) when the air column was well-mixed. The accumulation periods were 15 and 11 hours for CO<sub>2</sub> and CH<sub>4</sub>, respectively.

the following day eroded the vertical concentration gradient). I estimated an average flux of  $0.04 \pm 0.02 \text{ mol C m}^{-2} \text{ d}^{-1}$  which is consistent with eddy covariance measurements made in the vicinity of the tower in May 1999-2000 [Shibistova *et al.*, 2002b].

Unfortunately, I do not have any summer data for the fully constructed tower when fluxes would have been much larger. From summer 2006 data, with measurements up to 52 m, I observed significant diurnal gradients (up to 40 ppm at the 4 m height, compared to a maximum observed value of only 15 ppm in May 2007), but it is not possible to estimate the summer respiration flux since I lacked CO<sub>2</sub> concentration data in the ABL.

For CH<sub>4</sub>, in spring 2007, I did not observe as many events with diurnal gradients as for CO<sub>2</sub>. For the particular profile shown in Figure 5.17b., I estimated a flux of  $7.5 \times 10^{-4} \text{ mol CH}_4 \text{ m}^{-2} \text{ d}^{-1}$ ; a second event with a clear vertical CH<sub>4</sub> gradient on 23-24 May gave a similar result (not shown). I did not observe any diurnal variations or clear vertical profiles in CO concentrations.



## **CHAPTER 6. Regional model (REMO) simulations over Eurasia as compared to the ZOTTO measurements**

### **6.1 Introduction to Chapter**

The response of the terrestrial biosphere to increased atmospheric levels of CO<sub>2</sub> and to the changing climate has been long debated in the scientific community, but thus far no consensus has been reached. Recent models have predicted very different scenarios for biosphere response [e.g. *Friedlingstein et al.*, 2006]. The biosphere is an incredibly complex system; differences between the predictions result from limitations of the models to capture that complexity, and the scarcity of high quality observations that can be used to evaluate and improve the models. The lack of atmospheric observations in particular has been a problem for quite some time, especially in continental interiors where the influence of the terrestrial biosphere is the most profound. As was discussed earlier in this thesis (Chapter 1), the observational efforts of the scientific community have been mostly concentrated on making CO<sub>2</sub> measurements that can be considered representative of large areas; that is, marine stations or other remote stations, where there are no large local sources, and where the air is clean and unpolluted. Thus, the continental interiors have been under-represented in the CO<sub>2</sub> monitoring network. The same has been true of all other greenhouse gas monitoring.

In Chapters 3, 4 and 5, I presented the establishment, development and first measurement results from a mid-continental station, ZOTTO, that is one of the first such stations that is both remote and mid-continental at the same time. As I demonstrate in this chapter, the data from ZOTTO provide crucial insight into the response of the terrestrial biosphere.

Viable tools to study, model and predict the terrestrial biosphere's responses to climate change include regional atmospheric high-resolution models that account for the complex diurnal and seasonal patterns of CO<sub>2</sub> and other important greenhouse gases. Such atmospheric models, however, should incorporate process-based ecosystem models with realistic responses to short and long-term climatic variations, both natural and anthropogenic (e.g., deforestation, land use change, human induced fires), and particularly, any changes in carbon fluxes which could occur due to global warming. In Chapter 5, I compared observed seasonal cycles of CO<sub>2</sub>, O<sub>2</sub> and APO to those generated from model simulations with a global transport model (TM3) that can provide reliable results only on a rather coarse scale (5° x 4°). In contrast to Chapter 5, this chapter is devoted to analyses of the 'REgional MOdel' simulations (REMO; 0.5° x 0.5°) over the Eurasian continent with particular emphasis on comparison of the relevant stretches of the model simulations with data collected at ZOTTO in 2005-2007 on diurnal and

synoptic time scales. The model runs, described in more detail below, were performed by Ute Karstens (MPI-BGC) primarily for the purposes of this study. The REMO model results presented consist of simulations of CO<sub>2</sub>, CO, APO and several meteorological variables (temperature, wind speed, wind direction and surface pressure); these results are separately discussed in sections 6.4, 6.5, 6.6 and 6.3 respectively. The temporal overlap of the model-observation analyses is not the same for different species, with the longest comparison period available for CO<sub>2</sub> and the shortest for APO. The latter was restricted by availability of the relevant data input fields to the model simulations but could still be performed at a later date.

Along with simulations of meteorological variables, REMO's vertical transport (mixing) is discussed in detail in section 6.3. In the case of CO<sub>2</sub>, I pay special attention to the model-observation comparison of the diurnal and synoptic variations (Section 6.4), given that such short-term changes cannot be seen or accounted for in global transport models. In addition, section 6.4 presents a comparison between the carbon fluxes at ZOTTO from observations and modelled fluxes from the process-based biosphere model (BIOME-BGC), which provides biosphere related surface flux simulations for REMO. Section 6.5 presents the results of the first-ever comparison of an observed APO signal in the mid-continental interiors with REMO APO simulations. In the case of CO (Section 6.6), simulations of fire events (which were particularly frequent during the period of the measurements) are the most interesting feature of this model-observation comparison. Section 6.6 also discusses emission ratios (ER's) of several gas species (CO/CO<sub>2</sub>, CH<sub>4</sub>/CO<sub>2</sub>, CO/CH<sub>4</sub>) and O<sub>2</sub>/CO<sub>2</sub> exchange ratios that were observed during the fire events of summer 2006, and compares both modelled and observed fire emission ratios.

## 6.2 Description of REMO inputs and outputs

Detailed descriptions of the setup of the regional general circulation model REMO is available elsewhere [e.g. *Karstens et al.*, 2006; *Langmann*, 2000; *Jacob and Podzun*, 1997]. Here I only provide a short description crucial to the understanding of the simulations of the tracers, their initial and boundary conditions, and the output result formats (see Table 6.1 for a summary).

For each tracer the simulations were performed individually with no chemical interactions between them. The dynamic meteorological variables were simulated in REMO using global analyses from the European Centre for Medium-Range Weather Forecasts (ECMWF) as initial and boundary information. Each model run started daily at 00:00 UTC and used current weather diagnostics as input variables; from this point

onwards the development of each variable was simulated over a 30-hour period. The first six hours of the simulation forecast were discarded to allow the model to spin-up. The meteorological variables available for this study include air temperature, wind direction, wind speed and surface pressure at 1-hour frequency. The model domain is characterised by 0.5° horizontal resolution and twenty vertical layers (with six layers below 1500 m). For this study, however, I only used the model results that were interpolated to represent the same heights as those of the ZOTTO tower from which the measurements were made, i.e. 4, 52, 92, 227 and 300 m (see Chapter 3 for detailed sampling line descriptions). The observed meteorological variables used for the comparison with REMO were obtained from several locations within 100 km of ZOTTO (Sym-Faktorya, Bor, Yarcevo and Vorogovo) since no on-site meteorological measurements were operational at the time of my research. Table 6.2 contains a summary of all meteorological variables used for this study as well as the locations

<p><b>REMO model domain characteristics:</b></p> <ul style="list-style-type: none"> <li>• Model domain: ~ Area north of 30° N</li> <li>• 0.5° x 0.5° horizontal resolution on a rotated grid</li> <li>• 20 vertical layers (6 of which are below 1500 m) using a hybrid pressure-sigma coordinate system</li> </ul>
<p><b>REMO initial and boundary data:</b></p> <ul style="list-style-type: none"> <li>• Meteorological simulations: ECMWF analysis (6-hour frequency)</li> <li>• CO<sub>2</sub> simulations: global transport model TM3 (5° x 4° horizontal resolution)</li> <li>• CO simulations: global chemistry transport model ECHAM5-MOZ (3° x 3° horizontal resolution)</li> <li>• APO simulations: global transport model TM3 (5° x 4° horizontal resolution)</li> </ul>
<p><b>REMO CO<sub>2</sub> simulation tracers:</b></p> <ul style="list-style-type: none"> <li>• Terrestrial biosphere: BIOME-BGC (3-hourly fluxes)</li> <li>• Ocean fluxes: sea-air monthly fluxes from <i>Takahashi et al.</i> [1999] and inversion from <i>Mikaloff Fletcher et al.</i> [2006]</li> <li>• Fossil fuel emissions: EDGAR FT2000 V3.2, updated with BP statistics</li> <li>• Fire emissions: GEFDv2 (8-day frequency)</li> <li>• Atmospheric inversion: 3-hourly corrections to the forward TM3 simulations from <i>Rödenbeck et al.</i> [2008]</li> </ul>
<p><b>REMO APO simulation tracers:</b></p> <ul style="list-style-type: none"> <li>• APO fluxes over the ocean from the atmospheric inversion by <i>Rödenbeck et al.</i> [2008]</li> <li>• APO fluxes from fossil fuel burning from EDGAR FT2000 V3.2, updated with BP statistics</li> </ul> <p><b>REMO CO simulation tracers:</b></p> <ul style="list-style-type: none"> <li>• Anthropogenic and natural emissions: results from RETRO project (for 2000)</li> <li>• Fires: GEFDv2 (8-day frequency) for the actual years of the simulations</li> </ul> <p><b>Table 6.1:</b> Summary of REMO characteristics.</p>

at which they were measured. For the purpose of comparison with observations, all 30-hour forecasts were compiled into continuous records of the simulated variables. All meteorological variables are available for the period from January 2006 to May 2007.

The REMO CO<sub>2</sub> simulations start in January 2002 and finish at the end of April 2007, providing a long overlapping period with the ZOTTO observations (which covered the period from November 2005 to June 2007). The spatial domain of the REMO simulations used in this study includes only the region northwards of 30° N. Owing to the semi-hemispheric domain of the REMO simulations, the influence of the carbon sources outside of the model domain had to be accounted for by including global CO<sub>2</sub> concentrations fields from global transport model simulations, in this case TM3 [Rödenbeck *et al.*, 2008], to provide the initial and boundary conditions. The total modelled CO<sub>2</sub> composite consists of a sum of simulations of several tracers which represent changes within different CO<sub>2</sub> sources and sinks (and are treated as individual and independent tracers), namely: the terrestrial biosphere (C<sub>bio</sub>), the oceans (C<sub>ocean</sub>), fossil fuel emissions (C<sub>foss</sub>), fire emissions (C<sub>fire</sub>) and atmospheric inversion correction (C<sub>inversion</sub>). Individual model runs were performed for each of these tracers.

The 3-hourly BIOME-BGC model fluxes [e.g. Churkina and Running, 1998; Running and Gower, 1991] were used as input for modelling the terrestrial biospheric seasonal and diurnal variability to obtain the simulated biospheric CO<sub>2</sub> tracer. Oceanic fluxes were reproduced using monthly sea-air fluxes from Takahashi *et al.* [1999] and the inversion described by Mikaloff Fletcher *et al.* [2006]. The data representing CO<sub>2</sub> from fossil fuel emissions originated from the Emission Database for Global Atmospheric Research (EDGAR FT2000 V3.2) [Olivier *et al.*, 1996]. As this database only contains data up to 2005, the annual emissions were updated to the estimates representing the actual year of the simulations using British Petroleum (BP) statistical data on fossil fuel use (<http://www.bp.com/statisticalreview> ; the updated dataset is courtesy of C. Gerbig (MPI-BGC)). Seasonal, weekly and diurnal variations of fossil fuel emissions were introduced to the simulations using information on temporal profiles from the EDGAR database. Data on CO<sub>2</sub> emitted from fires were obtained from the Global Emission Fire Database (GEFD) [Randerson *et al.*, 2007]. The inversion component represents the combined 3-hourly corrections to the forward simulation of the TM3 model that were used to define the initial and boundary conditions for the REMO simulations. The total CO<sub>2</sub> composite can be calculated as either a sum of all components except the fire CO<sub>2</sub> tracer, or as a sum of all components except the inversion component, that is:

$$C_{\text{total}} = C_{\text{foss}} + C_{\text{bio}} + C_{\text{inversion}} + C_{\text{ocean}}, \text{ or}$$

$$C_{\text{total}} = C_{\text{foss}} + C_{\text{bio}} + C_{\text{fire}} + C_{\text{ocean}}$$

Adding the fire CO<sub>2</sub> tracer to the total CO<sub>2</sub> in the first case would result in double counting, as the fire emissions are already included in the inversion corrections. The REMO model does not provide absolute CO<sub>2</sub> concentrations but rather its temporal variations with respect to an arbitrary initial value. To compare the CO<sub>2</sub> simulation results with the observations I added an offset of 360.5 ppm to C<sub>total</sub> (the offset was defined within the TM3 inversion). Unlike the meteorological variables' simulations (which were restarted daily) the CO<sub>2</sub> tracers (as well as CO and APO) were simulated continuously over the whole period of the model run.

The time series of the REMO CO simulations are shorter than that for CO<sub>2</sub> covering the period from January 2002 to January 2007. The reason for the shorter time series is that initial and boundary data from ECHAM5-MOZ, a combination of the global circulation model ECHAM5 (European Centre HAMburg (ECHAM)) (<http://www.mpimet.mpg.de/en/wissenschaft/modelle/echam.html>) and the chemistry transport model MOZART (Model of Ozone And Related Tracer) (<http://www.mpimet.mpg.de/en/wissenschaft/modelle/mozart.html>) were not available for the year 2007 when the REMO simulations were performed. ECHAM5-MOZ simulation results were provided by C. Richter and M. Schultz (Forschungszentrum Jülich, Germany). The REMO CO simulations incorporate anthropogenic and natural CO emissions for the year 2000 reported by the Reanalysis of the TROpospheric chemical composition over the past 40 years (RETRO) project (<http://retro.enes.org>) and fire emissions from the GFED (at an 8-day frequency) for the actual years of the simulations. Seasonal CO variations are reflected in the RETRO data; however, no additional annual trend was applied to these data to update them to the CO concentration of the years for which the simulations were performed. In addition, diurnal and weekly variations of CO concentrations were incorporated in the REMO simulations by using time profile estimates from the EDGAR database. In the case of CO, the model simulations were performed for only two tracers: total CO (includes all emissions and the influence from chemical destruction of CO in the troposphere and stratosphere) and total CO without fire emissions. Thus, the contribution from fires was obtained by taking a difference between the above two CO tracers. In contrast to the CO<sub>2</sub> simulations, no offset value had to be added to the simulation results as the global model simulations provided total CO as initial conditions for the REMO simulations. Only CO simulation results from the model layers corresponding to the sampling heights of the ZOTTO tower (see above) were used in the following discussions and model-observation comparisons.

Station	Variable	Unit	Data Frequency	Data source
<i>Vorogovo</i> (61°00' N, 89°45' E); <i>Bor</i> (61°36' N, 90°01' E); <i>Sym-Faktorya</i> (60°22' N, 88°26' E); <i>Yarcevo</i> (60°16' N, 90°13' E)	Temperature wind speed wind direction surface pressure	°C m/sec deg mbar	6 hours	<a href="http://meteo.infospace.ru">http://meteo.infospace.ru</a>
Bor	Potential temperature from radiosonde	Kelvin	12 hours	<a href="http://www.esrl.noaa.gov/raobs/">http://www.esrl.noaa.gov/raobs/</a>

**Table 6.2:** Summary of all meteorological data.

The time series of the REMO APO simulations cover the period from January 2002 to January 2007. The APO fluxes were prescribed from the TM3 inversion results [Rödenbeck *et al.*, 2008] with the relevant APO concentration fields being used as initial and boundary information in the REMO simulations. An additional offset of -21 ppm (-100.8 per meg) (defined in the TM3 inversion) had to be added to the REMO APO simulations results to make them comparable with observations. Similarly to the other tracers described above, only REMO APO simulations from the layers corresponding to the sampling heights of the ZOTTO tower were used for model-observation comparison purposes.

### 6.3. Simulations of meteorological variables in REMO

As discussed above, all meteorological simulations within REMO were initialised with meteorological analyses from ECMWF, which clearly improves the quality of the model-observation comparisons (see below). The meteorological simulations presented in this subsection include temperature (at 2 m), wind speed (at 10 m), wind direction (at 10 m) and surface pressure. As no meteorological measurements were available at ZOTTO for the period of REMO simulations, I used measurements from four different locations situated within a radius of ~100 km from ZOTTO (Vorogovo, Bor, Sym-Faktorya and Yarcevo) as proxies for meteorology at ZOTTO. Table 6.2 presents a summary of all meteorological variables used in this study for comparing with REMO simulations. All variables were measured at surface or near surface level, which makes them compatible with those from REMO simulations. In addition, I have compared the vertical structure of the REMO simulations with measurements of potential temperature data from routine meteorological radiosondes (see Table 6.2).

### 6.3.1 Surface temperature

Figure 6.1 presents records of surface temperatures at four localities around ZOTTO compared to REMO temperature simulations (at 2 m above ground) at ZOTTO over 2006 and the first half of 2007. For simplicity, I use REMO simulations for the ZOTTO location only and not the nearby stations as the differences between them are

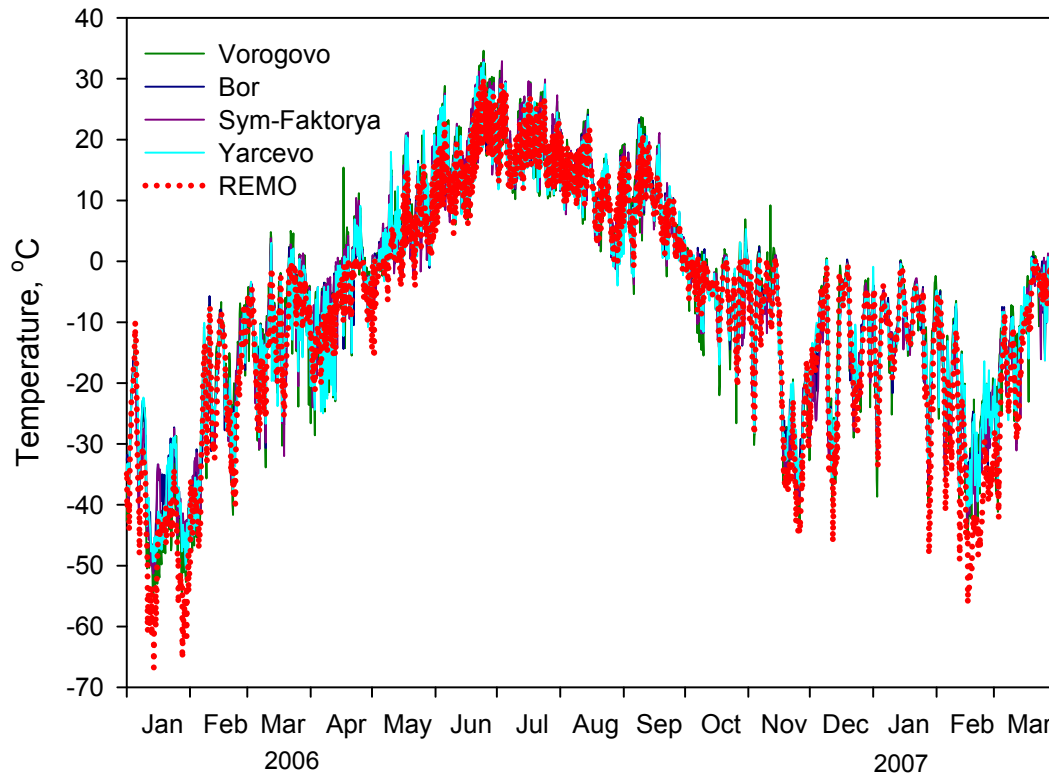


**Figure 6.1:** Surface temperature records at four localities around ZOTTO compared to REMO simulations (at ZOTTO).

usually negligible. The simulations (the dotted red line in the figure) are generally in very good agreement with the measurements (see legend), with some notable exceptions. The model frequently underestimates the winter temperature values as can be seen in January 2006 and throughout November 2006 – February 2007 (shown in detail in Fig. 6.2b). In addition, the diurnal cycle of summertime temperatures appears to be underestimated as well, with smaller simulated diurnal amplitudes for May, June and July 2006 (see also Fig. 6.2a).

Figures 6.2a. and b. show the temperature record at the same locations as in Fig. 6.1 but for July and November 2006 only. The upper plot (a) shows remarkably good agreement between the modelled daily temperature variations and the measurements. Figure 6.2b shows a detailed temperature record for November 2006, which includes the so-called ‘cold events’, previously discussed in Chapter 5, Section 5.6.1. This period

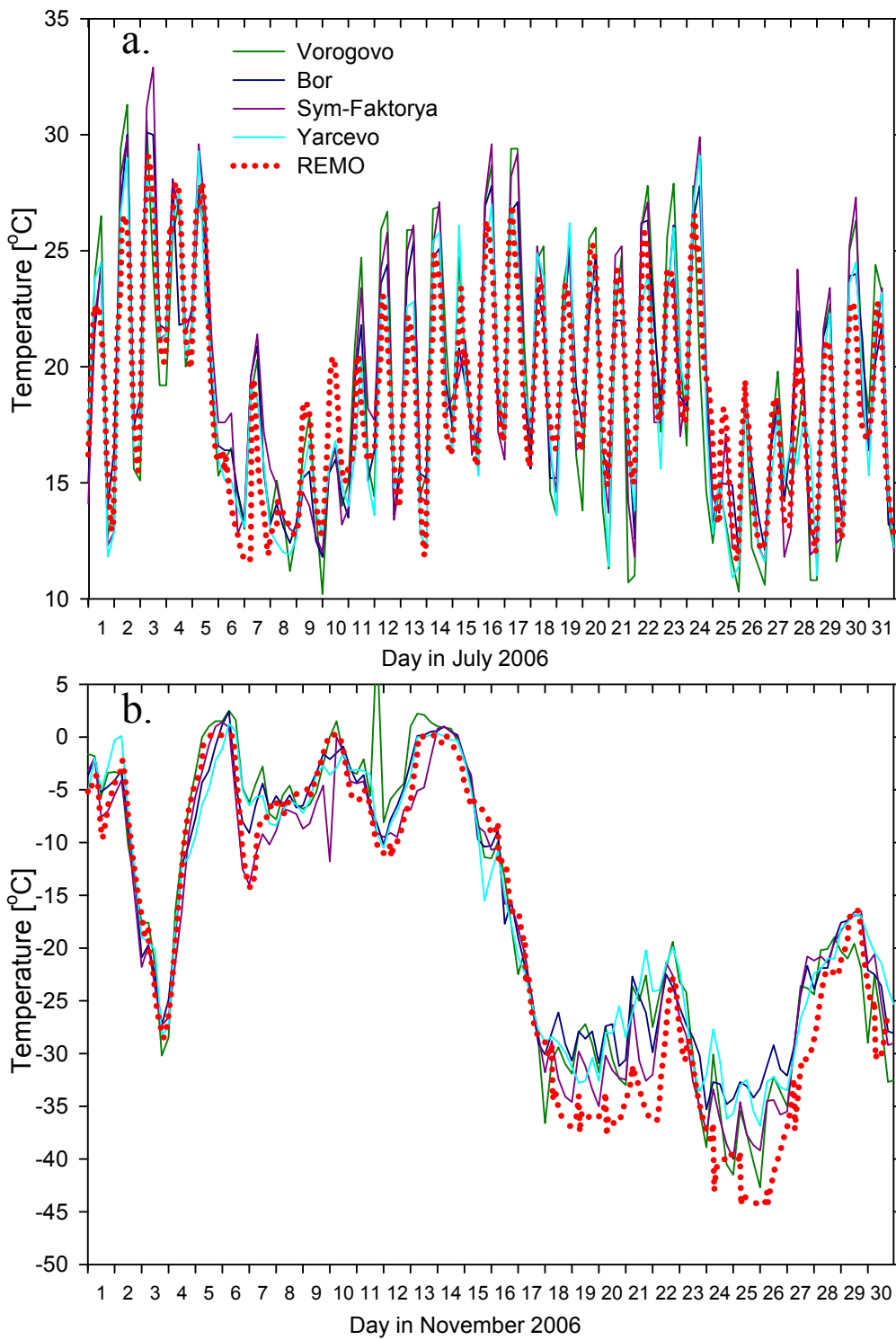


**Figure 6.2:** Surface temperature records at four localities around ZOTTO and REMO simulations (at ZOTTO) in July (a) and November (b) 2006.

(17-27 Nov 2006) was characterised by very cold temperatures, low wind speed conditions and large vertical CO<sub>2</sub> gradients at the low levels of ZOTTO tower. While the data at all four stations practically overlap in the beginning of the month, they start to diverge during the period of the cold events. The REMO simulations (dotted red

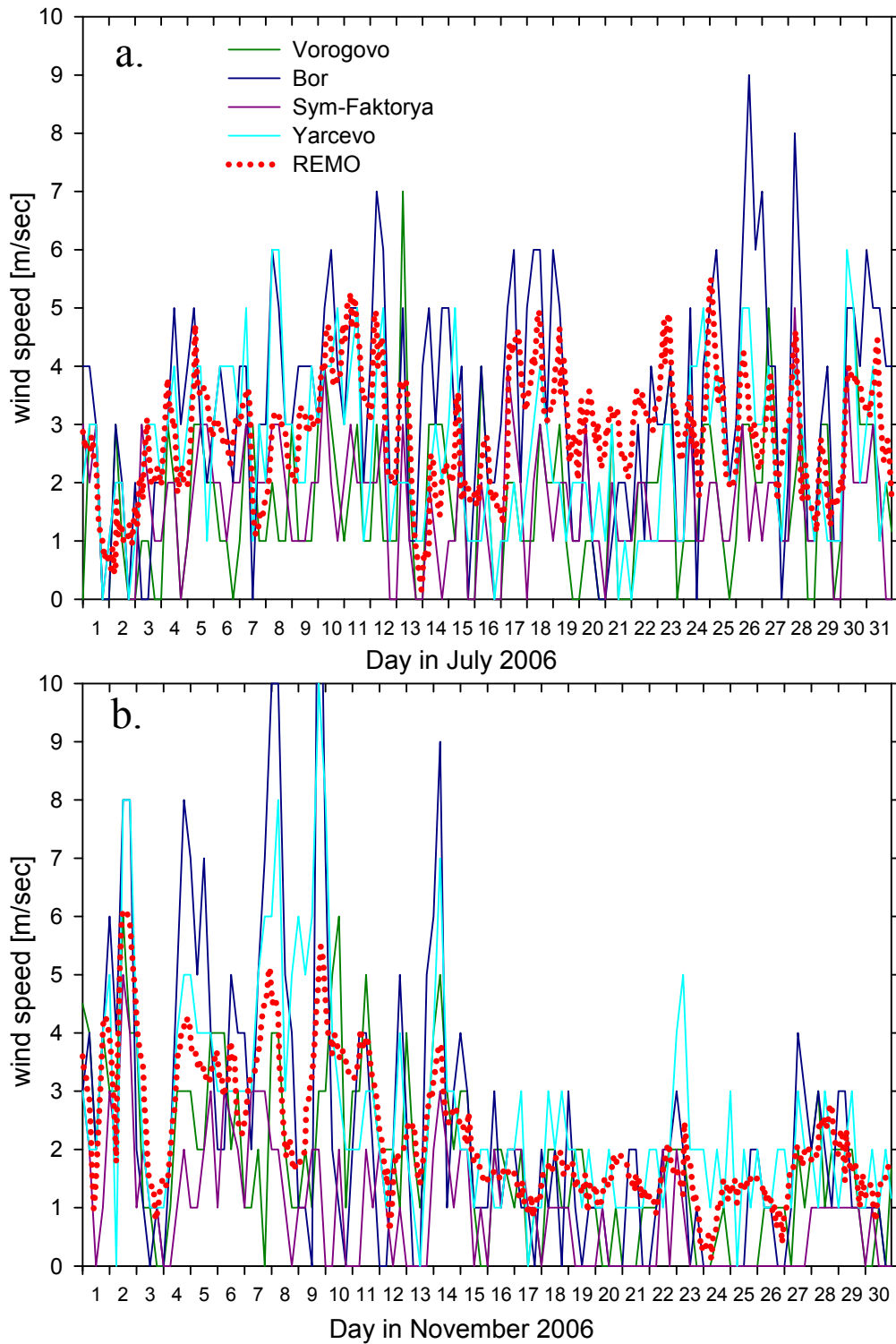


**Figure 6.3:** Wind speeds at four localities around ZOTTO compared to REMO simulations (at ZOTTO) in July (a) and November (b) 2006.

line), however, predict even lower temperatures than those recorded at all four stations, sometimes more than 10°C colder.

The conclusion from these comparisons is that surface temperatures are generally well captured by the model, including the diurnal cycles and high frequency features. However, the simulations do exhibit some clear offsets during very cold and

high-pressure weather conditions in winter, as well as underestimate the diurnal cycles of surface temperature in summer.

The existing good agreement between the measurements and simulations is clearly owing to the fact that the latter include ‘real’ observations in their initial input information, but certain differences are inevitable as the local weather conditions and the specific features of the ZOTTO location can not be captured perfectly by the simulations.

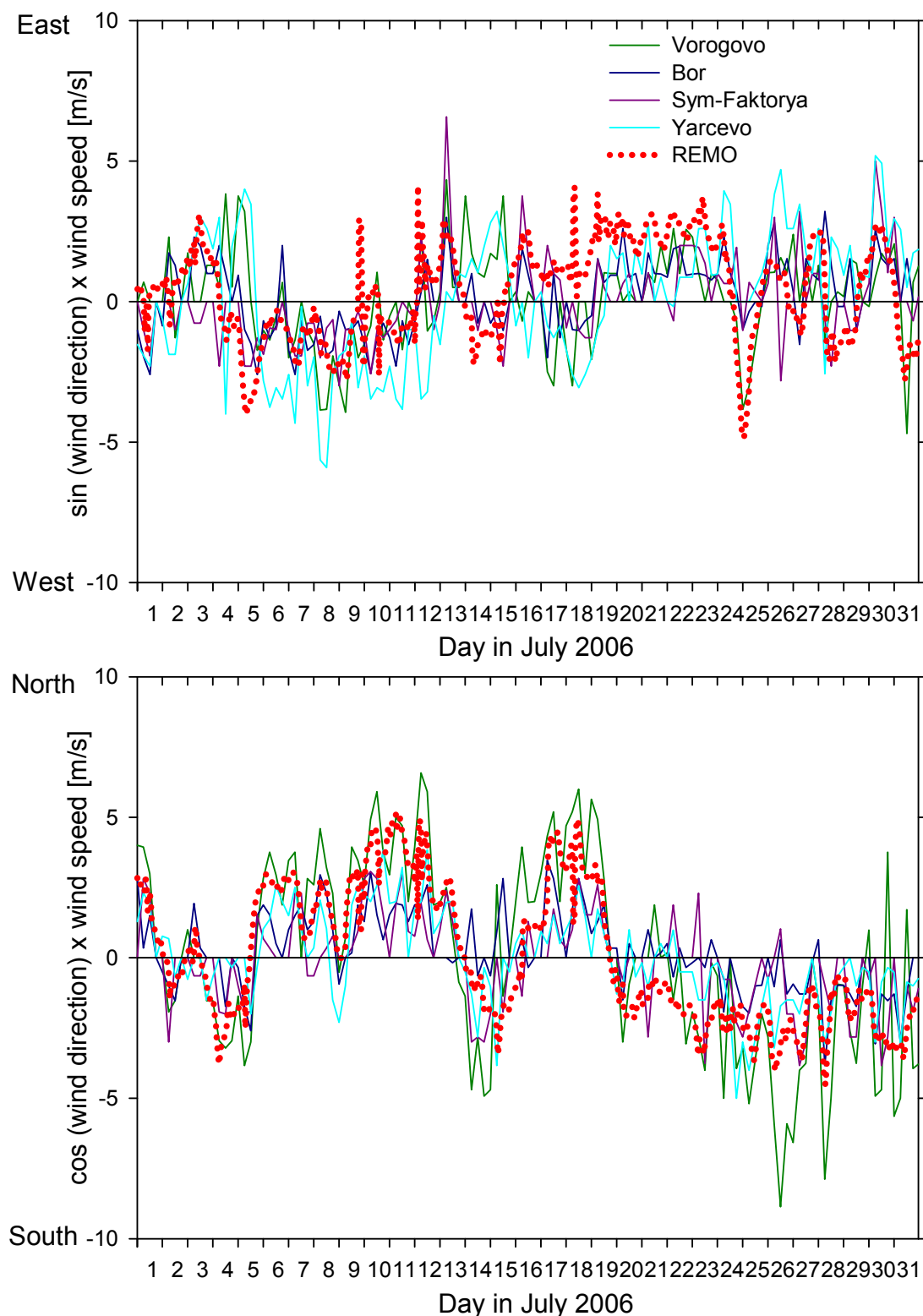
### **6.3.2 Wind speeds**

Figures 6.3a. and b. show wind speed measurements at four stations compared to REMO simulations. Both July (a) and November (b) 2006 wind speed data show a lot more scatter than the model results. Although general features of all observation records are similar, the model results often differ from the observations especially during very low (around 1 m/sec) wind speed conditions. REMO also does not capture short periods of very high wind speeds (greater than 6 m/sec). It is also important to note that the model simulations are available at higher frequency (every 1 hour ) than observations are made (every 6 hours). During the ‘cold events’ in November 2006 REMO simulations also show lower-wind speeds, but the simulations provide a much smoother record over this period as well.

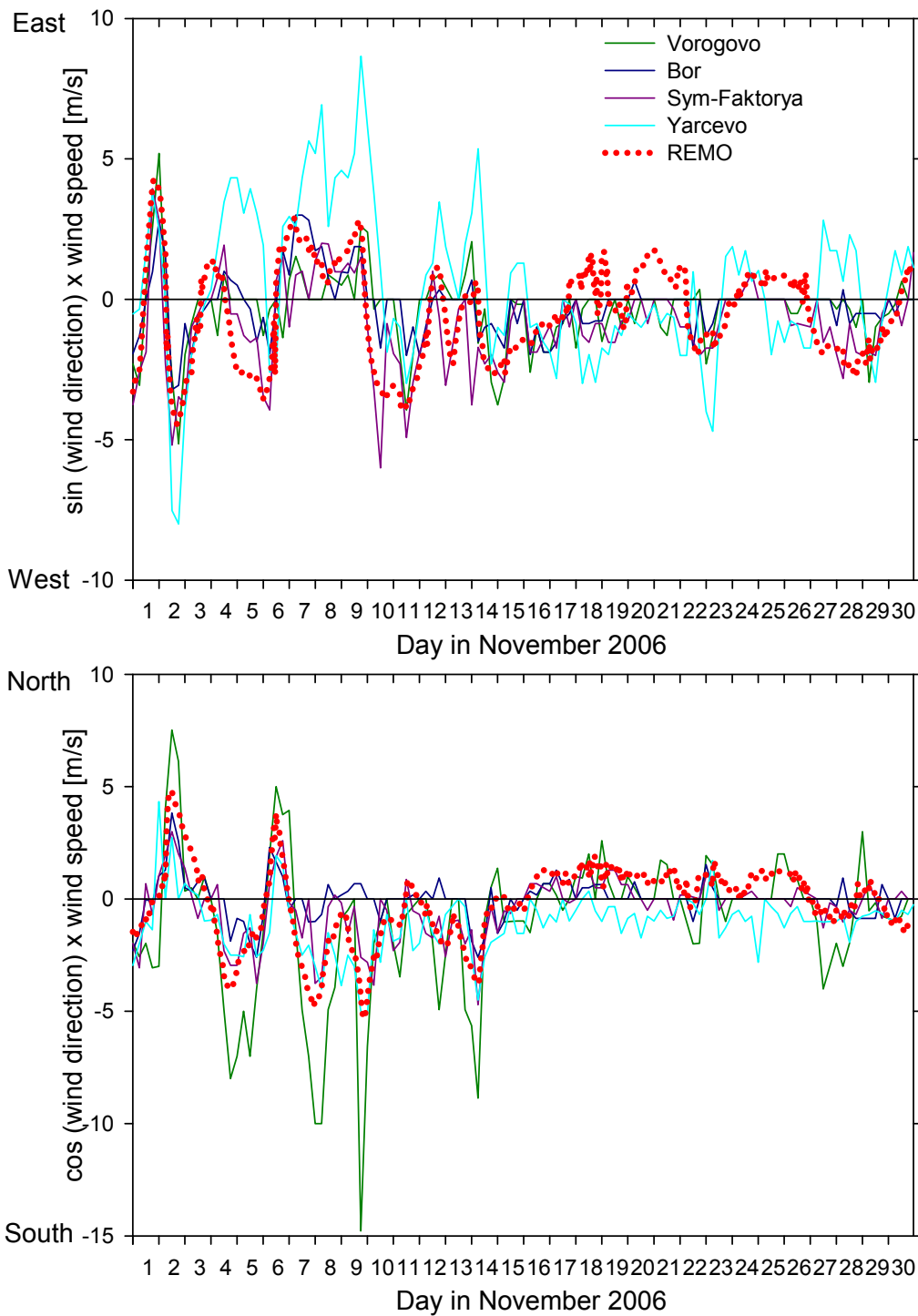
### **6.3.3 Wind direction**

Figure 6.4 shows the East-Western component (top panel) and the North-Southern component of the wind vector from four localities around ZOTTO and REMO simulations in July 2006. The wind vector components are shown as a sine (top panel) and cosine (bottom panel) of the wind direction angles multiplied by wind speed values. This plotting method avoids the uncertainty in the wind direction that occurs when wind speeds are very low. Figure 6.5 shows the same definitions but for November 2006. Both figures (6.4 and 6.5) demonstrate good agreement between the data and REMO simulations, with the latter being smoother and less scattered. Within the data record in November 2006 Yarcevo station is quite different from the others in both East-West and North-South directions. Vorogovo station seems to be exposed to higher Northern or Southern winds during both months shown much more than other stations. The simulations also show quite good agreement with the measurements over the period of the ‘cold events,’ demonstrating the change of wind direction around 22 November, when the stratification of CO<sub>2</sub> column was disturbed by higher wind speeds. It appears to be likely that not only the increased wind speed but also different wind direction

contributed to a change in the stratification of the air column and relevant CO<sub>2</sub> concentration observed during the ‘cold events’.



**Figure 6.4:** Top panel: East-Western component of the wind vector relative to its wind speed as observed at four localities around ZOTTO and REMO simulations in July 2006. Bottom panel: North-Southern component of the wind vector for the same period.



**Figure 6.5:** Top panel: East-Western component of the wind vector relative to its wind speed as observed at four localities around ZOTTO and REMO simulations in November 2006. Bottom panel: North-Southern component of the wind vector for the same period.

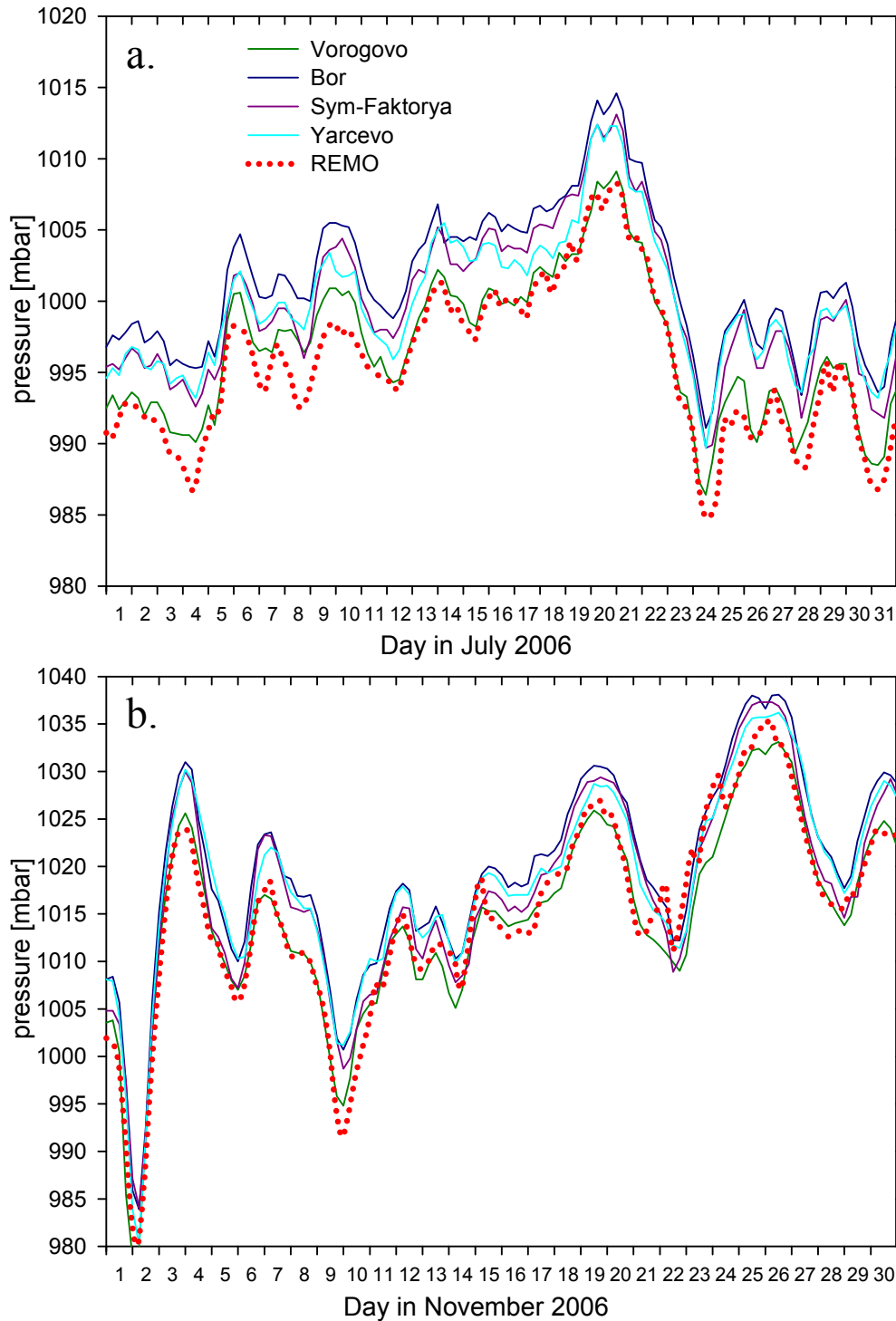


**Figure 6.6:** Surface pressure as observed at four localities around ZOTTO and REMO surface pressure simulations in July (a) and November (b) 2006.

### 6.3.4 Surface pressure

Figures 6.6a. and b. show surface pressure as observed at four localities around ZOTTO compared to the results from REMO simulations for July (a) and November (b) 2006. All four observation records show very similar patterns to each other, but with

Vorogovo pressure (solid green line) being consistently lower than the other three sites, which is most likely a result of a calibration offset, rather than a reflection of its altitude since this station is situated at the lowest altitude among those shown in the Figure. The simulations (dotted red line) practically overlap with the surface pressure values from Vorogovo during both summer (a) and winter (b) months. The general agreement between the measured and modelled pressure is very good. The slightly lower (the order of a few mbar) modelled pressure at ZOTTO is a consequence of its highest altitude among the chosen stations.

### 6.3.5 Vertical mixing

In the previous sections of this chapter, I discussed the simulations of several common meteorological parameters (temperature, wind speed, wind direction and surface pressure) and compared them to observations from four stations around ZOTTO. Such comparisons, however, do not provide any information about the vertical structure of the atmosphere since the observations were made at ground level. Nevertheless, it is very important to consider the vertical dimension of the model domain, as it is often a limiting factor in atmospheric model simulations.

Under low wind speed conditions the ambient concentration of a tracer is determined by its source at the ground as well as the volume of air where the mixing and dilution of this concentration occurs. During daytime, when vigorous vertical mixing prevails, this air volume represents the atmospheric boundary layer (ABL, or mixed layer, see Fig. 1.4). Even when the local sources are represented relatively well in the model, errors in vertical mixing often lead to large discrepancies in modelled concentrations. In this section I present the results of the comparison between the observed and modelled patterns of vertical mixing and their influence on the concentration of an inert air tracer, namely CO<sub>2</sub>, assuming that the errors resulting from the modelling of the sources themselves are relatively small.

Potential temperature is a common and convenient measure of the vertical stability of an air column, because it is directly proportional to the amount of energy required to transport an air parcel from lower to higher layers of the atmosphere, and is a function of vertically changing atmospheric pressure. Potential temperature ( $\theta$ ) of an air parcel can be calculated from Poisson's equation:

$$T_{potential} = \theta = T \times \left(\frac{P_0}{P}\right)^{R/c_p}, \quad \text{where}$$

$T$  is the absolute temperature of the air parcel (in Kelvin),  $P$  is the actual pressure of the air parcel,  $P_0$  is a standard reference pressure (1000 mbar),  $R$  is the air gas constant

( $287 \text{ J K}^{-1} \text{ kg}^{-1}$ ) and  $c_p$  is the heat capacity of air at constant pressure ( $1004 \text{ J K}^{-1} \text{ kg}^{-1}$ ).  $\theta$  can also be considered as the temperature of the air parcel if it were brought (adiabatically) to the pressure  $P_0$ . When potential temperature increases with height, i.e.  $\frac{\partial \theta}{\partial z} > 0$  (where  $z$  is the height of the air column), vertical mixing is suppressed, which corresponds to stable stratified conditions. When  $\frac{\partial \theta}{\partial z} < 0$ , the atmosphere is unstable with vigorous vertical mixing (convection). The transition between these two conditions defines the height of the atmospheric boundary layer, or so-called mixed layer.

Vertical profiles of potential temperatures around ZOTTO in both summer and winter were previously reported by Lloyd *et al.* [2002a] from several aircraft campaigns, demonstrating a very high ABL during daytime in summer (up to 2.5-3.0 km). The data which I used for the following model-observations comparison study were collected as a part of routine radiosonde measurements of vertical air columns at Bor (see Table 6.2 for details). The radiosondes were collected twice a day (7:00 and 19:00 local time (UTC+7 hours)) and their measurements were interpolated to the vertical levels of REMO simulations. I use the profiles collected at 19:00 as proxies for well-mixed daytime air columns. Normally, the period when the height of the mixed layer is at its maximum extends over about 6 hours (from 11:00 to 17:00) but no radiosonde measurements were available at this time. Especially in summer, these later measurements would not result in any significant changes in the vertical air stratification.

Figure 6.7 presents six correlation plots (from a. to f.) of radiosonde potential temperature and REMO potential temperature at six vertical levels (31, 129, 297, 500, 1127 and 2224 m agl) representing the possible range of typical heights of the ABL at ZOTTO. The radiosonde data and simulations are shown for the period from 01 January 2006 to 30 April 2007. Linear curves (black lines) were fitted to the points resulting in the equations shown above each plot. The errors of the fitting procedures are shown as standard errors (SE; in degrees of temperature). The blue and red lines define the limits of the 95% confidence and prediction intervals, respectively. The purpose of the figure is to show the discrepancies in the observed and simulated potential temperatures, particularly at the heights up to 300 m (plots a, b and c), and thus in the vertical structure of the ABL. These discrepancies were the most profound at the lower levels, with the largest regression errors and differences in slopes. In contrast, Figure 6.7f demonstrates that at heights of over 2 km the potential temperature is well captured by

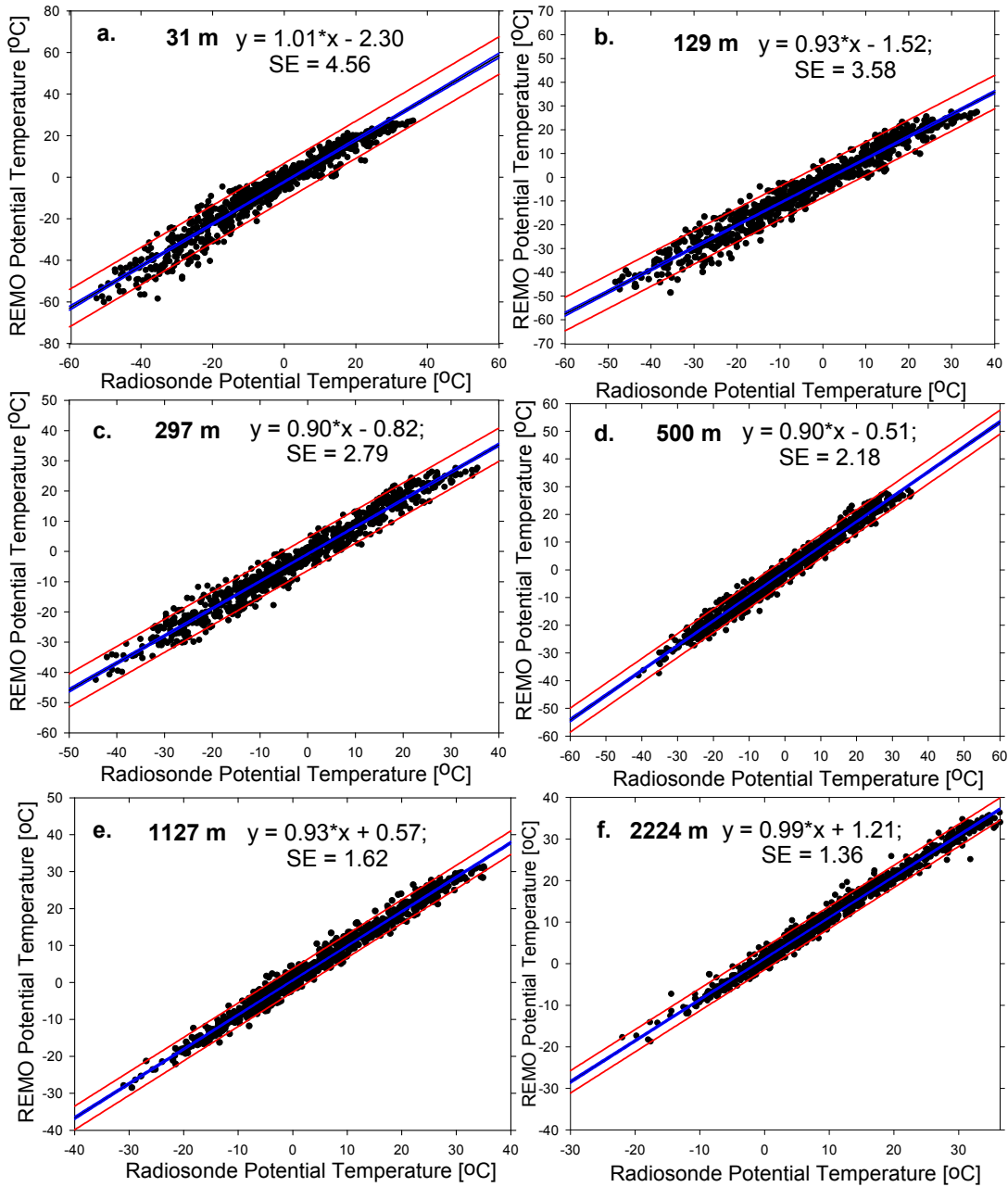


**Figure 6.7:** Correlation between the radiosonde potential temperature and simulated potential temperature at six vertical layers (plots a. through f.) of the REMO vertical domain (31, 129, 297, 500, 1127 and 2224 m), which represent a vertical profile over the atmospheric boundary layer. The data (and simulations) shown are from 01 Jan 2006 to 30 Apr 2007. The black solid line (covered by the blue lines in most plots) represents a linear fit to the data points. The blue lines enclose the 95% confidence interval of the fitting, while the red lines indicate the 95% prediction interval. The equation for each linear fit is given on the top of each plot. The errors of the fitting procedure are expressed as standard errors (SE) in °C.

the REMO simulations, with the slope of the fitted curve being close to 1.0 and the smallest SE of the fitting procedure (amongst the presented plots).

The discrepancies between the observed and simulated potential temperatures at the lower vertical layers suggest different patterns of the air vertical mixing thus resulting in differing vertical distribution of air tracers.

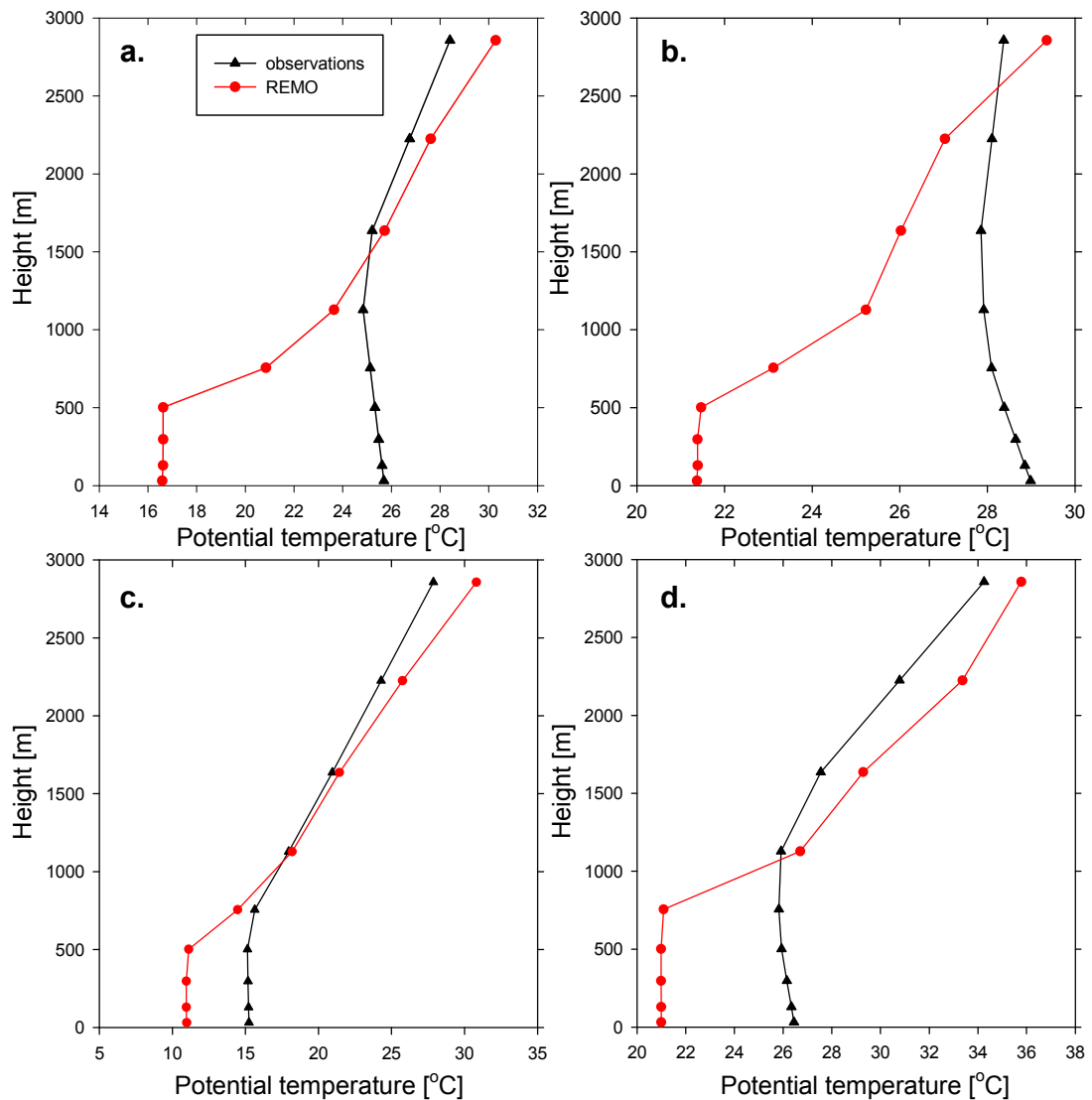


**Figure 6.8:** Vertical profiles of potential temperatures from radiosonde (black triangles and line) and REMO simulated potential temperatures (red circles and line) during four evenings (19:00 local time (UTC+7 hours)) in summer 2006: a) 04 June; b) 05 June; c) 08 June; d) 01 July.

Figure 6.8 shows vertical profiles of potential temperature from radiosonde (black triangles and line) and simulated potential temperatures (red circles and line) during four evenings in summer 2006 ((a) 04 June, (b) 05 June, (c) 08 June and (d) 01 July respectively). The profiles were obtained during a period when the air column was presumably well-mixed. In addition, the selected evenings were characterised by very low horizontal wind speeds (0-3 m/sec) thus allowing me to assume that the horizontal transport during these days was minimal, and it was the vertical mixing that mainly determined the ambient signatures of the air tracers. All four profiles show significant differences between the observed and simulated heights of the ABL. This can be seen most clearly in the plots a. and b., where the simulated height of the ABL was about 500 m in REMO, whereas the radiosonde data show that it was at least as high as 1500 m, which is reflected in the shape and slope of potential temperature

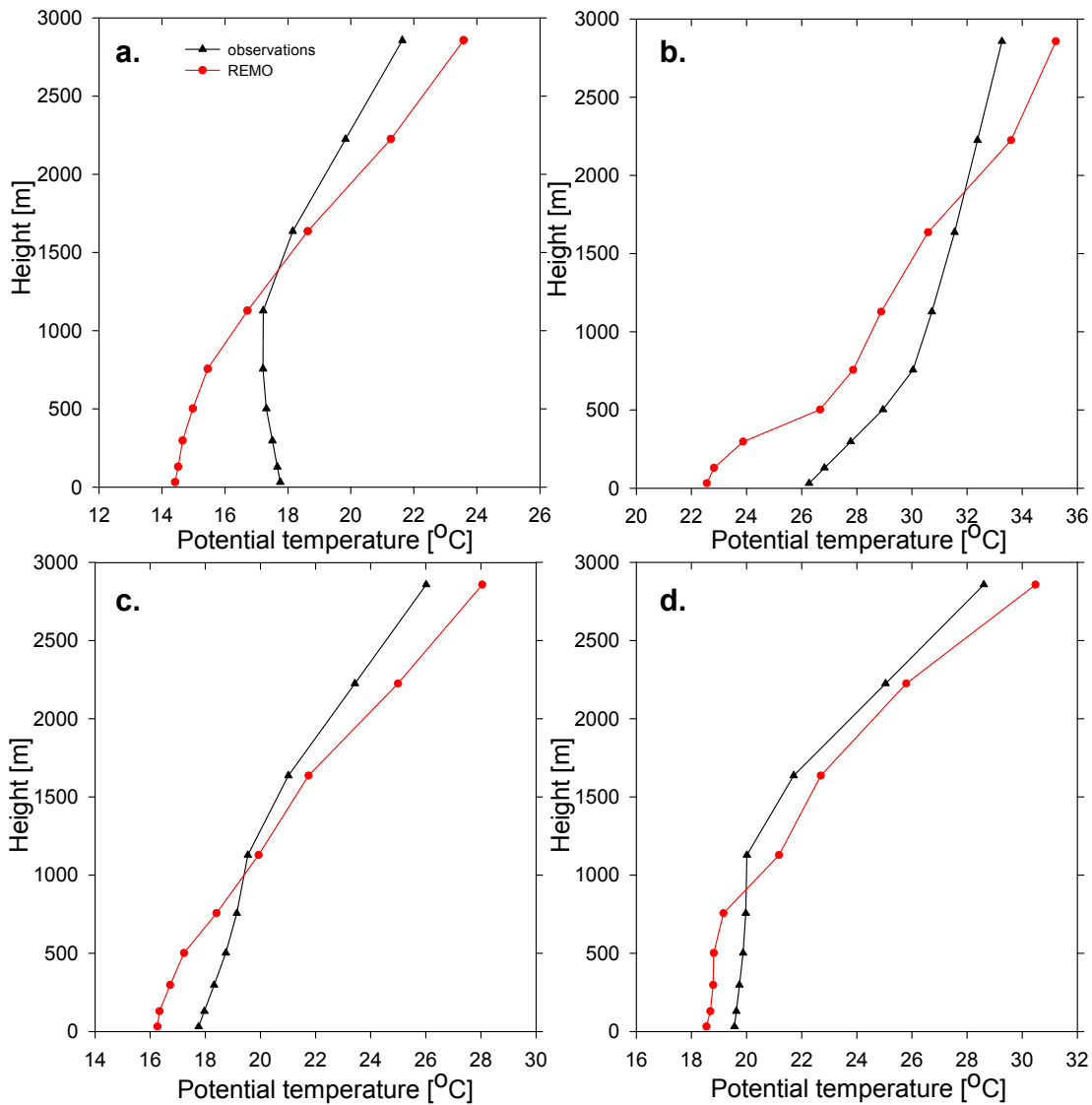


**Figure 6.9:** Vertical profiles of potential temperatures from radiosonde (black triangles and line) and REMO simulated potential temperatures (red circles and line) during four evenings (19:00 local time (UTC+7 hours)) in summer 2006: a) 15 June; b) 23 July; c) 25 July; d) 27 July.

changes (with height). Not surprisingly, the comparison between the observed and simulated concentrations of  $\text{CO}_2$  (see Figure 6.14a. below) show very large discrepancies during these two evenings of -16.5 and -23.2 ppm respectively (calculated as the REMO trimmed daily averages minus the ZOTTO trimmed daily averages). In other words, REMO significantly under-estimated the ambient  $\text{CO}_2$  concentrations during these two days, most likely owing to the fact that the simulated vertical mixing was insufficient as the height of the ABL was about 1 km lower than shown by the radiosonde observations. Since the surface acts as a strong  $\text{CO}_2$  sink in summer during the daytime, it is the height of the ABL that mainly defines the ambient  $\text{CO}_2$  concentration. During these two evenings the simulated height of the ABL was much lower than that observed thus leading to the lower atmospheric levels of  $\text{CO}_2$ . The simulated height of the ABL is also more shallow on 08 June (plot c.) but not as much

as during those two days above. As a result I found the smallest (out of these four days) discrepancy of the ambient CO<sub>2</sub> (~-6.7 ppm, see Figure 6.14a.).

In contrast to the profiles shown in Figure 6.8, the four profiles in Figure 6.9 demonstrate much more similar conditions in the model and observations with respect to the heights of the ABL. Correspondingly small CO<sub>2</sub> discrepancies were observed, with the smallest on 15 June and 23 July (0.63 and 0.1 ppm respectively). This good agreement can be explained by very similar vertical profiles of the observed and simulated potential temperatures. The profiles in the lower plots (c. and d.) of the Figure 6.9 show larger differences than in plots a. or b., which is consequently reflected by larger CO<sub>2</sub> discrepancies of 1.97 and 1.68 ppm respectively. In addition to differences in the slopes of potential temperature versus height, there almost always exist some offsets between the observed and simulated values of the potential temperature of at least 2-4°C but often much larger. These offsets are typically more pronounced at the lower levels, corresponding with the findings surrounding Figure 6.8 above.

Next I compared the vertical profiles obtained during much colder times of the year, i.e. the ZOTTO ‘cold events’ (17-27 November 2006). In winter, the surface is no longer a strong sink of CO<sub>2</sub>, and as it covered by snow I would not expect it to be a large source either. However, the phenomena of the ‘cold events’ have not been fully understood, as the sources of such high CO<sub>2</sub> emissions at this time of the year remain unclear. Figure 6.10 shows both observed (a) and simulated (b) CO<sub>2</sub> concentrations during the cold events of 17-27 November 2006. Taking into account the fact that these events were most likely the result of local meteorological and micro-climatic conditions at ZOTTO, it would be very difficult for any model, even a high resolution one, to simulate such conditions. Nevertheless, there is a resemblance in the shape of the simulated CO<sub>2</sub> accumulation during the beginning of the period. However, the model fails to predict the ‘second wave’ in the CO<sub>2</sub> build-up at 52 m after 24 November. Meteorological data show that the winds got stronger and changed direction (Figure 6.5) around 23 November, which probably resulted in breaking up the highly stratified air column and thus more vigorous mixing, which was then followed by another period of very calm conditions and further accumulation of CO<sub>2</sub> near the ground. But these latter events were not reflected in the modelled CO<sub>2</sub> simulations. The vertical profiles of potential temperatures for two days during the cold events, 21 November (c) and 25 November (d) in Figure 6.10 are very similar to each other. In both cases the model

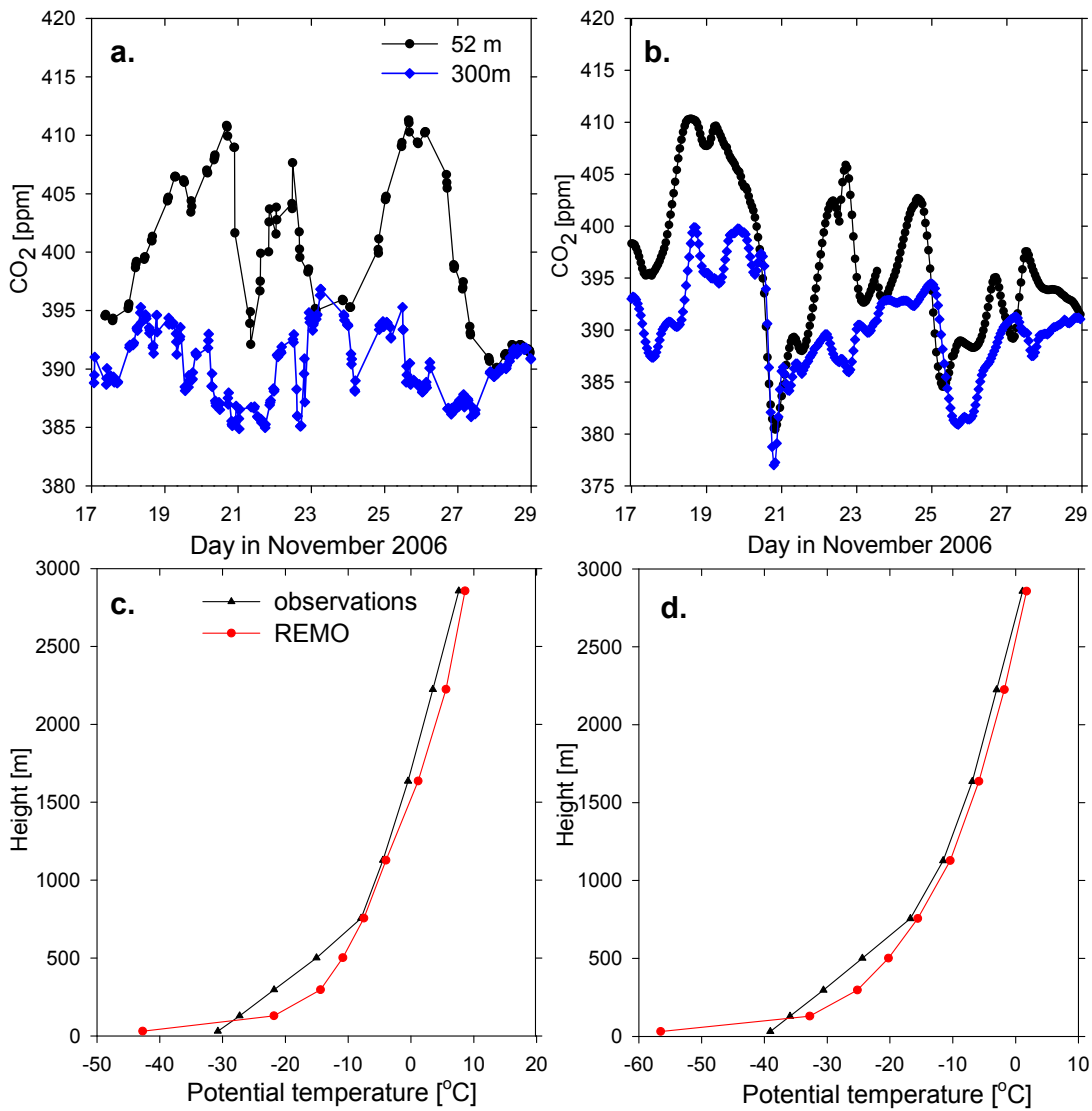


**Figure 6.10:** Observed (a) and simulated (b) ambient CO<sub>2</sub> concentrations at ZOTTO over the period of ‘cold events’ in November 2006. Data and simulations from 52 and 300 m are shown with black filled circles and blue diamonds in both plots respectively. Vertical profiles of the observed (black triangles and line) and simulated (red circles and line) potential temperatures on 21 November (c) and 25 November (d) 2006.

predicts much lower temperatures than those observed (by nearly 20°C in d.) close to the ground. Both observations and the simulation show a very stratified undisturbed air column (in fact, REMO shows this even more than the observations).

While the meteorological conditions such as observed during the cold events are not uncommon, they are not typical for the region around ZOTTO. To extend the comparison between the data and the model simulations to more ‘typical’ weather conditions, I plotted another set of vertical profiles (see Figures 6.11 and 6.12) for winter-early spring 2006-7. Figure 6.11 shows four evening profiles during those days when the discrepancies between the observed and simulated CO<sub>2</sub> concentrations were large: 12.4, 12.0, 8.5 and 22.2 ppm for plots a., b., c., and d. respectively. All differences are positive, meaning that the model significantly overestimates the CO<sub>2</sub>

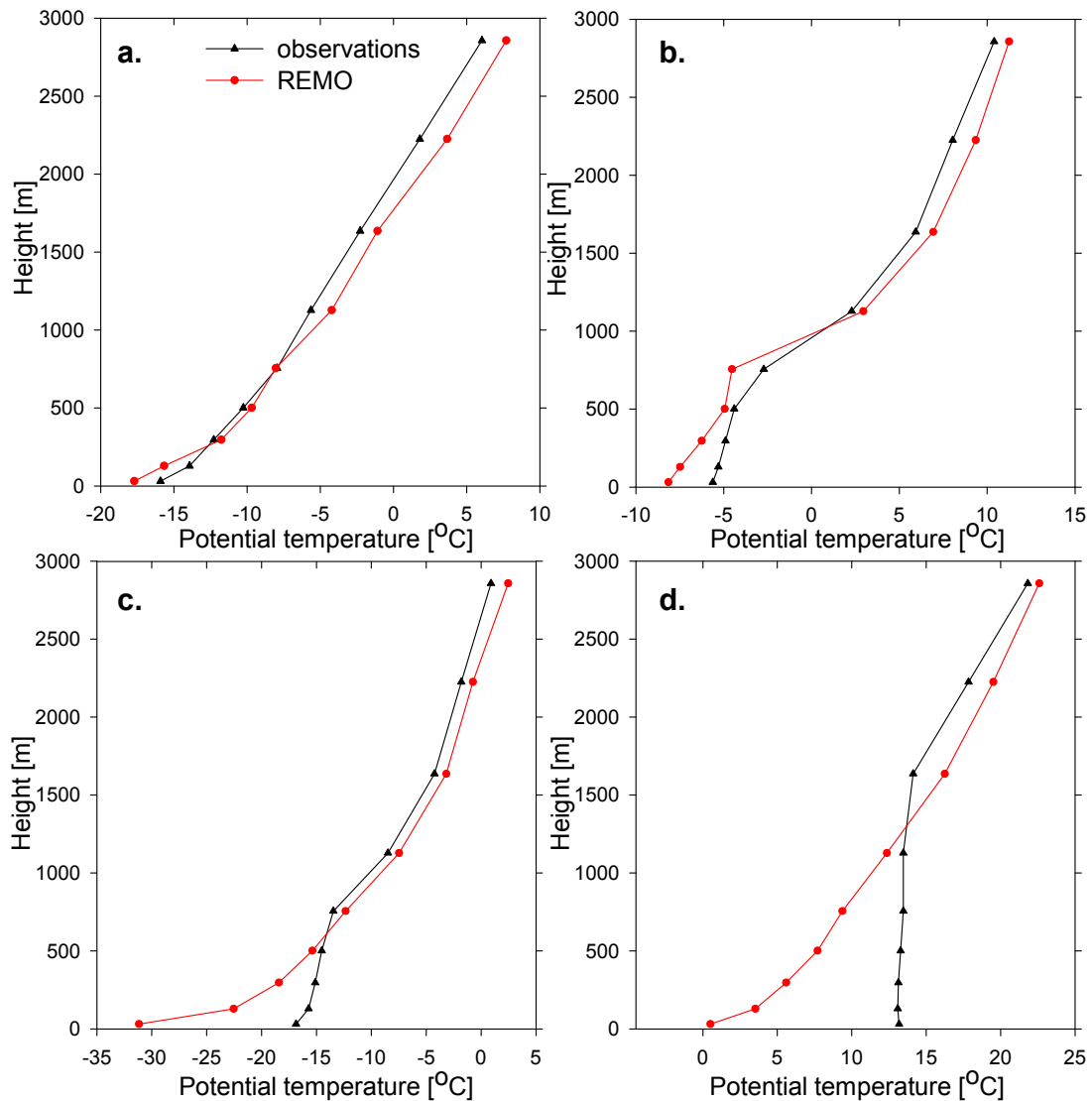


**Figure 6.11:** Vertical profiles of potential temperatures from radiosonde (black triangles and line) and REMO simulated potential temperatures (red circles and line) during four afternoons (19:00 local time (UTC+7 hours)) in winter – early spring 2007: a) 11 Jan; b) 20 Jan; c) 12 Mar; d) 20 Apr.

concentrations. Winter profiles are also more difficult to interpret. The surface is no longer a sink for  $\text{CO}_2$ , and ambient levels are determined by the  $\text{CO}_2$  brought from some distance away (or produced locally) from fossil fuel or wood burning. In contrast to summertime, the height of the ABL is much lower and not as well defined in winter [Lloyd *et al.*, 2002a; Styles *et al.*, 2002], which can be seen in Figures 6.11 and 6.12 as well. In winter, the surface is no longer well-heated during daytime, which suppresses vertical mixing and can lead to strong stratification of an air column, especially during low wind conditions. Once again, I selected only days with low wind speeds (0-3 m/s) for this comparison exercise. The profiles in Figure 6.11a. and b. are difficult to interpret. Despite the fact that they look quite different from each other, the  $\text{CO}_2$  discrepancies between the model and the observations are practically the same. This is a good example, however, showing that the ambient level of  $\text{CO}_2$  is not solely a function

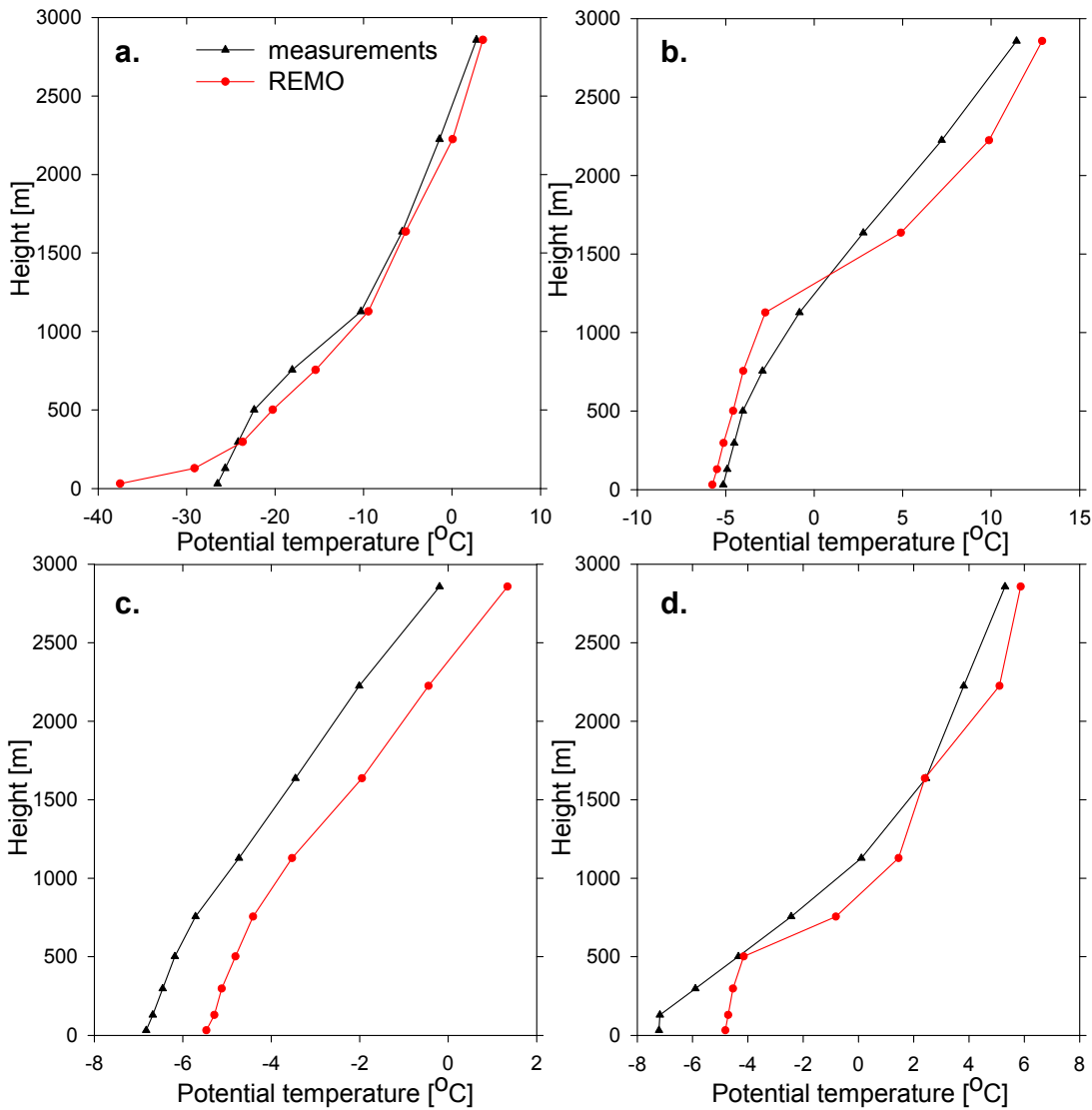


**Figure 6.12:** Vertical profiles of potential temperatures from radiosonde (black triangles and line) and REMO simulated potential temperatures (red circles and line) during four afternoons (19:00 local time (UTC+7 hours)) in winter 2006-7: a) 11 Dec; b) 17 Dec; c) 01 Jan; d) 06 Jan.

of vertical mixing, although it does play an important role, especially in summer. Profiles in Figure 6.11c. and d. demonstrate much higher ABL's in the observations compared to those in the model. This explain the significantly lower observed CO<sub>2</sub> concentrations compared to those predicted by the model.

All CO<sub>2</sub> values used for this comparison were taken from 52 m for both the observations and REMO. Also, it is important to remember that the CO<sub>2</sub> measurements were made at ZOTTO whereas the radiosonde data were collected about 100 km to the north in Bor, which obviously means that the comparison does not account for micro-meteorology and local emissions.

Figure 6.12 shows vertical profiles during another four evenings in December 2006 – January 2007, when only small discrepancies in CO<sub>2</sub> ambient levels between observations and REMO were recorded. For three out of four profiles (a., c. and d.) the

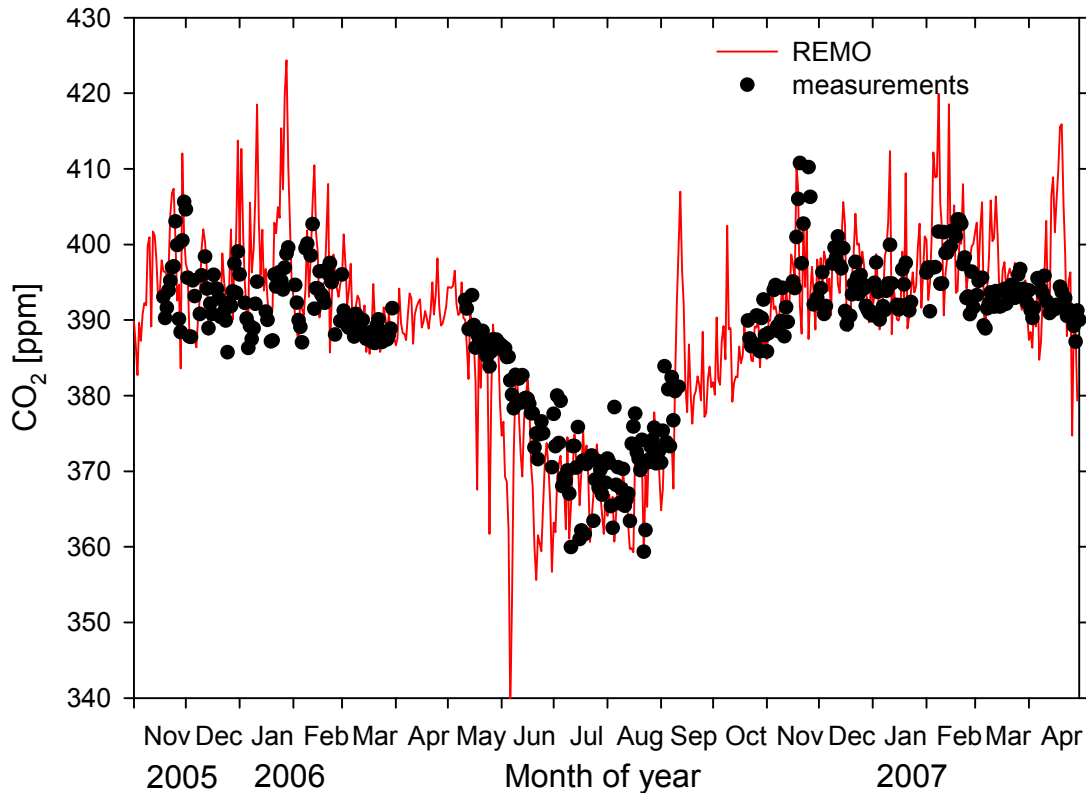


**Figure 6.13:** Observed (black circles) and simulated (red line) seasonal cycles of CO<sub>2</sub> at ZOTTO. All plotted data and simulations are shown as trimmed daily averages at 52 m (averages calculated from data between 11:00 – 17:00 local time only).

differences are small but still positive – 0.94, 0.43 and 0.27 ppm respectively. The profile shown in plot b. in Figure 6.12 demonstrates an unusual situation where the model demonstrates slightly lower CO<sub>2</sub> values than the observations (-0.42 ppm). Although this difference is not very significant, one can see a slightly more shallow ABL in the observations during this afternoon, which could explain the discrepancy (similar to my explanation of winter profiles in Figure 6.11).

The conclusion that can be drawn based on this study of vertical profiles is that vertical mixing is frequently insufficiently modelled in REMO, resulting in more shallow ABL's (than that in the observations), and thus influencing the concentration signatures of air tracers such as CO<sub>2</sub>. While this effect is most pronounced in summer, yielding anomalously low CO<sub>2</sub> concentrations during the daytime, errors in the ABL also exist in winter yielding too high CO<sub>2</sub> concentrations.

## 6.4 Atmospheric concentrations of CO<sub>2</sub>: model-observations comparison

CO<sub>2</sub> observations available for the comparison with the model simulations cover an 18 month period (from November 2005 to May 2007). This overlapping period is not very long, however, it offers the possibility of comparing the main features of the

seasonal cycles as well as shorter-term variations of CO<sub>2</sub>: diurnal cycles, synoptic events and fire events. The latter is discussed separately in Section 6.6 below.

Figure 6.13 displays observed (black circles) and REMO simulated (red line) seasonal cycles of CO<sub>2</sub> at ZOTTO at 52 m. The agreement between the two records is generally good, however, there exist certain problems in the way the model simulates the daytime daily averages of CO<sub>2</sub> (from 11:00 to 17:00, when the air is well-mixed), which is equally valid for both summer 2006 and winter 2007. For the convenience of the discussion, the summer 2006 and winter 2007 diurnal CO<sub>2</sub> variations are shown in Figures 6.14a. and b. respectively, on an expanded scale. The summer daytime averages of CO<sub>2</sub> at 52 m are shown in Figure 6.14a. for both the observations (black circles and line) and REMO (red line). The 52 m data were used owing to the longer record available from this height of the tower as the tower was only built to 300 m by October 2006. I discussed the comparison between the trimmed daily averages at 52 and 300 m in Chapter 5, and the interpolated differences between the daytime CO<sub>2</sub> concentrations from these two heights are shown in Figure 5.2. All values shown in the Figure are the daily trimmed averages, for both the observations and REMO, and include the CO<sub>2</sub> values solely from 11:00 to 17:00 local time (UTC+7 hours).

Figure 6.14a. shows an interesting feature in the simulated CO<sub>2</sub>. From the beginning of May 2006 up to the middle of July large discrepancies are frequently observed between the observations and the model, with the latter consistently predicting much lower CO<sub>2</sub> concentrations during the daytime. In contrast to the first part of summer, the second part is characterised by good agreement between the two records.

There could be several reasons responsible for the mismatch in the first half of this period. The two main reasons are discrepancies in the CO<sub>2</sub> fluxes which might have originated from errors in the modelled carbon fluxes by the BIOME-BGC model, and second, errors in the vertical mixing of the REMO domain, as discussed in detail in section 6.3.5 above. The results of my comparison of observed and simulated vertical profiles suggest insufficient summertime vertical mixing in REMO, resulting in more shallow ABL's (see Figures 6.8 and 6.9) and thus significantly (and consistently) lower (than observed) daytime concentrations of CO<sub>2</sub>. Figure 6.14b. presents winter and early spring CO<sub>2</sub> records, showing consistently higher CO<sub>2</sub> values predicted by the model which is in contrast to the summer record. The vertical mixing during winter months and the 'cold events' in particular were discussed in section 6.3.5 above, and illustrated in Figures 6.10, 6.11 and 6.12. Similar to summertime, there seem to be discrepancies in the wintertime vertical mixing, although they are more difficult to interpret owing to a more complex CO<sub>2</sub> source – sink relationship.

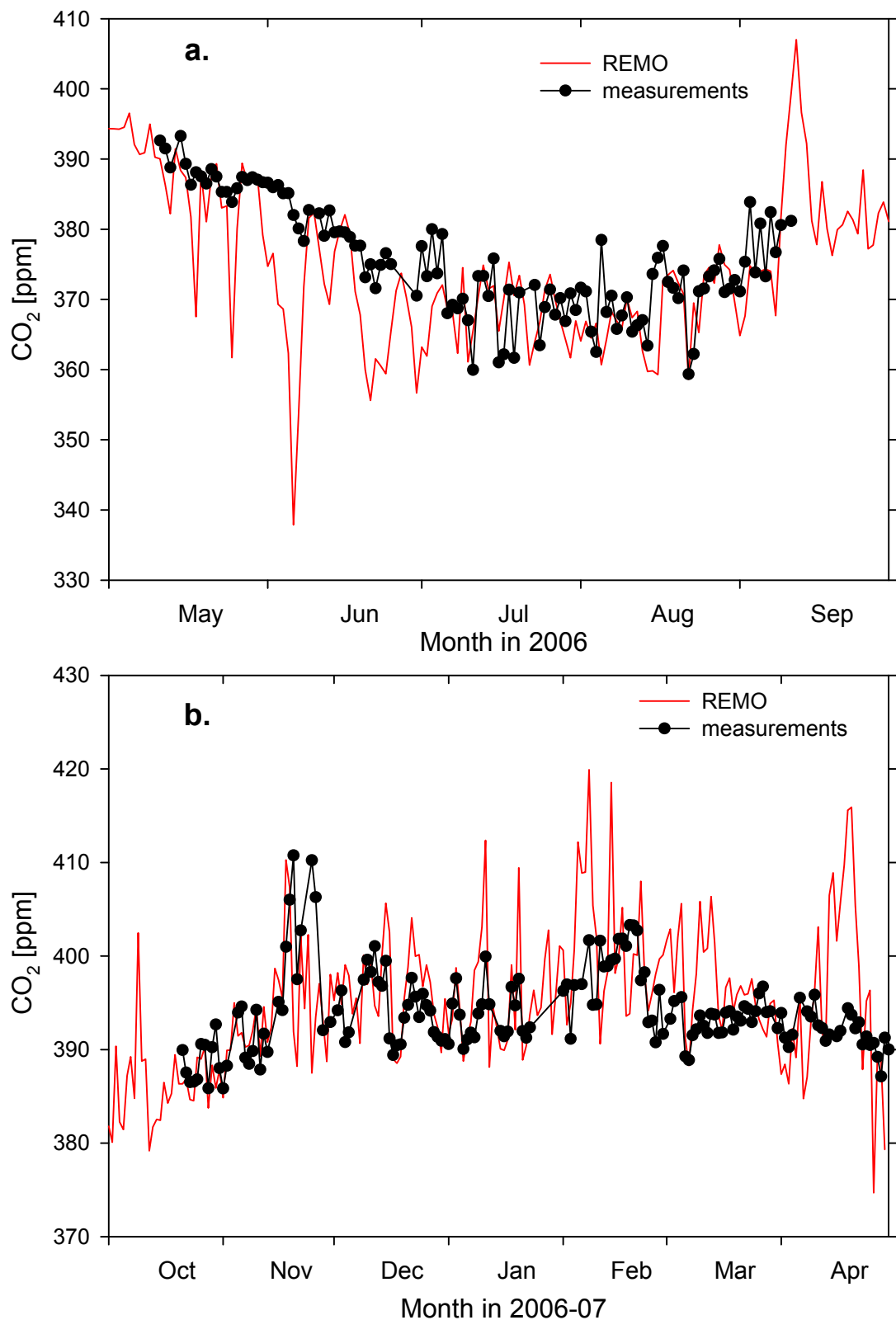


**Figure 6.14:** Observed (black circles and line) and simulated (red line) seasonal cycles of CO<sub>2</sub> at ZOTTO in May–Oct 2006 (a) and in Oct 2006–May 2007 (b). All observations and simulations are trimmed daily averages (from 11:00 – 17:00 local time) at 52 m.

Nevertheless, it is also possible that the errors in the modelled carbon fluxes within the BIOME-BGC model could have contributed to the observed discrepancies

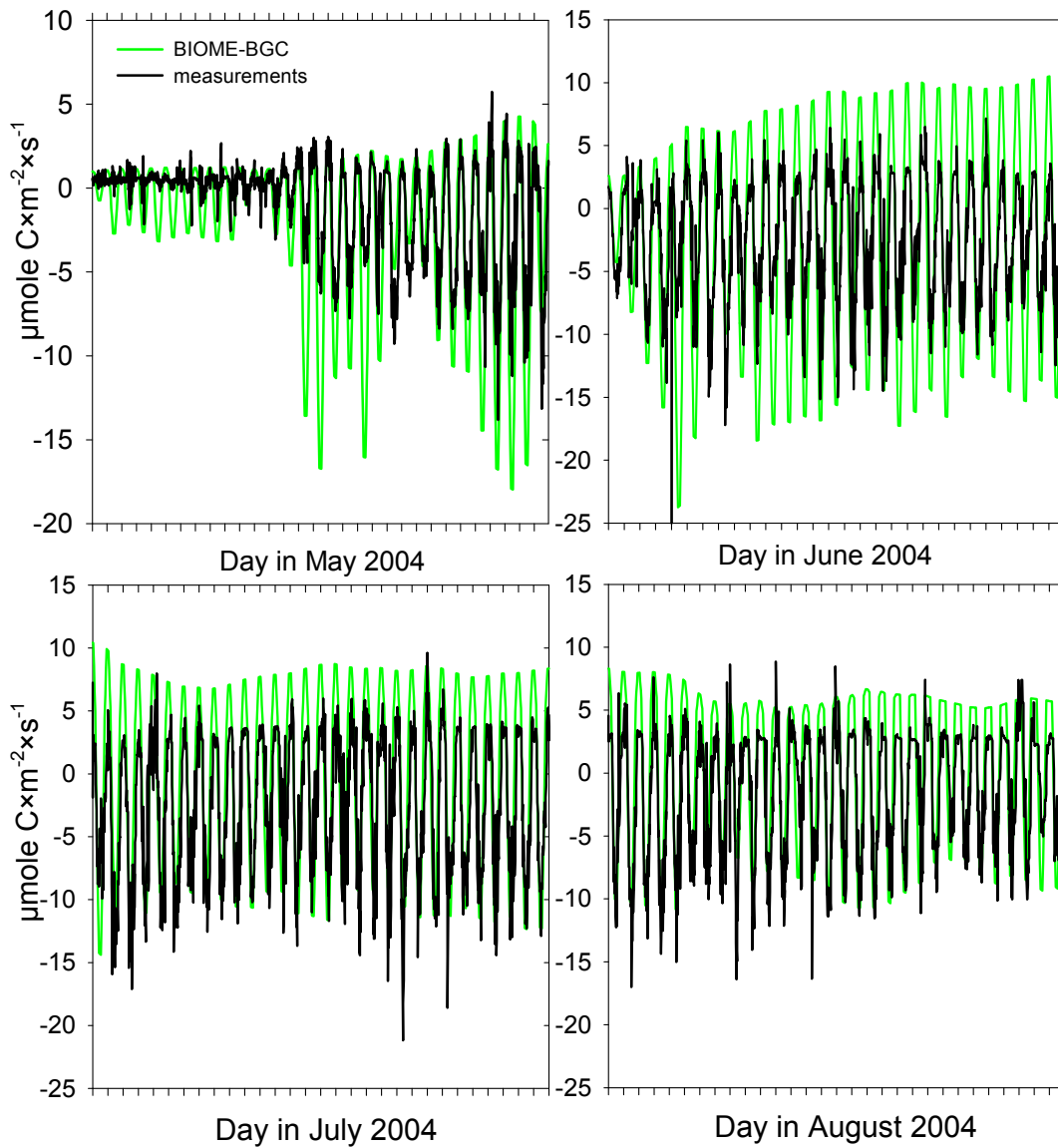


**Figure 6.15:** CO<sub>2</sub> fluxes as observed at ZOTTO (black line) and simulated by the BIOME-BGC biosphere model (green line) in spring – summer 2004. Positive fluxes indicate a source of CO<sub>2</sub> to the atmosphere, whilst negative fluxes indicate CO<sub>2</sub> uptake by the biosphere. Observed flux data are courtesy of O. Shibistova (Sukachev Institute of Forest, Krasnoyarsk, Russia) and C. Rebmann (MPI-BGC); BIOME-BGC flux simulations were provided by K. Trusilova (MPI-BGC) with diurnal cycles reconstructed by C. Rödenbeck (MPI-BGC).

between the observed and modelled daytime CO<sub>2</sub> concentrations. To test this hypothesis I compared the observed (a) and modelled (b) net CO<sub>2</sub> fluxes in Figure 6.15. Flux measurements near ZOTTO were only operational until 2005, and thus the results shown, over a 4-month period in spring-summer 2004, are prior to my concentration measurements which started in 2005. The May 2004 plot shows much higher (sometimes double) CO<sub>2</sub> uptake predicted by BIOME-BGC with its amplitude increasing towards the end of the month as temperatures become warmer. The June plot shows the same tendency of overestimated daytime CO<sub>2</sub> uptake. In addition, the nighttime CO<sub>2</sub> fluxes appear to be highly overestimated as well (shown by positive

fluxes). This tendency remains until the beginning of July when the agreement between the observed and modelled CO<sub>2</sub> uptake improves. In fact, over the last two months of summer 2004 (July and August) the agreement between the daytime CO<sub>2</sub> fluxes of the observed and modelled records is very good. Nevertheless, the large discrepancies in the nighttime fluxes persist over the whole period of the comparison.

Interestingly, a very similar pattern in the distribution of the CO<sub>2</sub> concentration discrepancies between the observed and modelled records can be seen in Figures 6.14a. and b., that is the largest discrepancies were observed in spring and early summer 2006 with only smaller ones in the second half of summer and autumn. This could mean that the observed errors in the prescribed terrestrial fluxes in REMO could have contributed to the observed discrepancies in the daytime concentrations of CO<sub>2</sub> along with insufficient vertical mixing. The comparison of the observed and modelled CO<sub>2</sub> fluxes over the same period in 2003 (not shown) demonstrated very similar tendencies in the distribution of the CO<sub>2</sub> flux discrepancies as that shown for 2004. Thus, it is apparent that there exist some significant errors in the process description of the BIOME-BGC model that are related to the beginning of the vegetative season at ZOTTO. At this point it is difficult to speculate which processes are modelled incorrectly, though they could be related to large changes in surface albedo or soil moisture content which normally occur at the break between seasons. In addition, there exist some persistent errors in the total respiration fluxes in the model leading to consistently higher nighttime fluxes over the whole vegetative period at ZOTTO, which is probably due to the assumption of the same (and constant) respiration fluxes in both daytime and nighttime in REMO.

These comparisons between measured and modelled CO<sub>2</sub> concentrations at ZOTTO have demonstrated large discrepancies in the daytime values that were observed during both summer and winter periods. The investigation of the reasons for the discrepancies shows that both errors in vertical mixing in REMO and CO<sub>2</sub> fluxes (uptake and respiration) obtained from BIOME-BGC contributed to these discrepancies.

## **6.5 Atmospheric concentrations of O<sub>2</sub> and APO: model-observations comparison**

REMO treats APO as a conservative tracer, and the total APO was modelled as:  

$$APO_{total} = APO_{ocean} - (\alpha_F - \alpha_B) \times C_{foss} = APO_{ocean} - 0.3 \times C_{foss},$$
 where  $APO_{ocean}$  is the APO flux over the ocean, and the term ' $0.3 \times C_{foss}$ ' accounts for the influence of fossil fuel emissions on APO and arises from using global average O<sub>2</sub>/CO<sub>2</sub> molar exchange ratios of 1.4 and 1.1, respectively, for fossil fuel combustion and land biota ( $\alpha_F$  and  $\alpha_B$ ) (see also Table 6.1).

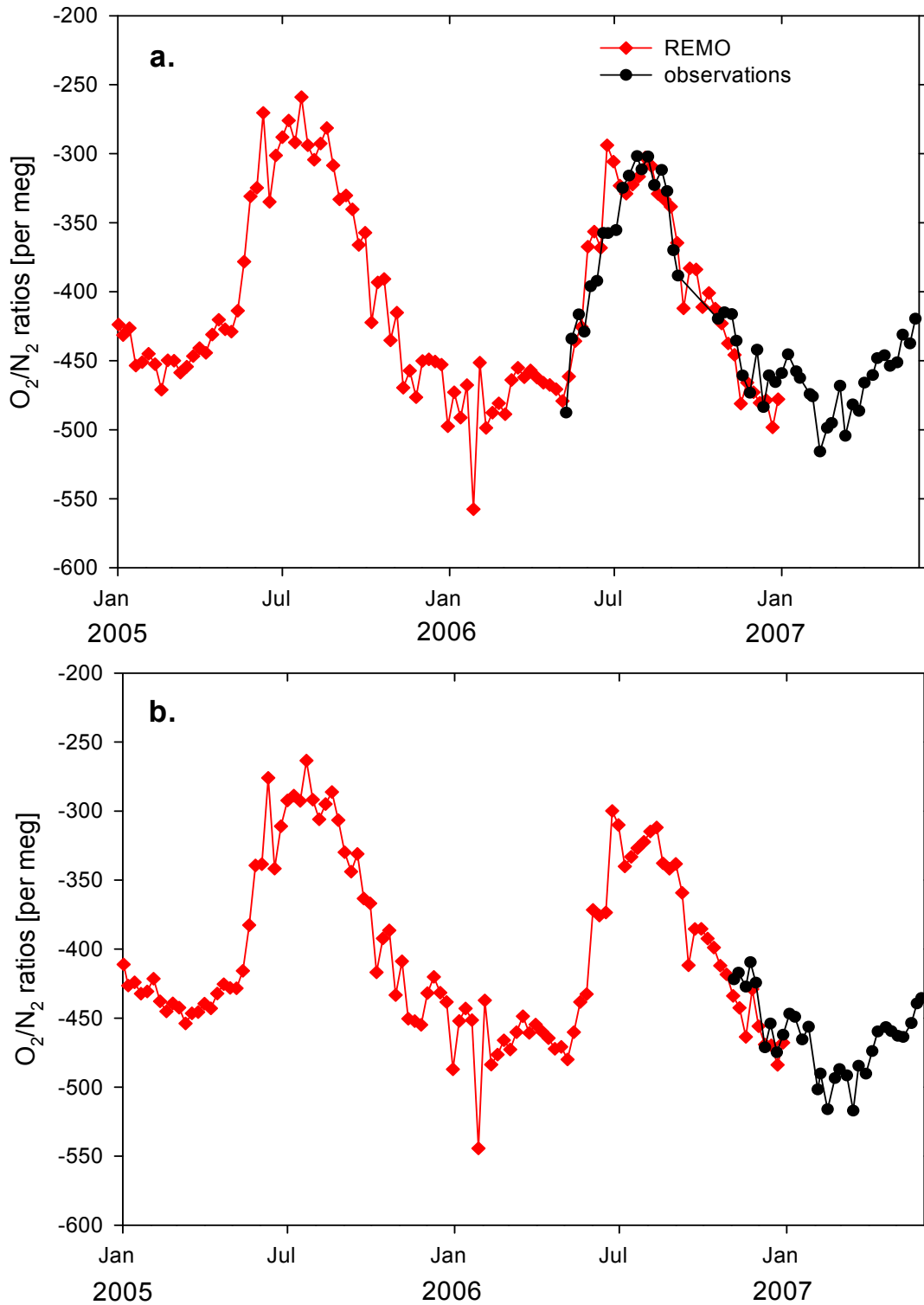
REMO simulations include APO simulations from January 2006 to May 2007. REMO O<sub>2</sub> concentrations (in per meg) were calculated from the simulated APO and CO<sub>2</sub> using the following equation:

$$O_2_{\text{model}} = APO_{\text{total}} - \alpha_B \times (C_{\text{bio}} + C_{\text{foss}} + C_{\text{inversion}})$$

The ZOTTO O<sub>2</sub> calibration scale was subjected to several significant changes. Some of the O<sub>2</sub> calibration scale problems were discussed in Chapter 4, Section 4.4.2. Because of the large errors in the initial MPI-BGC assignment of the O<sub>2</sub> concentrations to WSS cylinders (Figure 4.6), significant retrospective corrections had to be applied to all data that were based on the results from the reanalyses of all calibration cylinders in 2008 (see Section 4.4.2). The corrected data were published in Kozlova *et al.* [2008]. Undoubtedly, however, several technical problems with O<sub>2</sub> analysers themselves have contributed further to these scale problems. One of the most serious ones was a poor-quality O<sub>2</sub> sensor which was in use during spring and summer 2006 leading to a much noisier data record over this period. Based on comparison of the ZOTTO continuous O<sub>2</sub> data with air samples from flasks collected at ZOTTO from October 2006 to May 2007, I decided to make additional corrections to the data in 2009, after their publication. These newly corrected data are shown in all subsequent Figures below. I described in detail all corrections applied to the O<sub>2</sub> data in Chapter 5, Section 5.4.1.

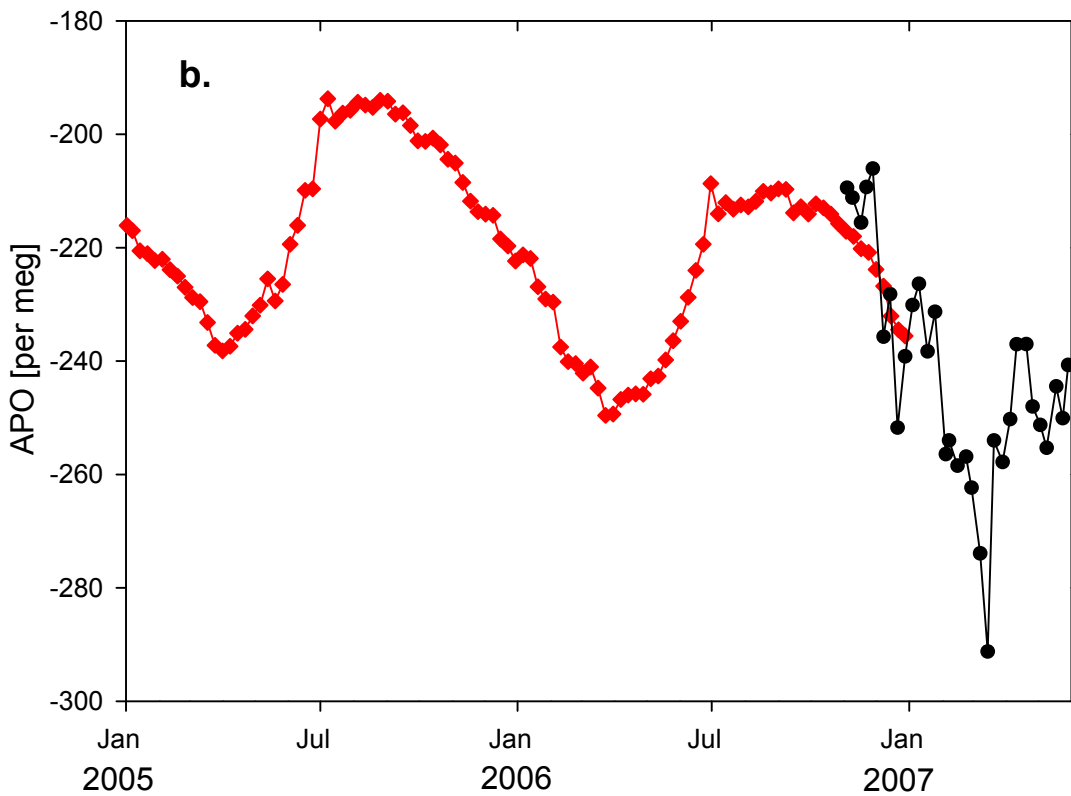
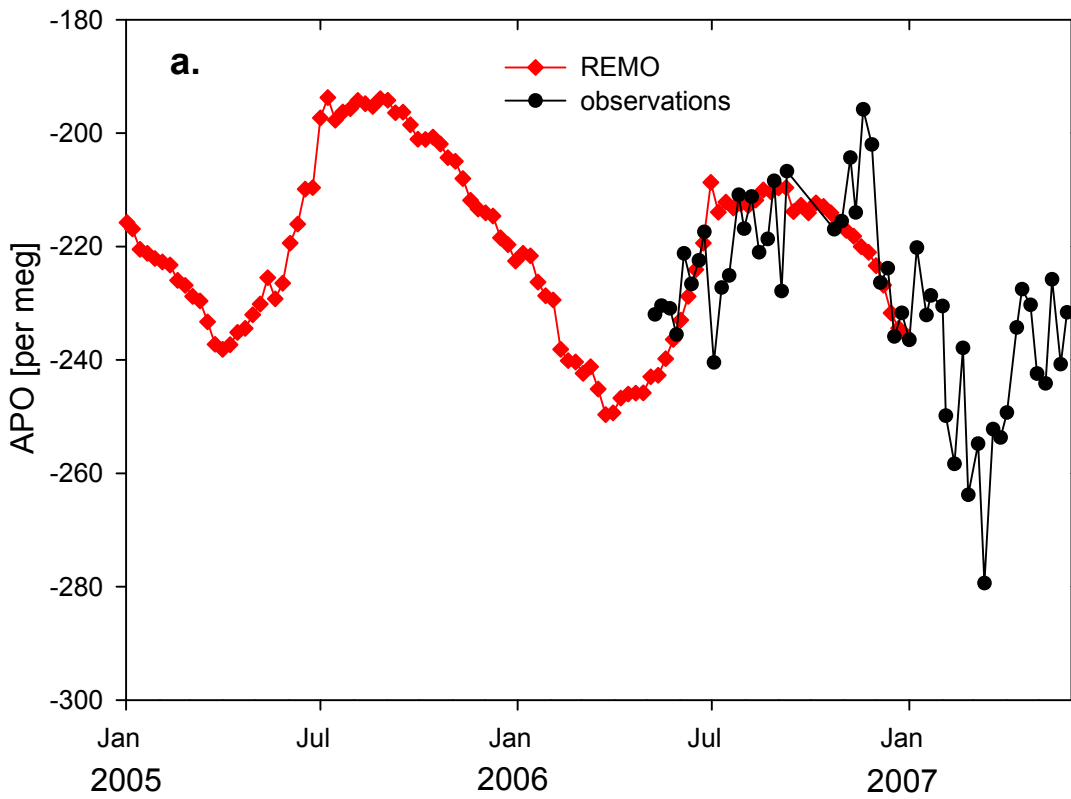
Figures 6.16a. and b. show the comparison between the REMO O<sub>2</sub> simulations with the measurements at 52 and 300 m respectively. Good agreement between the simulations and corrected measurements has given me additional confidence in the new corrections as well as their relevance. The overlap period of the observations and simulations is quite short, particularly for the 300 m height; however, the similarities of the seasonal minimum and maximum, with respect to the REMO simulations from the previous year, can be clearly seen in the Figure.

Figures 6.17a. and b. show the comparison of the modelled and observed APO records as trimmed weekly averages from 52 and 300 m. As expected, the discrepancies between the model and the observations are amplified in the APO record owing to the higher signal-to-noise ratio of APO compared to O<sub>2</sub>. The REMO APO record appears very 'smooth', whereas the APO calculated from the measurements shows higher variability, as well as some distinctive features (high and low excursions) which are not reflected in the simulations. This might be owing to errors in the APO fluxes within the model, particularly due to the continental location of ZOTTO and thus its remoteness from the main APO sources. As this is the first study where REMO APO simulations



**Figures 6.16:** Observed (black circles and line) and simulated (red diamonds and line) seasonal cycles of  $O_2$  at ZOTTO from Jan 2005 to Jun 2007 at 52 m (a.) and 300 m (b.). All observations and simulations are trimmed weekly daytime averages. The 300 m measurements were started only in October 2006 when the tower was fully constructed.

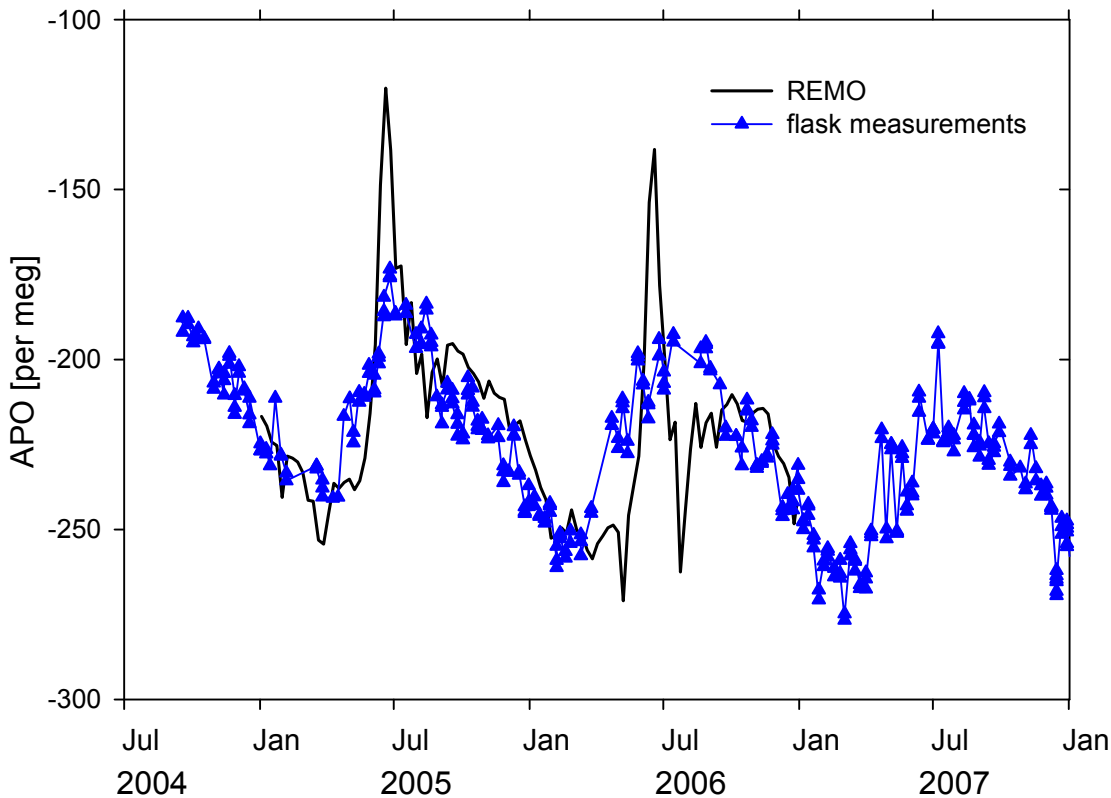
are discussed and challenged with observations, I do not have any other sources of comparisons but those presented above.



**Figures 6.17:** Observed (black circles and line) and simulated (red diamonds and line) seasonal cycles of APO at ZOTTO from Jan 2005 to Jun 2007 at 52 m (a.) and 300 m (b.). All observations and simulations are trimmed weekly daytime averages. The 300 m measurements were started only in October 2006 when the tower was fully constructed.

The comparison of the modelled and observed daily trimmed averages (not shown) revealed similar results, that is, - good agreement for O<sub>2</sub>, including short-term variability in summertime, but overly smooth modelled APO concentrations (practically identical to those in Fig. 6.17a. and b.) compared to much more variable APO measurements at ZOTTO. The better agreement (compared to APO) between the modelled and observed O<sub>2</sub> daily averages in summertime is probably a consequence of the large contribution from the terrestrial biosphere at ZOTTO. In contrast, as mentioned above the APO simulations might be influenced by the coarse resolution and remoteness of its sources that do not allow for any short-term variations in the modelled APO record at ZOTTO.

In Chapter 5, I used data from flask samples collected at Shetland Islands (SIS) as a marine reference site as both SIS and ZOTTO are located at a similar latitude. Figure 6.18 shows APO from flask samples collected at approximately weekly frequency at SIS (blue triangles) and REMO simulated APO (as weekly trimmed averages) at 30 m level (black line) for the overlapping period of the measurements with REMO simulations. The comparison highlights some problems in the simulated APO signal. In contrast to the measurements, the modelled APO signal shows greater short-term variability, particularly in summer. Plotting only weekly trimmed averages for REMO made the record slightly smoother but clearly did not eliminate the outliers dominating the record over both summers of 2005 and 2006. These extreme outliers are most likely artefacts produced during the simulations owing to poorly defined APO fluxes. Owing to the strong maritime character of the SIS station any errors in APO fluxes in this region will be directly reflected in the simulations. This is in contrast to APO simulations at ZOTTO with an overly smoothed APO signal predicted by REMO as a result of its attenuation across the large continent. As the performance of the model is generally worse at the lower vertical levels, I prepared the same figure but only using the APO simulations at 300 m (not shown), however, the results were very similar to those shown in Figure 6.17, providing further evidence for possible errors in APO fluxes in summer. Apart from the high excursions in the modelled APO signal in summertime the seasonal cycle (~56 per meg in the observations) and long-term trend were modelled quite realistically. However, more discrepancies were observed during the summer of 2006. The latter period was characterised by an unusual negative excursion in the model, which might have been an artefact, but unfortunately, no observations are available over this period to support this argument. There exist some problems in the observations as well, with several gaps in the measurements followed by values offset by ~20 per meg from the rest of the record, which was possibly caused



**Figures 6.18:** Averages of flask samples (collected in triplets) collected at approximately weekly intervals at Shetland Islands (SIS) from 01 Jul 2004 to 01 Jan 2008 (blue triangles and line) compared to weekly trimmed averages of REMO APO simulations at SIS at 30 m (black line).

by some technical problems with the sampling equipment. In general, it appears that the simulations of APO in summertime at a marine location are particularly prone to errors in APO fluxes, probably originating from the relevant errors in the TM3 inversion. The fact that the summertime seems to be the most problematic period is probably related to the positive fluxes of APO to the atmosphere that were overestimated in the TM3 inversion. Thus, both TM3 and REMO may need to correct the APO input fluxes, which would require more data and flux measurements from this location.

## 6.6 Atmospheric concentrations of CO<sub>2</sub>, CO, O<sub>2</sub> and CH<sub>4</sub> during fire events: model-observations comparison

Forest fires are an important source of CO<sub>2</sub>, CO, CH<sub>4</sub> and other carbon cycle related trace gases. The last decades have been characterised by an increased number of fires and burned areas throughout boreal and tropical ecosystems, with the majority being caused by humans [e.g. *Mollicone et al.*, 2006]. Observations of atmospheric concentrations of biogeochemical gases in fire plumes are useful tools for estimating the amount of carbon compounds emitted into the atmosphere.

REMO simulations of atmospheric CO concentrations at ZOTTO are available

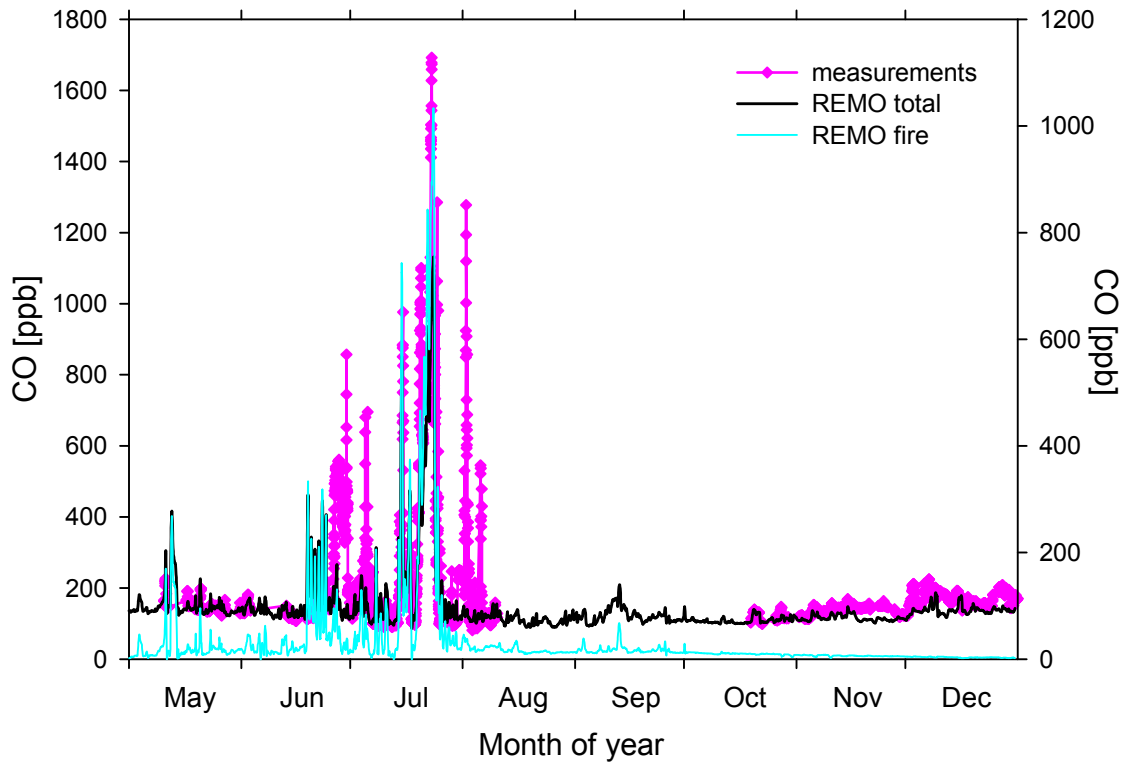
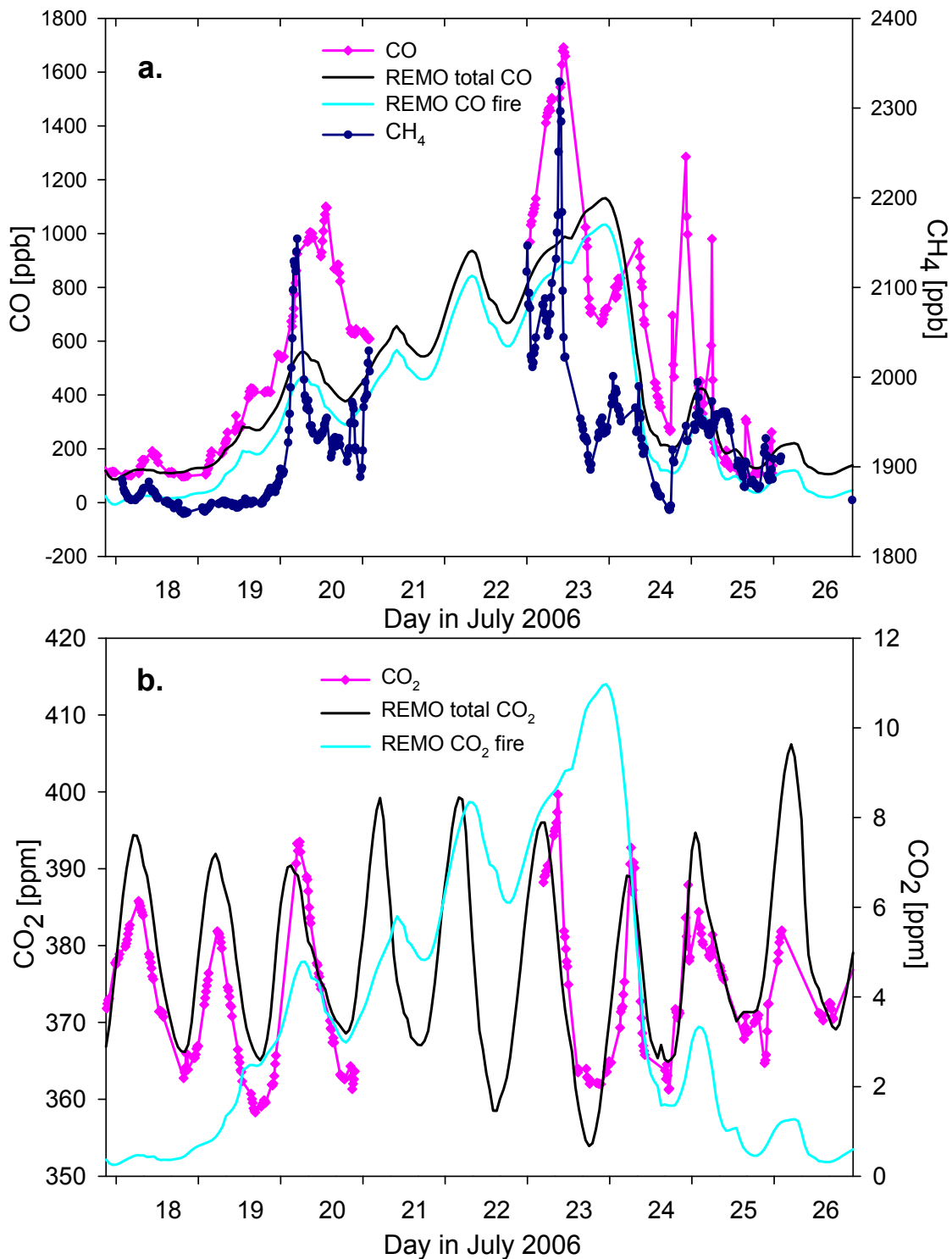


**Figure 6.19:** CO measurements (at a frequency of one measurement every 15 min) at ZOTTO (pink diamonds and line) compared to REMO CO simulations: total CO (solid black line) and fire component (solid cyan line) at hourly frequency. Left y-axis denotes CO concentration in ppb and is attributed to CO measurements and REMO total CO simulations. The right y-axis also denotes CO concentration in ppb but is attributed to the REMO fire component only.

for the period from 01 January 2005 to 01 January 2007. My continuous CO measurements were started in May 2006, thus providing only 8 months of direct comparison. Despite its short length, the overlapping period during summertime allowed me to compare several fire plume concentrations of CO and other tracers in both records. The summer of 2006 was characterised by a large number of fires, with some of them taking place only a few kilometres away from ZOTTO. The strongest fire events were detected in July 2006, whilst smaller fires were observed throughout the whole summer covering large areas around the tower as well as the neighbouring regions.

Figure 6.19 shows the observed and modelled records of CO concentrations at ZOTTO. The REMO simulations are shown as total CO concentrations (solid black line) and CO originating solely from fires (cyan solid line). The REMO CO fire component was simulated using data from GFED (see table 6.1), where fires are recorded at a 8-day frequency. For the simulations of the fire component, REMO uses the same mean fire emission value over a 8-day period; the higher frequency variations

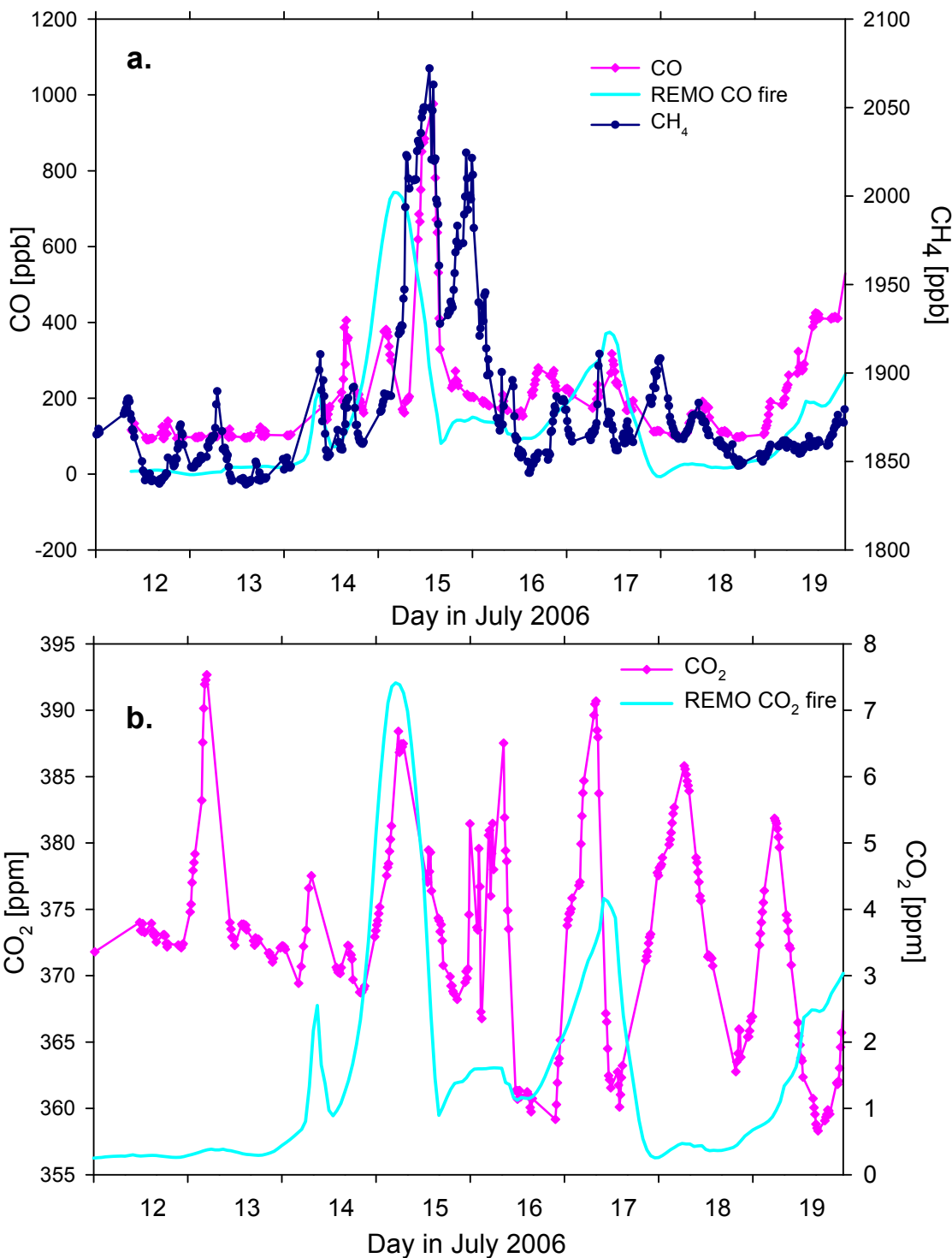


**Figures 6.20:** **a.** CO measurements (at a frequency of one measurement every 15 min) at ZOTTO (pink diamonds and line) compared to REMO CO simulations: total CO (solid black line) and fire CO component (solid cyan line) at hourly frequency during the largest fire event on 18-26 July 2006. CH<sub>4</sub> measurements (at the same frequency as CO) shown with blue circles and line on the right y-axes; **b.** CO<sub>2</sub> measurements (at a frequency of one measurement every 16 min) at ZOTTO (pink diamonds and line) compared to REMO CO<sub>2</sub> simulations: total CO<sub>2</sub> (solid black line) and fire CO<sub>2</sub> component (solid cyan line) during the same fire event as in plot a. The right y-axis (CO<sub>2</sub> in ppm) denotes the REMO fire component.

seen, however, in the CO fire component are caused by transport and changes in meteorological variables. In general, the agreement between the observed series of excursions in CO measurements and the modelled CO fire component is very good. I plotted the total modelled CO in Figure 6.19 to show that practically all high excursions in this record over spring and summer 2006 are reflected in the CO fire component as well, confirming the fire origin of high CO concentrations. Nevertheless, some high CO events seen in the measurements are not observed in the modelled record (for example, the series of fires in the beginning of August 2006), however, this can probably be explained by the frequency at which the fires are recorded, thus the GFED database may miss some short-duration fires.

Several distinctive small fire events can be clearly seen in both observed and modelled CO records in Figure 6.19. The highest atmospheric CO concentrations (up to 1700 ppb) were observed during the large fire event that occurred over an 8-day period (18-26 July). Figure 6.20a. shows atmospheric concentrations of CO in more detail for this period. The same figure also demonstrates the modelled total CO and its fire component. As the fire lasted for over a week, the CO concentrations were increasing gradually reaching their maximum on 23 July. The peak in the CO concentrations probably reflects the time when the fire was at its closest to ZOTTO. Though the measurements were halted for two days (21 and 22 July) during the event, the data integrity was not compromised.

Figure 6.20b. shows CO<sub>2</sub> concentrations, both observed and modelled, over the same period. The modelled CO<sub>2</sub> is also shown as total (black solid line) and fire attributed (cyan solid line). In the case of CO<sub>2</sub>, it is very difficult to detect any increase in ambient levels of CO<sub>2</sub> during the fire event owing to large diurnal cycles, clearly seen in both the observed and modelled concentrations. In addition, the background atmospheric CO<sub>2</sub> concentration is much higher than that of CO (three orders of magnitude) which makes it more difficult to observe small changes, particularly in summertime. Nevertheless, the fire component of the modelled CO<sub>2</sub> is of the same pattern as that of the CO, slowly increasing over the period of the fire, with a maximum on 23 July. Figure 6.20a. also shows the CH<sub>4</sub> concentrations during the same 8-day period. High concentrations of CO and CH<sub>4</sub> provide evidence that the fire was mainly smouldering, as flaming fires are characterised by more complete combustion (and thus predominantly CO<sub>2</sub> emissions). It is also more difficult to detect the atmospheric CO<sub>2</sub> increase as it is immediately reincorporated into the growing biomass in the middle of summer, whereas CO and CH<sub>4</sub> accumulate in the atmosphere. Figure 6.21 shows the observed and modelled CO (a) and CO<sub>2</sub> (b) concentrations during another fire during



**Figures 6.21:** **a.** CO measurements (at a frequency of one measurement every 15 min) at ZOTTO (pink diamonds and line) compared to REMO CO simulations: total CO (solid black line) and fire CO component (solid cyan line) at hourly frequency during the fire event on 12-18 July 2006. CH<sub>4</sub> measurements (at the same frequency as CO) are shown with blue circles and line on the right y-axis; **b.** CO<sub>2</sub> measurements (at a frequency of one measurement every 16 min) at ZOTTO (pink diamonds and line) compared to REMO CO<sub>2</sub> simulations: total CO<sub>2</sub> (solid black line) and fire CO<sub>2</sub> component (solid cyan line) during the same fire event as in plot a. The right y-axis denotes the REMO CO<sub>2</sub> fire component.

12-18 July 2006, which has very similar, although smaller scale, features to that discussed above. The first part of this fire event (14-15 July) is characterised by high

CO and CH<sub>4</sub> concentrations while the CO<sub>2</sub> level remains practically unchanged. The REMO simulations, however, show about a 6 ppm increase in the fire CO<sub>2</sub> component. The second part of the fire (16-18 July) shows only small peaks in both CO and CH<sub>4</sub>.

The ratios between the emitted atmospheric species are mainly determined by the nature of the fire, i.e. whether it is predominantly flaming or smouldering. The latter type of fire usually lasts much longer and is responsible for most of the production of non-CO<sub>2</sub> gaseous species [e.g. *Cofer et al.*, 1991]. The emission ratios (ER) between various gaseous compounds produced during biomass burning in relation to CO<sub>2</sub> have been previously studied, although most of those studies were focused on fires in tropical ecosystems and savannas. Since these ratios largely depend on the nature of the fire as well as the type of the burned biomass, the ratios that have been reported in the literature are variable and often have large uncertainties (see references below). For this study I calculated the ER's of several gaseous compounds relative to CO<sub>2</sub> and summarised them in Table 6.3. The ratios were calculated according to the following equation:

$$ER = \frac{\Delta C}{\Delta CO_2},$$
 where  $\Delta C$  is the difference between the atmospheric concentration of the

gas species of interest during the smoke plume and its average background concentration before and after the fire; and  $\Delta CO_2$  is the same but with respect to CO<sub>2</sub> concentrations. The reason for normalising the ER's to CO<sub>2</sub> is that the concentration of CO<sub>2</sub> during the fire event can be directly converted into the amount of burned biomass via simple stoichiometric relationships between CO<sub>2</sub> and organic matter [*van der Werf et al.*, 2003; *Levine*, 1994]. In this study the ER's are reported in units of 'ppb per ppm' ('ppb per ppb' for CO/CH<sub>4</sub> ER's, see below), and the uncertainties are calculated with the standard statistical method of error propagation.

The calculations of ER's show that selecting the period of the fire itself can influence the results significantly. The large 8-day fire (18-26 July) provided the most robust results for all the ER's and their uncertainties because the number of data points was large and the signals of all observed species were very strong. The average CO/CO<sub>2</sub> ratio was quite high (80.66±11.52), reflecting the very high CO concentrations observed during this fire. Interestingly, the REMO CO/CO<sub>2</sub> ratio (using total CO and total CO<sub>2</sub> concentrations) were very similar (78.27±17.03) to those obtained from the observations, and statistically not significantly different. In contrast, the CO/CO<sub>2</sub> ratios based solely on the REMO CO and CO<sub>2</sub> fire components showed significantly

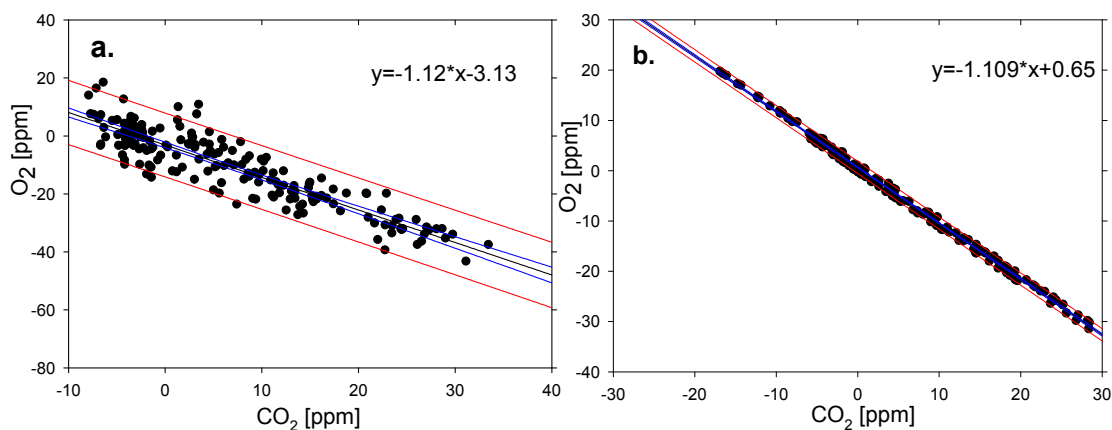


**Figure 6.22:** Average O<sub>2</sub>/CO<sub>2</sub> exchange ratio during the fire event on 18-26 July 2006 from ZOTTO measurements (a) and from the REMO simulations (b). The black solid line (in both plots) represents a linear fit to the data points. The blue lines enclose the 95% confidence interval of the fitting, while the red lines - the 95% prediction interval. The equation of each linear fit is given on the top of each plot. The uncertainties are given in Table 6.3.

higher ratio but smaller uncertainty ( $103.29 \pm 7.63$ ). This result shows that the model assumes higher emissions of CO during Siberian fires, or in other words, more smouldering fires. The average O<sub>2</sub>/CO<sub>2</sub> ratio for this 8-day event,  $1.12 \pm 0.04$  (Figure 6.22a.), was very similar to that expected from ecosystem net carbon exchange

Date in July	$\Delta\text{CO}/\text{CO}_2$ ppb/ppm	$\Delta\text{CO}/\text{CO}_2$ REMO <sup>a)</sup> ppb/ppm	$\Delta\text{CO}/\text{CO}_2$ REMO <sup>b)</sup> ppb/ppm	$\Delta\text{O}_2/\text{CO}_2$ ppm/ppm	$\Delta\text{O}_2/\text{CO}_2$ REMO ppm/ppm	$\Delta\text{CH}_4/\text{CO}_2$ ppb/ppm	$\Delta\text{CO}/\text{CH}_4$ ppb/ppb
18-26	80.66 $\pm 11.52$	78.27 $\pm 17.03$	103.3 $\pm 7.6$	1.12 $\pm 0.04$	$1.109 \pm 0.004$	14.84 $\pm 2.14$	5.43 $\pm 0.38$
12-18	318 $\pm 618$	27.17 $\pm 10.89$	219.80 $\pm 28.31$	NA, $R^2 < 0.6$	-	97.5 $\pm 187.7$	3.27 $\pm 0.39$
14-15	35.18 $\pm 6.73$	16.50 $\pm 4.04$	101.6 $\pm 18.8$	NA, $R^2 < 0.6$	-	10.33 $\pm 1.24$	3.41 $\pm 0.59$
16-18	6.37 $\pm 0.87$	8.34 $\pm 2.72$	94.27 $\pm 23.35$	1.12 $\pm 0.13$	-	1.09 $\pm 0.18$	5.83 $\pm 0.82$

a) Total CO and CO<sub>2</sub> simulations were used to obtain these ER's;

b) Fire CO and CO<sub>2</sub> components were used to obtain these ER's.

**Table 6.3:** Emission ratios (ER's) of gaseous species during the fire events in central Siberia in July 2006.

( $1.10 \pm 0.05$ , [Severinghaus, 1995]) and showed that the atmospheric concentrations of these gases were driven by photosynthesis, respiration and biomass burning with no significant contribution from fossil fuel burning (which have much higher stoichiometry except for coal burning). The same ratio derived from the REMO simulations showed the expected value of 1.1 (Figure 6.22b.) with a very small error estimate (0.004).

Originally I treated the fire event on 12-18 July as continuous, however, the average CO/CO<sub>2</sub> ratio showed a very large uncertainty (318±618). This illustrates the statement above that unless the fire-related atmospheric signals are very strong and the number of data points over this period is large (as shown for the fire event on 18-26 July), the ER's can be significantly influenced by the way the fire event is selected (i.e. how the start and end points of the fire event are defined) and the background concentrations of the given species. When I split this period into two distinctive fire events (following the two peaks in REMO CO<sub>2</sub> and CO fire components) the ER's have become very different from the first estimate and the uncertainties were significantly reduced (see Table 6.3). It can be seen from the ER's that the first stage of the fire on 14-15 July was characterised by much higher CO concentrations than the second stage on 16-18 July.

The comparison with the model showed practically the same values as for the fire on 18-26 July (101.6±18.8 and 94.3±23.4 for 14-15 July and 16-18 July respectively) when the fire components of simulated CO and CO<sub>2</sub> concentrations were used for the ER's calculations. In general, the REMO fire component ER's for all three fire events are statistically not different from each other, which shows that the model assumes a (roughly) constant CO/CO<sub>2</sub> emission ratios for Siberian fires that is higher than those observed. The CO/CO<sub>2</sub> ratios calculated from the total CO and CO<sub>2</sub> concentrations in REMO are the same magnitude for the first stage of the fire on 14-15 July, and statistically the same for the second stage on 16-17 July. The O<sub>2</sub> and CO<sub>2</sub> measurements show very low correlation ( $R^2 \sim 0.5$ ) over 14-15 July, and a ratio of 1.12 over 16-18 July but with large error estimate (0.13). The O<sub>2</sub>/CO<sub>2</sub> ratios from the model were assumed to be the same as for the fire event on 18-26 July.

As seen from Table 6.3, observed CO/CO<sub>2</sub> ER's vary significantly from one fire event to another. The fire on 18-26 July with high CO/CO<sub>2</sub> was predominantly smouldering and the ER estimate of ~81±12 ppb/ppm is comparable with those previously published. Cofer *et al.* [1991] reported average ratios of 121±19 and 67±12 for the smouldering and flaming fires in temperate boreal ecosystems respectively. Koppmann *et al.* [1997] reported an average ratio for wild fires (mainly wood) of ~94±13 in savannas. The ER's obtained during the fire experiment at the Bor Forest Island, close to ZOTTO ([http://www.fire.uni-freiburg.de/other\\_rep/research/rus/rus\\_re\\_1bor.htm#top](http://www.fire.uni-freiburg.de/other_rep/research/rus/rus_re_1bor.htm#top)) showed a high range of CO/CO<sub>2</sub> ratios depending on the stage of the fire, from 88±27 to 335±45 for flaming and smouldering fires respectively. However, owing to the large areas of wetlands around ZOTTO it would probably be incorrect to compare my estimates to those

obtained from wood burning only. Cofer *et al.* [1991] also provided estimates for the CO/CO<sub>2</sub> emission ratios from burning wetlands, which are much lower than those for the boreal ecosystems: 54±10 and 47±8.0 for smouldering and flaming fires respectively. Thus, my ER estimates probably reflect the biomass burning in a mixed (wood + wetlands) ecosystem. The fires observed over the periods of 18-26 July and 14-15 July were probably predominantly smouldering, whilst the fire event on 16-18 July was more flaming, as reflected in large differences in their ER's. It is also remarkable that the ER's obtained from the REMO simulations (total CO and CO<sub>2</sub>) are in such a good agreement with those from the observations. The higher values for the REMO ER's calculated when only using the fire components are closer to the literature estimates above obtained from the smouldering fires in boreal ecosystems when mostly wood was burned. Thus it is possible that the mixed nature of the burned organic matter in areas surrounding ZOTTO was not reflected in the model simulations of CO and CO<sub>2</sub> fire components.

Along with CO/CO<sub>2</sub> ER's I also investigated those of CH<sub>4</sub>/CO<sub>2</sub> for the same fire events (see Table 6.3). Although, there are no REMO CH<sub>4</sub> simulations available for the period of my interest the ER's of gases other than CO can provide additional information on the nature of the fire events. The production of CH<sub>4</sub> during fires, along with CO, reflects the incomplete burning of the organic matter and mostly occur during the smouldering fires. The CH<sub>4</sub>/CO<sub>2</sub> ER's obtained for fires on 18-26 July (14.84±2.14) and 14-15 July (10.33±1.24) are similar and provide additional evidence of the smouldering nature of these fires. Conversely, the CH<sub>4</sub>/CO<sub>2</sub> ratio for 16-18 July is very low (1.09±0.18), which shows that the combustion of the organic matter was much more complete, also in agreement with the above discussion. These estimates are in good agreement with the ER's previously published in literature. Cofer *et al.* [1991] reported CH<sub>4</sub>/CO<sub>2</sub> ratios of 12.1±3.2 and 4.6±2.0 for smouldering and flaming fires from boreal ecosystems and 3.4±1.2 and 2.7±1.1 from wetlands. Ward *et al.* [1992] found ratios of about 12.2 and 6.1 for smouldering and flaming fires in boreal ecosystems. Koppmann *et al.* [1997] reported average ratios of 10.3±1.7 from burning wood in savannas. The CH<sub>4</sub>/CO<sub>2</sub> ER's from the fire experiment at the Bor island also showed a similar range of ER's: from 5.0±1.0 to 13±2.0 for flaming and smouldering fires respectively (see reference above). It appears from my estimates as well as those reported by other workers that CH<sub>4</sub>/CO<sub>2</sub> ER's are generally much better defined than those for CO/CO<sub>2</sub> and have smaller uncertainties with values being ~10 for smouldering and ~1-5 for flaming fires.

I also calculated CO/CH<sub>4</sub> ER's for the same fire events discussed above (Table 6.3). Whilst CH<sub>4</sub>/CO<sub>2</sub> ratios characterise the nature of a fire (smouldering, flaming or mixed) the CO/CH<sub>4</sub> ratios quantify the relationship between these two species when incomplete organic matter combustion occurs. Unlike CO/CO<sub>2</sub> and CH<sub>4</sub>/CO<sub>2</sub> ER's, the ratios between CO and CH<sub>4</sub> during fires appear to be much more constant, varying from about 3 to 6 (ppb/ppb) with very small error bars. This observation might suggest that independent from the nature of the fire, the ratios at which CO and CH<sub>4</sub> are emitted to the atmosphere are quite constant. Obviously more research of these ratios (also based on larger datasets) during fires will be needed for stronger conclusions, however, these preliminary results show that pre-defined CO/CH<sub>4</sub> ratios could potentially be used for estimating either CO or CH<sub>4</sub> fire emissions when only measurements of one of these species are available. This could be useful for many fire related studies as not every greenhouse gas measurement system is equipped with the instrumentation for measuring both of these gases.



## CHAPTER 7. Summary and Outlook

This thesis is devoted to results and discussions of atmospheric multi-species measurements from natural ecosystems: the unmanaged old-aged mid-latitude Hainich Forest in Germany and the taiga in central Siberia. Unlike direct process studies, atmospheric measurements are unique in that they provide information on the integrated response from different parts of an ecosystem, and allow the determination of overall trends in the development of the ecosystem or its response to environmental changes. It is the latter that has made atmospheric measurements from natural ecosystems even more important now, as we do not possess enough information to predict how they will develop and respond to climate change. Both datasets presented this thesis, although short in their time duration, have provided interesting insights into processes occurring in these forest ecosystems, by taking full advantage of the multi-species nature of the measurements. In this chapter I summarise the results and conclusions of the thesis and provide a short outlook for future research.

The Hainich Forest measurements were obtained during two intensive sampling campaigns in May and July 2005. One-litre glass flasks were collected approximately every 3-4 hours and subsequently analysed for CO<sub>2</sub>, O<sub>2</sub>, CH<sub>4</sub>, CO, N<sub>2</sub>O, and SF<sub>6</sub> concentrations, as well as the isotopic composition of CO<sub>2</sub> ( $\delta^{13}\text{C-CO}_2$ ), at the Max Planck Institute for Biogeochemistry (MPI-BGC). Air samples were collected within the canopy at 1, 4 and 12 m, with an additional sampling line installed prior to the July campaign at 5 cm above ground.

Concentrations of CO<sub>2</sub>, O<sub>2</sub> and  $\delta^{13}\text{C-CO}_2$  were well correlated, as expected from their tight relationships in the processes of assimilation and respiration. The oxidative exchange ratios (O<sub>2</sub>/CO<sub>2</sub>) exhibited a small increasing trend from May to July, with some (although small) vertical gradients of the ratios. A previous study on O<sub>2</sub>/CO<sub>2</sub> ratios performed several years earlier in the Hainich Forest [*Seibt et al.*, 2004] was used to provide an O<sub>2</sub>/CO<sub>2</sub> ratio estimate for August, which was in agreement with the overall increasing trend of the ratios during the vegetative season. A similar increasing trend was observed in  $\delta^{13}\text{C-CO}_2$  determined from Keeling plots calculated separately for daytime and nighttime data, where the former represents the mixture of isotopic signatures of assimilation and respiration, while the latter can be solely attributed to the isotopic signature of respiration ( $\delta^{13}\text{C}_R$ ). A similar increasing trend in  $\delta^{13}\text{C}_R$  towards the end of the vegetative season was observed in a previous study in the Hainich Forest in 2001 [*Knohl*, 2004]. I speculate that the observed trends might be a result of seasonal changes in CO<sub>2</sub> assimilation and respiration rates. The observed trends could also be

related to differences in respired organic matter (with more complex molecules being oxidised later in the summer), and changes in plant and soil respiration partitioning.

The measurements collected at 5 cm above ground were distinctively different from those at the other heights for all gas species. CO<sub>2</sub> (and thus O<sub>2</sub> and  $\delta^{13}\text{C-CO}_2$ ) concentrations showed temporal accumulation patterns which were different from the ‘classical’ diurnal cycles observed at the other heights, with high concentrations in daytime and low in nighttime that clearly followed variations in soil temperature, indicating the impacts of soil respiration processes. Concentration records of CH<sub>4</sub>, CO and N<sub>2</sub>O at 5 cm were significantly lower than those at the other heights. This indicates soil sinks with respect to all three species, resulting from the processes of CH<sub>4</sub> and CO microbial oxidation, and denitrification.

Owing to its purely industrial origin, SF<sub>6</sub> concentrations were nearly constant during both campaigns except for a relatively large peak detected on 17 July 2005. Back trajectory analyses of air masses showed that the peak might have been related to either sporadic or regular emissions from Kassel, a city of about 200,000 people, located approximately 70 km away from the Hainich Forest.

My results from the Hainich Forest show that additional insights can be gained even from short-length flask sampling campaigns when making concurrent measurements of different gas species. My findings and their robustness, however, were restricted by data availability, particularly due to a lack of observations in the other seasons. I have shown, however, that it would be scientifically interesting to repeat such measurements, preferably on a much more frequent basis and over all months of the year at the Hainich Forest and to extend them to other ecosystems.

The following chapters in this thesis are devoted to the atmospheric high-precision measurements of CO<sub>2</sub>, O<sub>2</sub>, CH<sub>4</sub>, CO and N<sub>2</sub>O in central Siberia (Zotino Tall Tower Observatory (ZOTTO)). As was shown for measurements from the Hainich Forest, results and conclusions of such studies are mainly restricted by data availability since it is not always possible to detect small gradual changes in the atmospheric composition from short datasets. The significant difference of the Siberian measurements is that they were performed on a semi-continuous basis (one data point every 12-16 min) and were collected from five heights (4, 52, 92, 227 and 300 m) of a 300-m tall tower providing both high temporal resolution and extensive information on the vertical distribution of all gases. The uppermost two levels of the ZOTTO tower also provide a unique opportunity to sample air from the well-mixed part of the atmosphere (Atmospheric Boundary Layer, ABL) during the daytime that is representative of a large area around ZOTTO.

To measure all the gas species in real-time, I built a measurement system incorporating several different analysers within a single cohesive measurement and data acquisition unit. One advantage of such a measurement system is that it implements a common gas handling and calibration philosophy for all gas species. The system was controlled by a bespoke LabView™ software, which allowed the final concentrations of all species to be calculated in real-time, significantly simplifying data processing. From the perspective of the required precision and its bulk atmospheric concentration, O<sub>2</sub> measurements are the most technically challenging from the suite gas species measured at ZOTTO. Thus, many additional features were introduced to the system to achieve the high-precision O<sub>2</sub> measurements. These included a custom-built high stability ( $\pm 0.006^\circ\text{C}$  hourly variations) active temperature controlled enclosure which minimised the influence of room temperature variations on the paramagnetic O<sub>2</sub> analyser. Another important feature was the large thermally-insulated enclosure that holds fifteen horizontally oriented high-pressure calibration and reference cylinders. The horizontal placement is essential for making accurate and reproducible O<sub>2</sub> measurements (due to thermal and gravitational fractionation of O<sub>2</sub> relative to N<sub>2</sub> in vertically placed cylinders).

Although these special measures were employed mainly to improve the precision and accuracy of the O<sub>2</sub> measurements, they have also significantly improved the precision of the other gas measurements. For example, switching frequently (every 8 min) between air sample and reference gas (Working Tank), which is crucial for minimising temperature induced drift in the O<sub>2</sub> analyser baseline, has also allowed a much higher precision in CO<sub>2</sub> ( $\pm 0.003$  ppm) than would have been possible otherwise. The fractionation of O<sub>2</sub>/N<sub>2</sub> at air inlets and ‘Tee’ junctions was investigated, resulting in the installations of aspirated air inlets following Blaine et al. [2006] and ‘dip-tubes’ (tubing of a smaller diameter which is inserted upstream of the larger diameter Tee junction) at Tee junctions following Stephens et al. [2007] and my own field tests. These improvements resulted in significant reduction in the fractionation effects observed in the system. Finally, the system was designed to be highly reliable and easily tested, important characteristics for a remote installation.

One of the most important technical results was the observed O<sub>2</sub> concentration trends in both WT and calibration cylinders. The latter, however, was the consequence of wrongly assigned initial concentrations from MPI-BGC of some calibration cylinders, which had to be retrospectively corrected after the cylinders were re-analysed at MPI-BGC in 2008. Unusually high drift ( $\sim 5$  ppm Equiv over a lifetime of a cylinder) was observed in O<sub>2</sub> concentrations of ZOTTO WT cylinders, which, however, did not

compromise system performance. Interestingly, this feature had gone away once the system was moved to Cape Verde Islands, and significantly smaller drifts (<1 ppm Equiv) in O<sub>2</sub> WT concentrations were observed with identical system setup and measurements. The stability of CO<sub>2</sub> and all GC species concentrations (except for CO that showed drifts in some cylinders) in both WT and calibration cylinders was found to be very good. A very important quality control feature is the use of a Target Tank (TT), a cylinder with assigned (in my case by MPI-BGC) concentrations for all gases. This tank is routinely measured (at least twice as frequent as calibrations) by the system. TT measurements allow for monitoring of, not only the precision of the measurements, but also their accuracy, since the internally defined TT concentrations (calculated based on regular calibrations) can be compared to their assigned concentrations. These TT measurements can help in the diagnosis of various technical problems as they occur.

To ensure the long-term consistency of concentration records of all gas species, a suite of ‘Archive’ cylinders (with a projected lifetime of 10-20 years) was introduced to the system, whose occasional measurements provide a basis for future calibration scale updates. Another important innovation that allows for consistency of the internal calibration scales is that the concentrations of all new calibration cylinders are defined in the course of about 3-4 months of measurements based on the routine calibrations (and not assigned from external sources). This mechanism of calibration scale propagation ensures the consistency of the internal scales without introducing errors or trends from external measurements. Four-point calibrations for all gas species are also run much more frequently than at other stations: daily for O<sub>2</sub>/CO<sub>2</sub>, and weekly and later twice-weekly for GC measurements. These features allowed me to achieve measurement precisions and accuracies within the WMO-specified targets for most of the measured species, with the exception of CO and N<sub>2</sub>O. The precision and accuracy of the CO measurements achieved the WMO targets after the measurement system was moved to Cape Verde Islands. N<sub>2</sub>O measurements, however, still needs additional attention, and indeed is a difficult species to meet the WMO targets.

The measurement system described above was operating at ZOTTO from November 2005 to June 2007. The first period of the measurements (Nov 2005 – Sept 2006) includes those from up to 52 m height, whilst the second (after the tower was fully constructed) contains measurements from all five heights up to 300 m. In this thesis I present a 19-month concentration record of CO<sub>2</sub>, finding a seasonal amplitude of 26.6 ppm. O<sub>2</sub> measurements were started later, in May 2006; however, the 12 month record was sufficient for a seasonal cycle analysis that resulted in an amplitude estimate of ~190 per meg (which corresponds to ~39.8 ppm of CO<sub>2</sub>). The O<sub>2</sub> measurements

presented in this thesis have been revised since their publication in Kozlova *et al.* [2008]. The revision was based on flask sample analyses (from flasks collected at ZOTTO over this period and analysed at MPI-BGC) and included a method of accounting for an O<sub>2</sub>/N<sub>2</sub> mass dependent fractionation in pressurised flasks. For the seasonal cycle analysis I used CO<sub>2</sub> and O<sub>2</sub> concentration data from 52 m as it provides the longest record for both gas species. To minimise the influence of local effects which may be present at 52 m, only the daytime trimmed averages (from 11:00 to 17:00) were used in the fitting curve computations. A direct comparison of daytime trimmed means for 52 and 300 m, however, showed that the largest differences existed during wintertime when vertical mixing is largely suppressed, with only minor differences in spring.

To study the continental carbon uptake and transport of air masses, I compared the ZOTTO data with weekly flask samples from Shetland Islands (SIS, Scotland), situated at a similar latitude. An observed west-east gradient of -7 ppm in CO<sub>2</sub> (in July 2006) between SIS and ZOTTO represents the summertime uptake by the terrestrial biosphere over Eurasia, which correlates with the O<sub>2</sub> maximum (for the same month) of a similar magnitude. Lower wintertime O<sub>2</sub> concentrations at ZOTTO compared to SIS can most likely be attributed to wintertime fossil fuel burning in Europe and Russia. The SIS CO<sub>2</sub> seasonal cycle is much smaller than that at ZOTTO (14.4 ppm compared to 26.6 ppm), and has different phasing, which is expected due to the maritime character of the SIS station. Overall, the SIS seasonal cycles for both CO<sub>2</sub> and O<sub>2</sub> were smaller than those observed at ZOTTO; however, the contribution of the oceanic O<sub>2</sub> signal (or Atmospheric Potential Oxygen, APO) was larger at SIS (~56 and 45 per meg at SIS and ZOTTO respectively). The reduction of the seasonal amplitude of APO at ZOTTO reflects the attenuation of the APO signal over the continent. This is the first study to present and quantify the attenuation of the seasonal APO signal in the continental interiors. A 2-month gap in the ZOTTO measurements during tower construction probably masked the seasonal maximum of the APO concentrations, leading to less robust estimates of its seasonal cycle. In addition, there appears to be a 2-month lag between the observed SIS APO maximum and the time when it probably occurred at ZOTTO, which is longer than expected from horizontal transport. Owing to probably large interannual variability in seasonal cycles at ZOTTO, it is crucial to extend such seasonal cycle analysis to much longer temporal scales to be able to reliably estimate both seasonal amplitudes and interannual concentration trends.

A comparison of CO<sub>2</sub>, O<sub>2</sub> and APO seasonal cycles at ZOTTO and SIS with TM3 model simulations (5°×4° horizontal resolution) showed generally good agreement

for all measured species, although some discrepancies were observed between the observed and modelled seasonal cycles at SIS in February-March, probably associated with the wintertime outgassing of O<sub>2</sub> from the ocean. Nevertheless, the coarse resolution of the model did not allow for a more detailed model-observations comparison on shorter time scales.

Seasonal variations of CH<sub>4</sub> and CO from May 2006 to June 2007 were studied using different data selection and presentation procedures owing to significant contribution of fire emissions and thus very high atmospheric concentrations of both gases in summertime. As the summer of 2006 was characterised by a very large number of fires, some of them very close to ZOTTO, the largest scatter and maxima in both CH<sub>4</sub> and CO concentrations occurred over this period. In winter, however, concentration maxima for both CH<sub>4</sub> and CO were driven by pollution events (see below). Similar to the analysis on CO<sub>2</sub> and O<sub>2</sub>, I used CO concentrations from weekly flask samples at SIS as a marine reference for 60°N and the marine boundary layer references at 58°N for both CH<sub>4</sub> and CO concentrations. Interestingly, in spite of very large scatter observed in both ZOTTO concentration records (CH<sub>4</sub> in particular), the minima of their monthly averages (and their seasonal variations) were very similar to concentration records at SIS and the marine boundary layer reference [*GLOBALVIEW-CO: Cooperative Atmospheric Data Integration Project - Carbon Monoxide. CD-ROM*]. This fact shows that the ZOTTO minima monthly averages are probably representative of clean background marine air brought to ZOTTO from a long distance. Owing to particularly scattered CH<sub>4</sub> concentrations it was difficult to estimate its seasonal cycle based on a single year of measurements. Long-term observations of CH<sub>4</sub> at ZOTTO are very important for any carbon cycle studies conducted in this area. Close to one of its natural sources, wetlands, CH<sub>4</sub> measurements at ZOTTO can provide a unique insight when studying the response of this natural ecosystem to a changing climate. In addition, as shown in this thesis (see below), large emissions of CH<sub>4</sub> in this area are also associated with fires and pollution events which can be traced and identified with back trajectory analysis.

The CO seasonal cycle appears to be slightly smoother than that of CH<sub>4</sub>, although with high values in summer and wintertime. The monthly minima, however, exhibited very similar seasonal amplitudes (with minimum in July and maximum in February) to the seasonal cycles at SIS and the marine boundary layer. In contrast to CH<sub>4</sub>, CO does not have any significant biogenic sources (except fires) around ZOTTO, and as shown below, CO measurements are very useful for tracking polluted air masses. In summer, the ZOTTO region is a large source of CO from abundant boreal fires.

Longer-term CO measurements could thus help to monitor regional scale fire emissions in the middle of Eurasia.

Analyses of synoptic scale variations were mainly focused on ‘cold events’ - variations of all gas species at air temperatures below  $-30^{\circ}\text{C}$  - and pollution events. The winter of 2006-7 was quite severe, with temperatures reaching  $-40^{\circ}\text{C}$ , which presented me an opportunity to observe the behaviour of the biogeochemical gases measured at ZOTTO under such meteorological conditions. The very cold and low wind conditions led to a highly stratified air column, with very large vertical gradients. Accumulation of  $\text{CO}_2$  (up to 22 ppm) and  $\text{CH}_4$  (and CO to a smaller extent) was observed at the lower levels of the ZOTTO tower, with a concurrent smaller depletion at the upper levels. I speculate that such cold and calm weather could have led to the formation of two separate air layers, at the bottom and top of the tower, characterised by different air circulation patterns. Lack of vertical mixing in this case would result in local  $\text{CO}_2$  emissions being trapped at the lower heights. The sources of such high emissions of  $\text{CO}_2$  in wintertime, however, remain unclear as no associated elevations in CO concentrations, which are expected to accompany fossil fuel or wood burning, were observed. Analysis of  $\text{O}_2/\text{CO}_2$  ratios during these events reveals very low values ( $<0.9$ ) at the bottom of the vertical column and higher ratios (1.1-1.4) at the top, which suggests a hypothesis of gravitational mass-dependent fractionation of different molecules [Adachi *et al.*, 2006] which can sometimes be observed under very cold and calm conditions. However, the fact that  $\text{CH}_4$  and CO also showed depletion at the top levels of the tower seems to disprove this hypothesis; because the  $\text{CH}_4$  molecule is lighter than air, higher  $\text{CH}_4$  concentrations should be expected at the top, whereas CO, having a similar molecular weight to air, should remain largely unaffected by the phenomena. Analysis of the entire wintertime data record showed that the ‘cold events’, even though they occurred only under very specific meteorological conditions, are not uncommon at ZOTTO (at least over the studied period).

Multi-species measurements at ZOTTO presented me with an opportunity to study pollution signatures reflected in elevated concentrations of all measured species. I use analyses of  $\text{O}_2/\text{CO}_2$ ,  $\text{CO}/\text{CO}_2$  and  $\text{CH}_4/\text{CO}_2$  emission ratios to study two pollution events captured in the ZOTTO measurements in December 2006 and February 2007. The isolation of pollution signatures from concentration records of all gas species was done by subtracting the averages of background concentration values shortly before and after the peaks from the elevated concentrations characterising the pollution plume. Errors of both background and pollution averages are then propagated to the ratios estimates. Analysis of emission ratios were accompanied by back trajectory analysis

[Draxler and Hess, 1998] to track the origin of the polluted air masses arriving at ZOTTO. I suggest that separate estimates of emission ratios for the bottom and top heights are beneficial to their interpretation. For example, the December pollution event was characterised by significant differences in CO/CO<sub>2</sub> ratios for the bottom (1.43±0.16 ppb/ppm) and top (2.21±0.42 ppb/ppm) heights of the tower. CH<sub>4</sub>/CO<sub>2</sub> ratios followed the same tendency, with the top heights estimates about double those at the bottom (26.25±4.67 and 12.23±1.49 ppb/ppm respectively).

As discussed above, the low wind conditions that result in highly stratified vertical air columns with very limited exchange between the top and bottom levels of the tower are not unusual for ZOTTO. As local emissions are often trapped within the first hundred meters of the air column, the upper levels of the tower (227 and 300 m) represent air signatures of much larger areas around ZOTTO, which could equally be clean background air from the north or pollution brought from great distance. The back trajectory analysis for this particular December pollution event indicates that it originated from only about 100 km away from ZOTTO, leading to significantly higher emission ratios for both gas pairs at the bottom of the tower. Conversely, the February 2007 event was probably caused by pollution plumes that arrived at ZOTTO from some distance away, thus leading to the observed opposite vertical gradients in emission ratios of both gas pairs; that is, significantly lower ratios at the bottom and higher ratios at the top.

For both pollution events, the CO/CO<sub>2</sub> ratios (ranging from ~1.2 to 3.9 ppb/ppm) were significantly lower than those previously reported for European emissions (11.0±1.1 ppb/ppm, [Gamnitzer *et al.*, 2006]). The latter estimate, however, was based on <sup>14</sup>C derived fossil fuel CO<sub>2</sub> estimate, whereas at ZOTTO total CO<sub>2</sub> (as measured at the tower) concentrations were used for these calculations. Nevertheless, with regard to wintertime I can safely assume that practically all CO<sub>2</sub> variations are driven by fossil fuel burning as there is only minimal influence of photosynthesis and respiration. Thus, I assume that no significant errors were introduced to wintertime CO/CO<sub>2</sub> estimates by using total CO<sub>2</sub> concentrations as proxies for anthropogenic CO<sub>2</sub>. Such large differences in the fossil fuel CO/CO<sub>2</sub> emission ratios are probably the reflection of the different types of fuel burned in Russia as opposed to central Europe. Further research is needed on dominant types of fossil fuels used in this area, combined with more regional back trajectory analyses and continuous measurements at ZOTTO. Such work could result in approximate maps of fossil fuel emission ratios for different areas around ZOTTO. In summertime, however, this approach would be less accurate owing to the large influence from photosynthesis and respiration.

Since most of the data that I collected from the fully constructed tower (up to 300 m) is wintertime data, the analysis of diurnal cycles of all gas species was mainly limited to measurements collected in April-May 2007. Owing to relatively cold air temperatures, the diurnal cycles of CO<sub>2</sub> (and O<sub>2</sub>) were still small. Nevertheless, I analysed about twenty vertical profiles in both April and May 2007 and estimated the relevant carbon flux (based on the gradients between the bottom and top of the tower and integration over the chosen accumulation period) as  $0.04 \pm 0.02 \text{ mol C m}^{-2} \text{ d}^{-1}$  which is consistent with eddy covariance measurements made in the vicinity of the tower in May 1999-2000 [*Shibistova et al.*, 2002b]. No significant diurnal vertical gradients in CH<sub>4</sub> and CO concentrations were observed during the spring months.

I compared ZOTTO CO<sub>2</sub>, APO and CO measurements with atmospheric regional model (REMO) simulations of these gas species for the same time period (all REMO simulation results are courtesy of U. Karstens at MPI-BGC). In contrast to the coarse grid global TM3 model simulations described above, the REMO model provides a much higher resolution ( $0.5^\circ \times 0.5^\circ$  and 20 vertical layers), presenting a unique opportunity for comparison of the model to observations on synoptic and diurnal time scales. In addition to the gas species concentrations, I performed a comparison of several common meteorological variables (air temperature, wind speed and direction, and surface pressure) modelled in REMO with those observed at four weather stations in the vicinity of ZOTTO, since there were no meteorological measurements available at ZOTTO at the time of my measurements.

The comparison between the summertime and wintertime meteorological variables showed very good agreement in both general trends and high-resolution features. Nevertheless, my analysis showed that REMO tends to underestimate the diurnal cycles of spring-summer air temperatures. The wintertime temperatures are frequently underestimated as well; such discrepancies are most profound during high pressure cold weather conditions, for example, during the ‘cold events’ in November 2006, when the model predicts significantly colder (up to 10°C) air temperatures. With regard to wind speed and direction, REMO shows relatively good agreement with the observations, with the largest discrepancies once again over the period of ‘cold events’. This is not surprising, as it is very challenging to simulate such local meteorological conditions even in a high-resolution model. In general, the modelled wind speed and direction records appear to lack the short term variability that is clearly seen in the observation records from all four stations. The modelled surface pressure shows very good agreement with measurements at all stations.

In addition to the comparison with the observed meteorological variables, I also present results from a study on the vertical mixing of air within the REMO domain. The simulated potential temperature vertical profiles in the lower troposphere were directly compared with those from routine radiosonde measurements at Bor, situated about 100 km away from ZOTTO. The largest discrepancies between model and observations are observed at lower heights, especially up to 500 m. Analysis of both summer and wintertime data showed insufficient vertical mixing in the model, resulting in a too shallow ABL during daytime. The insufficient vertical mixing directly influences the simulated daytime concentrations of atmospheric gas species. Thus modelled CO<sub>2</sub>, compared with the ZOTTO observations, revealed significant discrepancies even between the daytime trimmed averages, which supposedly represent concentration signatures of well-mixed air columns. In addition, the largest CO<sub>2</sub> concentration discrepancies (with significantly lower values predicted by REMO) were found during the days with largest vertical mixing model-observations discrepancies. This is as expected, since the surface acts as a strong CO<sub>2</sub> sink in summer during the daytime, with the height of the ABL significantly influencing the ambient CO<sub>2</sub> concentration. During wintertime some large CO<sub>2</sub> discrepancies occurred between the model and observations, especially during very calm high pressure conditions, such as the ‘cold events’.

Further analysis of the modelled daytime CO<sub>2</sub> concentrations showed that in addition to insufficient vertical mixing, there exist some discrepancies between the simulated carbon fluxes from the terrestrial biosphere in the BIOME-BGC model (the model that feeds terrestrial carbon fluxes to REMO) in spring and up to mid summer, leading to significantly lower daytime CO<sub>2</sub> concentrations predicted by REMO. Around mid July this tendency changes, and further comparison shows good agreement between the modelled and observed fluxes up to the end of the vegetative season. There also exist some persistent errors in the diurnal distribution of total respiration fluxes in the BIOME-BGC model leading to consistently higher nighttime fluxes over the whole vegetative season at ZOTTO.

The comparison between the observed and modelled O<sub>2</sub> and APO concentration records showed good agreement in seasonal cycles and amplitudes. Nevertheless, the observed short-term variability of these gases was not captured by the model, resulting in overly smooth modelled concentrations of both species. The modelled and observed APO concentrations at SIS showed large discrepancies around mid summer, with very large spikes in the modelled concentrations. These are believed to be artefacts, possibly

originating from errors in oceanic fluxes inherited from the global TM3 model (which provided oceanic APO fluxes for the REMO simulations) in this particular region.

The comparison between the observed and modelled CO concentrations showed good agreement on both seasonal and synoptic time scales. During the abundant fire events in summer 2006, characterised by periods of elevated levels of CO concentrations at ZOTTO, the model exhibited very good agreement with observations, which allowed for a detailed comparison of the observed and modelled emission ratios of CO/CO<sub>2</sub>. In addition, I also discuss CH<sub>4</sub>/CO<sub>2</sub> emission ratios for the same fire events, but only in the observations, since no REMO simulations for CH<sub>4</sub> concentrations were available. With regard to the modelled CO/CO<sub>2</sub> ratios I use both total concentrations of both gases as well as only their fire components for the comparisons with the observed ratios. I found that the CO/CO<sub>2</sub> ratios from the total CO and CO<sub>2</sub> simulations were in better agreement with the observations. In general, the observed CO/CO<sub>2</sub> and CH<sub>4</sub>/CO<sub>2</sub> emission ratios were found to be quite variable with the former being lower than previously reported estimates from wood burning in boreal ecosystems. This might reflect the mixed nature of organic matter burned in this area (wood + wetland vegetation), that might have different emission ratios than pure wood. The observed ranges of CO/CO<sub>2</sub> and CH<sub>4</sub>/CO<sub>2</sub> ratios most likely correspond to the flaming and smouldering stages of the fires, with the latter characterised by incomplete burning of organic matter and thus higher emissions of CO and CH<sub>4</sub> compared to CO<sub>2</sub>. The observed CH<sub>4</sub>/CO<sub>2</sub> ratios followed the same tendency, however, were more consistent for different fire events.

In addition to the ratios above I introduced another emission ratio, namely CO/CH<sub>4</sub>, that represents the relationship between these two species when incomplete organic matter combustion occurs. Unlike CO/CO<sub>2</sub> and CH<sub>4</sub>/CO<sub>2</sub>, the ratios between CO and CH<sub>4</sub> during different fire events appear to be much more constant, varying from about 3 to 6 (ppb/ppb) with very small error bars. Obviously, more research is needed here, using larger datasets. Nevertheless, my preliminary results show that pre-defined CO/CH<sub>4</sub> ratios could potentially be used for estimating either CO or CH<sub>4</sub> fire emissions when only measurements of one of these species are available. This could be useful for many fire related studies as not every greenhouse gas measurement system is equipped with the instrumentation for measuring both of these gases. In addition, such an approach could be applied to other types of observations, e.g. satellite measurements of CO, which would allow for concurrent CH<sub>4</sub> emission estimates.

In conclusion, the results presented in this thesis demonstrate the scientific potential of continuous multi-species atmospheric measurements. Such observations

from this or other natural ecosystems, particularly in the interior of the continents, are crucial, since these areas are highly under-represented in the current global observational networks. Given the interesting results generated by the relatively short records from this single station, it is clear that increasing the number of such stations will dramatically improve our knowledge on the spatial and temporal patterns of trace gas exchanges between the land biosphere and the atmosphere. This knowledge is also important to better quantify and model the climate feedbacks on terrestrial ecosystems and their development under a changing environment.

## APPENDIX 1. Derivation of equation describing O<sub>2</sub>/N<sub>2</sub> changes in ambient air

This appendix provides the derivation of equation 4.1 (See Chapter 4, Section 4.2.1), which is used for calculations of changes in O<sub>2</sub>/N<sub>2</sub> ratio.

$$\partial(O_2 / N_2) = \frac{\partial X_{O_2} + (X_{CO_2} - CO_{2ref})S_{O_2}}{S_{O_2}(1 - S_{O_2})}, \quad (4.1)$$

where  $\partial(O_2 / N_2)$  is expressed in ‘per meg’ units, and  $\partial X_{O_2}$  is the change in O<sub>2</sub> mole fraction of the air sample as determined by the Servomex sensor, multiplied by 10<sup>6</sup>, and relative to an arbitrary ‘zero’ defined in the SIO international calibration scale.  $X_{CO_2}$  is the CO<sub>2</sub> mole fraction of the air sample (in ppm), and  $CO_{2ref}$  is an arbitrary CO<sub>2</sub> reference value (363.29 ppm) implicit in the definition of the SIO O<sub>2</sub>/N<sub>2</sub> per meg scale.  $S_{O_2}$  is the standard mole fraction of O<sub>2</sub> in air, given as 0.20946 [Machta and Hughes, 1970].

For small changes in O<sub>2</sub> and N<sub>2</sub> in an air sample we can write

$$\begin{aligned} O_2 &= (O_2)ref + dO_2 \\ N_2 &= (N_2)ref + dN_2 \end{aligned}$$

For simplicity,  $(O_2)ref$  and  $(N_2)ref$  will now be considered equal to O<sub>2</sub> and N<sub>2</sub> in cases where they are referred to as reference levels.

Thus, a change in O<sub>2</sub>/N<sub>2</sub> ratio is given by:

$$d\left(\frac{O_2}{N_2}\right) = \frac{O_2 + dO_2}{N_2 + dN_2} - O_2 / N_2 \quad (A)$$

Also in standard notation  $\partial(O_2 / N_2)$  is a fractional change in ratio, and

$$\partial(O_2 / N_2) = \frac{d(O_2 / N_2)}{(O_2 / N_2)}.$$

Rearranging for  $dO_2$  in (A):

$$\frac{O_2 + dO_2}{N_2 + dN_2} - \frac{O_2}{N_2} + \frac{O_2}{N_2} = d\left(\frac{O_2}{N_2}\right) + \frac{O_2}{N_2},$$

$$O_2 + dO_2 = \left[ d\left(\frac{O_2}{N_2}\right) + \frac{O_2}{N_2} \right] (N_2 + dN_2)$$

$$\therefore O_2 + dO_2 = N_2 \times d\left(\frac{O_2}{N_2}\right) + dN_2 \times \frac{O_2}{N_2} + O_2 + dN_2 \times \frac{O_2}{N_2}$$

After subtracting  $O_2$  and ignoring very small terms with product  $dN_2 \times d\left(\frac{O_2}{N_2}\right)$ :

$$dO_2 = N_2 \times d\left(\frac{O_2}{N_2}\right) + dN_2 \times \frac{O_2}{N_2}$$

Dividing by  $O_2$  and subtracting  $\frac{dN_2}{N_2}$  term:

$$\frac{dO_2}{O_2} - \frac{dN_2}{N_2} = \frac{N_2}{O_2} \times d\left(\frac{O_2}{N_2}\right) + \frac{dN_2}{N_2} - \frac{dN_2}{N_2}$$

$$\begin{aligned} \therefore \frac{dO_2}{O_2} - \frac{dN_2}{N_2} &= d\left(\frac{O_2}{N_2}\right) \times \frac{N_2}{O_2} = \\ &= \frac{d(O_2/N_2)}{(O_2/N_2)} = \hat{\partial}(O_2/N_2) \end{aligned} \quad \text{(B)}$$

This gives the general rule that a fractional change in a ratio = (fractional change in the numerator) - (fractional change in the denominator).

The  $O_2$  mole fraction in air,  $S_{O_2}$ , is defined as:

$$S_{O_2} = \frac{O_2}{N_2 + O_2 + CO_2 + R}, \text{ where R is the rest of gas species in air} \quad \text{(C)}$$

When applying rule (B) to this ratio, we get

$$\frac{dX_{O_2}}{S_{O_2}} = \frac{dO_2}{O_2} - \frac{[dN_2 + dO_2 + dCO_2 + dR]}{[N_2 + O_2 + CO_2 + R]}$$

Put minor gas species on L.H.S so that

$$\frac{dX_{O_2}}{S_{O_2}} + \frac{dCO_2 + dR}{[N_2 + O_2 + CO_2 + R]} = \frac{dO_2}{O_2} - \frac{dN_2 + dO_2}{[N_2 + O_2 + CO_2 + R]} \quad \text{(D)}$$

From (C):  $N_2 + O_2 + CO_2 + R = \frac{O_2}{S_{O_2}}$ ,

and similarly to (C)

$$S_{N_2} = \frac{N_2}{N_2 + O_2 + CO_2 + R}$$

$$\therefore N_2 + O_2 + CO_2 + R = \frac{N_2}{S_{N_2}}$$

Thus, R.H.S of (D) becomes:

$$\frac{dO_2}{O_2} - \frac{dN_2 + dO_2}{[N_2 + O_2 + CO_2 + R]} = \frac{dO_2}{O_2} - \frac{dN_2}{N_2 + O_2 + CO_2 + R} - \frac{dO_2}{N_2 + O_2 + CO_2 + R}$$

$$\frac{dO_2}{O_2} - \frac{dN_2}{N_2/S_{N_2}} - \frac{dO_2}{O_2/S_{O_2}} =$$

$$= \frac{dO_2}{O_2}(1 - S_{O_2}) - \frac{S_{N_2} \times dN_2}{N_2} \quad (E)$$

Returning to (B):

$$\partial\left(\frac{O_2}{N_2}\right) = \frac{dO_2}{O_2} - \frac{dN_2}{N_2} \therefore$$

$$\frac{dO_2}{O_2} = \partial\left(\frac{O_2}{N_2}\right) + \frac{dN_2}{N_2}$$

Then substituting into (E),

$$\frac{dO_2}{O_2} - \frac{dN_2 + dO_2}{[N_2 + O_2 + CO_2 + R]} = \left[ \partial\left(\frac{O_2}{N_2}\right) + \frac{dN_2}{N_2} \right] (1 - S_{O_2}) - \frac{S_{N_2} \times dN_2}{N_2}$$

$$= \partial\left(\frac{O_2}{N_2}\right)(1 - S_{O_2}) + \frac{dN_2}{N_2}(1 - S_{O_2}) - \frac{S_{N_2} \times dN_2}{N_2}$$

$$= \partial\left(\frac{O_2}{N_2}\right)(1 - S_{O_2}) + \frac{dN_2}{N_2}(1 - S_{O_2} - S_{N_2}) \quad (F)$$

Ignore the last product  $\frac{dN_2}{N_2}(1 - S_{O_2} - S_{N_2})$ , since both factors are very small.

Therefore, returning to (D), with the result from (F):

$$\frac{dX_{O_2}}{S_{O_2}} + \frac{dCO_2}{[N_2 + O_2 + CO_2 + R]} + \frac{dR}{[N_2 + O_2 + CO_2 + R]} \approx \partial\left(\frac{O_2}{N_2}\right) \times (1 - S_{O_2}),$$

$$\text{i.e. } \partial\left(\frac{O_2}{N_2}\right) = \frac{dX_{O_2} + \left(\frac{dCO_2}{m} + \frac{dR}{m}\right)S_{O_2}}{(1 - S_{O_2})S_{O_2}},$$

where  $m = [N_2 + O_2 + CO_2 + R]$ .

In the case where  $dR$  is zero, and considering  $dCO_2$  to be  $(X_{CO_2} - CO_{2ref})$ , this equation can be seen to be equal to 4.1. This equation should be a good approximation even in cases where  $N_2$  changes since the term  $(1 - S_{O_2} - S_{N_2})$  in (F) is small.

## APPENDIX 2. The practical implementation for propagating calibration scales for long-term atmospheric measurements

This appendix describes the practical procedures with which to implement the long-term propagation of the “S1” calibration scales for both O<sub>2</sub> and CO<sub>2</sub>, and GC measurement systems at ZOTTO. This provides an illustration of a possible practical implementation of our calibration philosophy described in Chapter 4, Section 4.2.

A scheme for replacing older WSS (Working Secondary Standard) calibration cylinders with newer ones (for both O<sub>2</sub> and CO<sub>2</sub>, and GC measurement systems) is shown in the table below.

<b>O<sub>2</sub> and CO<sub>2</sub> measurement system</b>						
<b>Step</b>	<b>Cal_1</b>	<b>Cal_2</b>	<b>Cal_3</b>	<b>Cal_4</b>	<b>NextCal_a</b>	<b>NextCal_b</b>
0	A1	B1	C1	D1		
1	A1	B1	C1	D1	<b>F1*</b>	
2	A1	B1	C1	<b>F1</b>	<b>G1</b>	
3	A1	B1	<b>C2(G1)</b>	F1	<b>G2</b>	
4	A1	<b>G2</b>	C2(G1)	F1		
5	A1	G2	C2(G1)	<b>D2(F1)</b>	<b>F2</b>	
6	<b>F2</b>	<b>B2(G2)</b>	C2(G1)	D2(F1)	<b>G3</b>	
<b>GC measurement system</b>						
0	A1	B1	D1	E1		
1	A1	B1	D1	E1	<b>F1</b>	
2	A1	B1	D1	E1	F1	
3	A1	B1	D1	E1	F1	<b>G2</b>
4	A1	B1	D1	E1	F1	G2
5	A1	B1	<b>D2(F1)</b>	E1	<b>F2</b>	G2
6	A1	<b>B2(G2)</b>	D2(F1)	E1	F2	<b>G3</b>

\* Bold cylinder codes indicate a change from the previous step.

**Table A2.1: Propagation of S1 calibration scales via WSS cylinder replacement.**

Cal\_1, Cal\_2, Cal\_3 and Cal\_4 represent the role of four WSS cylinders used in the calibration procedures for both analysis systems. Each system uses four WSS cylinders, but typically not the same set of four, spanning a range of concentration in the relevant gas species. Thus, for example, at Step 0 in Table A2.1, the O<sub>2</sub> and CO<sub>2</sub> system uses WSS cylinders A1, B1, C1 and D1, whilst the GC system uses A1, B1, D1, and E1. It is also possible for the same actual cylinder to serve different roles on the two

systems. For example, again in Step 0, cylinder D1 serves the role of Cal\_4 on the O<sub>2</sub> and CO<sub>2</sub> system, and the role of Cal\_3 on the GC system. The positions NextCal\_a and NextCal\_b are for the purposes of providing an overlap period and analysing up to two new WSS cylinders along with the existing ones in order to define the concentrations of the new cylinders on the internal “S1” scale.

The **first letter** of the cylinder code given in the Table represents the physical position of a WSS cylinder in the Blue Box (equivalent to the position given in the LabView code and on Valco valve VA5 (See Chapter 3, Figure 3.1). Letters A to G are reserved for WSS cylinders, including any ‘new’ cylinders used during overlap periods. The **first number** of the cylinder code represents the historical sequence of cylinders in a particular physical position of the Blue Box. For example, ‘A1’ shows that the given cylinder occupies position ‘A’ in the Blue Box, and it is the first cylinder to be used in this position.

The **second letter** of the cylinder code (if present) indicates the previous position of a given cylinder in the Blue Box. The **second number** (if present) represents once again the sequence of cylinders in a given position. For example, ‘C2 (G1)’ indicates that this particular cylinder is the second cylinder to be in the ‘C’ position of the Blue Box, and it was previously the first cylinder to occupy position ‘G’.

The cylinder code should be comprised of no more than two letters as the cylinders are usually moved from one position of the Blue Box to another only once, but the numbers, indicating their sequence, will increase indefinitely. Note that when I discuss ‘moving’ a cylinder from one position to another, what is actually meant is that it is connected to a different regulator and hence is associated with a different position on the Valco valve (as indicated by the new cylinder code letter). The cylinder may or may not be physically moved to a different slot in the Blue Box depending if the length of high pressure tubing is long enough to extend to the new position.

## **Description of the Steps in Table A2.1**

**Step 0:** Initially there are a total of five cylinders used for the calibrations of both systems, with three being shared: A1, B1, C1 and D1 for O<sub>2</sub> and CO<sub>2</sub>; and A1, B1, D1 and E1 for GC;

**Step 1:** A new cylinder (F1) is placed into the Blue Box, which will eventually be used to replace cylinder D1 for both O<sub>2</sub> and CO<sub>2</sub>, and GC calibrations. This cylinder has the role NextCal\_a;

**Step 2:** F1 replaces the D1 cylinder in the role of Cal\_4 cylinder, but only on the O<sub>2</sub> and CO<sub>2</sub> system. Note that in this case F1 is not physically moved to the ‘D’ position of the

Blue Box because we need to keep analysing F1 in the 'NextCal\_a' role on the GC to get more concentration data for this new cylinder. This complication occurs because of the difference in the calibration frequencies between O<sub>2</sub> and CO<sub>2</sub>, and GC systems (approximately daily and weekly, respectively). We also add one more new cylinder in the 'G' position, which will eventually replace C1 (Cal\_3) for the O<sub>2</sub> and CO<sub>2</sub> system only (C1 is not used on the GC system);

**Step 3:** G1 physically replaces C1 in the O<sub>2</sub> and CO<sub>2</sub> calibration in the Cal\_3 role, and becomes C2(G1). Since this cylinder is not being used for the GC calibration, it is physically moved into the 'C' position of the Blue Box. Additionally, a new cylinder is put in the position 'G', which will eventually replace B1 (Cal\_2) for both systems. This cylinder has the role NextCal\_a on the O<sub>2</sub> and CO<sub>2</sub> system, and the role NextCal\_b on the GC system (because the cylinder F1 is still being run in the NextCal\_a position on the GC);

**Step 4:** G2 replaces B1 in the O<sub>2</sub> and CO<sub>2</sub> calibration in the role of Cal\_2. G2 is not moved physically into position 'B' since it needs to be analysed for a longer period on the GC;

**Step 5:** The F1 cylinder is now ready to replace D1 in the GC calibration Cal\_3 role. After being physically moved to position 'D', it becomes D2(F1) on both systems. At the same time, a new cylinder F2 is put into the now free position 'F' of the Blue Box, which will eventually replace A1 (Cal\_1 role) on both systems;

**Step 6:** The F2 cylinder replaces A1 in the Cal\_1 role in the O<sub>2</sub> and CO<sub>2</sub> calibration. F2 remains physically in the 'F' position of the Blue Box because it is still being analysed on the GC. At the same time, G2 is physically moved to the 'B' position and now becomes B2(G2) in the role of Cal\_2 on both systems. A new cylinder G3 is now installed in the 'G' position, filling the role of NextCal\_a on the O<sub>2</sub> and CO<sub>2</sub> system and NextCal\_b on the GC system. G3 will eventually replace D2(F1) on both systems.

At this point, after 6 steps, the O<sub>2</sub> and CO<sub>2</sub> system now has a completely new suite of four WSS cylinders used in the daily calibrations, although one of them (F2) is not in one of the 'traditional' positions (A, B, C, and D) because it is still being analysed in the NextCal\_a role on the GC. A1, B1, C1, and D1 have all been retired from the O<sub>2</sub> and CO<sub>2</sub> system, but A1 is still in the Blue Box, because it is still part of the GC calibration. A further cylinder, G3, is being analysed in preparation for the second cycle of replacements.

On the GC system after 6 steps, two cylinders have been replaced, whilst two are still the original cylinders. In the case of E1, because this cylinder is not used on the O<sub>2</sub> and CO<sub>2</sub> system, its lifetime will be significantly longer than all other WSS cylinders.

Two cylinders are being analysed on the GC system in preparation for future replacements.

### **APPENDIX 3. Zotino Tall Tower File Structure**

This appendix provides a summary of the output files generated by the custom LabVIEW™ program that was employed for collecting and processing atmospheric measurement data at ZOTTO from Nov 2005 until June 2007. The LabVIEW™ program was written by computer programmer, Thomas Seifert (MPI-BGC), under the supervision of Dr. Andrew Manning between 2004-2006.

All data processing, calibration and quality evaluation are carried out almost simultaneously with the data acquisition to minimise the need for post-processing of data. The concentration, calibration and diagnostics data are stored separately to facilitate data analyses. The final calibrated sample air data of O<sub>2</sub>, CO<sub>2</sub> and GC species (reported in concentration units of per meg, ppm and ppb respectively) are sorted by sampling heights.

The input parameters (for example, valve switching, line flushing times, amount of time the calibration gases are measured) are set (and can be easily modified) in the following initialisation (INI) files:

**zotSys.ini**

**zotCycles.ini**

**zotGCcycles.ini**

**zotGases.ini**

**zotWTanks.ini**

**zotGCWT.ini**

**zotQualFlag.ini**

**zotGCqualFlag.ini**

**zotSys.ini** – the main initialisation file that contains most of vital parameters to the system operation (for example, length of time of each measurement, number of times each calibration or Target Tank (TT) cylinder is analysed, duration of cylinder regulators' purging, etc).

**zotCycles.ini** – contains information about O<sub>2</sub> and CO<sub>2</sub> air and calibration cycles that is the air from which heights/calibration cylinders should be measured, in which order and for how long;

**zotGCcycles.ini** - contains information about GC air and calibration cycles;

**zotGases.ini** – stores information about all calibration (and other) cylinder's concentrations for all gas species which are used for the calculations of the final air concentrations;

**zotWTanks.ini** – contains O<sub>2</sub> and CO<sub>2</sub> concentration data for the currently used WT;

**zotGCWT.ini** – contains the concentration data for the currently used GC WT;

**zotQualFlag.ini** - allows setting limitations for the quality control of O<sub>2</sub> and CO<sub>2</sub> sample air data (see Appendix 4 for details);

**zotGCqualFlag.ini** – allows setting limitations for the quality control of GC species sample air data (see Appendix 4 for details);

The output data are sorted and written to six separate folders: ‘DEBUG’, ‘LOG’, ‘RAW’, ‘PRELIM’, ‘CALIB’, and ‘FINAL’. Below I give a brief description of the contents of each folder and their file structure.

### **DEBUG:**

The files in this folder are used for ‘debugging’ or detecting any functional errors in the system’s performance, in particular related to the LabView™ code itself.

**zotYYYYMMProtocol.txt** – registers all activities of O<sub>2</sub> and CO<sub>2</sub> system;

**zotYYYYMMProtocolGC.txt** – the same but for GC system;

**zotYYYYMMProtocolValve.txt** – contains information about switching of all valves in both O<sub>2</sub> and CO<sub>2</sub> and GC systems;

**zotYYYYMMDD.ai** – daily analog input diagnostics data (at 60 sec frequency)

**zotYYYYMMDD.aia** – daily average analog input diagnostics data (at 60 sec frequency).

### **LOG:**

The files in this folder are normally used for identification of errors in the system’s operation as well as simply a record of all changes in the initialisation files made by users.

**zotYYYYMMChiller.log** – a monthly log file of chiller trap changes performed by the onsite technician;

**zotYYYYMMcycles.log** – a monthly log file of all O<sub>2</sub> and CO<sub>2</sub> system cycles’ changes;

**zotNextSeq.log** – an input log file containing the latest information about all O<sub>2</sub> and CO<sub>2</sub> cycles and their measurement frequencies, used by the program to setup the required scheduling. Any changes in the cycles’ scheduling made in this file by an operator become operational as soon as LabVIEW™ is restarted (the program must be shut down when changes are being made);

**zotYYYYMMSys.log** – a monthly log file which contains information on all changes made by users in the zotSys.ini file (see above);

**zotNextDiag.log** - a log file which contains calibration parameters for all measurement equipment (e.g., pressure gauges, flow meters, etc);

**zotLimits.log** – contains input information on tolerances of concentration and diagnostic data ranges used for data quality control ('flags');

**zotSpan.log** – a log file which contains records of analyser calibration parameters from the last 'good' O<sub>2</sub> and CO<sub>2</sub> calibration (see Appendix 4 for criteria of 'good' calibrations);

**zotYYYYMMGases.log** – a monthly log file of all cylinder IDs and their concentrations for all measured species used in real-time LabVIEW™ calculations;

**zotYYYYMMWT.log** – a monthly log file of all WT cylinder changes in the Blue Box;

**zotAnalogInput.log** – an explanatory text file of all analog input ports;

**zotDigitalOutput.log** – an explanatory text file of all digital output ports;

**zotGCspan** - a log file which contains records of calibration parameters from the last 'good' GC calibration (see Appendix 4 for more details);

**zotYYYYMMNTS.txt** – a monthly log file of all user-entered notes;

**zotYYYYMMMSG.txt** – a monthly log file of all LabVIEW™-generated system messages.

### **RAW:**

The data in this folder are the original ('raw') data collected directly from analysers and diagnostic sensors. In the case of analyser data, they are stored in analyser units and are not calibrated. All files in this folder are created daily.

**zotYYYYMMDD.dat** –contains measurement data averaged over 60 sec for O<sub>2</sub> and CO<sub>2</sub> analysers. This file is generally not subsequently used, as it was intended for averaging the raw O<sub>2</sub> data from measurements of the fuel cells of an Oxzilla™ O<sub>2</sub> analyser which was never installed at ZOTTO;

**zotYYYYMMDD.sec** – all measurement data from O<sub>2</sub> and CO<sub>2</sub> analysers at 1 sec frequency;

**zotYYYYMMDD.dig** – all diagnostic and measurement data from all pieces of equipment (except internal GC characteristics) averaged and reported at 60 sec frequency;

**zotYYYYMMDDGC.dig** – all diagnostic values of the GC related equipment and average values of the internal GC characteristics at 60 sec frequency.

### **PRELIM:**

The data in this folder are processed relative to WT measurements for all analysers (see Chapter 4 for more detail). The O<sub>2</sub> and CO<sub>2</sub> measurements are reported as the interpolated difference between an air measurement (air jogs) and the average of

two bracketing WT measurements (WT jogs). The GC measurements are reported as ratios of air jogs and bracketing WT jogs. All files in this folder are created monthly. These data are crucial for air concentration recalculations (for all species) in the event of failure of their calibration, or retrospective concentration changes to S1 scale (see Chapter 4).

**zotYYYYMMPRX.cor** – interpolated differences of O<sub>2</sub> and CO<sub>2</sub> air and cylinder measurements at 16 min frequency;

**zotYYYYMMGC.cor** - interpolated ratios of GC air and cylinder measurements at 15 min frequency;

**zotAirYYYYMM.dat** – O<sub>2</sub> and CO<sub>2</sub> air measurements (all heights) as interpolated differences and in concentration units at 16 min frequency;

**zotAirYYYYMMGC.dat** –GC air measurements (all heights) in concentration units at 15 min frequency;

**zotYYYYMMGC.pol** – all GC data (air and cylinder measurements) fitted to a polynomial equation (calibration curves) in concentration units at 15 min frequency.

### **CALIB:**

The files in this folder contain calibration data for all analysers as well as TT (see Chapter 4) measurement results.

**zotYYYYspan.dat** – a yearly file of O<sub>2</sub> and CO<sub>2</sub> calibration parameters and WT concentrations (recalculated after every calibration);

**zotYYYYGCCalib.dat** – a yearly file of GC calibration parameters and GCWT concentrations (recalculated after every calibration);

**zotYYYYhsls.dat** – a yearly file of all calibration cylinder measurements for O<sub>2</sub> and CO<sub>2</sub> system (as interpolated differences);

**zotYYYYMMWT.dat** - a monthly file of all WT measurements for O<sub>2</sub> and CO<sub>2</sub> system in analyser units;

**zotYYYYMMTarget.dat** – a monthly file of all Target Tank measurements for the O<sub>2</sub> and CO<sub>2</sub> system (both as interpolated differences and in concentration units);

**zotYYYYGCTarget.dat** – a yearly file of all Target Tank measurements for the GC system (both as interpolated ratios and in concentration units).

### **FINAL:**

This folder contains final (sorted by heights) air measurement data for all species (in concentration units) that were calculated with the calibration parameters recorded in the CALIB folder.

**zot300AYYYMMDDCO<sub>2</sub>.dat** – a monthly file of calibrated O<sub>2</sub> and CO<sub>2</sub> data for 300-m height updated at the measurement frequency (16 min). The example shown here refers to the air measurements from the 300-m height; however, measurements from other heights are reported in the same file format (with the only difference of a sampling height in the files' names). Normally, letter 'A' after the height definition refers to a ¼" sampling line, whereas 'B' represents a 12-mm sampling line (see Chapter 3 for description of the sampling lines);

**zot300BYYYYMMDDGC.dat** – a monthly file of calibrated GC data from 300-m height updated at measurement frequency (15 min).



## APPENDIX 4. Protocols for automated data quality control

### at Zotino Tall Tower

This appendix describes data quality control procedures implemented within the custom-written LabView™ code that was used to operate the ZOTTO measurement system between Nov 2005 and Jun 2007. The main goal of the established protocols is to minimise the need for manual data processing.

I will describe the five quality control indicators or ‘flags’ used within ZOTTO LabView™ code, namely:

- diagnostic flags;
- air concentration limits flags;
- calibration quality flags;
- Target Tank (TT) flags;
- summary (final) flags.

Each of these flag types is defined for both O<sub>2</sub> and CO<sub>2</sub> and GC measurement systems (see Chapter 3, Figures 3.1, 3.5 and 3.9).

#### **1. Diagnostic flags**

The flags can be seen in daily diagnostic files (subdirectory RAW), for example, ZOT20061101.DIG. All diagnostic values (pressure, temperature, flowrate) are assigned a separate flag (see also Table A4.1). If a given flag is not raised, it is represented by an underscore. A row of data in a \*.DIG file represents a 30-sec average of 1-sec data values. A row will receive a flag value if it is raised for any of the 1-sec data values.

The first flag column contains only flags for diagnostic values of the O<sub>2</sub> and CO<sub>2</sub> system.

O<sub>2</sub> and CO<sub>2</sub> system diagnostic flags (for definitions see Fig. 3.1):

- P (pressure: P1, P4, P8, P10, P18, P19),
- X (OXP<sub>1-7</sub> pressure values),
- F (flowmeters: FL1, FL2, FL3),
- M (MFC’s: OXM<sub>1-7</sub>, M1),
- T (temperature: T6 and T7 only).

**Example:** if all parameters are out of range a column with O<sub>2</sub> and CO<sub>2</sub> diagnostic flags will appear as ‘PXFMT’. If nothing needs flagging, the column will be left with 5 underscores ‘\_\_\_\_\_’. Note that a ‘P’ flag does not specify exactly which pressure transducer is out of range, only that one or more of the 6 pressures listed above is out of range.

The second flag column contains the temperature flag (T) for temperature values that belong and have influence on both O<sub>2</sub> and CO<sub>2</sub> and GC systems (T1 to T5, T8 and T9).

The third column contains the flags for diagnostic values characterising GC performance.

GC system diagnostic flags:

- P (pressure: P12, P13, P15, P16, P17),
- G (GCP<sub>1-5</sub> pressure values),
- F (flowmeter: FL5),
- M (MFC: M2).

**Example:** if all parameters are out of range a column of GC flags will appear as 'PGFM'. If nothing needs flagging, the column will be left with underscores '\_\_\_\_'. Acceptable ranges for all the diagnostic flags are written to ZotLimitsLena.LOG file (see also Table A4.1 below).

The first two of the three columns described above also appear identically in the daily \*.DAT file (Subdirectory RAW).

## **2. Air concentration limits flags**

The flags for O<sub>2</sub> and CO<sub>2</sub> concentration values can be found in monthly \*.DAT files, for example, ZOTAIR200611.DAT (subdirectory PRELIM). The limits for the 'acceptable' concentration ranges are written to ZotQualFlag.ini file (see also Table A4.1).

The following limits were designated as cut-off values for CO<sub>2</sub> and O<sub>2</sub>:

- CO<sub>2</sub>: low limit 340.0 ppm  
high limit 480 ppm
- O<sub>2</sub>: low limit -900.0 per meg  
high limit -200.0 per meg

If ambient concentrations of O<sub>2</sub> and/or CO<sub>2</sub> are outside of these ranges the concentration limits flag will be given to a data row.

**Example:** flags for CO<sub>2</sub> and O<sub>2</sub> appear as 'C' and 'O' respectively.

The first two diagnostic flag columns from \*.DIG files for O<sub>2</sub> and CO<sub>2</sub> system will be also shown here to provide additional information on data quality. Since \*.DIG

files have a data acquisition frequency of 60 sec, and \*.DAT files collect data over a 15 min interval the flags in \*.DAT files are a sum of all diagnostic flags over 15 min. In other words, if a flag is raised in any of the 30 rows of data in the \*.DIG file corresponding to one 15-min average row of data in the \*.DAT file, then the \*.DAT file will also contain the relevant flag. In theory, this means that it is possible that a flag is raised in a 15-min averaged row of data even though the relevant parameter may have only been ‘bad’ for one second.

The flags for GC species concentrations are given in monthly \*.DAT files, for example, ZOTAIR200611GC.DAT (subdirectory PRELIM). The limits for the ‘acceptable’ concentration ranges are written to ZotGCqualFlag.ini file and shown in Table A4.1 below.

The following limits were designated as cut-off values for GC species:

- CH<sub>4</sub>: low limit 1700 ppb  
high limit 2200 ppb
- CO: low limit 100 ppb  
high limit 1000 ppb
- N<sub>2</sub>O: low limit 315 ppb  
high limit 330 ppb

If the ambient concentration of any/all GC species is outside of these ranges the concentration limits flag will be given to a data row.

**Example:** flags for CH<sub>4</sub>, CO and N<sub>2</sub>O appear as ‘M’, ‘X’ and ‘N’ respectively.

GC diagnostic flags from \*.DIG files are also shown here to provide additional information on data quality. These flags are given as a sum of the diagnostic flags in \*.DIG files over 15 min owing to the difference in the reporting frequency of \*.DIG (60 sec) and \*.DAT files (15 min).

### **3. Calibration quality flags**

The quality of calibrations is monitored with the calibration quality flags. In the beginning, I used WT concentrations (re-assigned after every calibration) as the criteria for ‘bad/good’ calibrations of each measured species. However, due to the possibility of relatively large concentration drifts over the lifetime of a WT, especially for O<sub>2</sub> (see Chapter 4, Section 4.3), I have decided to use a different criterion, namely the least squares residuals of a 4-point calibration ( $R^2$ ), which is calculated at the end of every calibration. It proved to be a reliable indicator for ‘bad’ or ‘failed’ (due to technical

problems with the system) calibrations, particularly for those species which are calibrated with linear fits (O<sub>2</sub>, CH<sub>4</sub> and CO). The flags for ‘bad’ calibrations appear in the yearly span files, for example ZOT2006SPAN.DAT (subdirectory CALIB) for O<sub>2</sub> and CO<sub>2</sub>, and in GC calibration files, for example ZOT2006GCCALIB.DAT (subdirectory CALIB).

In addition to R<sup>2</sup>, I defined an ‘acceptable’ range for the instrument’s span (first order coefficient of a fitted curve, sometimes called the instrument’s ‘sensitivity’) for O<sub>2</sub> and CO<sub>2</sub>. Normally, low R<sup>2</sup> values lead to very different (from average) span values as well. Thus, both parameters are taken into account when evaluating calibration quality. For CO<sub>2</sub>, I also defined an ‘acceptable’ range for zero coefficients, which correspond to WT concentrations. In the case of CO<sub>2</sub>, the concentration drifts in WT cylinders are minor (see Chapter 4, Figure 4.4) thus it is possible to use WT concentrations (re-assigned daily) to evaluate the quality of calibrations. For GC species, only the R<sup>2</sup> parameter is used (and proved sufficient) to evaluate calibration quality.

For the O<sub>2</sub> and CO<sub>2</sub> system, ‘acceptable’ ranges for all these parameters are written to ZotQualFlag.ini file. These ranges for all quality calibration flags are given below (see also Table A4.1):

CO<sub>2</sub> calibration is declared as ‘good’ if:

- R<sup>2</sup> is greater than or equal to 0.99991, and/or
- CO<sub>2</sub> span [instrument units/ppm] is greater than or equal to 0.94 and less than or equal to 1.03, and/or
- CO<sub>2</sub> zero coefficient [ppm] varies by less than or equal to 0.015 ppm from the average zero coefficient for a given WT (the average WT value is updated after every daily calibration). The very first WT estimate (after the WT change) is ignored as it might be affected by insufficient conditioning of a new WT cylinder regulator.

O<sub>2</sub> calibration is declared as ‘good’ if:

- R<sup>2</sup> is greater than or equal to 0.986, and/or
- O<sub>2</sub> span [instrument units/ppm Equiv] is greater than or equal to 0.535 and less than or equal to 0.56.

**Example:** if all parameters above are out of range for both O<sub>2</sub> and CO<sub>2</sub> a column with the calibration quality flag will appear as ‘RSWRS’.

If only CO<sub>2</sub> has out of range parameters then the column will appear as 'RSW\_\_'.

For GC species, the R<sup>2</sup> deviation ranges are written to ZotGCQualFlag.ini file.

CH<sub>4</sub> calibration is declared as 'good' if:

- R<sup>2</sup> is greater than or equal to 0.9998.

CO calibration is declared as 'good' if:

- R<sup>2</sup> is greater than or equal to 0.998.

N<sub>2</sub>O calibration is declared as 'good' if:

- R<sup>2</sup> is greater than or equal to 0.995.

**Example:** if R<sup>2</sup> values are out of range for CH<sub>4</sub>, CO, N<sub>2</sub>O a column with the calibration quality flag will appear as 'MXN'. If only CH<sub>4</sub> has out of range R<sup>2</sup> then the column will appear as 'M\_\_'.

#### **4. The Target Tank (TT) flags**

The accuracy of Target Tank (TT) measurements provides us with an important tool for evaluating sample air data quality. A certain 'acceptable' range for the variability of TT measurement accuracy is defined for each measured species. Unlike WT concentrations, those of TT measurements can be compared with the declared (independent and initial) values provided by MPI-BGC. If the TT concentration is outside of the defined range, the TT flag will be shown in target files, for example, ZOT200611TARGET.DAT (subdirectory CALIB) for O<sub>2</sub> and CO<sub>2</sub>, and ZOT2006GCTARGET.DAT (subdirectory CALIB) for GC species (see also Table A4.1).

The 'acceptable' limits for the TT accuracy range are written to ZotQualFlag.ini (for O<sub>2</sub> and CO<sub>2</sub>) and ZotGCQual.Flag.ini files (for GC species).

**NOTE:** The TT flags also appear in ZOTAIR.DAT and ZOTAIRGC.DAT. These files have a collection of all flags to provide detailed information about sample air data quality.

The maximum deviation of internally defined O<sub>2</sub> concentration of a TT can be ± 8 ppmEquiv (from the declared value). This deviation is defined as a difference between the internally defined O<sub>2</sub> TT concentration (after regular calibration) and the declared value from MPI-BGC.

The max deviation of internally defined CO<sub>2</sub> concentration of a TT can be ±0.2 ppm (from the declared value).

The max deviation of internally defined CH<sub>4</sub> concentration of a TT can be ±5 ppb (from the declared value).

The max deviation of internally defined CO concentration of a TT can be ±5 ppb (from the declared value).

The max deviation of internally defined N<sub>2</sub>O concentration of a TT can be ±0.4 ppb (from the declared value).

**Example 1 (O<sub>2</sub> and CO<sub>2</sub>):** If TT concentrations are out of range for both species, the TT flag will look like ‘CO’.

**Example 2 (GC species):** If TT concentrations are out of range for all GC species the TT flag will look like ‘MXN’. If CO TT concentration is the only one out of range, the TT flag will look like ‘\_X\_’.

#### **5. Final Data Quality Record (Summary Flags):**

The final data quality flags are saved in a ‘database friendly’ format in files like ZOT300A20061101CO2.DAT and ZOT300A20061101GC.DAT (subdirectory FINAL). The data from the O<sub>2</sub> and CO<sub>2</sub> system are written to the files of the above format separately for each height. Since these files are the last step in the data monitoring, they should contain a ‘flags summary’ for all gas species. Unlike other flags described above the summary flags are numeric: 0 or 1 (0 – no flag; 1 – raised flag) (see also Table A4.1).

The structure of the summary flags is the following:

- diagnostic flags; air concentration limits flags; calibration quality flags; TT flags.

**Example:** 0 0 0 0 - a data row with no flags;

0 0 1 1 - a data row with calibration quality and TT flags. As suggested, these flags are a summary, and will be ‘1’ if any of the relevant flags (defined in sections 1 to 4 above) for those gas species have occurred.

**NOTE:** Normally, if a data row has no flag of any kind, it will be left blank (\_\_\_\_). The FINAL flag is the only exception – a data row without any flag will be signed with ‘0’s.

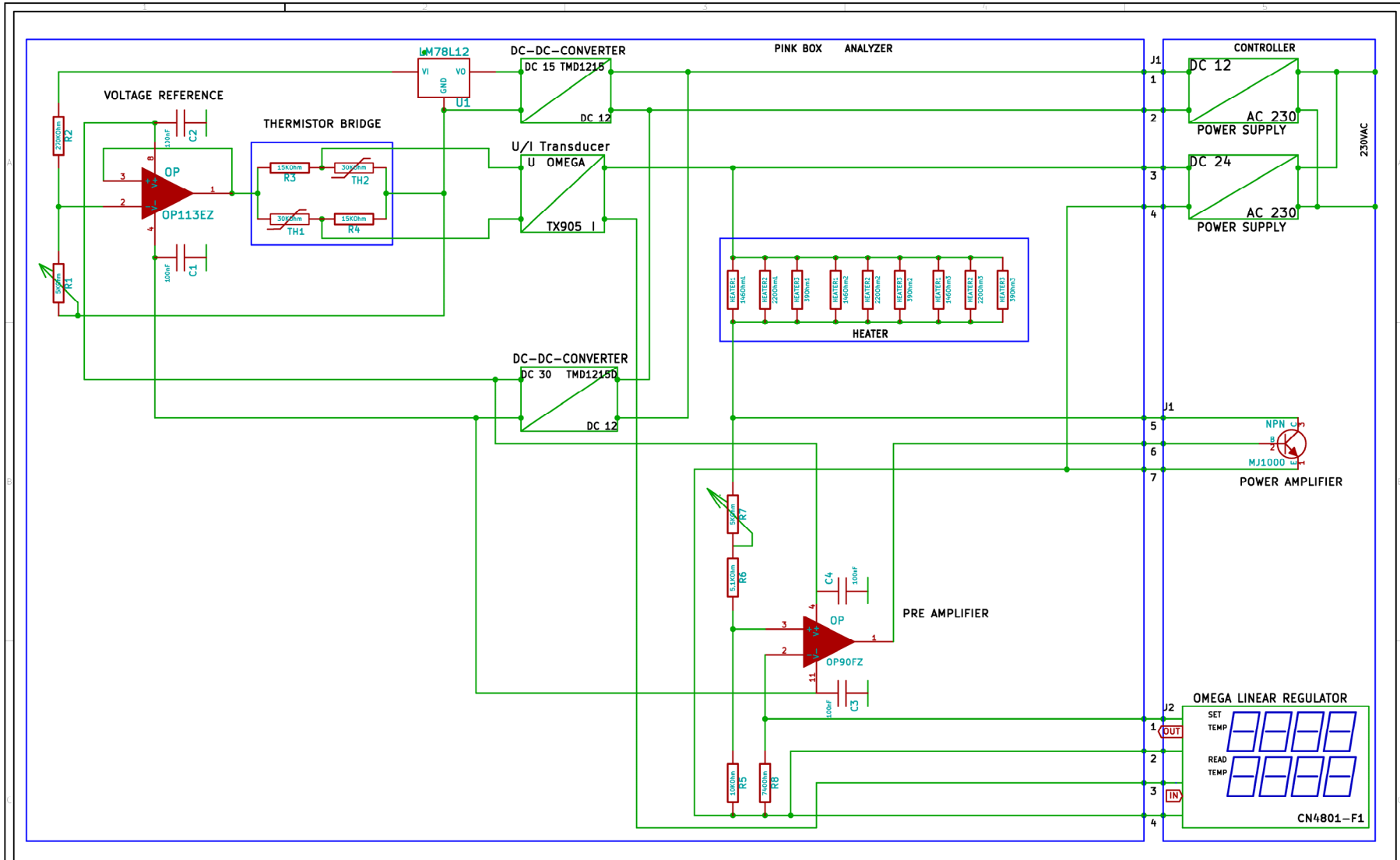
Table A4.1 (below) provides summarised information on all types of quality flags, as well as their definitions and abbreviations.

Parameter	Parameter Limits	Units	Flag Type	Flag	Appears in Files
P1,P4	$1400 \leq X \leq 1600$	mbar	D-CO	P	ZOT20061101.DIG, ZOTAIR200611.DAT
P8	$1300 \leq X \leq 1360$	mbar	D-CO	P	ZOT20061101.DIG, ZOTAIR200611.DAT
P10	$1140 \leq X \leq 1200$	mbar	D-CO	P	ZOT20061101.DIG, ZOTAIR200611.DAT
(P18+P19)	$X \geq 200$	psig	D-CO	P	ZOT20061101.DIG, ZOTAIR200611.DAT
OX P1-7	$500 \leq X \leq 700$	mbar	D-CO	X	ZOT20061101.DIG, ZOTAIR200611.DAT
FL1	$100 \leq X \leq 160$	mL/min	D-CO	F	ZOT20061101.DIG, ZOTAIR200611.DAT
FL2	$10 \leq X \leq 30$	mL/min	D-CO	F	ZOT20061101.DIG, ZOTAIR200611.DAT
FL3	$120 \leq X \leq 135$	mL/min	D-CO	F	ZOT20061101.DIG, ZOTAIR200611.DAT
OX M1-7	$149 \leq X \leq 151$	mL/min	D-CO	M	ZOT20061101.DIG, ZOTAIR200611.DAT
M1	$29.7 \leq X \leq 30.2$	mL/min	D-CO	M	ZOT20061101.DIG, ZOTAIR200611.DAT
T6	$43 \leq X \leq 45$	°C	D-CO	T	ZOT20061101.DIG, ZOTAIR200611.DAT
T7	$33.95 \leq X \leq 34.20$	°C	D-CO	T	ZOT20061101.DIG, ZOTAIR20061101.DAT
T1=T2	$20 \leq X \leq 21.5$	°C	D-Temp	T	ZOT20061101.DIG, ZOTAIR20061101.DAT, ZOTAIR200611GC.DAT
T3	$1 \leq X \leq 10$	°C	D-Temp	T	ZOT20061101.DIG, ZOTAIR200611.DAT, ZOTAIR200611GC.DAT
T4	$-91 \leq X \leq -90$	°C	D-Temp	T	ZOT20061101.DIG, ZOTAIR200611.DAT, ZOTAIR200611GC.DAT
T5	$21 \leq X \leq 23$	°C	D-Temp	T	ZOT20061101.DIG, ZOTAIR200611.DAT, ZOTAIR200611GC.DAT
T8=T9	$15 \leq X \leq 20$	°C	D-Temp	T	ZOT20061101.DIG, ZOTAIR200611.DAT, ZOTAIR200611GC.DAT
P12,P13	$1300 \leq X \leq 1700$	mbar	D-GC	P	ZOT20061101.DIG, ZOTAIR200611GC.DAT
P15	$1160 \leq X \leq 1220$	mbar	D-GC	P	ZOT20061101.DIG, ZOTAIR200611GC.DAT
(P16+P17)	$X \geq 225$	psig	D-GC	P	ZOT20061101.DIG, ZOTAIR200611GC.DAT
GCP1-5	$400 \leq X \leq 700$	mbar	D-GC	G	ZOT20061101.DIG, ZOTAIR200611GC.DAT
FL5	$60 \leq X \leq 140$	mL/min	D-GC	F	ZOT20061101.DIG, ZOTAIR200611GC.DAT
M2	$90 \leq X \leq 110$	mL/min	D-GC	M	ZOT20061101.DIG, ZOTAIR200611GC.DAT

CO <sub>2</sub>	340≤X ≤480	ppm	AIR-C	C	ZOTAIR200611.DAT
O <sub>2</sub>	-900≤X ≤-200	per meg	AIR-O	O	ZOTAIR200611.DAT
CH <sub>4</sub>	1700≤X≤22000	ppb	AIR-M	M	ZOTAIR200611GC.DAT
CO	100≤X≤1000	ppb	AIR-X	X	ZOTAIR200611GC.DAT
N <sub>2</sub> O	315≤X≤330	ppb	AIR-N	N	ZOTAIR200611GC.DAT
CO <sub>2</sub> R <sup>2</sup>	≥0.99991	-	CAL-C	R	ZOT2006SPAN.DAT
CO <sub>2</sub> span	0.94≤X≤1.03	raw/ppm	CAL-C	S	ZOT2006SPAN.DAT, ZOTAIR200611.DAT
CO <sub>2</sub> WT	≤0.015 from avg.	ppm	CAL-C	W	ZOT2006SPAN.DAT, ZOTAIR200611.DAT
O <sub>2</sub> R <sup>2</sup>	≥0.986	-	CAL-O	R	ZOT2006SPAN.DAT, ZOTAIR200611.DAT
O <sub>2</sub> span	0.535≤X≤0.56	raw/ppmEq	CAL-O	S	ZOT2006SPAN.DAT, ZOTAIR200611.DAT
CH <sub>4</sub> R <sup>2</sup>	≥0.9998	-	CAL-GC	M	ZOT2006GCCALIB.DAT, ZOTAIR200611GC.DAT
CO R <sup>2</sup>	≥0.998	-	CAL-GC	X	ZOT2006GCCALIB.DAT, ZOTAIR200611GC.DAT
N <sub>2</sub> O R <sup>2</sup>	≥0.995	-	CAL-GC	N	ZOT2006GCCALIB.DAT, ZOTAIR200611GC.DAT
CO <sub>2</sub> TT	Decl. TT ±0.2	ppm	TT-C	C	ZOT200611TARGET.DAT, ZOTAIR200611.DAT
O <sub>2</sub> TT	Decl. TT ±8	ppmEq	TT-O	O	ZOT200611TARGET.DAT, ZOTAIR2006011.DAT
CH <sub>4</sub> TT	Decl. TT ±5	ppb	TT-M	M	ZOT2006GCTARGET.DAT, ZOTAIR200611GC.DAT
CO TT	Decl. TT ±5	ppb	TT-X	X	ZOT2006GCTARGET.DAT, ZOTAIR200611GC.DAT
N <sub>2</sub> O TT	Decl. TT ±0.4	ppb	TT-N	N	ZOT2006GCTARGET.DAT, ZOTAIR200611GC.DAT
CO <sub>2</sub> flag summary	Bad CO <sub>2</sub> DACT	flag	SUM-C	1111	ZOT300A20061101CO <sub>2</sub> .DAT
O <sub>2</sub> flag summary	Bad O <sub>2</sub> DACT	flag	SUM-O	1111	ZOT300A20061101CO <sub>2</sub> .DAT
CH <sub>4</sub> flag summary	Bad CH <sub>4</sub> DACT	flag	SUM-M	1111	ZOT300A20061101GC.DAT
CO flag summary	Bad CO DACT	flag	SUM-X	1111	ZOT300A20061101GC.DAT
N <sub>2</sub> O flag summary	Bad N <sub>2</sub> O DACT	flag	SUM-N	1111	ZOT300A20061101GC.DAT

**Table A4.1: ZOTTO flags summary**

# APPENDIX 5. Electronics schematic for temperature control of Servomex O<sub>2</sub> analyser in Pink Box





## BIBLIOGRAPHY

- Adachi, Y., K. Kawamura, L. Armi, and R. F. Keeling, Diffusive separation of the lower atmosphere, *Science*, 311 (5766), 1429-1429, 2006.
- Andres, R. J., G. Marland, I. Fung, and E. Matthews, A 1 degrees x 1 degrees distribution of carbon dioxide emissions from fossil fuel consumption and cement manufacture, 1950-1990, *Global Biogeochemical Cycles*, 10 (3), 419-429, 1996.
- Anthoni, P. M., A. Knohl, C. Rebmann, A. Freibauer, M. Mund, W. Ziegler, O. Kolle, and E.-D. Schulze, Forest and agricultural land-use-dependent CO<sub>2</sub> exchange in Thuringia, Germany, *Global Change Biology*, 10 (12), 2005-2019, 2004.
- Arrhenius, S., On the influence of carbonic acid in the air upon the temperature on the ground, *Philos. Mag.*, 41, 237-276, 1896.
- Bakwin, P. S., D. F. Hurst, P. P. Tans, and J. W. Elkins, Anthropogenic sources of halocarbons, sulfur hexafluoride, carbon monoxide, and methane in the southeastern United States, *Journal of Geophysical Research-Atmospheres*, 102 (D13), 15915-15925, 1997.
- Bakwin, P. S., P. P. Tans, D. F. Hurst, and C. L. Zhao, Measurements of carbon dioxide on very tall towers: results of the NOAA/CMDL program, *Tellus Series B-Chemical and Physical Meteorology*, 50 (5), 401-415, 1998.
- Bakwin, P. S., P. P. Tans, C. L. Zhao, W. Ussler, and E. Quesnell, Measurements of Carbon-Dioxide on a Very Tall Tower, *Tellus Series B-Chemical and Physical Meteorology*, 47 (5), 535-549, 1995.
- Battle, M., M. Bender, T. Sowers, P. P. Tans, J. H. Butler, J. W. Elkins, J. T. Ellis, T. Conway, N. Zhang, P. Lang, and A. D. Clarke, Atmospheric gas concentrations over the past century measured in air from firm at the South Pole, *Nature*, 383 (6597), 231-235, 1996.
- Battle, M., S. E. Mikaloff Fletcher, M. L. Bender, R. F. Keeling, A. C. Manning, N. Gruber, P. P. Tans, M. B. Hendricks, D. T. Ho, C. Simonds, R. Mika, and B. Paplawsky, Atmospheric potential oxygen: New observations and their implications for some atmospheric and oceanic models, *Global Biogeochemical Cycles*, 20 (1), 2006.
- Bender, M., T. Ellis, P. Tans, R. Francey, and D. Lowe, Variability in the O<sub>2</sub>/N<sub>2</sub> ratio of southern hemisphere air, 1991-1994: Implications for the carbon cycle, *Global Biogeochemical Cycles*, 10 (1), 9-21, 1996.
- Blaine, T. W., Continuous measurements of atmospheric argon/nitrogen as a tracer of air-sea heat flux: Models, methods, and data, Ph.D. thesis, University of California, San Diego, La Jolla, 2005.
- Blaine, T. W., R. F. Keeling, and W. J. Paplawsky, An improved inlet for precisely measuring the atmospheric Ar/N<sub>2</sub> ratio, *Atmospheric Chemistry and Physics*, 6, 1181-1184, 2006.
- Broecker, W. S., and T. H. Peng, *Tracers in the Sea*, Lamont Doherty Geological Observatory, Palisades, NY, USA, 1982.
- Callendar, G. S., The artificial production of carbon dioxide and its influence on temperature, *The Quarterly Journal of the Royal Meteorological Society*, 64, 223-237, 1938.
- Chapin, F. S., M. Sturm, M. C. Serreze, J. P. McFadden, J. R. Key, A. H. Lloyd, A. D. McGuire, T. S. Rupp, A. H. Lynch, J. P. Schimel, J. Beringer, W. L. Chapman, H. E. Epstein, E. S. Euskirchen, L. D. Hinzman, G. Jia, C. L. Ping, K. D. Tape, C. D. C. Thompson, D. A. Walker, and J. M. Welker, Role of land-surface changes in Arctic summer warming, *Science*, 310 (5748), 657-660, 2005.

- Chapman, W. L., and J. Walsh, Recent Variations of Sea Ice and Air-Temperature in High-Latitudes *Bulletin of the American Meteorological Society*, 74 (1), 33-47, 1993.
- Chevillard, A., U. Karstens, P. Ciais, S. Lafont, and M. Heimann, Simulation of atmospheric CO<sub>2</sub> over Europe and western Siberia using the regional scale model REMO, *Tellus Series B-Chemical and Physical Meteorology*, 54 (5), 872-894, 2002.
- Ciais, P., P. P. Tans, J. W. C. White, M. Trolier, R. J. Francey, J. A. Berry, D. R. Randall, P. J. Sellers, J. G. Collatz, and D. S. Schimel, Partitioning of Ocean and Land Uptake of Co<sub>2</sub> as Inferred by Delta-C-13 Measurements from the Noaa Climate Monitoring and Diagnostics Laboratory Global Air Sampling Network, *Journal of Geophysical Research-Atmospheres*, 100 (D3), 5051-5070, 1995.
- Cofer, W. R. I., J. S. Levine, E. L. Winstead, and B. J. Stocks, Trace gas and particulate emissions from biomass burning in temperate ecosystems, in *Global Biomass Burning: Atmospheric, Climatic, and Biospheric Implication*, edited by Levine, J. S., pp. pp.203-208, MIT Press, Cambridge, Mass., 1991.
- Conrad, R., Soil microorganisms as controllers of atmospheric trace gases (H<sub>2</sub>, CO, CH<sub>4</sub>, OCS, N<sub>2</sub>O, and NO), *Microbiological Reviews*, 60 (4), 609-&, 1996.
- Denman, K. L., G. Brasseur, A. Chidthaisong, P. Ciais, P.M. Cox, R.E. Dickinson, D. Hauglustaine, C. Heinze, E. Holland, D. Jacob, U. Lohmann, S Ramachandran, P.L. da Silva Dias, S. C. Wofsy, and a. X. Zhang, Couplings Between Changes in the Climate System and Biogeochemistry, in *Climate Change 2007: The Physical Science Basis. Contribution of Working Group I to the Fourth Assessment Report of the Intergovernmental Panel on Climate Change*, edited by Solomon, S., D. Qin, M. Manning, Z. Chen, M.C. Marquis, K.B. Averyt, M.Tignor and H.L. Miller, Cambridge University Press, Cambridge, United Kingdom and New York, NY, USA, 2007.
- Denning, A. S., M. Holzer, K. R. Gurney, M. Heimann, R. M. Law, P. J. Rayner, I. Y. Fung, S. M. Fan, S. Taguchi, P. Friedlingstein, Y. Balkanski, J. Taylor, M. Maiss, and I. Levin, Three-dimensional transport and concentration of SF<sub>6</sub> - A model intercomparison study (TransCom 2), *Tellus Series B-Chemical and Physical Meteorology*, 51 (2), 266-297, 1999.
- Dlugokencky, E. J., E. G. Dutton, P. C. Novelli, P. P. Tans, K. A. Masarie, K. O. Lantz, and S. Madronich, Changes in CH<sub>4</sub> and CO growth rates after the eruption of Mt Pinatubo and their link with changes in tropical tropospheric UV flux, *Geophysical Research Letters*, 23 (20), 2761-2764, 1996.
- Draxler, R. R., and G. D. Hess, An overview of the HYSPLIT\_4 modelling system for trajectories, dispersion, and deposition, *Aust. Met. Mag.*, 47, 295-308, 1998.
- Ehleringer, J. R., D. R. Bowling, L. B. Flanagan, J. Fessenden, B. Helliker, L. A. Martinelli, and J. P. Ometto, Stable isotopes and carbon cycle processes in forests and grasslands, *Plant Biology*, 4 (2), 181-189, 2002.
- Enting, I. G., C. M. Trudinger, and R. J. Francey, A Synthesis Inversion of the Concentration and Delta-C-13 of Atmospheric CO<sub>2</sub>, *Tellus Series B-Chemical and Physical Meteorology*, 47 (1-2), 35-52, 1995.
- Forster, P., V. Ramaswamy, P. Artaxo, T. Berntsen, R. Betts, D. W. Fahey, J. Haywood, J. Lean, D. C. Lowe, and G. Myhre, Changes in atmospheric constituents and radiative forcing in *Climate Change 2007: The Physical Science Basis (Contribution of Working Group I to the Fourth Assessment Report of the Intergovernmental Panel on Climate Change)*, edited by Solomon, S., Qin, D., Manning, M., Chen, Z., Marquis, M., Averyt, KB, Tignor, M. and Miller, HL, pp. 129-234, Cambridge University Press, Cambridge, UK and New York, NY, USA, 2007.
- Fourier, J., Mémoire Sur Les Températures Du Globe Terrestre Et Des Espaces Planétaires, *Mémoires de l'Académie Royale des Sciences*, 7, 569-604, 1827.

- Friedlingstein, P., P. Cox, R. Betts, L. Bopp, W. von Bloh, V. Brovkin, P. Cadule, S. Doney, M. Eby, I. Fung, G. Bala, J. John, C. Jones, F. Joos, T. Kato, M. Kawamiya, W. Knorr, K. Lindsay, H. D. Matthews, T. Raddatz, P. Rayner, C. Reick, E. Roeckner, K.-G. Schnitzler, R. Schnur, K. Strassmann, A. J. Weaver, C. Yoshikawa, and N. Zeng, Climate-carbon cycle feedback analysis: Results from the C<sup>4</sup>MIP model intercomparison, *Journal of Climate*, 19 (14), 3337-3353, 2006.
- Gamnitzer, U., U. Karstens, B. Kromer, R. E. M. Neubert, H. A. J. Meijer, H. Schroeder, and I. Levin, Carbon monoxide: A quantitative tracer for fossil fuel CO<sub>2</sub>?, *Journal of Geophysical Research-Atmospheres*, 111 (D22), 2006.
- García, H. E., and R. F. Keeling, On the global oxygen anomaly and air-sea flux, *Journal of Geophysical Research-Oceans*, 106 (C12), 31155-31166, 2001.
- Gibson, J. K., P. Kallberg, S. Uppala, A. Hernandez, A. Nomura, and E. Serrano, ERA description, ECMWF Re-Analysis Project Report Series 72 pp., Reading, England, U.K., 1997.
- GLOBALVIEW-CH<sub>4</sub>: Cooperative Atmospheric Data Integration Project - Methane. CD-ROM, N. E., Boulder, Colorado [Also available on Internet via anonymous FTP to ftp.cmdl.noaa.gov, Path: ccg/ch4/GLOBALVIEW], 2009.
- GLOBALVIEW-CO<sub>2</sub>, Cooperative Atmospheric Data Integration Project - Carbon Dioxide., CD-ROM, NOAA GMD, Boulder, Colorado [Also available on Internet via anonymous FTP to ftp.cmdl.noaa.gov, Path: ccg/co2/GLOBALVIEW], 2007.
- GLOBALVIEW-CO: Cooperative Atmospheric Data Integration Project - Carbon Monoxide. CD-ROM, N. E., Boulder, Colorado [Also available on Internet via anonymous FTP to ftp.cmdl.noaa.gov, Path: ccg/co/GLOBALVIEW], 2009.
- Gloor, M., P. Bakwin, D. Hurst, L. Lock, R. Draxler, and P. Tans, What is the concentration footprint of a tall tower?, *Journal of Geophysical Research-Atmospheres*, 106 (D16), 17831-17840, 2001.
- Gurney, K., R. Law, P. Rayner, and A. S. Denning, "Transcom 3 Experimental Protocol", Paper No.707, USA, 2000.
- Haszpra, L., Z. Barcza, P. S. Bakwin, B. W. Berger, K. J. Davis, and T. Weidinger, Measuring system for the long-term monitoring of biosphere/atmosphere exchange of carbon dioxide, *Journal of Geophysical Research-Atmospheres*, 106 (D3), 3057-3069, 2001.
- Heimann, M., The cycle of atmospheric molecular oxygen and its isotopes, in *Global Biogeochemical Cycles in the Climate System*, edited by Schulze, E.-D., pp. 235-244, Academic Press, San Diego, California, 2001.
- Heimann, M., and S. Koerner, The global atmospheric tracer model TM3, in *Max-Planck-Insitut fuer Biogeochemie 5*, 131 pp., Jena, Germany, 2003.
- Hollinger, D. Y., F. M. Kelliher, J. N. Byers, J. E. Hunt, T. M. McSeveny, and P. L. Weir, Carbon dioxide exchange between an undisturbed old-growth temperate forest and the atmosphere, *Ecology*, 75 (1), 134-150, 1994.
- Hurst, D. F., P. S. Bakwin, R. C. Myers, and J. W. Elkins, Behavior of trace gas mixing ratios on a very tall tower in North Carolina, *Journal of Geophysical Research-Atmospheres*, 102 (D7), 8825-8835, 1997.
- Jiang, X., W. L. Ku, R. L. Shia, Q. B. Li, J. W. Elkins, R. G. Prinn, and Y. L. Yung, Seasonal cycle of N<sub>2</sub>O: Analysis of data, *Global Biogeochemical Cycles*, 21 (1), doi:10.1029/2006gb002691, 2007.
- Jordan, A., A. C. Manning, U. Schultz, T. Seifert, M. Gloor, M. Heimann, and E.-D. Schulze, Continuous GC measurements of trace gases at the Ochsenkopf monitoring station, in *Report of the Twelfth WMO/IAEA Meeting of Experts on Carbon Dioxide Concentration and Related Tracers Measurement Techniques*, edited by Worthy, D. E., and L. Huang, Toronto, 2005.

- Karstens, U., M. Gloor, M. Heimann, and C. Rodenbeck, Insights from simulations with high-resolution transport and process models on sampling of the atmosphere for constraining midlatitude land carbon sinks, *Journal of Geophysical Research-Atmospheres*, 111 (D12), 2006.
- Kasischke, E. S., E. J. Hyer, P. C. Novelli, L. P. Bruhwiler, N. H. F. French, A. I. Sukhinin, J. H. Hewson, and B. J. Stocks, Influences of boreal fire emissions on Northern Hemisphere atmospheric carbon and carbon monoxide, *Global Biogeochemical Cycles*, 19 (1), 2005.
- Keeling, C. D., The concentration and isotopic abundances of atmospheric carbon dioxide in rural areas, *Geochimica et Cosmochimica Acta*, 13 (4), 322-334, 1958.
- Keeling, C. D., The concentration and isotopic abundance of carbon dioxide in the atmosphere, *Tellus*, 12, 200-203, 1960.
- Keeling, R. F., Development of an interferometric oxygen analyzer for precise measurement of the atmospheric O<sub>2</sub> mole fraction, Ph.D. thesis, Harvard University, Cambridge, Massachusetts, U.S.A., 1988.
- Keeling, R. F., T. Blaine, B. Paplawsky, L. Katz, C. Atwood, and T. Brockwell, Measurement of changes in atmospheric Ar/N<sub>2</sub> ratio using a rapid-switching, single-capillary mass spectrometer system (vol 56B, pg 322, 2006).  
Corrigendum, *Tellus Series B-Chemical and Physical Meteorology*, 58 (3), 255-255, 2006.
- Keeling, R. F., A. C. Manning, E. M. McEvoy, and S. R. Shertz, Methods for measuring changes in atmospheric O<sub>2</sub> concentration and their application in southern hemisphere air, *Journal of Geophysical Research-Atmospheres*, 103 (D3), 3381-3397, 1998.
- Keeling, R. F., A. C. Manning, W. J. Paplawsky, and A. C. Cox, On the long-term stability of reference gases for atmospheric O<sub>2</sub>/N<sub>2</sub> measurements, *Tellus Series B-Chemical and Physical Meteorology*, 59 (1), 3-14, 2007.
- Keeling, R. F., and S. R. Shertz, Seasonal and Interannual Variations in Atmospheric Oxygen and Implications for the Global Carbon-Cycle, *Nature*, 358 (6389), 723-727, 1992.
- Keppler, F., J. T. G. Hamilton, M. Brass, and T. Rockmann, Methane emissions from terrestrial plants under aerobic conditions, *Nature*, 439 (7073), 187-191, 2006.
- Khalil, M. A. K., and R. A. Rasmussen, Carbon-Monoxide in the Earths Atmosphere - Indications of a Global Increase, *Nature*, 332 (6161), 242-245, 1988.
- King, G. M., and C. F. Weber, Distribution, diversity and ecology of aerobic CO-oxidizing bacteria, *Nature Reviews Microbiology*, 5 (2), 107-118, 2007.
- Knohl, A., Carbon Dioxide Exchange and Isotopic Signature (<sup>13</sup>C) of an Unmanaged 250-year-old Deciduous Forest, Universität Göttingen, Göttingen, 2004.
- Knohl, A., E.-D. Schulze, O. Kolle, and N. Buchmann, Large carbon uptake by an unmanaged 250-year-old deciduous forest in Central Germany, *Agricultural and Forest Meteorology*, 118 (3-4), 151-167, 2003.
- Kocache, R., The Measurement of Oxygen in Gas-Mixtures, *Journal of Physics E-Scientific Instruments*, 19 (6), 401-412, 1986.
- Koppmann, R., A. Khedim, J. Rudolph, D. Poppe, M. O. Andreae, G. Helas, M. Welling, and T. Zenker, Emissions of organic trace gases from savanna fires in southern Africa during the 1992 Southern African Fire Atmosphere Research Initiative and their impact on the formation of tropospheric ozone, *Journal of Geophysical Research*, 102 (D15), 18879-18888, doi:10.1029/97JD00845, 1997.
- Kozlova, E. A., and A. C. Manning, Methodology and calibration for continuous measurements of biogeochemical trace gas and O<sub>2</sub> concentrations from a 300-m tall tower in central Siberia, *Atmospheric Measurement Techniques*, 2 (1), 205-220, 2009.

- Kozlova, E. A., A. C. Manning, Y. Kisilyakhov, T. Seifert, and M. Heimann, Seasonal, synoptic, and diurnal-scale variability of biogeochemical trace gases and O<sub>2</sub> from a 300-m tall tower in central Siberia, *Global Biogeochemical Cycles*, 22 (4), doi:10.1029/2008GB003209, 2008.
- Kurbatova, J., A. Arneth, N. N. Vygodskaya, O. Kolle, A. V. Varlargin, I. M. Milyukova, N. M. Tchepakova, E. D. Schulze, and J. Lloyd, Comparative ecosystem-atmosphere exchange of energy and mass in a European Russian and a central Siberian bog I. Interseasonal and interannual variability of energy and latent heat fluxes during the snowfree period, *Tellus Series B-Chemical and Physical Meteorology*, 54 (5), 497-513, 2002.
- Kutsch, W. L., O. Kolle, C. Rebmann, A. Knohl, W. Ziegler, and E.-D. Schulze, Advection and resulting CO<sub>2</sub> exchange uncertainty in a tall forest in central Germany, *Ecological Applications*, 18 (6), 1391-1405, 2008.
- Langenfelds, R. L., M. V. van der Schoot, R. J. Francey, L. P. Steele, M. Schmidt, and H. Mukai, Modification of air standard composition by diffusive and surface processes, *Journal of Geophysical Research - Atmospheres*, 110, D13307, doi:10.1029/12004JD005482, 2005.
- Law, B. E., P. E. Thornton, J. Irvine, P. M. Anthoni, and S. Van Tuyl, Carbon storage and fluxes in ponderosa pine forests at different developmental stages, *Global Change Biology*, 7 (7), 755-777, 2001.
- Le Treut, H., R. Somerville, U. Cubasch, Y. Ding, C. Mauritzen, A. Mokssit, T. Peterson, and M. Prather, Historical Overview of Climate Change, in *Climate Change 2007: The Physical Science Basis (Contribution of Working Group I to the Fourth Assessment Report of the Intergovernmental Panel on Climate Change)*, edited by Solomon, S., Qin, D., Manning, M., Chen, Z., Marquis, M., Averyt, K.B., Tignor, M. and Miller, H.L., pp. 93-128, Cambridge University Press, Cambridge, UK and New York, NY, USA, 2007.
- Lelieveld, J., P. J. Crutzen, and F. J. Dentener, Changing concentration, lifetime and climate forcing of atmospheric methane, *Tellus Series B-Chemical and Physical Meteorology*, 50 (2), 128-150, 1998.
- Levin, I., P. Ciais, R. Langenfelds, M. Schmidt, M. Ramonet, K. Sidorov, N. Tchepakova, M. Gloor, M. Heimann, E. D. Schulze, N. N. Vygodskaya, O. Shibistova, and J. Lloyd, Three years of trace gas observations over the EuroSiberian domain derived from aircraft sampling - a concerted action, *Tellus Series B-Chemical and Physical Meteorology*, 54 (5), 696-712, 2002.
- Lindzen, R. S., "Can Increasing Carbon Dioxide Cause Climate Change", *Proceedings of the National Academy of Sciences*, 94, 8335-8342, 1997.
- Lloyd, J., R. L. Langenfelds, R. J. Francey, M. Gloor, N. M. Tchepakova, D. Zolotoukhine, W. A. Brand, R. A. Werner, A. Jordan, C. A. Allison, V. Zrazhewske, O. Shibistova, and E. D. Schulze, A trace-gas climatology above Zotino, central Siberia, *Tellus Series B-Chemical and Physical Meteorology*, 54 (5), 749-767, 2002a.
- Lloyd, J., O. Shibistova, D. Zolotoukhine, O. Kolle, A. Arneth, C. Wirth, J. M. Styles, N. M. Tchepakova, and E. D. Schulze, Seasonal and annual variations in the photosynthetic productivity and carbon balance of a central Siberian pine forest, *Tellus Series B-Chemical and Physical Meteorology*, 54 (5), 590-610, 2002b.
- Luyssaert, S., E.-D. Schulze, A. Börner, A. Knohl, D. Hessenmöller, B. E. Law, P. Ciais, and J. Grace, Old-growth forests as global carbon sinks, *Nature*, 455 (7210), 213-215, 2008.
- Machida, T., T. Nakazawa, Y. Fujii, S. Aoki, and O. Watanabe, Increase in the Atmospheric Nitrous-Oxide Concentration During the Last 250 Years, *Geophysical Research Letters*, 22 (21), 2921-2924, 1995.
- Machta, L., and E. Hughes, Atmospheric oxygen in 1967 to 1970, *Science*, 168, 1582-1584, 1970.

- Manning, A. C., Temporal variability of atmospheric oxygen from both continuous measurements and a flask sampling network: Tools for studying the global carbon cycle, Ph.D. thesis, University of California, San Diego, La Jolla, California, U.S.A., 2001.
- Manning, A. C., A calibration and intercomparison scheme for continuous, multi-species measurements from a network of tall towers in Europe, in *Report of the Twelfth WMO/IAEA Meeting of Experts on Carbon Dioxide Concentration and Related Tracers Measurement Techniques*, edited by Worthy, D. E., and L. Huang, Toronto, 2005.
- Manning, A. C., and R. F. Keeling, Global oceanic and land biotic carbon sinks from the Scripps atmospheric oxygen flask sampling network, *Tellus Series B-Chemical and Physical Meteorology*, 58 (2), 95-116, 2006.
- Manning, A. C., R. F. Keeling, and J. P. Severinghaus, Precise atmospheric oxygen measurements with a paramagnetic oxygen analyzer, *Global Biogeochemical Cycles*, 13 (4), 1107-1115, 1999.
- Marland, G., T. A. Boden, and R. J. Andres, Global, Regional, and National Annual CO<sub>2</sub> Emissions from Fossil-Fuel Burning, Cement Production, and Gas Flaring: 1751-1999, In: Carbon Dioxide Information Analysis Center, Oak Ridge National Laboratory, U.S. Department of Energy, Oak Ridge, Tennessee, U.S.A., 2002.
- McGuire, A. D., L. G. Anderson, T. R. Christensen, S. Dallimore, L. Guo, D. J. Hayes, M. Heimann, T. D. Lorenson, R. W. Macdonald, and N. Roulet, Sensitivity of the carbon cycle in the Arctic to climate change, *Ecological Monographs*, 79 (4), pp. 523-555, 2009.
- Meure, C. M., D. Etheridge, C. Trudinger, P. Steele, R. Langenfelds, T. van Ommen, A. Smith, and J. Elkins, Law Dome CO<sub>2</sub>, CH<sub>4</sub> and N<sub>2</sub>O ice core records extended to 2000 years BP, *Geophysical Research Letters*, 33 (14), -, 2006.
- Mikaloff Fletcher, S. E., N. Gruber, A. R. Jacobson, S. C. Doney, S. Dutkiewicz, M. Gerber, M. Follows, F. Joos, K. Lindsay, D. Menemenlis, A. Mouchet, S. A. Müller, and J. L. Sarmiento, Inverse estimates of anthropogenic CO<sub>2</sub> uptake, transport, and storage by the ocean, *Global Biogeochemical Cycles*, 20, GB2002, doi:2010.1029/2005GB002530, 2006.
- Miller, J. B., Report of the Thirteenth WMO/IAEA Meeting of Experts on Carbon Dioxide Concentration and Related Tracers Measurement Techniques, edited by Miller, J. B., Boulder, CO, 2007.
- Mollicone, D., H. D. Eva, and F. Achard, Human role in Russian wild fires, *Nature*, 440 (7083), 436-437, 2006.
- Nisbet, R. E. R., R. Fisher, R. H. Nimmo, D. S. Bendall, P. M. Crill, A. V. Gallego-Sala, E. R. C. Hornibrook, E. Lopez-Juez, D. Lowry, P. B. R. Nisbet, E. F. Shuckburgh, S. Sriskantharajah, C. J. Howe, and E. G. Nisbet, Emission of methane from plants, *Proceedings of The Royal Society - B*, doi:doi: 10.1098/rspb.2008.1731, 2009.
- Novelli, P. C., L. P. Steele, and P. P. Tans, Mixing Ratios of Carbon-Monoxide in the Troposphere, *Journal of Geophysical Research-Atmospheres*, 97 (D18), 20731-20750, 1992.
- Olivier, J. G. J., A. F. Bouwman, C. W. M. van der Maas, J. J. M. Berdowski, C. Veldt, J. P. J. Bloos, A. J. H. Visschedijk, P. Y. J. Zandveld, and J. L. Haverlag, Description of EDGAR version 2.0: A set of global emission inventories of greenhouse gases and ozone-depleting substances for all anthropogenic and most natural sources on a per country basis and on 1° x 1° grid, 141 pp., Bilthoven, The Netherlands, 1996.
- Orr, J. C., Ocean Carbon-Cycle Model Intercomparison Project (OCMIP), 27 pp., 1997.
- Overpeck, J., K. Hughen, D. Hardy, R. Bradley, R. Case, M. Douglas, B. Finney, K. Gajewski, G. Jacoby, A. Jennings, S. Lamoureux, A. Lasca, G. MacDonald, J.

- Moore, M. Retelle, S. Smith, A. Wolfe, and G. Zielinski, Arctic environmental change of the last four centuries, *Science*, 278 (5341), 1251-1256, 1997.
- Pitter, R. L., W. G. Finnegan, B. A. Hinsvark, T. R. McGuire, B. Argyle, J. L. Sarmiento, and N. Gruber, More on Carbon Sinks, *Physics Today*, 56 (5), 12-14, doi:doi:10.1063/1.1583517, 2003.
- Ramaswamy, V., O. Boucher, J. Haigh, D. Hauglustaine, J. Haywood, G. Myhre, T. Nakajima, S. G.Y., and S. Solomon, Radiative Forcing of Climate Change, in *Climate Change 2001: The Scientific Basis. Contribution of Working Group I to the Third Assessment Report of the Intergovernmental Panel on Climate Change (IPCC)*, edited by Houghton, J. T., Y. Ding, D. J. Griggs, M. Noguer, P. J. van der Linden, X. Dai, K. Maskell, and C. A. Johnson, Cambridge University Press, Cambridge, 2001.
- Randerson, J. T., C. B. Field, I. Y. Fung, and P. P. Tans, Increases in early season ecosystem uptake explain recent changes in the seasonal cycle of atmospheric CO<sub>2</sub> at high northern latitudes, *Geophysical Research Letters*, 26 (17), 2765-2768, 1999.
- Randerson, J. T., G. R. van der Werf, L. Giglio, G. J. Collatz, and P. S. Kasibhatla, Global Fire Emissions Database, Version 2 (GFEDv2.1), in <http://daac.ornl.gov/>, Oak Ridge National Laboratory Distributed Active Archive Center, Oak Ridge, Tennessee, U.S.A., doi:10.3334/ORNLDAAAC/849, 2007.
- Revelle, R., and H. E. Suess, Carbon dioxide exchange between atmosphere and ocean and the question of an increase of atmospheric CO<sub>2</sub> during the past decades, *Tellus*, 9, 18-27, 1957.
- Rödenbeck, C., C. Le Quere, M. Heimann, and R. F. Keeling, Interannual variability in oceanic biogeochemical processes inferred by inversion of atmospheric O<sub>2</sub>/N<sub>2</sub> and CO<sub>2</sub> data, *Tellus*, 60B (5), 685-705, 2008.
- Rödenbeck, C., S. Houweling, M. Gloor, and M. Heimann, CO<sub>2</sub> flux history 1982-2001 inferred from atmospheric data using a global inversion of atmospheric transport, *Atmospheric Chemistry and Physics*, 3, 1919-1964, 2003.
- Röser, C., L. Montagnani, E. D. Schulze, D. Mollicone, O. Kolle, M. Meroni, D. Papale, L. B. Marchesini, S. Federici, and R. Valentini, Net CO<sub>2</sub> exchange rates in three different successional stages of the "Dark Taiga" of central Siberia, *Tellus Series B-Chemical and Physical Meteorology*, 54 (5), 642-654, 2002.
- Sabine, C. L., R. A. Feely, N. Gruber, R. M. Key, K. Lee, J. L. Bullister, R. Wanninkhof, C. S. Wong, D. W. R. Wallace, B. Tilbrook, F. J. Millero, T. H. Peng, A. Kozyr, T. Ono, and A. F. Rios, The oceanic sink for anthropogenic CO<sub>2</sub>, *Science*, 305 (5682), 367-371, 2004.
- Sarmiento, J. L., and N. Gruber, Sinks for Anthropogenic Carbon, *Physics Today*, 55 (8), 30-36, doi:doi:10.1063/1.1510279, 2002.
- Schulze, E. D., N. N. Vygodskaya, N. M. Tchebakova, C. I. Czimczik, D. N. Kozlov, J. Lloyd, D. Mollicone, E. Parfenova, K. N. Sidorov, A. V. Varlagin, and C. Wirth, The Eurosiberian Transect: an introduction to the experimental region, *Tellus Series B-Chemical and Physical Meteorology*, 54 (5), 421-428, 2002.
- Schuur, E., J. Bockheim, J. Canadell, E. Euskirchen, C. Field, S. Goryachkin, S. Hagemann, P. Kuhry, P. Lafleur, and H. Lee, Vulnerability of permafrost carbon to climate change: implications for the global carbon cycle, *BioScience*, 58 (8), 701-714, 2008.
- Seibt, U., W. A. Brand, M. Heimann, J. Lloyd, J. P. Severinghaus, and L. Wingate, Observations of O<sub>2</sub>:CO<sub>2</sub> exchange ratios during ecosystem gas exchange, *Global Biogeochemical Cycles*, 18 (4), 2004.
- Severinghaus, J. P., Studies of the terrestrial O<sub>2</sub> and carbon cycles in sand dune gases and in Biosphere 2, Ph.D. thesis, Columbia University, New York, U.S.A., 1995.

- Shibistova, O., J. Lloyd, S. Evgrafova, N. Savushkina, G. Zrazhevskaya, A. Arneth, A. Knohl, O. Kolle, and E. D. Schulze, Seasonal and spatial variability in soil CO<sub>2</sub> efflux rates for a central Siberian *Pinus sylvestris* forest, *Tellus Series B-Chemical and Physical Meteorology*, 54 (5), 552-567, 2002a.
- Shibistova, O., J. Lloyd, G. Zrazhevskaya, A. Arneth, O. Kolle, A. Knohl, N. Astrakhantceva, I. Shijneva, and J. Schmerler, Annual ecosystem respiration budget for a *Pinus sylvestris* stand in central Siberia, *Tellus Series B-Chemical and Physical Meteorology*, 54 (5), 568-589, 2002b.
- Sohngen, B., K. Andrasko, M. Gytarsky, G. Korovin, L. Laestadius, B. Murray, A. Utkin, and D. Zamolodchikov, Carbon Inventory and Mitigation Potential of the Russian Forest and Land Base, edited by Barrell, S., pp. 62, World Resources Institute, Washington, DC, 2005.
- Stephens, B. B., P. Bakwin, P. P. Tans, and R. Teclaw, Measurements of atmospheric O<sub>2</sub> variations at the WLEF tall-tower site, in *Sixth International Carbon Dioxide Conference, Extended Abstracts*, edited by Nakazawa, T., Sendai, Japan, 2001.
- Stephens, B. B., P. S. Bakwin, P. P. Tans, R. M. Teclaw, and D. D. Baumann, Application of a differential fuel-cell analyzer for measuring atmospheric oxygen variations, *Journal of Atmospheric and Oceanic Technology*, 24 (1), 82-94, doi:10.1175/JTECH1959.1171, 2007.
- Stephens, B. B., R. F. Keeling, M. Heimann, K. D. Six, R. Murnane, and K. Caldeira, Testing global ocean carbon cycle models using measurements of atmospheric O<sub>2</sub> and CO<sub>2</sub> concentration, *Global Biogeochemical Cycles*, 12 (2), 213-230, 1998.
- Stephens, B. B., R. F. Keeling, and W. J. Paplawsky, Shipboard measurements of atmospheric oxygen using a vacuum-ultraviolet absorption technique, *Tellus Series B-Chemical and Physical Meteorology*, 55 (4), 857-878, 2003.
- Styles, J. M., J. Lloyd, D. Zolotoukhine, K. A. Lawton, N. Tchebakova, R. J. Francey, A. Arneth, D. Salamakho, O. Kolle, and E.-D. Schulze, Estimates of regional surface carbon dioxide exchange and carbon and oxygen isotope discrimination during photosynthesis from concentration profiles in the atmospheric boundary layer, *Tellus Series B-Chemical and Physical Meteorology*, 54 (5), 768-783, 2002.
- Svensmark, H., and E. Friis-Christensen, Variation of cosmic ray flux and global cloud coverage - a missing link in solar-climate relationships, *Journal of Atmospheric and Solar-Terrestrial Physics*, 59 (11), 1225-1232, 1997.
- Takahashi, T., R. H. Wanninkhof, R. A. Feely, R. F. Weiss, D. W. Chipman, N. Bates, J. Olafsson, C. Sabine, and S. C. Sutherland, Net sea-air CO<sub>2</sub> flux over the global oceans: An improved estimate based on the sea air pCO<sub>2</sub> difference, in *2nd CO<sub>2</sub> in Oceans Symposium*, Centre for Global Environ. Res. Natl. Inst. for Environ. Studies, Tsukuba, Japan, 1999.
- Tans, P., Observational Strategy for Assessing the Role of Terrestrial Ecosystems in the Global Carbon Cycle: Scaling Down to Regional Levels, in *Scaling Physiological Processes: Leaf to Globe*, edited by Ehleringer, J. R., and C. B. Field, pp. 179-190, Academic Press, Inc., San Diego, 1993.
- Tarasova, O. A., C. A. M. Brenninkmeijer, S. S. Assono, N. F. Elansky, T. Rockmann, and M. Brass, Atmospheric CH<sub>4</sub> along the Trans-Siberian railroad (TROICA) and river Ob: Source identification using stable isotope analysis, *Atmospheric Environment*, 40 (29), 5617-5628, 2006.
- Trenberth, K. E., P. D. Jones, P. Ambenje, R. Bojariu, D. Easterling, A. Klein Tank, D. Parker, F. Rahimzadeh, J. A. Renwick, M. Rusticucci, B. Soden, and P. Zhai, Observations: Surface and Atmospheric Climate Change, in *Climate Change 2007: The Physical Science Basis. Contribution of Working Group I to the Fourth Assessment Report of Intergovernmental Panel on Climate Change*, edited by Solomon, S., D. Qin, M. Manning, Z. Chen, M. Marquis, K. B.

- Averyt, M. Tignor, and H. L. Miller, Cambridge University Press, Cambridge, United Kingdom and New York, NY, USA, 2007.
- Trivett, N., and A. Koehler, Guide on Sampling and Analysis Techniques for Chemical Constituents and Physical Properties in Air and Precipitation as Applied at Stations of the Global Atmosphere Watch, Part 1: Carbon Dioxide, 39 pp., Geneva, 2000.
- Tyndall, J., On the absorption and radiation of heat by gases and vapours, and on the physical connection, *Philos. Mag.*, 22, 277-302, 1861.
- Valentini, R., G. Matteucci, A. J. Dolman, E.-D. Schulze, C. Rebmann, E. J. Moors, A. Granier, P. Gross, N. O. Jensen, K. Pilegaard, A. Lindroth, A. Grelle, C. Bernhofer, T. Grünwald, M. Aubinet, R. Ceulemans, A. S. Kowalski, T. Vesala, Ü. Rannik, P. Berbigier, D. Loustau, J. Guomundsson, H. Thorgeirsson, A. Ibrom, K. Morgenstern, R. Clement, J. Moncrieff, L. Montagnani, S. Minerbi, and P. G. Jarvis, Respiration as the main determinant of carbon balance in European forests, *Nature*, 404 (6780), 861-865, 2000.
- van der Molen, M. K., and A. J. Dolman, Regional carbon fluxes and the effect of topography on the variability of atmospheric CO<sub>2</sub>, *Journal of Geophysical Research-Atmospheres*, 112 (D1), D01104, doi:01110.01029/02006JD007649, 2007.
- Vermeulen, A. T., G. Pieterse, A. Hensen, W. C. M. van den Bulk, and J. W. Erisman, COMET: a Lagrangian transport model for greenhouse gas emission estimation forward model technique and performance for methane, *Atmospheric Chemistry and Physics Discussions*, Vol. 6, pp 8727-8779, 2006.
- Vermeulen, A. T., A. Hensen, M. Gloor, A. C. Manning, P. Ciais, R. Eisma, W. C. M. van den Bulk, J. J. Mols, and J. W. Erisman, CHIOTTO - Continuous High precision Tall Tower Observations of greenhouse gases, in *Inverse modelling of national and EU greenhouse gas emission inventories*, edited by P., B., H. Behrend, and A. Jol, Ispra, 2004.
- Ward, D. E., R. A. Susott, J. B. Kaufman, R. E. Babbit, D. L. Cummings, B. Dias, B. N. Holben, Y. J. Kaufman, R. A. Rasmussen, and A. W. Setzer, Smoke and fire characteristics for cerrado and deforestation burns in Brazil: Base-B Experiment, *Journal of Geophysical Research*, 97, 14601-14619, 1992.
- Warneck, P., *Chemistry of the Natural Atmosphere*, 770 pp., Academic Press, San Diego, California, 1988.
- Watson, A. J., and J. R. Ledwell, Oceanographic tracer release experiments using sulphur hexafluoride, *Journal of Geophysical Research-Oceans*, 105 (C6), 14325-14337, 2000.
- Weart, S., *The Discovery of Global Warming*, 240 pp., Harvard University Press, MA, Cambridge, 2003.
- Weiss, R. F., The solubility of nitrogen, oxygen and argon in water and seawater, *Deep-Sea Research*, 17, 721-735, 1970.
- WMO, Greenhouse Gas Bulletin, No. 4, <ftp://ftp.wmo.int/Documents/PublicWeb/arep/gaw/ghg-bulletin-4-final-english.pdf>, 2008.
- Worthy, D. E. J., I. Levin, N. B. A. Trivett, A. J. Kuhlmann, J. F. Hopper, and M. K. Ernst, Seven years of continuous methane observations at a remote boreal site in Ontario, Canada, *Journal of Geophysical Research-Atmospheres*, 103 (D13), 15995-16007, 1998.
- Worthy, D. E. J., A. Platt, R. Kessler, M. K. Ernst, and S. Racki, The greenhouse gases measurement program: Measurement procedures and data quality, in *Canadian Baseline Program, Summary of Progress to 2002*, edited by Worthy, D. E. J., 97-120 pp., Downsview, Ontario, 2003.

Zimov, S. A., I. P. Semiletov, S. P. Daviodov, Y. V. Voropaev, S. F. Prosyannikov, C. S. Wong, and Y. H. Chan, Wintertime CO<sub>2</sub> Emission from Soils of Northeastern Siberia, *Arctic*, 46 (3), 197-204, 1993.